SIMULATION OF THE MANUFACTURE OF

CLOSED SHAPE COMPOSITE STRUCTURES

by

ZHONG   CAI

B.E.   East China Institute of Textile Technology
(1982)

M.S. Massachusetts Institute of Technology
(1986)

Submitted to the Department of
Mechanical Engineering
in Partial Fulfillment of the
Requirements for the Degree of

DOCTOR OF SCIENCE

IN MECHANICAL ENGINEERING

at the

MASSACHUSETTS INSTITUTE OF TECHNOLOGY

April 1990

Copyright (c) 1990 Massachusetts Institute of Technology

Signature of Author _____
Department of Mechanical Engineering
April 10, 1990

Certified by _____
Prof. Timothy G. Gutowski
Thesis Supervisor

Accepted by _____
Prof. Ain A. Sonin
Chairman, Department Graduate Committee

SIMULATION OF THE MANUFACTURE OF

CLOSED SHAPE COMPOSITE STRUCTURES

by

ZHONG   CAI

Submitted to the Department of Mechanical Engineering
On April 10, 1990 in partial fulfillment of the
requirements for the Degree of Doctor of Science
in Mechanical Engineering

ABSTRACT

A process model was developed for the fabrication of closed shape
composite structures such as thick-wall cylinders, with the emphasis on
fiber bundle deformation and its effect on the process physics. A con-
tinuum mechanics model for fiber bundle deformation in the composite
manufacturing processes was proposed. Based on this model, the winding and
consolidation processes for thick wall cylindrical composite structure were
analyzed, and a process model was developed. Fiber bundle deformation was
considered as the combination of elastic and viscous responses. In some of
the manufacturing processes, such as winding, pultrusion, and molding, the
elastic response can be dominant. A compliance matrix for the fiber bundle
was proposed and three independent compliance terms were evaluated
quantitatively by assuming a statistical distribution of imperfect condi-
tions in the fiber bundle. These included small waviness, misalignment, and
fiber crossover. These compliance terms were found to be functions of the
fiber deformation state, which can be expressed by using the fiber volume
fraction. This relationship was then used in the analysis of the winding
and consolidation processes. It was found that two constants determined
whether the process was an elastic dominated or a fiber deformation/resin
flow process. If the winding time was much shorter than the flow time con-
stant, the winding process can be thought as elastic dominant. On the
other hand if the flow time constant was much less than the winding time,
flow was substantial in the winding. When winding operation was finished,
the consolidation of composite layers was also completed. Nonlinear analy-
sis on fiber deformation can be applied in this case. Under general condi-
tions, the process consisted of material deformation coupled with the mass
flow. A series of experiments on fiber deformation compliance, fiber mo-
tion and distribution in molding, winding and consolidation process time
evaluation, and simulation of the winding and consolidation were designed
and carried out. Experimental results verified the computer simulation
model predictions and helped understanding of various process mechanisms.

Thesis Committee:
Professor Timothy Gutowski (Chairman)
Professor Stanley Backer
Professor Rohen Abeyaratne

ACKNOWLEDGEMENTS

I am grateful to my thesis supervisor, Professor Timothy Gutowski, for his direction, inspiration, and encouragement throughout the duration of this thesis. I would like to thank Professor Stanley Backer and Professor Rohen Abeyaratne for their assistance and advice. Special thanks go to Dr. Steven Allen now retired from Draper Lab, for initiating this project and obtaining funding, for helping me with my programming and experiments, and for proof-reading of my thesis.

This research work was sponsored by the Charles Starker Draper Laboratory and the MIT-Industry Composite and Polymer Processing Program, whose members were Aluminum Company of America (Alcoa), Boeing Commercial Airplane, DuPont, Lord Corporation, Hysol Division of Dexter, Kraft, Martin Marietta Aerospace, Norton Performance Plastics, and Nashua Corporation. I am grateful for the financial support provided by Draper Lab throughout my four year doctoral study at MIT.

Thanks to Mr. Tom Heimann of Draper Lab for helping me through the last part of experiments. Also thanks to Mr. Archie Bice of DuPont for helpful discussions about my test devices. Thanks to DuPont for their donation of the autoclave equipment.

I am obliged to many people in the Laboratory for Manufacturing and Productivity. I would like to thank Professor Ming Tse for various helps and encouragements, and to Dr. Greg Dillon for his generous help in setting

3

TABLE OF CONTENTS

LIST OF FIGURES

8

LIST OF TABLES

1. INTRODUCTION

1-1. Background

Composite materials have been widely used in various structures in recent years. As the manufacturing methods and processing techniques for composite materials are very different from the conventional machining methods for metals and alloys, researchers have been working on analyzing, developing, and controlling these processes and techniques. Currently the most widely used composite materials are fiber reinforced thermoplastics and thermosets, in which fibers are used as the backbone of the material for stiffness and strength, while the polymeric materials are used as adhesive to form the composite and at the same time to improve material properties. One significant difference of the processing techniques from the metal machining is that the process is additive. Another concern is to make the material homogeneous through the processing. In order to obtain high stiffness and high strength in the finished material, the consolidation and cure are the most important issue in the processing. While the cure process is mainly a chemical reaction process of the resin matrix material, the consolidation process can be considered as mechanical deformation of the material, which in the processing, is the mixture of solid fibers and liquid resin. To insure a good quality of the final micro-structure of the material, certain process parameters, such as fiber volume fraction, fiber distribution, residual stress, and void content, are widely used to evaluate the material quality and performance. The manufacturing process of the composite material usually involves applying heat and

11

pressure to the material, as a result of which the material undergoes deformation, flow, and chemical reaction. The basic physics of the process from the mechanical engineering point of view, includes heat transfer, mass flow, forced deformation, and micro and macro structural changes. Understanding such a complicated process is a real challenge to research engineers and scientists working in this field.

With the rapid development of various processing techniques In the late 70s and early 80s, systematic research on modeling and analyzing composite manufacturing processes were conducted. Among numerous individual efforts, Springer and coworkers did substantial work on developing manufacturing process models of laminate composite materials [1,2,3,4,5,6,7]. They also developed simulation software which analyzes the physical mechanism of the process and predicts the final product quality. As more and more new processes were introduced into production, such as pultrusion, winding, thermal forming, and resin transfer molding, a large number of papers and reports were published on these techniques. Computer software was also developed and used to help design and control the processes. Since these manufacturing processes are complicated, the approaches and assumptions of various models are sometimes very different. This helps a better understanding of the process mechanisms from different aspects. Because the manufacturing processes also involve several different disciplines, such as material science, chemical engineering, and mechanical engineering, people working in the different fields may also have different insights on problems. In general, the process modeling of the composite manufacturing is still a developing field which needs great effort and cooperation.

The work being discussed here is the manufacturing process analysis of so called closed shape composite structures, with a particular interest on fiber deformation and its effect during the process. Typical examples of such structures are cylindrical shaped pressure vessel, and spherical shaped container. The most widely used manufacturing method for such products is winding. For simple structure such as cylindrical and elliptical tubes, both tape winding and filament winding may be used. For other very complicated geometry shapes, usually only filament winding can be used. With newly developed computer controlled multi-axial winder, that task has been greatly simplified. As the winding equipment was dramatically improved, the analysis of the winding process becomes a great challenge to the process modeling workers. The whole manufacturing process involves not only the winding, but also several important and complicated stages after the winding. After the shape and dimensions of the product are formed in the winding operation, the whole composite part is heated and sometimes also pressurized in order to consolidate and cure the material, which is still the mixture of fibers and uncured resin matrix. Usually excess resin is removed and a higher fiber volume fraction is achieved by the consolidation. In order to improve the final product quality, some post-cure heat treatment is often applied to improve the residual stress within the structure and to insure the material is fully cured. One significant difference of this kind of structure from laminate composite is the complex stress state of the fiber network during the manufacturing process and in the following applications. If not handled properly, defects can be easily introduced in the structure, such as buckled fibers, wrinkled layer, interfacial delamination, uneven fiber distribution, etc. A thorough under-

standing of the material micro-structure and properties is necessary in order to obtain the desired product quality.

1-2. Review of Other Work

The use of filament winding process to fabricate composite structures started over forty years ago. With the great changes in materials and equipment over decades, it has become one of the main composite manufacturing techniques, and is widely used in industry. For certain closed shape complicated composite structures, it is probably the only technique used in production. The cost effectiveness of different manufacturing processes has been recently evaluated by Krolewski and Gutowski [8], which indicates that pultrusion and filament winding are more cost effective than other processes. Future applications of this technique also seem very bright since the overall growth of the composite structure market is assured. Recently, Munro [9] and Wilson [10] presented very thorough reviews of this technique and also discussed its future development.

As this technique was introduced in the composite manufacturing area, research workers put great effort on analyzing and modeling the process. Early research work was concentrated on measuring and calculation of residual stresses in the filament wound structures. The material was treated as transversely isotropic but linear elastic material. Liu and Chamis gave out an analytical solution on residual stress of wound cylindrical structure, and also presented an optimum winding tension method to reduce the residual stress [11]. Fourney presented similar theoretical calculations and experimental results of residual strain in filament-wound

rings [12]. Dewey and Knight applied approximate curved beam theory to approach the same problem, which allowed variation of the material modulus in the circumferential direction [13]. Tarnopol'skii and Portnov obtained an analytic solution for winding anisotropic elastic materials on a cylindrical mandrel and found strong relationship between the winding tension and the stress distribution [14]. Beil, Portnov, Sanina, and Yakushin proposed an alternate way to control the stress by varying the winding angle over the thickness [15]. Later, Grabovskii also solved similar problem on winding of magnetic tape in which only elastic deformation was taken into account, and they found that varying the winding tension over layers was an effective way to change the residual stress distribution [16]. These early studies emphasized the residual stresses within the material but did not look at the manufacturing process.

As the winding technique is also widely used in other industry for materials such as paper, film, plastic sheet, and magnetic tape, analysis for the winding mechanics was presented in numerous studies. One early work was done by Altmann [17] which was probably the most widely used analysis in these fields. One important assumption in his study was that the tape reel was linear elastic in the radial direction. This restriction was relaxed and removed later by other models, with some of them using the viscoelastic approach. Willett and Poesch presented an excellent summary of the research literature in this area and they also proposed a nonlinear approach to the problem [18]. Recently, Lin and Westmann proposed a viscoelastic model for analyzing the winding, winding-pause, and unwinding history of the tape system by assuming that the modulus of the material

followed the Maxwell model for creep and changed as a function of the process time [19].

As this technique was widely used further in 70s and 80s in the composite area, research on process modeling and design was further developed. One significant difference between the magnetic tape, paper, or film material and the composite layer is that the former does not have mass flow in the winding process, while the latter has. This makes the modeling work much more complicated. Reuter did some pioneer work on predicting material stress in the winding process. Later Springer and Calius developed a more complete computer model which included resin flow, heat transfer, material chemical reaction, heat generation, and stress distribution. Spencer also developed a general model which consists of several sub-models to describe the process step by step. Research work was also reported by Tarnopol'skii and coworkers in U.S.S.R. These studies will be reviewed here. There was also other research work on some specific filament-wound structures and products especially for aerospace structures and pressure vessels.

Reuter [20] constructed an analytical model to predict and control the stress state of a filament-wound cylindrical product. In his model the material was considered to be linear elastic, but no elasticity in the radial direction was considered. This suggests that the calculation was based on the "thin" shell assumption, in which the ratio of the layer thickness t to the outer radius of the mandrel R was bounded. The migration of the layer during the process was considered, but no resin flow was included in the modeling. The effect of varying the winding tension over

16

layers was also studied and the result showed that it had great influence on the stress distribution.

Spencer [21,22,23] improved Reuter's model by including the resin flow and cure reaction during the process. His model was more complete and was divided into eight sub-models to cover all different operation stages. Among them there were four main physical models. A composite layer stiffness model accounted for the varying stiffness of the material with the increasing contribution of the resin as cure progressed. A resin flow model included both the axial and radial flow through the laminate. A cure kinetics model included resin viscosity, cure state, and heat of reaction for the epoxy resin. A heat transfer model accounted for the resin heat of reaction and the curing effect. In his resin flow sub-model, he considered both the radial flow and the axial flow. The radial flow was treated as flow through porous media, and the axial flow as channel flow. He did not include either fiber network deformation or load carried by fiber network in the radial direction.

Springer, Calius, and coworkers developed a complete model for the filament winding process [24,25,26,27,28,29,30], based on their previous work on the modeling of laminate curing process. Their model includes a large set of process variables which determines the material state and product dimensions. Their model also consists of three sub-models, with each of the separate models following a particular set of effects. The thermochemical model describes the heat transfer and resin curing portion of the process. The fiber motion model looks at the movement of the wound fibers due to the tension in the fibers in the winding operation. The

stress model simulates the deformations and strains in the wound shell after it has been hardened. For the fiber motion model, fibers were represented as a solid fiber sheet encapsulated within the resin layers, so that no load was carried by fibers in the radial direction. This assumption for the fiber layer motion was based on the observation that the time required to wind each layer was generally negligible compared to the total time involved in winding the entire shell. In fact this assumption is reasonable only if the time required to wind each layer was small compared to some time constant for the fiber motion through the resin, which would be the consolidation time for each layer.

Based on their earlier work, Tarnopol'skii, Portnov, and Beil developed detailed theoretical analysis on mechanics problems in composite winding [31,32]. Because the material physical-mechanical properties and the stress-strain state changed substantially during the whole process, their solution involved the division of the mechanical history into several stages. This allowed a series of simplification to be employed in each stage. In the winding analysis, they presented both a linearly elastic ring model and a nonlinearly elastic ring model, of which the latter took into account the nonlinear deformation behavior of the prepreg tape in the transverse direction. Then they proposed a linearly thermoelastic anisotropic ring model for the thermal effect. Stress calculations were performed continuously throughout these stages. They discussed several ways to control the stress state of the material, such as programmed winding, pressing and rolling while winding, winding with layer-by-layer curing, and variation of the reinforcement pattern.

In all these different models about the winding and subsequent cure and post-cure process, the fiber deformation behavior was not considered or was just simplified. In the development of computer models for the open structure such as laminate composite, it was found that the fiber bundle or fiber network deformation cannot be neglected if the fiber volume fraction is high, such as 0.6 to 0.7. Same is true in the winding and consolidation of the closed shape structure. In the filament-wound structure, fiber volume fraction is usually high compared with other processing techniques. Our work here is to study the fiber network or fiber bundle deformation behavior in the winding and consolidation processes, and based on this study to develop a computer simulation model which can be used in designing and controlling of the manufacturing process.

1-3. Review of Previous Work in This Group

In the previous work of this group on modeling the composite manufacturing process, fiber deformation behavior in the transverse direction was considered for the molding of laminate composites, and a fiber deformation model for the transverse loading condition in the open structure was proposed [33,34,35]. It was found that fiber bundles may carry a large portion of the load in the transverse direction when fiber volume fraction becomes high ($V_f > 0.6$-0.65). This resulted from the fact that fiber tows or bundles were not perfect in the processing. As there are thousands of fibers within a tow, it is usually unavoidable to have some waviness, misalignment, entanglement, or even breakage within a fiber tow or bundle. This was verified by tracing fiber positions within the tow in the experiment observations. This fiber tow condition resulted in great

19

influence on material behavior not only in the finished composite parts but also in the manufacturing process. The study showed that in the laminate molding case, fiber network deformation resulted in load transfer from the fluid to the fibers. Resin pressure dropped substantially in some applied consolidation conditions, although the applied load in these cases was still high enough. This transverse fiber deformation model helped design and control the molding process and determine the process variables.

In the case of closed shape composite structure, fiber network still plays an important role. For structures such as cylinder, elliptical tube, or sphere, radial resin flow dominates the consolidation process. In the consolidation process, the applied load is mainly in the fiber bundle transverse direction. The load transfer observed in the open shape laminate molding case also appears here. However, now the fiber tows are under a more complex stress state. Usually there is a large tension in the longitudinal direction and compression in the transverse direction. This is very different from the open shape laminate case, in which only transverse compression exists. There are also restrictions of the fiber motion in the circumferential direction because of the closed shape geometry. In some cases this would produce a large compression stress in the fiber axial direction during the fabrication. The result would be defects of buckled fibers or wrinkled layers. This kind of defects have been reported in closed shape composite structures. Understanding of the fiber bundle deformation behavior will help control the process and eliminate these defects.

In this study we concentrate on deformation of the fiber bundle and its influence to the process. Based on the previous transverse fiber bundle deformation model, we propose a more general continuum mechanics model for the fiber deformation and to describe the behavior of the fiber-resin mixture. Then we use this model in the analysis of the winding and consolidation processes. Fiber bundle deformation behavior and the winding and consolidation of the material were also studied experimentally. This part of the work was then be incorporated into an overall computer simulation model for the manufacturing of thick-wall cylindrical shape composite structures. In the development of the computer model, we also include analysis of other processes, such as heat transfer, resin flow, cure kinetics, viscosity variation, post-cure thermal stress, and material properties. These were incorporated by using some existing models and by revising of these models.

1-4. Overview of the Thesis

Following this introduction chapter, there is a presentation of the general model in Chapter 2 about the manufacturing of the cylindrical shaped product, which includes analyses of winding, consolidation, heat transfer, and thermal stress, etc. Numerical formulation of the computer simulation programs and the structure of the computer simulation software are also presented. Some of the problems encountered in the numerical formulation are discussed. Then in Chapter 3 a detailed discussion of the fiber bundle deformation in composite manufacturing processes is presented, which covers more general manufacturing processes other than the winding. The discussion includes observations of various fiber deformation modes,

21

elastic and viscous responses of a fiber bundle under different loading conditions, and evaluation of the elastic compliance terms. The next chapter discusses the numerical formulation of the computer simulation program, which uses the finite difference method and a series of iteration loops to solve the nonlinear and time dependent partial differential equations. Chapter 5 covers a series of experiments performed in this project, such as measurement of different fiber bundle compliance terms, fiber distribution and resin flow in laminate molding, wet filament winding simulation, winding and consolidation time constant evaluation, and consolidation of the cylindrical sample part. Fiber model developed in Chapter 3 is applied and verified in various tests. Comparisons between the model predictions and the experiment measurements are discussed. The last Chapter comes to the conclusions and suggestions of this project. Various test data are included in Appendices.

2. PROCESS MODEL

2-1. Introduction

Our process model assumes a cylindrical structure formed by using fibrous polymeric composite materials, which consists of continuous and aligned high strength fibers and polymeric resin matrix. As usual the manufacturing process includes several different stages: winding, consolidation or debulking, curing, and post-cure heat treatment. In some of these stages, only simple physics is involved, such as elastic deformation of the material in the prepreg tape winding operation. In other cases, very complicated processes take place simultaneously, such as heat transfer, chemical reaction, and fluid flow in the curing stage. In order to simplify the problem, process modeling usually divides the whole model into several sub-models, and different sub-models are proposed for each stage or sub-process. The same approach was also used by Spencer [21,22,23], Calius and Springer [24,27], and Tarnopol'skii and coworkers [31,32] in their studies.

In this modeling, we emphasize fiber bundle deformation and material consolidation during the whole manufacturing process. In the following discussion, we present a detailed discussion of this subject, the winding and consolidation part of the problem. Then we discuss the heat transfer and thermal stress calculation, which cover the cure and post-cure stages. The main parameters in this approach will be fiber volume fraction, fiber stress, resin pressure, and product dimensions.

2-2. Winding and Consolidation

2-2-1. Introduction

Winding is the first step in the filament or tape winding process for manufacturing composite structures, in which the shape of the product is formed by winding tapes or fibers on to a mandrel. Winding tension force is usually applied and controlled to consolidate the structure and to keep tension stress in fiber tows. The stress distribution resulted from the winding operation will affect the consequent operations as well as the final residual stress. The product dimensions are also partially determined by the winding tension force.

The material used in winding can be either the prepreg tape, which is the combination of uncured resin and fibers, or fiber tows soaked with wet resin. Usually aligned and continuous high strength fibers are used for the operation. Various geometric shapes can be formed although the most common structures are cylindrical or elliptical tubes.

Since in some cases the resin content is high during and after the winding, consolidation becomes a necessary step to bring the fiber volume fraction to the desired higher range by squeezing out the excess resin. For the prepreg tape winding process, if the initial resin viscosity is high, flow is negligible in the winding, the process can then be thought as an elastic deformation dominated process. This approach was used by Reuter [20], Spencer [21,22,23], and Tarnopol'skii [31,32]. On the other hand,

24

wet filament and tow winding process involves using relatively low vis-
cosity resin systems. In this case, resin flow and fiber repositioning
have to be taken into account. Calius and Springer [24,27] considered this
case, but they modeled fiber bundle as a solid fiber sheet encapsulated in
the resin, which meant that the time required to wind each layer was much
smaller than the time needed to consolidate the layer.

In this discussion, we use a more general approach to consider the
winding and consolidation stages together. We treat winding as a dynamic
process which combines the application of the winding tension, the squeez-
ing flow of the uncured resin, and the deformation of the fiber network.
The winding tension force builds up the internal pressure, which then con-
solidates the composite layers and squeezes out resin. The fiber network
acts as a deformable porous medium. Under this consolidation pressure,
fibers are compacted, which makes fiber bundle stiffer and the flow
resistance higher. Depending on the flow time constant and the winding
process time, the flow process can be either included or neglected. We
will discuss two special cases in which elastic deformation is dominant.
One is the tape winding with very high viscosity resin system, which is
similar to the case presented by Reuter in [20]. We present a more general
model without any of the restrictions in [20]. This is especially useful
in the analysis of filament winding process for composites since the
material is usually anisotropic and the ratio of layer thickness to the
radius varies according to different structural designs. The second case
is the wet filament winding process, in which the resin squeezing flow is
substantial and the consolidation of the material is almost completed after
the winding. In this case the deformation of the fiber network determines

the final dimensions of the product and the stress state. Thus nonlinear

elastic analysis on fiber bundles can be applied to this case to calculate

the material responses.

2-2-2. Analysis of winding with consolidation

The process of winding a cylindrical structure is shown in Fig. 2-

1. A mandrel is used to support the structure in the operation. Since the

structure is axially symmetric, the main flow is in the radial direction,

and flow at both ends in the axial direction is not desirable and can

usually be neglected. Fibers are under a complex stress state because of

the winding tension applied, which makes them tend to move inward to a new

equilibrium state. This is shown in Fig. 2-2.

For each layer wound onto the mandrel, there exists an equilibrium

condition between the winding tension force and radial pressure on the

layer or mandrel. This can be written as

$$T \cos^2\theta = p R \qquad\qquad (2-1)$$

where T is the winding tension force over one layer per unit length, p is

the total radial pressure, which is also called consolidation pressure; R

is the radial position vector of the wound layer, which changes with dif-

ferent layers, and θ is the winding angle or helix angle of the layer which

is measured from the "hoop direction" as shown in the figure, so that when

$\theta=0$ the winding is done in the circumferential direction. Usually each

layer is designed with different winding angles to achieve better struc-

tural performance. Often the winding pattern is symmetric in the axial

FIBER   **MANDREL**

θ
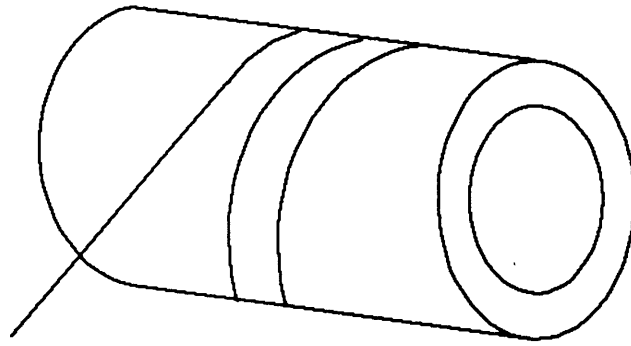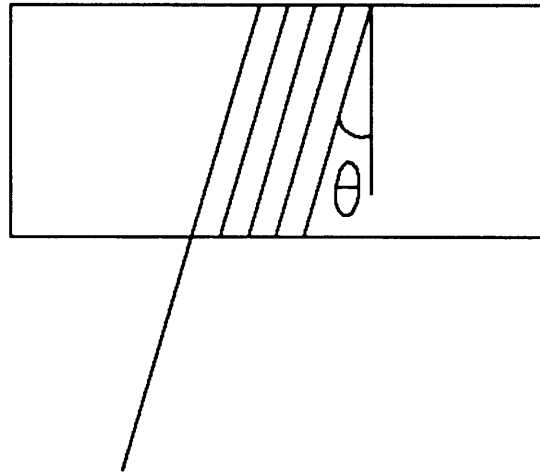
Fig. 2-1: Winding of a cylindrical structure

RESIN FLOW

FIBER STRESS

WINDING TENSION

FIBER TOW

CONSOLIDATION PRESSURE
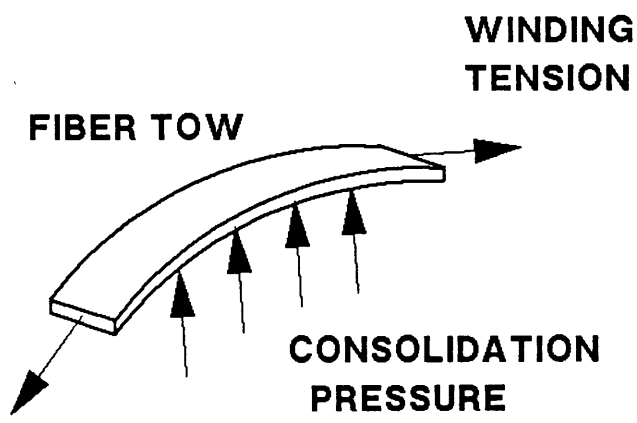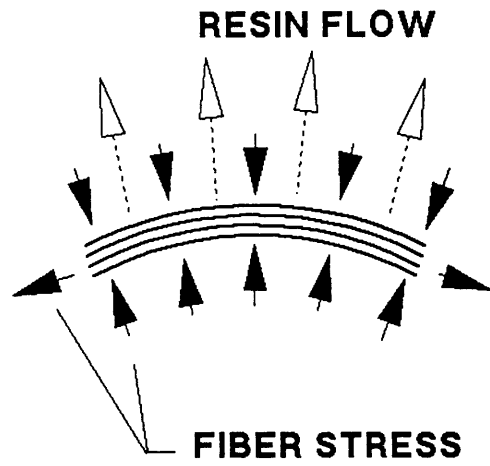
Fig. 2-2: Fiber stress and resin flow state during and after the winding

direction, which means equal numbers of layers are wound in the plus θ and

minus θ directions. If we only consider the induced deformation in the

radial direction, the problem can be simplified as a plane problem.

When the first layer is wound on to the mandrel, the consolidation

pressure p is established at the mandrel/composite interface. This con-

solidation pressure is balanced by the winding tension applied to the

layer. Since the composite layer is the mixture of the fiber and uncured

resin matrix, this consolidation pressure will cause resin to flow out of

the material. For this first layer, the inner boundary pressure, which is

the pressure at the mandrel/layer interface, is a finite consolidation

pressure, while the outer boundary pressure, which is at the outer surface

of the layer, must be the atmospheric pressure, or zero gage pressure.

This pressure gradient over the layer will induce the outward resin flow.

At any later moment, when k-1 layers are already wound on to the

mandrel, and layer k is being wound, similar analysis can still be applied.

Because of the winding tension, the consolidation pressure is established

between the newly wound layer and the existed layers. For the k-1 layers

already wound, there is a pressure increase at the outer surface. For

layer k being wound, the situation is similar to the case when the first

layer is wound on to the mandrel.

Since the material is the mixture of the uncured resin matrix and

the fiber bundle, and the pressure at the boundary changes with the winding

operation, the whole wound structure is not at the stable state. Fibers

try to move to the new equilibrium state and release some tension, and

resin flows out from the structure. This is also shown in Fig. 2-2. How fast this consolidation happens depends on the material condition and winding process parameters. In some cases the consolidation could be neglected, but in general this consolidation is important to the whole process analysis.

To analyze this consolidation process, we need to consider both the fiber bundle deformation and the resin flow. The consolidation pressure p, which is in the radial direction, must be balanced by two components, the load carried by the fiber and the resin pressure. This becomes

$$p = p_r - (\sigma_f)_r \qquad\qquad\qquad (2\text{-}2)$$

where p_r is the resin pressure, and $(\sigma_f)_r$ is the fiber stress in the radial direction. We should note the sign convention in this expression, in which minus $(\sigma_f)_r$ is the compression stress in the fiber bundle transverse direction. How the load is partitioned between fiber and resin depends on the fiber bundle deformation state. For very low fiber content, σ_f is zero, since fibers are separated and surrounded by resin matrix. Therefore the whole load becomes the resin pressure. Then resin flow dominates the consolidation process. On the other hand, if resin pressure p_r is small, the load is used to consolidate the fiber bundle. The fiber deformation becomes the dominant factor to the process. In general, this is the process combined with fiber deformation and resin flow, which is similar to the consolidation of the open shape laminate composites as discussed in [34,35].

For layers already wound, we take an element as shown in Fig. 2-3 for consolidation analysis. Since the deformation of the material is non-linear, we always use the incremental form in the analysis and calculation. The consolidation process is time dependent. For each small time step we use the parameters at the current time as the reference state, and then calculate the new states of these parameters at the new time. In the figure r refers to the reference position vector of a layer, and ξ is the position vector after the deformation at the new time step. Suppose the flow rate of the resin is q and the fiber volume fraction for the element we choose is V_f, we have the mass conservation relation for the element shown in the figure as

$$\frac{\partial}{\partial t} [(1-V_f)\xi d\xi] = -qd\xi - \xi dq \qquad (2-3)$$

Also we have the continuity condition for the fiber bundle or fiber network as

$$\frac{(V_f)_o}{V_f} = \frac{\xi}{r} \frac{\partial \xi}{\partial r} \qquad (2-4)$$

where $(V_f)_o$ is the fiber volume fraction at the reference time when the layer is at position r, and V_f is the fiber volume fraction at the new time when the layer is at position ξ. By using Darcy's Law for the fluid flow through porous media [36], we also have

$$q = -\frac{S}{\mu} \frac{\partial p_r}{\partial \xi} \qquad (2-5)$$
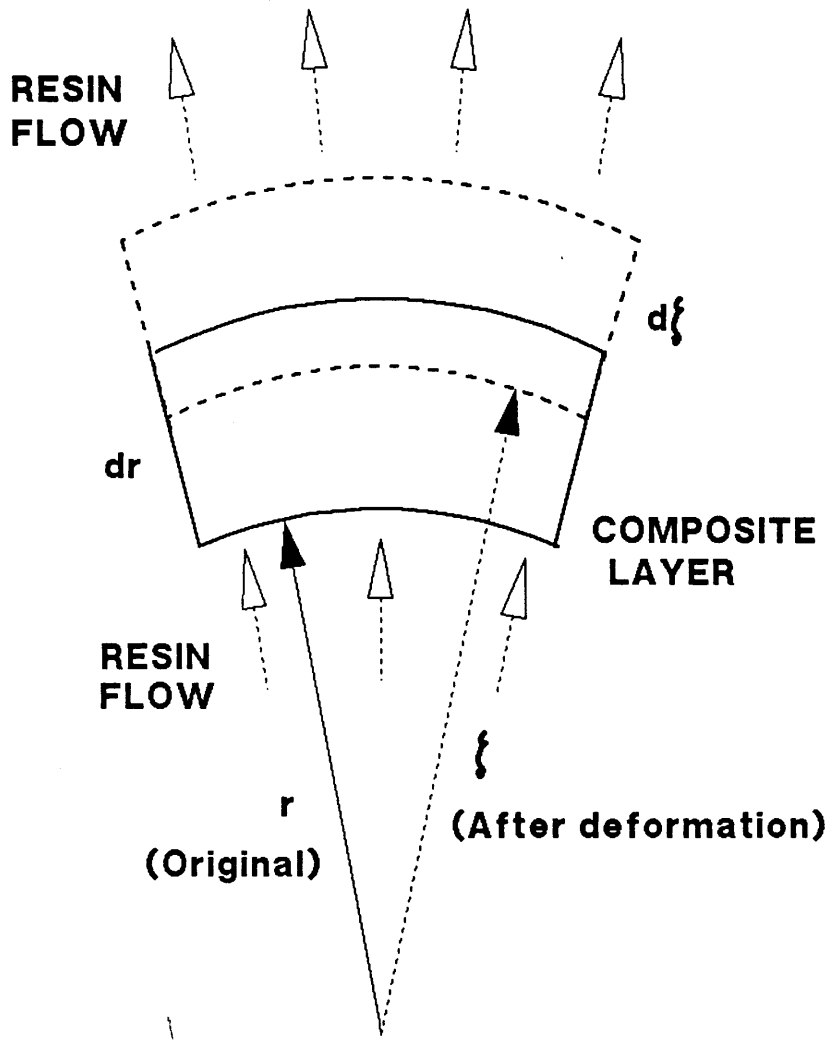
Fig. 2-3: Element of composite layer in consolidation

where S is the permeability of the fiber network in the radial direction, μ is the resin viscosity, and p_r is the resin pressure. Combining (2-3), (2-4), and (2-5), we have the following consolidation equation

$$\frac{1}{V_f} \frac{\partial V_f}{\partial t} = -\frac{1}{\xi} \frac{S}{\mu} \frac{\partial p_r}{\partial \xi} - \frac{\partial}{\partial \xi} \left(\frac{S}{\mu} \frac{\partial p_r}{\partial \xi} \right) \tag{2-6}$$

which gives us the relation between the resin pressure and the fiber volume fraction, and both of them change with time. We also have the other equilibrium relations between these two parameters. Between position variables ξ and r, we have the relation

$$\xi = r + u \tag{2-7}$$

where u is the radial displacement. When we use the incremental method for calculation, for each time step the displacement u is small compared to either r or ξ.

If we write out the equilibrium condition for the element shown in Fig. 2-2, we have

$$\frac{d\sigma_r}{dr} + \frac{\sigma_r - \sigma_\theta}{r} = 0 \tag{2-8}$$

where σ_r and σ_θ are the total stress for the composite in radial and circumferential directions respectively. Here we still use r for the layer radial position which is the reference position for this time step, and r varies with each time step. Since terms σ_r and σ_θ are the total stress of the composite, they can be decomposed into two components [37]

$$\sigma_r = (\sigma_f)_r - p_r \tag{2-9}$$

$$\sigma_\theta = (\sigma_f)_\theta - p_r \tag{2-10}$$

where σ_f is the fiber stress which is defined as the load divided by the fiber bundle cross section area. The negative sign is used before the resin pressure to match the sign convention used for pressure and stress.

As we mentioned above, within each incremental step the deformation is relatively small, that is, $|\xi/r-1| \ll 1$. Therefore, we can use the first order expression of strain to represent the deformation

$$\epsilon_r = \frac{du}{dr} = \frac{\partial \xi}{\partial r} - 1 \tag{2-11}$$

$$\epsilon_\theta = \frac{u}{r} = \frac{\xi}{r} - 1 \tag{2-12}$$

To relate the deformation to the stress we need constitutive relations for the fiber bundle or fiber network. We can write them as

$$\epsilon_\theta = S_{\theta\theta}\,(\sigma_f)_\theta + S_{\theta r}\,(\sigma_f)_r + \alpha_\theta\,T \tag{2-13}$$

$$\epsilon_r = S_{r\theta}\,(\sigma_f)_\theta + S_{rr}\,(\sigma_f)_r + \alpha_r\,T \tag{2-14}$$

where S_{ij} terms are compliances of the fiber network. These are functions of fiber bundle deformation state V_f, so that they are not constant. However within the incremental step, they can be considered as constant in the calculation. Thermal effect is introduced here by including the thermal expansion coefficients α_θ and α_r. Usually winding operation is performed at a constant temperature so that no thermal effect needs to be taken into account. If an elevated temperature debulking process is used, or if an

34

exothermic process involved, temperature effect must be included. Equations (2-13) and (2-14) are nonlinear, so that the incremental forms are always used. The derivation and experiment verification of terms S_{ij} were presented in [38], and will be discussed in detail in the following chapters. For V_f ranging from 0.5 to 0.8, which is the range of advanced composite material, we can write S_{ij} terms as

$$S_{\theta\theta} = 1/(0.9 V_f E_f) \qquad\qquad (2\text{-}15)$$

$$S_{rr} = \frac{(\dfrac{\sqrt{V_a}}{\sqrt{V_f}} - 1)^5}{A_s \dfrac{\sqrt{V_a}}{\sqrt{V_o}} [\ 2.5 - 0.5 \dfrac{\sqrt{V_f}}{\sqrt{V_a}} - 2 \dfrac{\sqrt{V_o}}{\sqrt{V_f}}\ ]} \qquad\qquad (2\text{-}16)$$

$$S_{r\theta} = S_{\theta r} = -\ 0.0156\ (V_f)^{-5.94}/E_f \qquad\qquad (2\text{-}17)$$

where E_f is the fiber longitudinal stiffness, A_s is the spring constant which has the dimension of an elastic modulus and is determined by experiments, V_a is the available fiber volume fraction or maximum packing efficiency which is around 0.8 to 0.85 for practical unidirectional fiber bundle conditions, and V_o is the reference fiber volume fraction below which fibers carry no load. For the fiber tows used in our study, which were AS4 carbon fibers from Hercules, these values were chosen as [35]: $E_f = 34 \times 10^6$ (*psi*), $A_s = 0.06$ (*psi*), $V_a = 0.8$, and $V_o = 0.5$. All of these compliance terms are functions of V_f.

Another constitutive relation is needed to solve this set of equations, which is the permeability of the fiber network in the radial direction. The permeability S which is used in equation (2-5) and (2-6) is related to the fiber volume fraction V_f. As fibers are compacted more and

35

more, the flow resistance of the fiber network becomes higher and higher, and the permeability drops substantially. This was discussed in [35] for the case of transverse flow in the laminate molding, and the relation can be expressed as

$$
S = \frac{r_f^2}{4k_z} \frac{(\frac{\sqrt{V_a'}}{\sqrt{V_f}} - 1)^3}{(\frac{V_a'}{V_f} + 1)}
\qquad (2\text{-}18)
$$

where r_f is the fiber radius, k_z is the Kozeny constant which was determined experimentally, and V_a' is the available fiber volume fraction or packing efficiency at which the transverse flow stops. For the graphite fibers used in our experiments, these values were chosen as r_f=0.004 (mm), k_z=0.2, and V_a'=0.8 [35]. The relation of S versus V_f is plotted in Fig. 2-4.

With these constitutive relations we have a complete set of equations, (2-4), and (2-6) to (2-14), for solving variables V_f, p_r, ξ, u, ϵ_r, ϵ_θ, σ_r, σ_θ, $(\sigma_f)_r$, and $(\sigma_f)_\theta$. We also need boundary and initial conditions for these equations. The already-wound layers interact with the mandrel at the inside boundary and with the newly-wound layer at the outside boundary. For the inside interface, we need to consider the deformation of the mandrel and assume that the displacement and pressure are compatible between the mandrel and the inner-most layer. We treat the mandrel as a hollow cylinder made of an isotropic linear elastic material. Under the axially symmetric load, the radial displacement u is given as [39]
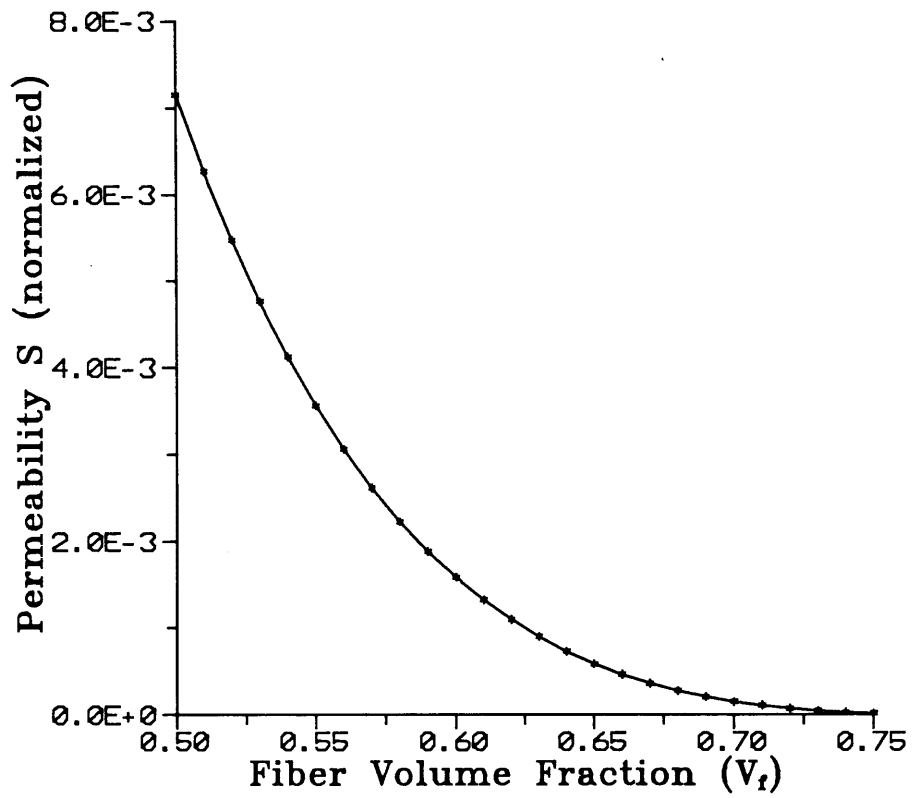
Fig. 2-4: Normalized permeability of aligned fiber bundle
in the transverse direction $[S/(r_f^2/4k_z)]$

$$u = \frac{1-\nu_m}{E_m} \frac{a_m^2 p_i - b_m^2 p_o}{b_m^2 - a_m^2} r + \frac{1+\nu_m}{E_m} \frac{a_m^2 b_m^2 (p_i - p_o)}{b_m^2 - a_m^2} (1/r) \qquad (2\text{-}19)$$

where E_m is the mandrel material stiffness, ν_m is the Poisson ratio, a_m is the inner radius, b_m is the outer radius, p_i is the internal pressure, and p_o is the external pressure. Assuming the boundary conditions: $r = a_m$, $p_i = 0$, and $r = b_m$, $p_o = (p_o)_m$, we can derive the displacement at the mandrel outer surface $(u_o)_m$

$$(u_o)_m = \frac{b_m}{E_m(b_m^2 - a_m^2)} [-(b_m^2 + a_m^2) + \nu_m(b_m^2 - a_m^2)] (p_o)_m \qquad (2\text{-}20)$$

where $(p_o)_m$ is equal to the radial stress or total radial pressure at the inner surface of the first composite layer. This interface boundary condition is

$$(p_o)_m = -\sigma_r \qquad (2\text{-}21)$$

Here the minus sign takes into account the sign conventions for the stress and pressure. Since at this interface there is no resin flow, the radial resin pressure is equal to zero, or $\partial p_r / \partial \xi = 0$ at $r = r_m$.

At the outer surface the boundary condition is that the total radial pressure must be equal to the applied pressure, which means

$$p = -\sigma_r \qquad (2\text{-}22)$$

where p is the applied pressure. Usually in the winding operation, no pressure is applied so that $p = 0$. This also implies that the resin pressure at the outer surface is zero. At the instant a new layer is wound on to

the previously wound structure, we have a pressure increase at the outer surface. This pressure increase is equal to the consolidation pressure given in (2-1). Since this pressure increase is within a very short time period, we assume there is no change in the fiber volume fraction, and thus the increased pressure is carried by the fluid resin. For the newly wound layer, the situation is similar to the case when the first layer is wound on to the mandrel, as discussed in the previous sections. We assume that the initial fiber volume fraction is unchanged, and σ_θ is balanced with the winding tension.

For general winding condition, resin flow and consolidation begin as the first layer is wound onto the mandrel. In the calculation, we consider winding of each layer as putting a ring onto the already-wound structure. The hoop stress in the newly-wound "ring" is determined by the winding tension. The boundary radial pressure changes according to the consolidation pressure, which is also related to the winding tension. The time needed to wind a layer is used to calculate the consolidation for one time period. Also we assume the resin being squeezed out from the layer is removed during the process by using the bleeder material. This kind of calculation is then repeated for each layer until the winding operation is finished. Then we assume bleeder paper is added onto the structure for further consolidation or resin flow. Pressure and heat are applied so that the consolidation at this stage, which is sometimes called debulking, involves changes of the temperature, thermal stress, and resin viscosity.

For very thick composite structures, sometimes the debulking procedure is repeated after certain numbers of layers are wound. In this case

we just do the calculation first for the winding and consolidation stage, and then for the consolidation after winding. This kind of calculation is then repeated for many times according to the process given conditions.

In short, this analysis of the winding and consolidation covers the winding operation, the consolidation during the winding, and the consolidation after winding, which includes the debulking process in which thermal effects are usually involved, and the sitting time period after winding in which no temperature effect is involved. The common feature of all these different stages is the fiber network deformation and fluid resin flow which determine the final product micro-structure and dimensions.

2-2-3. Process time evaluation

As discussed in the previous section, the winding and consolidation processes are coupled so that in general the analysis and calculation are complicated. However, in some cases the process can be simplified so that we can separate the winding analysis from the consolidation process. The parameter to be used to determine if the simplification is possible is the process time constant. Since we have two processes coupled together, which are winding and consolidation, we need to evaluate these two process time constants.

The consolidation process time constant is equivalent to the resin flow time constant. Resin flow in the winding process can be considered as one dimensional outward flow, which is similar to the autoclave molding of a flat laminate composite where the resin flow is upward and transverse to

the laminate. The laminate flow case was well studied in [34] and [35]. As shown in Fig. 2-5, which shows the pressure history according to the laminate model calculation, the dimensionless time t^* is important in analyzing the flow process. This dimensionless time is the process time divided by τ or t_o, which is the flow process time constant. As discussed in [34], τ or t_o is defined as

$$\tau = \frac{4k_z \, \mu \, h_o^2}{A_s \, r_f^2} \tag{2-23}$$

in which k_z is the Kozeny constant for flow in the transverse direction, h_o is the original layer thickness, μ is the fluid viscosity, A_s is the fiber network spring constant with the dimension of elastic modulus, and r_f is the fiber radius. To determine the process resin flow time t_f, we can use Fig. 2-5 to determine the required dimensionless time t^* at which the fluid pressure has dropped substantially, say $t^*=0.5$. Then the flow time t_f is equal to

$$t_f = t^* \tau \tag{2-24}$$

In the physical sense, this process time can be thought as the time needed for flow to complete in one layer. Usually in the process, parameters k_z, A_s, h_o, and r_f are known quantities depending on material properties and conditions. However, the viscosity of the resin μ changes all the time in the process, and sometimes the change is substantial. The integrated form of (2-23) must be used in evaluation t_f in this case. For evaluation of winding process at the room temperature, μ can be treated as constant without introducing large errors.

41
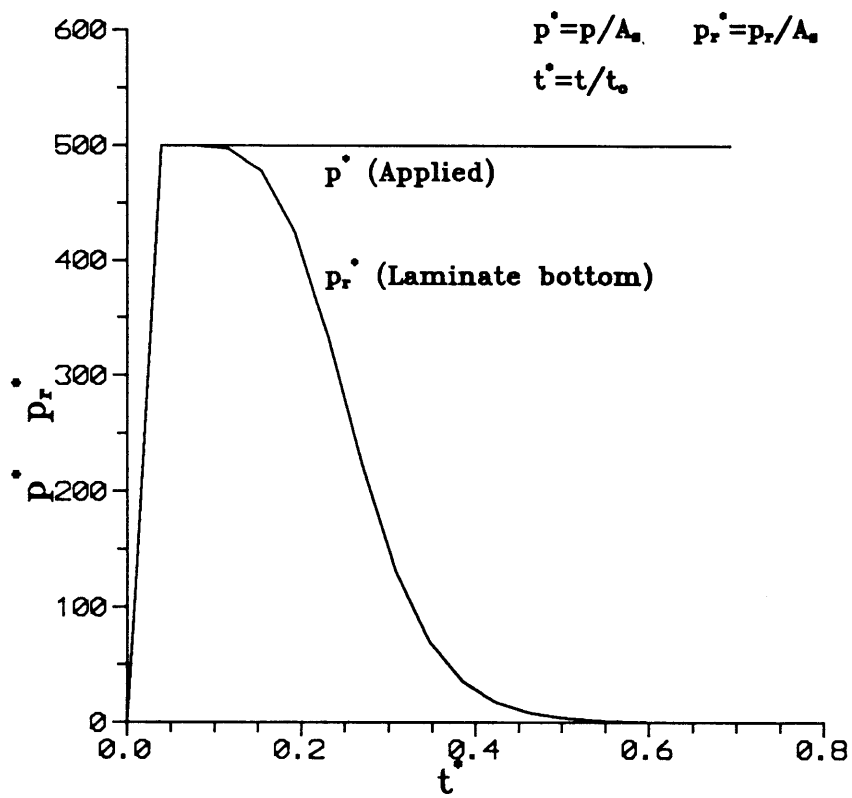
Fig. 2-5: Resin pressure history in the laminate molding
process (with dimensionless parameters)

For the winding process, the process time can be taken as the time to wind one layer, that is, t_w=time to wind one layer. This is totally determined by the manufacturing process design. Clearly the shorter the winding time, the higher the productivity. Usually t_w is limited by the process conditions such as the wetting time for the fiber tow in the wet filament process, or the running speed of the fiber handling device.

The parameter μ can vary over several orders of magnitude for different winding cases. There are low viscosity resin for wet filament winding process such as Hercules HBRF-55 resin [40]. When uncured its viscosity is around 1 poise (0.1 $Pa*s$). However for prepreg tape winding the viscosity of the uncured resin can be very high. For example, the viscosity of Hercules 3501-6 resin when uncured, is around 100 $Pa*s$ (1,000 poise) or even higher [2]. Therefore when the winding process ends, the flow or consolidating state of the wound layer can be very different depending on the different values of r (or t_o) and t^*. In the case of winding prepreg tapes at room temperature, the viscosity of the resin is so high that almost no flow takes place when winding time is relatively short. This is the case where $t_w \ll t_f$. In the case of the wet filament winding the viscosity of the resin is relatively low so that the flow is substantial. If the layer is also thin and the winding tension is high, which also means the consolidation pressure is high, flow process can finish right after the winding operation. This is the case where $t_f \ll t_w$. These two extreme cases are shown in Fig. 2-6 by comparing them with t^* observed in Fig 2-5. The process data are from different experiments. From the figure we can see that one process ends before the flow really happens, and the other ends after the flow is almost completed.

t_{w2}·

t_f^*

t_{w1}·

0.01	0.1	1	10

Process & flow time (dimensionless)
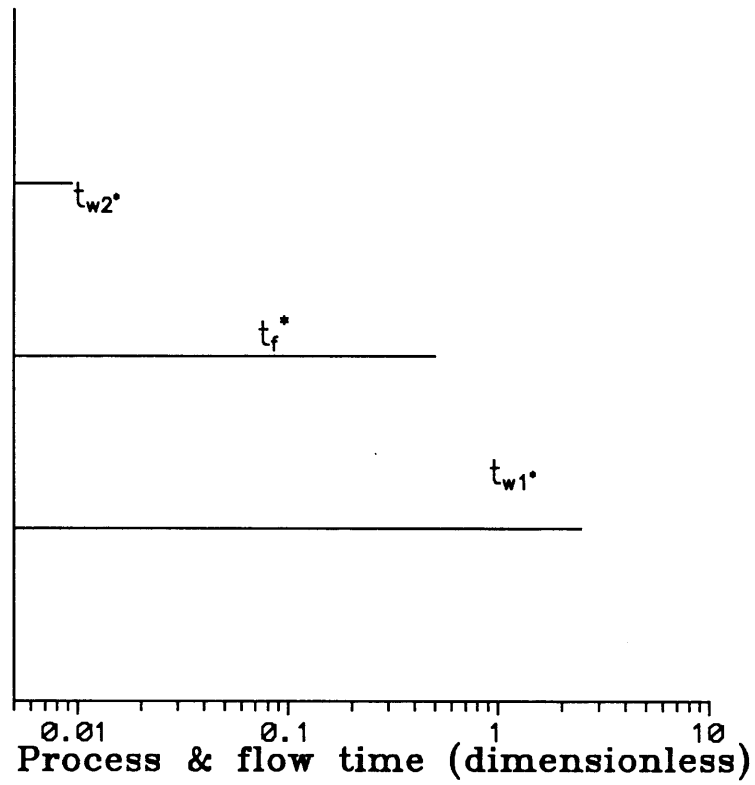
Process data:
1) AS4 3k h_o=0.006 *in* μ=10 *Pa*s*   65 tow/layer t_w=90 *sec*
                    r_f=3.5e-6 *m* A_s=0.06 *psi* k_z=0.2

2) RK 30-40k h_o=0.01 *in* μ=100 *Pa*s*   8 tow/layer t_w=10 *sec*
                    r_f=3.4e-6 *m* A_s=0.06 *psi* k_z=0.2

Fig. 2-6: Process time constant evaluation by using laminate
          molding process model

These are the cases where we can simplify the analysis. For the tape winding without flow, the approximation is to treat the material as linear elastic solid material. The elastic stiffness modulus consists of both the fiber stiffness and the resin matrix stiffness. For the wet filament winding process, we can neglect the flow process between winding different layers, so that the process can be simplified as applying consolidation pressure to press the fiber network. Only fiber stiffness needs to be considered. Since fibers behave nonlinearly in the transverse direction, which is the radial direction, nonlinear elastic analysis is used in the calculation. We will discuss these two simplified cases separately in the following sections.

2-2-4. Tape winding without resin flow

For tape winding process of thermoplastic composites, usually the material can be treated as a solid, and in most cases a linear approximation is a reasonable assumption for analysis. For tape winding with thermoset composites, in which prepreg tape is the most common form, if the viscosity of the uncured resin is high and the time of a winding operation cycle is relatively short, the material can still be considered as linear elastic material as we discussed in the previous section. In both cases the material is transversely isotropic ($E_r \neq E_\theta$). We also make following assumptions to simplify the analysis: a) Plane stress, or $\sigma_z = 0$; b) Layers are visualized as discrete rings, each with its own radial dimension and position; c) Mandrel is made of an isotropic linear elastic material.

45

For each layer, we treat it as a ring made of transversely isotropic material under an axially symmetric load. The equilibrium equation and the deformation relations are the same as (2-8), (2-11), and (2-12). The stress-strain relations are

$$\epsilon_\theta = \frac{1}{E_\theta}\sigma_\theta - \frac{\upsilon_{r\theta}}{E_r}\sigma_r \qquad (2\text{-}25)$$

$$\epsilon_r = -\frac{\upsilon_{\theta r}}{E_\theta}\sigma_\theta + \frac{1}{E_r}\sigma_r \qquad (2\text{-}26)$$

where ϵ_θ, ϵ_r are strains, E_θ, E_r are elastic moduli, and $\upsilon_{r\theta}$, $\upsilon_{\theta r}$ are Poisson ratios. Note that here we have relation $\upsilon_{r\theta}/E_r = \upsilon_{\theta r}/E_\theta$.

By using these relations, we can obtain an equation for the radial displacement u

$$\frac{d^2u}{dr^2} + \frac{1}{r}\frac{du}{dr} - \lambda^2\frac{u}{r^2} = 0 \qquad (2\text{-}27)$$

where $\lambda^2 = E_\theta/E_r$.

Assume the boundary conditions are: $r=a$, $\sigma_r = -p_i$; $r=b$, $\sigma_r = -p_o$, where p_i and p_o are internal and external pressure respectively. The solution of (2-27) is

$$u = \frac{1}{E_\theta(ab)^{\lambda-1}(b^{-2\lambda}-a^{-2\lambda})}\{[-(\lambda-\upsilon_{\theta r})b^{-\lambda-1}r^\lambda-(\lambda+\upsilon_{\theta r})b^{\lambda-1}r^{-\lambda}]p_i$$

$$+ [(\lambda-\upsilon_{\theta r})a^{-\lambda-1}r^\lambda+(\lambda+\upsilon_{\theta r})a^{\lambda-1}r^{-\lambda}]p_o\} \qquad (2\text{-}28)$$

Suppose for k-th layer, we have

46

$$(u_i)_k = (c_i)_k (p_i)_k + (c_o)_k (p_o)_k \qquad (2\text{-}29)$$

$$(u_o)_k = (d_i)_k (p_i)_k + (d_o)_k (p_o)_k \qquad (2\text{-}30)$$

where $(u_i)_k, (p_i)_k$ are the displacement and pressure at the inner surface of the k-th layer respectively, and $(u_o)_k, (p_o)_k$ are the displacement and pressure at the outer surface of the k-th layer respectively. The coefficient terms are

$$(c_i)_k = \left\{ \frac{(ab)^\lambda}{E_\theta (a^{2\lambda} - b^{2\lambda})} \, (-a) \, [(\lambda + \upsilon_{\theta r})(b/a)^\lambda + (\lambda - \upsilon_{\theta r})(a/b)^\lambda] \right\}_k$$

$$(2\text{-}31)$$

$$(c_o)_k = \left[\frac{(ab)^\lambda}{E_\theta (a^{2\lambda} - b^{2\lambda})} \, (2\lambda b) \right]_k \qquad (2\text{-}32)$$

$$(d_i)_k = \left[\frac{(ab)^\lambda}{E_\theta (a^{2\lambda} - b^{2\lambda})} \, (-2\lambda a) \right]_k \qquad (2\text{-}33)$$

$$(d_o)_k = \left\{ \frac{(ab)^\lambda}{E_\theta (a^{2\lambda} - b^{2\lambda})} \, (b) \, [(\lambda - \upsilon_{\theta r})(b/a)^\lambda + (\lambda + \upsilon_{\theta r})(a/b)^\lambda] \right\}_k$$

$$(2\text{-}34)$$

where a is the inner radius of the layer, and b is the outer radius of the layer. After the deformation, the new radii of the k-th layer are

$$(r_i)_k = a_k + (u_i)_k \qquad (2\text{-}35)$$

$$(r_o)_k = b_k + (u_o)_k \qquad (2\text{-}36)$$

The equation for the mandrel deformation is given in (2-19). If we know the boundary conditions for the mandrel as: $r = a_m$, $p_i = 0$, and $r = b_m$, $p_o = (p_o)_m$, we can write the inner and outer displacements as

$$(u_i)_m = \frac{-2 a_m b_m^2}{E_m (b_m^2 - a_m^2)} \, (p_o)_m \qquad (2\text{-}37)$$

47

$$(u_o)_m = \frac{b_m}{E_m(b_m^2 - a_m^2)} \ [-(b_m^2 + a_m^2) + v_m(b_m^2 - a_m^2)] \ (p_o)_m \qquad (2\text{-}38)$$

where a_m and b_m are mandrel inner and outer radii. Equation (2-38) is same as (2-20), and we repeat it here just for convenience. In order to use the same form as (2-29) and (2-30), we can write (2-37) and (2-38) as

$$(u_i)_m = (c_o)_m(p_o)_m \qquad (2\text{-}37a)$$

$$(u_o)_m = (d_o)_m(p_o)_m \qquad (2\text{-}38a)$$

where $(c_o)_m$ and $(d_o)_m$ correspond to the terms in (2-37) and (2-38).

The winding process is visualized as a "shrink fit" process. Before winding, the inner radius of the layer to be wound is smaller than the outer radius of the layer already wound. Then the layer is expanded and fitted on to the layer already wound. This induces the tension in the layer being wound. After fitting, the whole combination reaches to a new equilibrium state. The circumferential stress in the outer-most layer is equal to the winding tension stress.

Assuming that we already wound k-1 layers on to the mandrel and now we are winding the k-th layer. We have following relations,

a) interface pressure:

$$(p_o)_m = (p_i)_1$$
$$(p_o)_1 = (p_i)_2$$
$$\ldots \ldots \qquad\qquad\qquad \text{(k equations)} \qquad (2\text{-}39)$$

$(p_o)_{k-1} = (p_i)_k$

b) interface radius and displacement:

$a_1 + (u_i)_1 = b_m + (u_o)_m$

$a_2 + (u_i)_2 = b_1 + (u_o)_1$

... ...   (k equations)   (2-40)

$a_k + (u_i)_k = b_{k-1} + (u_o)_{k-1}$

c) pressure and displacement:

$(u_o)_m = (d_o)_m (p_o)_m$

$(u_i)_1 = (c_i)_1 (p_i)_1 + (c_o)_1 (p_o)_1$

$(u_o)_1 = (d_i)_1 (p_i)_1 + (d_o)_1 (p_o)_1$

... ...   (2k equations)   (2-41)

$(u_i)_{k-1} = (c_i)_{k-1} (p_i)_{k-1} + (c_o)_{k-1} (p_o)_{k-1}$

$(u_o)_{k-1} = (d_i)_{k-1} (p_i)_{k-1} + (d_o)_{k-1} (p_o)_{k-1}$

$(u_i)_k = (c_i)_k (p_i)_k$

Note that in these coefficient terms we have the variables of layer dimension a_1, b_1, a_2, b_2, ..., and a_k, b_k. Except for a_k and b_k, these terms are already solved from the previous calculation. For the k-th layer, we have

$$b_k = a_k + t_k \qquad\qquad (2-42)$$

where t_k is the original thickness of the k-th layer.

If the winding force per width for the k-th layer is w_k, we have the equilibrium equation

$$(p_o)_{k-1} = \frac{w_k}{(r_o)_{k-1}} \tag{2-43}$$

and also

$$(r_o)_{k-1} = b_{k-1} + (u_o)_{k-1} \tag{2-44}$$

This new equilibrium state is the state after the k-th layer is wound. Therefore we have in total 4k+3 equations, (2-39) to (2-44). The 4k+3 unknowns are

$$(u_o)_m, \ (u_o)_1, \ (u_o)_2, \ \ldots, \ (u_o)_{k-1};$$
$$(u_i)_1, \ (u_i)_2, \ \ldots, \ (u_i)_{k-1}, \ (u_i)_k;$$
$$(p_o)_m, \ (p_o)_1, \ (p_o)_2, \ \ldots, \ (p_o)_{k-1};$$
$$(p_i)_1, \ (p_i)_2, \ \ldots, \ (p_i)_{k-1}, \ (p_i)_k;$$
$$a_k, \ b_k, \ (r_o)_{k-1}.$$

Thus we have a complete set of equations to solve all these variables.

After we solved these variables, we can go further to obtain stresses and strains. The strains and stresses for each layer can be calculated as follows

$$\epsilon_r = A_1 \lambda r^{\lambda-1} - A_2 \lambda r^{-\lambda-1} \tag{2-45}$$

$$\epsilon_\theta = A_1 r^{\lambda-1} + A_2 r^{-\lambda-1} \tag{2-46}$$

$$\sigma_r = \frac{E_\theta}{\lambda^2 - v_{\theta r}^2} \left[(\lambda + v_{\theta r})A_1 r^{\lambda-1} - (\lambda - v_{\theta r})A_2 r^{-\lambda-1} \right] \tag{2-47}$$

$$\sigma_\theta = \frac{\lambda E_\theta}{\lambda^2 - v_{\theta r}^2} \left[(\lambda + v_{\theta r})A_1 r^{\lambda-1} + (\lambda - v_{\theta r})A_2 r^{-\lambda-1} \right] \tag{2-48}$$

where

$$A_1 = \frac{\lambda - v_{\theta r}}{E_\theta} \; \frac{-p_i b^{-\lambda - 1} + p_o a^{-\lambda - 1}}{(ab)^{\lambda - 1}(b^{-2\lambda} - a^{-2\lambda})} \qquad (2\text{-}49)$$

$$A_2 = \frac{\lambda + v_{\theta r}}{E_\theta} \; \frac{-p_i b^{\lambda - 1} + p_o a^{\lambda - 1}}{(ab)^{\lambda - 1}(b^{-2\lambda} - a^{-2\lambda})} \qquad (2\text{-}50)$$

Here we omitted all subscripts k but all the variables in (2-45) to (2-50) are defined for the k-th layer, where $k=1,2,\ldots,n$, and n is the total layer number.

A numerical scheme was constructed to solve these equations. After each layer is wound, we repeat a similar calculation to obtain dimensions a_k and b_k for the new layer, which is necessary for the following calculation. This information about the new equilibrium state can be used to monitor the winding operation. Therefore from this calculation we can obtain not only the final stress state within the structure, but also information about these intermediate states.

One difficulty in the calculation is to determine the transverse elastic modulus of the prepreg layer, especially in the case of thermoset material. Unlike the longitudinal modulus, which is determined by the fiber modulus and the fiber volume fraction, the transverse modulus is dominated by the resin matrix, which is not a solid. One approximation says that the modulus is proportional to the resin viscosity [22,41]. Therefore for a specific resin the modulus can be determined by experiments. The transverse modulus for the cured composite laminate is given in [42] as

$$E_r = \frac{V_f + 0.5\ (1.0 - V_f)}{\dfrac{V_f}{E_f} + 0.5\ \dfrac{(1.0 - V_f)}{E_R}} \qquad (2\text{-}51)$$

where E_r is the layer modulus in the radial direction which is the layer transverse direction, E_f and E_R are moduli of the fiber and resin respectively. E_R changes with the viscosity of the resin material and can be calculated as follows according to [22]

$$E_R = C_R\ \mu \qquad (2\text{-}52)$$

where C_R is a constant which can be determined experimentally.

The solution of an example of prepreg tape winding with constant tension is shown in Fig. 2-7. There is stress relaxation for inner layers when more and more layers are wound. Without considering the following thermal and curing effect, apparently one way to change this stress distribution is to vary the winding tension force for different layers. This idea was proposed by Liu and Chamis in very early studies [11].

2-2-5. Wet filament winding

In this case, the flow process completes or almost completes during the winding operation. Therefore fibers dominate the deformation process. In other words, the material deformation state after the winding is mainly determined by fibers. The fiber bundle deformation model developed in [38] can be applied to this case. Since the fiber bundle response is highly nonlinear in the transverse deformation, the incremental form will be used
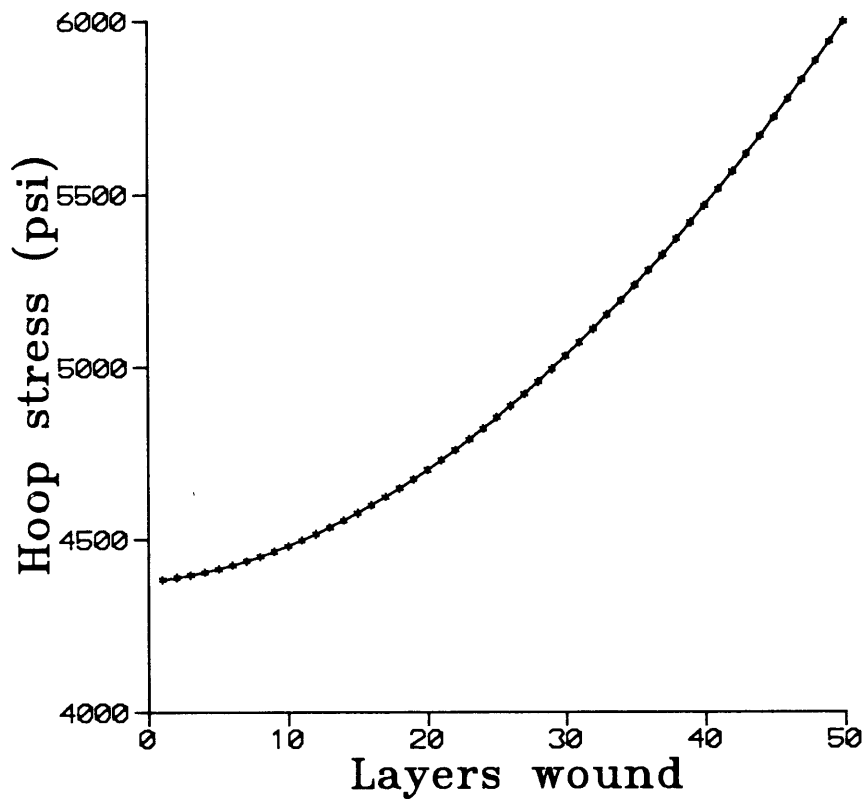
Running data:
Mandrel: $E_m = 10^7$ psi, $\nu_m = 0.3$, $b_m = 5.0$ in, $a_m = 1.0$ in.
Layer: $E_\theta = 1.5*10^7$ psi, $E_r = 0.1*10^6$ psi, $\nu_{\theta r} = 0.25$, $t = 0.005$ in.
Winding Tension: 30 lbf/in.

Fig. 2-7: Stress distribution in composite layer after tape
         winding with constant tension

in the analysis. The material stress, displacement, and deformation are all considered at the current reference state. Equation (2-8) is still applicable but r refers to the current radius. Equations (2-11) and (2-12) still hold if the deformation at each increment step is small, which has to be true if we use the incremental approach to approximate the nonlinear material response. Since the total load is carried by fibers only, equations (2-13) and (2-14) become

$$\Delta\epsilon_\theta = S_{\theta\theta} \Delta(\sigma_f)_\theta + S_{\theta r} \Delta(\sigma_f)_r \qquad (2\text{-}53)$$

$$\Delta\epsilon_r = S_{r\theta} \Delta(\sigma_f)_\theta + S_{rr} \Delta(\sigma_f)_r \qquad (2\text{-}54)$$

where S_{ij} terms are not constant. Here we assume the isothermal condition. However, as an approximation, we can treat them as constant within the incremental step. In this case, equation (2-27) is still valid except that the term $\lambda^2 - S_{rr}/S_{\theta\theta}$ is not constant either. Within an incremental step, we treat the material as linear elastic and the deformation is very small, so that the above calculation for the tape winding process is valid. Under these assumptions, we can still use forms (2-25) and (2-26) for the calculation but we need to repeat the derivation for terms E_θ, E_r, and $\nu_{\theta r}$ for each incremental step. For the Hercules AS4 fibers we used in the calculation and experiment, and by using the fiber compliance terms evaluated in [38], we obtain values of these terms as

$$E_\theta = 3.1*10^7 \, V_f \ (psi) \qquad (2\text{-}55)$$

$$E_r = 0.06 \ \frac{\dfrac{\sqrt{V_a}}{\sqrt{V_o}} \left[2.5 - 0.5 \dfrac{\sqrt{V_f}}{\sqrt{V_a}} - 2 \dfrac{\sqrt{V_o}}{\sqrt{V_f}} \right]}{\left(\dfrac{\sqrt{V_a}}{\sqrt{V_f}} - 1\right)^5} \ (psi) \qquad (2\text{-}56)$$

$$(V_o = 0.5; \quad V_a = 0.8)$$

$$v_{\theta r} = 7.0*10^{-3} \, (V_f)^{-5.94} \tag{2-57}$$

where V_o and V_a are constants as stated before. The modulus of the fiber $E_f = 34 \times 10^6$ *psi* is used in the evaluation. These relations are valid for the range of fiber volume fraction V_f of 0.5 to 0.8. From these expressions we can know if V_f is fixed for an incremental step, these terms are constant within that step.

Calculations can be performed as in the case of tape winding but we have to use the incremental approach, which adds a small incremental load for each step, and then sums the results. Calculations of wet fiber tow winding with constant tension are shown in Fig. 2-8. In the figure the result shows fiber volume fraction distribution over layers. Varying of winding tension over different layers can change this distribution, which is a control factor in the manufacturing process design.

2-2-6. Summary

The sub-model for the winding and consolidation process has been presented here. The model includes a set of partial differential equations and algebraic equations for the process variables. These equations are nonlinear and time dependent. Except for the two special cases discussed above, in which we eliminate the calculation of partial differential equations, the solution can only be obtained by numerical simulations. As the viscosity of the resin changes dramatically because of the temperature variation in the manufacturing process, and the thermal properties of the
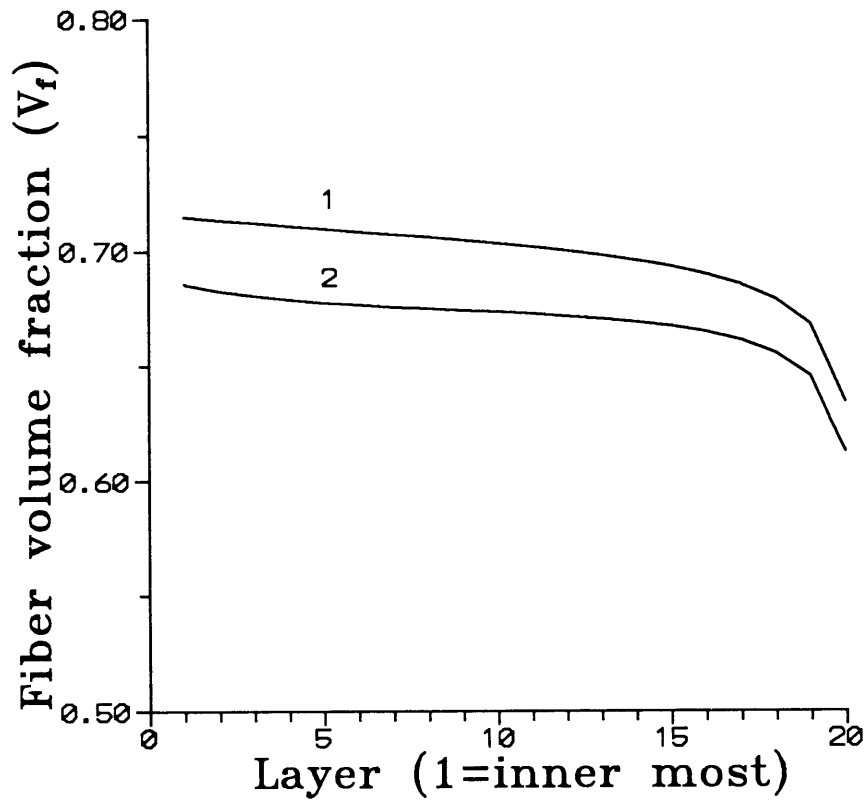
1) Tension=110 *lbf/in*   2) Tension=55 *lbf/in*

Layer: t=0.007 *in*, V_f=0.5
Mandrel: E_m=10^7 *psi*, v_m=0.3, b_m=5.0 *in*, a_m=1.0 *in*.

Fig. 2-8: Fiber volume fraction distribution over layers in
         wet filament winding process

layer are related to the fiber volume fraction, the calculation of the flow

and consolidation process is coupled with the thermal calculation. This

will be discussed in the following sections.

2-3. Heat Transfer and Temperature Calculation

Heat transfer is considered as axially symmetric for the cylindri-

cal composite structure. Also we neglect the temperature variation in the

axial direction. Therefore we simplify the problem to one dimensional heat

transfer in the radial direction only. Fig. 2-9 shows an element of the

composite layer with heat conduction, convection, and heat generation. We

can write the heat balance equation for this element as

$$\frac{\partial}{\partial t}(\rho c T \xi d\xi) = -\frac{\partial q}{\partial \xi}\xi d\xi - qd\xi - m'cTd\xi - \frac{\partial(m'cT)}{\partial \xi}\xi\ d\xi + \rho H'\xi d\xi$$

$$(2-58)$$

where ρ is the average material density, and c is the average specific

heat, which includes both fiber and resin components, ξ is the radial posi-

tion vector, q is the heat flow, m' is the mass flow, and H' is the heat

generation rate. Within each incremental calculation step, ξ, ρ and c can

be treated as constant. The equations for heat flow and mass flow are

$$q = -K_T\frac{\partial T}{\partial \xi} \qquad (2-59)$$

$$m' = -\rho\frac{S}{\mu}\frac{\partial p_r}{\partial \xi} \qquad (2-60)$$

RESIN
FLOW

HEAT
FLOW

dζ

dr

COMPOSITE
LAYER

RESIN
FLOW

ζ

r
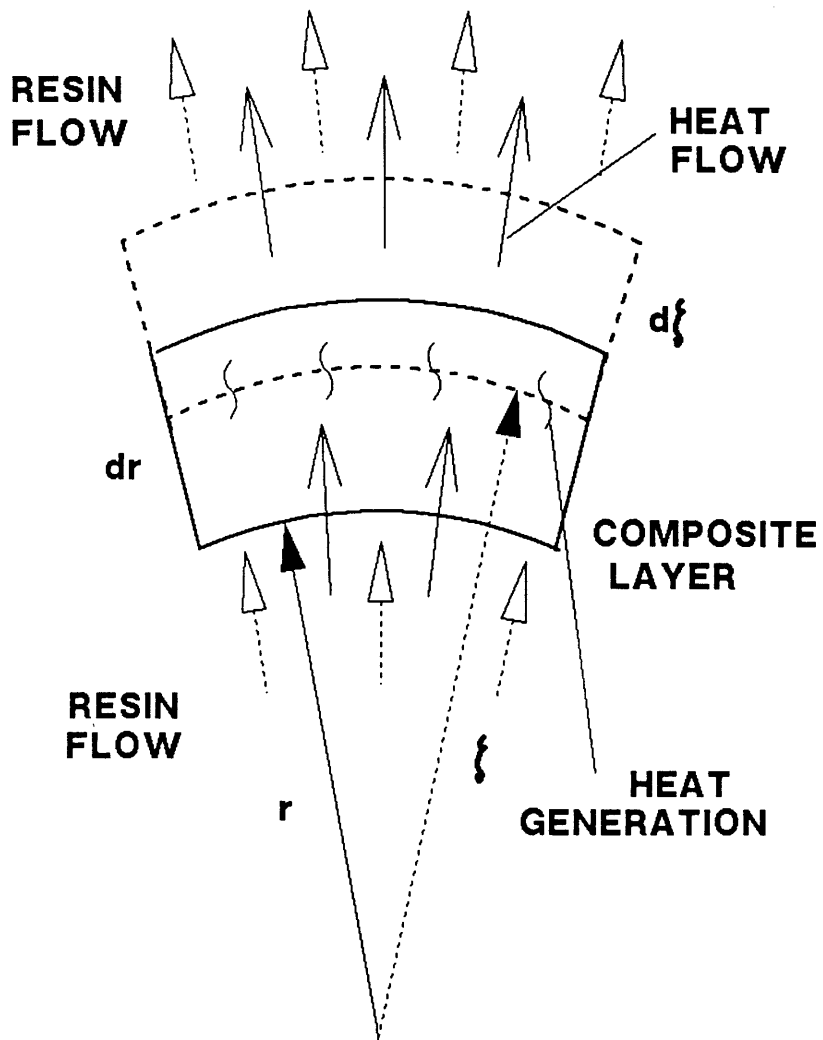
HEAT
GENERATION

Fig. 2-9: Element of composite layer with heat transfer and
heat generation

where K_T is the thermal conductivity, S is the permeability, μ is the viscosity, and p_r is the resin pressure. By substituting (2-59) and (2-60) into (2-58), and using the fiber continuity relation (2-4), we can obtain the following heat transfer equation for the numerical calculation

$$\rho c \frac{\partial}{\partial t} \left(\frac{T}{V_f}\right) = \frac{K_T}{V_f} \frac{\partial^2 T}{\partial \xi^2} + \frac{K_T}{V_f \xi} \frac{\partial T}{\partial \xi} + \frac{\rho c T S}{\mu \xi V_f} \frac{\partial p_r}{\partial \xi} +$$

$$+ \frac{\rho c}{V_f} \frac{\partial}{\partial \xi} \left(T - \frac{S}{\mu} \frac{\partial p_r}{\partial \xi}\right) + \frac{\rho H'}{V_f} \qquad (2\text{-}61)$$

This is the heat transfer equation for the composite layer. We also need equations for the mandrel and the bleeder layers on top of the composite layer. For the mandrel we only need to consider the heat conduction, so that we have

$$\frac{\partial T}{\partial t} = \left(\frac{K_T}{\rho c}\right)_m \left(\frac{1}{r} \frac{\partial T}{\partial r} + \frac{\partial^2 T}{\partial r^2}\right) \qquad (2\text{-}62)$$

where ρ, c, and K_T are density, specific heat, and thermal conductivity of the mandrel respectively. For the bleeder on top of the composite layers, we consider the heat conduction and heat generation. There is heat convection because of the resin flow. However the fluid pressure gradient inside bleeder is much smaller than that in the composite layer, so that convection is much smaller in this case. The thermal conductivity of the bleeder is not constant because of the accumulation of the fluid within the bleeder in the flow process. Therefore we have

$$\frac{\partial T}{\partial t} = \frac{1}{\xi} \frac{\partial}{\partial \xi} \left[\left(\frac{K_T}{\rho c}\right)_b \xi \frac{\partial T}{\partial \xi}\right] + \frac{H'}{c} \qquad (2\text{-}63)$$

59

where ρ, c, and K_T are density, specific heat, and thermal conductivity of the bleeder material. As fluid accumulates in the bleeder, these terms will change. Within an incremental step we treat them as constant, then we recalculate them for each new time step.

The boundary conditions for these equations are the continuity of the temperature and heat flow. The temperature at the inner surface of the mandrel and at the outer surface of the bleeder would be equal to the applied temperature, which is an input parameter. At the interfaces of the mandrel/composite layer and the composite layer/bleeder, temperature and heat flow must be continuous. These conditions will be discussed in detail in Chapter 4 in the numerical formulation section.

In other models of the heat transfer analysis on similar composite structures, the convection heat transfer by resin mass flow was omitted [24,27]. By using the dimensional analysis, we found that this is not always a reasonable assumption. Therefore we include the convection term in our calculation. Taking an element as shown in Fig. 2-9 we now compare only heat conduction with convection. In other words we assume there is no heat source within the element. The heat convection is from the mass flow. From [43,44] we can obtain the energy conservation equation as

$$\frac{\partial(\rho cT)}{\partial t} = -\frac{\partial q}{\partial x} - \frac{\partial(m'cT)}{\partial x}$$
(2-64)

where m' is the mass flow, q is the heat flow, ρ is the average material density, and c is the average specific heat. For simplicity we neglect the

geometric effect so that we just use x as the coordinate. From Fourier's Law we have

$$q = -K_T \frac{\partial T}{\partial x} \qquad (2\text{-}65)$$

where K_T is the thermal conductivity. From Darcy's Law [36] we have

$$m' = -K_p \frac{\partial p}{\partial x} \qquad (2\text{-}66)$$

and

$$K_p = \rho S/\mu \qquad (2\text{-}67)$$

where K_p is called permeability constant or coefficient of permeability, S is the permeability of the material and its unit is length square, and μ is the fluid viscosity. With these relations we can write (2-64) as follows

$$\rho c \frac{\partial T}{\partial t} = \frac{\partial}{\partial x}(K_T \frac{\partial T}{\partial x}) + cT \frac{\partial}{\partial x}(K_p \frac{\partial p}{\partial x}) + cK_p \frac{\partial T}{\partial x} \frac{\partial p}{\partial x} \qquad (2\text{-}68)$$

In order to do the dimensional analysis, we approximate terms at the right hand side of the equation as

$$1)\ K_T \frac{\Delta T}{(\Delta x)^2} \ ; \qquad 2)\ cTK_p \frac{\Delta p}{(\Delta x)^2} \ ; \qquad 3)\ cK_p \Delta T \frac{\Delta p}{(\Delta x)^2}$$

Clearly the magnitude of term 3 is much smaller than term 2, so that we only need to compare term 1 with term 2. We choose some typical values in composite manufacturing process. From [45], we have $K_T = 0.72$ (J/ms°C), c $= 1.0 \times 10^3$ (J/kg°C), and $\rho = 1.6 \times 10^3$ (kg/m^3). The permeability S was discussed in [35] and was shown as function of the fiber volume fraction V_f. For fiber radius of 0.004 mm, Kozeny constant $K_z = 0.2$, and available fiber

volume fraction for flow V_a'=0.8, we have, S=1.43×10^{-13} m^2 for V_f=0.5, and

S=3.17×10^{-14} m^2 for V_f=0.6. With these numbers we can estimate the magnitude of these terms by using our experimental data. We list the results of two selected cases in Table 2-1.

Table 2-1. Comparison of heat conduction vs. convection

	ΔT (°K)	T (°K)	Δp (psi)	μ (P_a*s)	1) $K_T \Delta T$ (J/ms)	2) $cTK_p \Delta p$ (J/ms)
Case 1	10	400	100	100	7.2	0.14-0.63
Case 2	1	400	100	10	0.72	1.4-6.3

Here ΔT and Δp are the temperature and pressure difference across the composite layer. Δp is chosen as the possible applied pressure. ΔT is determined by the applied temperature cycle. The table shows two possible extreme cases. The results show that which term is dominant depends on the process conditions, and also changes at different process stages. The ratio of these two terms is plotted as a function of V_f in Fig. 2-10.

The solution of the heat transfer equation yields the temperature distribution and history, which is important to the resin viscosity calculation and thermal stress evaluation. The viscosity of the Hercules 3501-6 resin has been investigated by Springer [2], and was used here in the calculation. The heat transfer equation is also coupled with resin flow and fiber consolidation, so that great difficulty was encountered in the numerical formulation. Several iteration schemes were designed for the numerical simulation and will be discussed later.
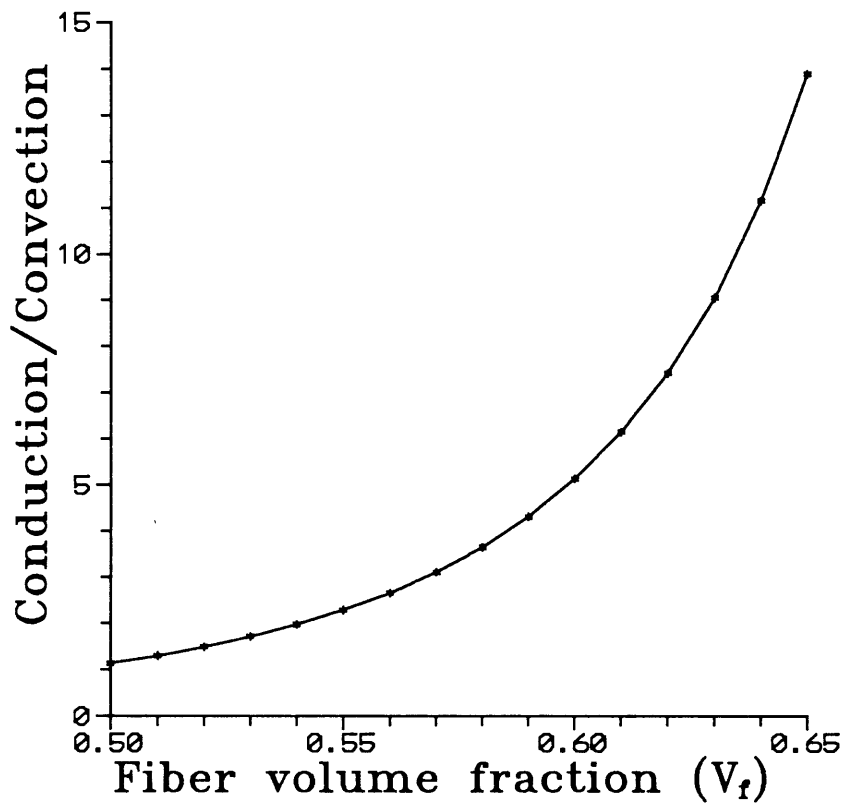
Conduction/Convection $= (K_T \Delta T)/(c T K_p \Delta p)$

K_T=0.72 (J/ms°C)   c=1.0*10^3 (J/kg°C) ρ=1.6*10^3 (kg/m^3)
ΔT=10 °K Δp=100 (psi)   T=400°K μ=10 (*Pa*sec*)

Fig. 2-10: Heat conduction versus heat convection for different
          process variables

2-4. Resin Viscosity and Cure Reaction

Resin viscosity and degree of cure are essential process variables in the analysis. For Hercules 3501-6 resin, this was studied in detail by Springer and coworkers [2]. We used their results in the process analysis. Here we just summarize the main points of their results.

The viscosity of the resin was calculated according to temperature cycle or temperature history. The suggested expression was

$$\mu = \mu_o \exp(U/RT + K\alpha) \qquad (2\text{-}69)$$

where μ_o is a constant, U is the activation energy for viscosity, R is the universal gas constant, T is the absolute temperature, K is a constant independent of temperature, and α is the degree of cure. The data used here are all from [2] as follows: $\mu_o = 7.93 \times 10^{-14}$ PaSec, K = 14.1, U = 9.08 $\times$ 10^4 J/mol.

The calculation of the degree of cure α was given as

$$d\alpha/dt = (K_1 + K_2\alpha)(1-\alpha)(B-\alpha) \qquad \alpha \leq 0.3 \qquad (2\text{-}70)$$

$$d\alpha/dt = K_3(1-\alpha) \qquad \alpha > 0.3 \qquad (2\text{-}71)$$

where
$$K_1 = A_1 \exp(-\Delta E_1/RT)$$

$$K_2 = A_2 \exp(-\Delta E_2/RT)$$

$$K_3 = A_3 \exp(-\Delta E_3/RT) \qquad (2\text{-}72)$$

where B, A_i's and ΔE_i's were found by curve fitting to the experiment data and listed in Table 2-2.

Table 2-2. The values of the constants in equation (2-72)
(From ref. [2])

$$B = 0.47 \pm 0.07$$

$$A_1 = 2.101 * 10^9 \text{ min}^{-1}$$

$$A_2 = -2.104 * 10^9 \text{ min}^{-1}$$

$$A_3 = 1.960 * 10^5 \text{ min}^{-1}$$

$$\Delta E_1 = 8.07 * 10^4 \text{ J/mol}$$

$$\Delta E_2 = 7.78 * 10^4 \text{ J/mol}$$

$$\Delta E_3 = 5.66 * 10^4 \text{ J/mol}$$

In the calculation the degree of cure α was calculated first by integration of (2-70) and (2-71), then the viscosity of the resin μ was obtained by using (2-69). The experiment verification of this viscosity model was also given [2].

2-5. Post-Cure Thermal Stress

After the whole structure is cured, the material becomes a solid composite, which is a mixture of fiber and polymeric resin matrix. The cure temperature applied to the material is high. When the structure is cooled, thermal stress will be induced, which contributes to the total residual stress distribution. For the thermal stress calculation, a simple way to deal with the material is to treat it as linear elastic but anisotropic material. Here we also make the assumption that there is no substantial thermal stress or temperature variation in the axial direction. Therefore we only consider the temperature variation in the radial direction.

This is a problem of thermal stress in an anisotropic hollow cylinder with transient temperature variation in the radial direction. This kind of problem was studied by many researchers. Longcope, Forrestal, and Warren solved thermal stress problem in a transversely isotropic hollow cylinder with temperature distribution at both radial and circumferential directions [46]. Misra and Achari derived a solution for temperature variation at both radial and axial directions [47]. Later Chen presented the results for a similar problem with finite cylinder length [48]. Hyer, Cooper, and Cohen discussed stress and deformation in different cross-ply composite tubes subjected to a uniform temperature change [49]. Our prob-lem here is simpler than these ones since we only consider the radial temperature variation, but the temperature variation changes with time.

For a cylindrical shaped product, the stress-strain relation including the thermal effect can be written as

$$\epsilon_r = S_{r\theta} \ \sigma_\theta + S_{rr} \ \sigma_r + \alpha_r \ T \qquad (2\text{-}73)$$

$$\epsilon_\theta = S_{\theta\theta} \ \sigma_\theta + S_{\theta r} \ \sigma_r + \alpha_\theta \ T \qquad (2\text{-}74)$$

These are the same as (2-13) and (2-14) and we repeat them for convenience. However the compliance terms here are for the composite material after the cure, which are different from the terms in (2-13) and (2-14). The inverse forms of (2-73) and (2-74) are

$$\sigma_\theta = \frac{1}{S_{r\theta}S_{\theta r} - S_{\theta\theta}S_{rr}} \ [S_{\theta r}\epsilon_r - S_{rr}\epsilon_\theta + (S_{rr}\alpha_\theta - S_{\theta r}\alpha_r) \ T]$$

$$(2\text{-}75)$$

$$\sigma_r = \frac{1}{S_{r\theta}S_{\theta r} - S_{\theta\theta}S_{rr}} [S_{r\theta}\epsilon_\theta - S_{\theta\theta}\epsilon_r + (S_{\theta\theta}\alpha_r - S_{r\theta}\alpha_\theta) T]$$

(2-76)

Here S_{ij} terms are the compliance terms for the composite material, α_i terms are the thermal expansion coefficients, and T is the temperature difference relative to the reference temperature. The equilibrium equation and the displacement-strain relations are the same as before but we write out them here

$$\frac{d\sigma_r}{dr} - \frac{\sigma_r - \sigma_\theta}{r} = 0$$

(2-77)

$$\epsilon_\theta = \frac{u}{r}$$

(2-78)

$$\epsilon_r = \frac{du}{dr}$$

(2-79)

By substituting these relations and simplification, also noticing that $S_{r\theta} = S_{\theta r}$ by definition, we can obtain

$$\frac{d^2u}{dr^2} + \frac{1}{r}\frac{du}{dr} - \frac{S_{rr}}{S_{\theta\theta}}\frac{u}{r^2} = \frac{1}{S_{\theta\theta}}(S_{\theta\theta}\alpha_r - S_{r\theta}\alpha_\theta - S_{rr}\alpha_\theta + S_{\theta r}\alpha_r)\frac{T}{r}$$

$$+ \frac{1}{S_{\theta\theta}}(S_{\theta\theta}\alpha_r - S_{r\theta}\alpha_\theta)\frac{dT}{dr}$$

(2-80)

which we can write as

$$\frac{d^2u}{dr^2} + \frac{1}{r}\frac{du}{dr} - n^2\frac{u}{r^2} = A_T\frac{T}{r} + B_T\frac{dT}{dr}$$

(2-81)

where we have

$$n^2 = S_{rr}/S_{\theta\theta} \tag{2-82}$$

$$A_T = (S_{\theta\theta}\alpha_r - S_{r\theta}\alpha_\theta - S_{rr}\alpha_\theta + S_{\theta r}\alpha_r)/S_{\theta\theta} \tag{2-83}$$

$$B_T = (S_{\theta\theta}\alpha_r - S_{r\theta}\alpha_\theta)/S_{\theta\theta} \tag{2-84}$$

This equation can be solved by using an approximation method. Assuming the temperature distribution can be expressed as

$$T(r) = \sum_{m=0}^{\infty} A_m \, r^m = A_0 + A_1 r + A_2 r^2 + \ldots \ldots \tag{2-85}$$

and the special solution for u of equation (2-81) is

$$u(r) = \sum_{m=0}^{\infty} B_m \, r^{m+1} = B_0 r + B_1 r^2 + \ldots \ldots \tag{2-86}$$

We obtain

$$B_m = \frac{A_T + B_T m}{(m+1)^2 - n^2} A_m \tag{2-87}$$

Here we assume the denominator is not equal to zero. The general solution of the above equation is

$$u = C_1 \, r^n + C_2 \, r^{-n} + \sum_{m=0}^{\infty} B_m \, r^{m+1} \tag{2-88}$$

By substitution, we can obtain the expressions for strain and stress

$$\epsilon_r = C_1 n r^{n-1} - C_2 n r^{-n-1} + \sum_{m=0}^{\infty} B_m \, (m+1) r^m \tag{2-89}$$

$$\epsilon_\theta = C_1 r^{n-1} + C_2 r^{-n-1} + \sum_{m=0}^{\infty} B_m \, r^m \tag{2-90}$$

$$\sigma_r = \frac{1}{S_{r\theta}S_{\theta r} - S_{\theta\theta}S_{rr}} \{ \ C_1(S_{r\theta}-nS_{\theta\theta})r^{n-1} + C_2(S_{r\theta}+nS_{\theta\theta})r^{-n-1}$$

$$+ \sum_{m=0}^{\infty}[S_{r\theta} - S_{\theta\theta}(m+1)] \ B_m r^m + (S_{\theta\theta}\alpha_r - S_{r\theta}\alpha_\theta) \ T \ \}$$

$$(2\text{-}91)$$

$$\sigma_\theta = \frac{1}{S_{r\theta}S_{\theta r} - S_{\theta\theta}S_{rr}} \{ \ C_1(S_{\theta r}n-S_{rr})r^{n-1} - C_2(S_{\theta r}n+S_{rr})r^{-n-1}$$

$$+ \sum_{m=0}^{\infty}[S_{\theta r}(m+1) - S_{rr}] \ B_m r^m + (S_{rr}\alpha_\theta - S_{\theta r}\alpha_r) \ T \ \}$$

$$(2\text{-}92)$$

If the boundary conditions are set as $r=a$, $\sigma_r=-p_i$, and $r=b$, $\sigma_r=-p_o$, constants C_1 and C_2 can be easily solved.

$$C_1 = a^{n+1}b^{n+1} \{-b^{-n-1}(S_{r\theta}S_{\theta r}-S_{\theta\theta}S_{rr})p_i + a^{-n-1}(S_{r\theta}S_{\theta r}-S_{\theta\theta}S_{rr})p_o$$

$$+ (I_o a^{-n-1} - I_i b^{-n-1})\} \ / \ [(S_{r\theta}-nS_{\theta\theta})(a^{2n}-b^{2n})] \qquad (2\text{-}93)$$

$$C_2 = a^{n+1}b^{n+1} \{-b^{n-1}(S_{r\theta}S_{\theta r}-S_{\theta\theta}S_{rr})p_i + a^{n-1}(S_{r\theta}S_{\theta r}-S_{\theta\theta}S_{rr})p_o$$

$$+ (I_o a^{n-1} - I_i b^{n-1})\} \ / \ [(S_{r\theta}+nS_{\theta\theta})(b^{2n}-a^{2n})] \qquad (2\text{-}94)$$

where

$$I_i = \sum_{m=0}^{\infty}[S_{r\theta}-S_{\theta\theta}(m+1)] \ B_m a^m + (S_{\theta\theta}\alpha_r - S_{r\theta}\alpha_\theta) \ T_a \qquad (2\text{-}95)$$

$$I_o = \sum_{m=0}^{\infty}[S_{r\theta}-S_{\theta\theta}(m+1)] \ B_m b^m + (S_{\theta\theta}\alpha_r - S_{r\theta}\alpha_\theta) \ T_b \qquad (2\text{-}96)$$

where T_a and T_b are temperatures at boundary $r=a$, $r=b$ respectively.

Since the calculation is based on each layer and the layer thickness is small, the expression for $T(r)$ can be simplified as

$$T(r) = A_0 + A_1 \ r \qquad (2\text{-}97)$$

which is the linear distribution of the temperature over the layer. With the boundary conditions $r=a$, $T=T_a$, and $r=b$, $T=T_b$

$$A_0 = \frac{T_a b - T_b a}{b-a} \qquad (2-98)$$

$$A_1 = \frac{T_b - T_a}{b-a} \qquad (2-99)$$

By substituting these relations into the expression for B_m terms, we have

$$B_0 = \frac{A_T}{1 - n^2} A_0 \qquad (2-100)$$

$$B_1 = \frac{A_T + B_T}{4 - n^2} A_1 \qquad (2-101)$$

$$I_i = (S_{r\theta} - S_{\theta\theta}) B_0 + (S_{r\theta} - 2S_{\theta\theta}) B_1 a + (S_{\theta\theta}\alpha_r - S_{r\theta}\alpha_\theta) T_a \qquad (2-102)$$

$$I_o = (S_{r\theta} - S_{\theta\theta}) B_0 + (S_{r\theta} - 2S_{\theta\theta}) B_1 b + (S_{\theta\theta}\alpha_r - S_{r\theta}\alpha_\theta) T_b \qquad (2-103)$$

In the process of solving this thermal stress equation, the known quantities are the temperature distributions, which are calculated by solving the heat transfer equations. The unknowns are interface pressure, displacement, as well as strain and stress. From the above derivation, we can write the displacement u_i and u_o of each layer as

$$u_i = (c_i) p_i + (c_o) p_o + c_c \qquad (2-104)$$

$$u_o = (d_i) p_i + (d_o) p_o + d_c \qquad (2-105)$$

where

$$c_i = a^n e_i + a^{-n} f_i \tag{2-106}$$

$$c_o = a^n e_o + a^{-n} f_o \tag{2-107}$$

$$c_c = a^n e_c + a^{-n} f_c + B_0 a + B_1 a^2 \tag{2-108}$$

$$d_i = b^n e_i + b^{-n} f_i \tag{2-109}$$

$$d_o = b^n e_o + b^{-n} f_o \tag{2-110}$$

$$d_c = b^n e_c + b^{-n} f_c + B_0 b + B_1 b^2 \tag{2-111}$$

with

$$e_i = -b^{-n-1}(S_{r\theta}S_{\theta r} - S_{\theta\theta}S_{rr}) J_1 \tag{2-112}$$

$$e_o = a^{-n-1}(S_{r\theta}S_{\theta r} - S_{\theta\theta}S_{rr}) J_1 \tag{2-113}$$

$$e_c = (I_o a^{-n-1} - I_i b^{-n-1}) J_1 \tag{2-114}$$

$$J_1 = \frac{a^{n+1} b^{n+1}}{(S_{r\theta} - nS_{\theta\theta})(a^{2n} - b^{2n})} \tag{2-115}$$

$$f_i = -b^{n-1}(S_{r\theta}S_{\theta r} - S_{\theta\theta}S_{rr}) J_2 \tag{2-116}$$

$$f_o = a^{n-1}(S_{r\theta}S_{\theta r} - S_{\theta\theta}S_{rr}) J_2 \tag{2-117}$$

$$f_c = (I_o a^{n-1} - I_i b^{n-1}) J_2 \tag{2-118}$$

$$J_2 = \frac{a^{n+1} b^{n+1}}{(S_{r\theta} + nS_{\theta\theta})(b^{2n} - a^{2n})} \tag{2-119}$$

For total L layers, the interface relations of displacement and pressure become

$$(u_i)_k = (u_o)_{k-1} \tag{2-120}$$

$$(p_i)_k = (p_o)_{k-1} \tag{2-121}$$

$$(u_o)_{k-1} = (d_i)_{k-1}(p_i)_{k-1} + (d_o)_{k-1}(p_o)_{k-1} + (d_c)_{k-1} \tag{2-122}$$

$$(u_i)_k = (c_i)_k(p_i)_k + (c_o)_k(p_o)_k + (c_c)_k \tag{2-123}$$

$$(k=1,2,\ldots,L)$$

Within a small time step these coefficient terms can be treated as constant. This becomes a set of linear algebraic equations and can be solved if the boundary conditions are known.

Inside the composite layer, we still have the mandrel which is made of linear elastic material. The boundary condition for the mandrel and composite interface is

$$(u_m)_o = \frac{2a_m^2 b_m}{E_m(b_m^2 - a_m^2)} (p_i)_m - \frac{(1-v_m)b_m^3 + (1+v_m)a_m^2 b_m}{E_m(b_m^2 - a_m^2)} (p_o)_m$$

$$+ \alpha_m \frac{2b_m}{b_m^2 - a_m^2} \int_{a_m}^{b_m} T_m r \, dr \qquad (2\text{-}124)$$

where subscript m represents the mandrel, $(p_i)_m$ is determined by the applied condition, $(p_o)_m$ and $(u_m)_o$ must be compatible with the layer displacement and pressure until the shrinkage on cooling makes it possible to remove the mandrel. When the mandrel is removed, only composite layer stress and displacement need to be calculated from the previous equations but with new boundary conditions. In this calculation, the stress or strain we calculated is based on the reference state, which is the state right after the cure at the cure temperature. There are pre-existing stress and strain distributions in the material at this point because of previous operations such as winding, consolidation, and debulking. We assume that the stresses and strains resulted from the previous operation are retained within the material. Therefore the stresses and strains at different stages can be superposed. The final residual stress and strain will be the summation of all these calculations. The change of the structural dimensions is also the summation of the calculation of each operation

72

stage. In the program each sub-model uses the final state of the previous sub-model as the reference state, and the result calculated is used as the new reference state for the following calculations.

2-6. Summary

In this chapter the process model is presented with the emphasis on the winding and consolidation analysis. The winding and consolidation process are treated as the combination of fiber bundle deformation and resin flow with the applied winding tension as the boundary conditions. Two simplified cases of the winding process are discussed. One is the winding of prepreg tape in which there is almost no flow in the process. The problem is then treated as winding of elastic solid material. Another is the wet filament winding process with low viscosity resin in which flow is substantial and flow time constant is very short compared with winding time constant. In this case only the elastic deformation of the fiber bundle is considered. In the heat transfer modeling, the problem is simplified as axially symmetric. Conduction, convection and heat generation are all included in the calculation. For the thermal stress calculation after the cure, an approximate solution is presented for the axial symmetric structure with the linear and anisotropic material. For the resin viscosity and cure kinetics analysis, we use part of the model presented by Springer in [2,3]. The computer simulation program is developed from this process analysis and will be presented in Chapter 4.

3. FIBER BUNDLE DEFORMATION IN COMPOSITE PROCESSING

3-1. Introduction

As stated in the introduction, fibers occupy most of the volume in advanced composite parts and structures. For advanced fiber reinforced composites, high fiber volume fraction is required to take the advantage of the material. Aligned continuous fibers with high strength are used for this purpose. In fabrication of advanced composite materials, the deformation of the fiber bundle is equal to, if not more important than, that of the resin matrix. One of the purposes in the fabrication is to achieve high fiber volume fraction and uniform fiber distribution. This is closely related to the fiber mechanical properties and deformation behavior in the processing. The work presented in this chapter is the development of a fiber bundle deformation model to be used in composite manufacturing process modeling. This fiber bundle deformation model is not only useful to the winding and consolidation processes discussed in Chapter 2, but also helpful to other manufacturing processes, such as compression molding, autoclave molding, pultrusion, resin transfer molding, and thermal forming.

The fiber bundle or fiber network under consideration is continuous high strength fibers, such as graphite fibers, Kevlar fibers, and glass fibers. The mechanical behavior of the fiber bundle is highly anisotropic. Fibers are made to be straight and well aligned in order to achieve the maximum material stiffness and strength. However, since there are thousands of fibers within a bundle, it is inevitable to introduce some defects

74

or imperfections, such as fiber misalignment, crossover, entanglement, and waviness in the manufacturing and processing. Experimental observation of the fibrous composite found that there were small waviness and misalignment of fibers within the bundle or composite material [50]. This would affect the material behavior in processing and performance in applications. We develop a fiber bundle deformation model which can describe the material response due to imperfections.

A typical element of such a fiber bundle and the coordinates used for the analysis are shown in Fig. 3-1. In the manufacturing process of composites, fibers are soaked or impregnated with resin matrix, which in most cases can be considered as fluid. Therefore, we only consider the case of fiber bundle with lubricant, which greatly reduces the friction between fibers. Since the lubricant is in a fluid state during the processing, it only contributes to the viscous response of a bundle, but not the elastic response. In general, we are not concerned with deformation of each individual fiber, but rather the average behavior of a bundle, which is usually several orders of magnitude larger than the size of a fiber. In this sense the bundle can be treated as a continuum. This method was also suggested in [51], and was used in various studies in textile industry for yarns or fabrics [52,53,54,55]. This treatment is similar to the case of an ordinary solid if the material dimensions considered are much larger than that of the molecular structure.

As we can clearly see from Fig. 3-1, the mechanical properties of an aligned fiber bundle must be very different in different directions. In the discussion we always use "1" or "x" to refer to the longitudinal or
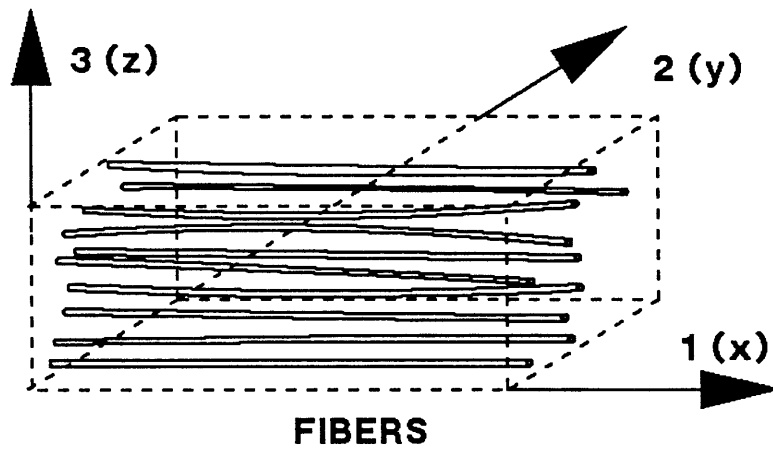
Fig. 3-1: Illustration of an element of aligned fiber bundle and the coordinate system

axial direction, and "2","3", or "y","z" for the transverse directions. For a laminate composite, "3" or "z" is the direction transverse to the laminate. In most processing, a fiber bundle is under compression stress state in the transverse directions, such as pultrusion, compression molding, forming, and filament winding. We will limit our discussions to this common condition. In other words the fiber volume fraction of a bundle is relatively high, such as $V_f > 0.5$, because of the transverse constraints.

In the previous work of this group, the deformation of a fiber network under the transverse loading condition was studied in detail. The results showed that the fiber network behaved as nonlinear and quickly stiffening elastic media [33,49]. In our present work, we extended our study to a more general case, in which the fiber bundle was subject to a complex stress state. Fig. 3-2 shows fiber deformation states in several commonly used composite manufacturing processes. Fig. 3-3 shows the corresponding fiber stress states. We develop a continuum mechanics model to describe the main features of the fiber bundle deformation behaviors.

3-2. Observations on the Fiber Deformation Behavior

We first summarize some of the observed deformation behavior of fiber bundles and aligned fiber composites in processing. We assume the coordinate system for a nominally aligned fiber bundle as shown in Fig. 3-1. The bundle is transversely isotropic in the 2-3 plane. We are concerned with the deformation behavior of this fiber bundle under complex but homogeneous states of stress. Furthermore, the fiber bundle is in the "drained" state in which fibers are lubricated but the lubricant carries no
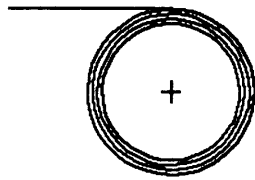
WINDING
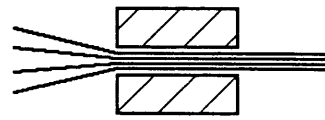
PULTRUSION
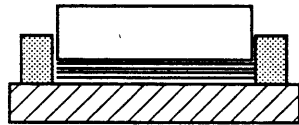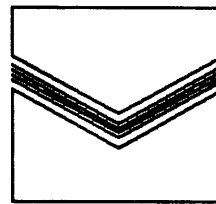
MOLDING

FORMING

Fig. 3-2: Fiber bundle deformation in composite manufacturing
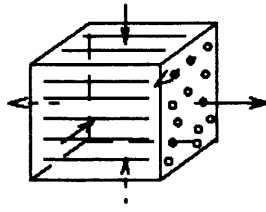
WINDING
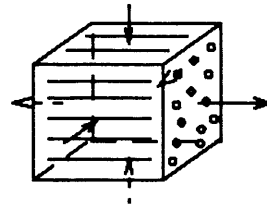
PULTRUSION
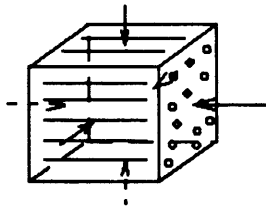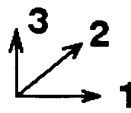
MOLDING
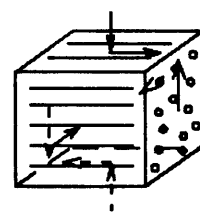
FORMING

Fig. 3-3: Fiber bundle stress state in composite manufacturing

load or very low load. In other words, the pressure in the resin (p_r) is negligible. We use average stress of a fiber bundle which is defined as load divided by the fiber bundle cross-section area. The real stress in each individual fiber is not equal to this average stress and usually shows some kind of statistical distribution. Following is a list of observed deformation behavior of this system.

1) $\sigma_{11}>0$. When pulled along the fiber bundle axis, the bundle behaves in a linear elastic manner [56].

2) $\sigma_{11}<0$. Confined fiber bundles may support small compressive axial loads and then buckle [57,58]. We assume that they behave linear elastically up to the buckling load.

3) $\sigma_{22}=\sigma_{33}<0$. This is a type of "hydrostatic" compression in the 2-3 plane. Fiber bundles have been shown to support this kind of loads elastically with a strongly non-linear response. For loads in the range of the pressures applied during processing, the stiffness of the fiber bundle is usually well below one percent of the transverse modulus for a single fiber. Note that in general this is a difficult stress to apply. If the two stresses are not exactly equal, some viscous slipping effects can be noted [35,50].

4) $\sigma_{23}\neq0$. This shearing mode occurs, for example, when $\sigma_{22}\neq\sigma_{33}$. Cogswell [60] has observed this deformation mode for thermoplastic composites and found that there is a yield stress on the order of 10^3Pa followed by a region where the slip velocity is proportional to the shear

stress. He observes that the composite viscosity, $\eta \approx 30\eta_{TP}$ where η_{TP}=shear viscosity of the thermoplastic resin. There is also some evidence of deformation hardening at large strains. This is probably due to fiber entanglement [59,60].

5) $\sigma_{22}<0,\sigma_{33}=0$. This is a squeezing flow deformation mode which probably leads to a viscoelastic response. From measurements which we have conducted on graphite epoxy prepregs heated to 38°C (100°F), we were able to describe the gross spreading behavior assuming shear deformation in the core and using a non-Newtonian power law viscosity [60]. Whether shear actually does take place in the core as opposed to slipping at the boundary depends on the presence of resin rich layers and needs to be confirmed.

6) $\sigma_{12}\neq0$ and/or $\sigma_{13}\neq0$. This shearing mode has also been observed by Cogswell [59] for thermoplastic composites. He has observed a yield stress at about 10^3Pa followed by viscous slip where $\eta \approx 30\eta_{TP}$. This is an extremely important mode for the formation of complex geometry parts.

These are the different fiber bundle deformation modes appearing in various manufacturing processes. They are illustrated in Fig. 3-4, 3-5 and 3-6. Some of them are dominated by elastic deformation, and others are by viscous effect or shearing. In some cases these two kinds of deformation modes are coupled together. A continuum mechanics model is developed to cover these different deformation modes in composite manufacturing and processing.
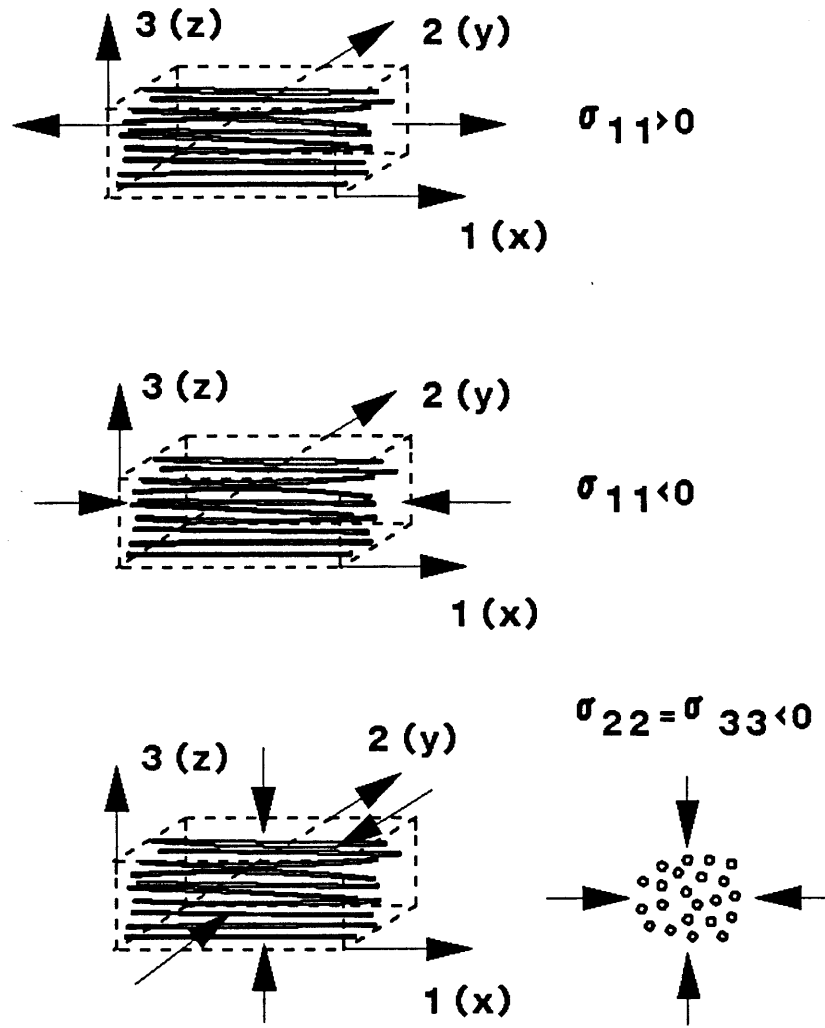
Fig. 3-4: Observations of fiber bundle stress states (1)
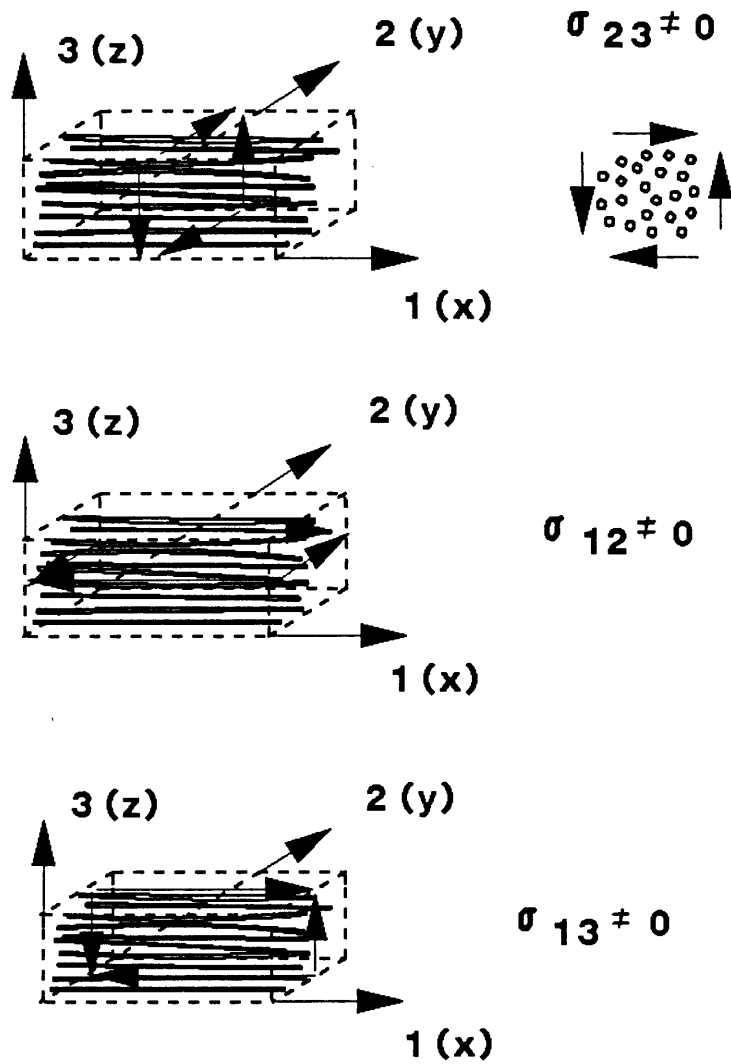
Fig. 3-5: Observations of fiber bundle stress states (2)

3 (z)   2 (y)

1 (x)

Squeezing flow $\sigma_{22} = 0$

                        $\sigma_{33} < 0$

3 (z)   2 (y)

1 (x) $\sigma_{22} = 0$

Tow splitting $\sigma_{33} > 0$
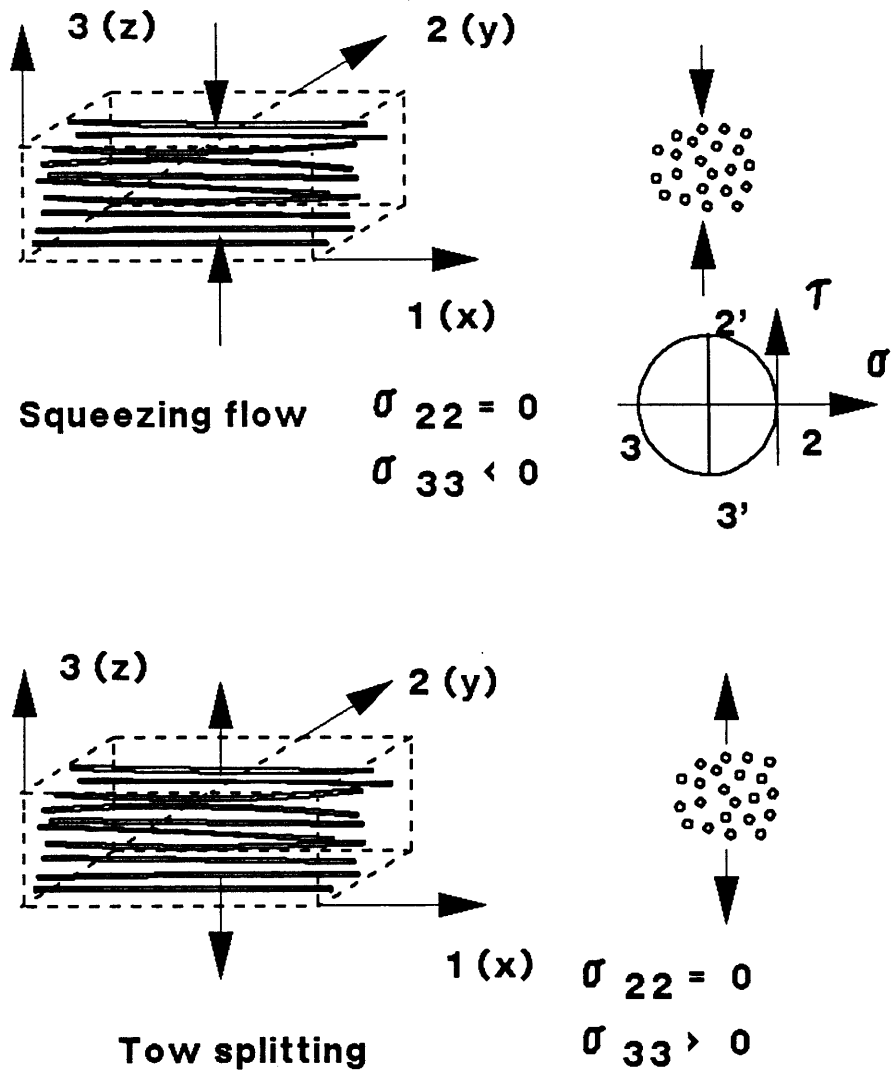
Fig. 3-6: Observations of fiber bundle stress states (3)

3-3. A Continuum Mechanics Model for Fiber Deformation

As we mentioned before, we can use the conventional terms of stress and deflection to describe the average fiber bundle deformation behavior. We assume the average fiber bundle stress as σ_{ij}, which is identical to the stress used in the mechanics of solids in the physical sense. Since we assume that fiber responses can be thought as a combination of elastic and viscous components, we subdivide the stress correspondingly. We define the average fiber stress as follows

$$\sigma_{ij} = p_{ij} + \tau_{ij} \qquad (3-1)$$

Here p_{ij} is called the "cylindrical" state of stress, where

$$p_{11} = \sigma_{11}$$

$$p_{22} = p_{33} = \frac{1}{2}(\sigma_{22} + \sigma_{33})$$

$$p_{ij} = 0 \quad \text{where } i \neq j \qquad (3-2)$$

From these definitions, we can see p_{ij} terms are similar to the static hydrostatic pressure but here we follow the sign convention that p_{ij} terms are positive for tension. In our discussion, we only deal with practical cases in manufacturing processes, so that $p_{11} > \sigma_c$, where σ_c is the critical buckling load, and $p_{22} \leq 0$, $p_{33} \leq 0$. Terms τ_{ij} are called the "deviatoric" stresses, which are simply defined as the difference between the fiber stress and the "cylindrical" stress,

$$\tau_{ij} = \sigma_{ij} - p_{ij} \qquad (3-3)$$

Here terms τ_{ij} represent stress components which cause the shearing modes of deformation.

Since the composite material consists of two components, the total load applied to the composite is carried by both the fiber and the resin or matrix. The stress relation can be expressed as

$$T_{ij} = \sigma_{ij} - p_r \, \delta_{ij} \qquad (3\text{-}4)$$

Where T_{ij} is the total stress carried by the composite, δ_{ij} is the Kronecker delta term ($\delta_{ij}=1$, $i=j$; $\delta_{ij}=0$, $i{\neq}j$), and p_r is the resin pressure. If p_r is much smaller than σ_{ij}, we can say the deformation of the fiber bundle dominates the process. Then the partitioning of the stress as given in (3-1) shows that the composite will respond elastically to states of stress $p_{ij}{\neq}0$, and viscously to states of stress $\tau_{ij}{\neq}0$. Therefore we can separate these two responses by using different constitutive relations.

For the elastic response, we also note that the fiber bundle is transversely isotropic in the 2-3 or y-z plane. Therefore we can simplify the stress and deflection by using only two components, the axial stress and deflection, and the "cylindrical" stress and deflection. The contracted form of this constitutive relation can be written as

$$p_i = C_{ij} \, \epsilon_j \qquad (i,j = 1,b) \qquad (3\text{-}5)$$

where subscript 1 refers to the longitudinal direction, and b refers to the bulk properties. In the expression p_i is the stress and is positive for tension, and ϵ_j is the deflection and is positive for extension or expan-

sion. Terms C_{ij} form the stiffness matrix. For elastic deformation in the

"x" direction, term ϵ_1 is always very small and the conventional Euler

strain can be used. However, in the transverse direction, the deformation

of the fiber bundle can be as high as 20-30%. Therefore either the in-

cremental form of the deflection, or the fiber volume fraction V_f, which

accounts for the stretch or contraction of the material, must be used.

For the viscous response of a fiber bundle, we have the following

form

$$\tau_i = \eta_{ij} \, \gamma'_j \qquad\qquad (i,j = 1,2,\ldots,6) \qquad\qquad (3\text{-}6)$$

where terms γ'_j are the usual rate of deformation tensor terms as given in

[61,62,63], terms η_{ij} are viscosities, and terms τ_i are "deviatoric"

stresses which induce the shear deformation.

Fig. 3-7 shows examples of stresses and responses of a fiber bundle

corresponding to different states in (3-5) and (3-6). The constitutive re-

lations (3-5) and (3-6) can capture many deformation modes of fiber bundle

deformation during various composite manufacturing processes. In many

manufacturing processes, such as compression molding of laminates, pultru-

sion, autoclave molding, and filament winding, fiber stresses coincide with

fiber bundle principal axes. Fibers are also constrained and there is no

gross movement of the fiber bundle. Therefore the response of a fiber

bundle is mainly elastic and in the bundle principal directions. In the

following discussion, we present our analysis and experiments on evaluating

elastic compliance terms in equation (3-5) quantitatively.

ELASTIC DEFORMATION: CONSOLIDATION
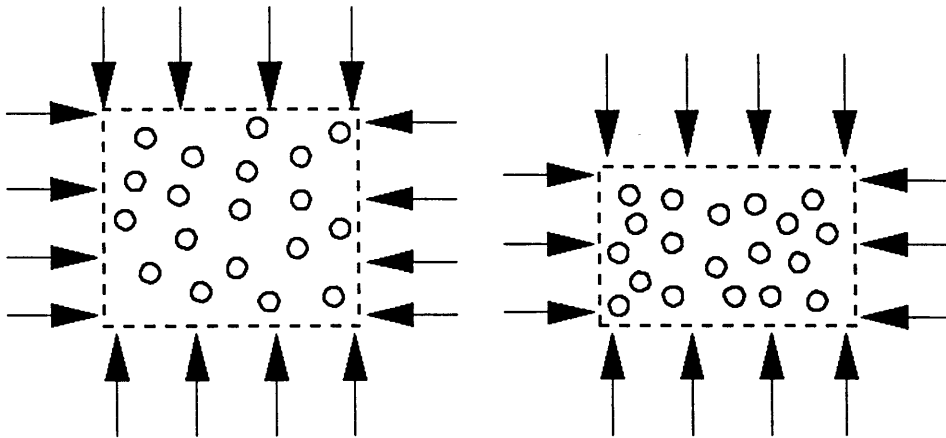
VISCOUS DEFORMATION: FORMING
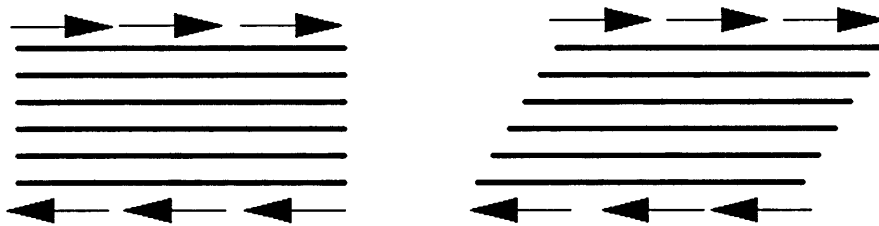
Fig. 3-7: Stress and response of an aligned fiber bundle
        in different cases

3-4. Constitutive Relations for Elastic Response

As mentioned above, the deformation of the fiber bundle can be much larger than that of most solids. The deformation behavior can also be highly nonlinear. Thus we introduce the incremental form to describe the stress-deflection relation. In the following discussion, we also use the conventional term of stress σ to replace term p in (3-5). We should mention here that under practical processing conditions, the fiber bundle motion is usually restricted in the transverse directions. In other words the internal shear of fibers is avoided so that the fiber bundle is under a hydrostatic stress state in the transverse direction. To capture such deformation behavior of the fiber bundle, we present the incremental form of the relationship between stress and deformation as

$$\Delta \epsilon_i = [S_{ij}(\sigma_o, \epsilon_o)] \, \Delta \sigma_j \qquad (i,j = 1,b) \qquad (3-7)$$

where subscript 1 refers to the longitudinal direction, and subscript b refers to the bulk properties, which can be visualized as the average of directions 2 and 3. This form is physically identical to (3-5). Here the usual form of stress and strain is used. $\Delta \epsilon_1$ is the deflection in direction 1 or x, and $\Delta \epsilon_b$ is the cross section area change of the bundle, which is also the total deflection in y and z directions. $\Delta \sigma_1$ is the stress in direction 1, and $\Delta \sigma_b$ is the stress in transverse directions. S_{ij} terms are the compliances in different directions. The subscript "o" refers to the reference state, since the compliance terms are no longer constant but change with the fiber bundle state. In (3-7) S_{11} is the longitudinal compliance of a fiber bundle, S_{bb} is the transverse bulk compliance, and S_{1b} and S_{b1} reflect the coupling between the longitudinal stress and the trans-

verse deformation, and vise versa. These are the so-called "coupling terms" which are used to account for the Poisson ratio effect. For elastic deformation, because of the energy conservation, S_{1b} must be equal to S_{b1}. Therefore only three terms in the compliance matrix are independent.

The term fiber volume fraction V_f is widely used in the literature to express the state of 2-d dilatation of a fiber bundle. The longitudinal deformation of a fiber bundle contributes very little to the change of V_f so that in most cases $\Delta V_f \approx \Delta A_f$, where ΔA_f is the change of fiber area fraction in the x direction. We also have the relation between $\Delta \epsilon_b$ and V_f

$$\Delta \epsilon_b = \Delta \epsilon_{22} + \Delta \epsilon_{33} \approx -\Delta V_f / V_f \qquad (3\text{-}8)$$

where V_f refers to the reference state. The minus sign here shows that when $\Delta \epsilon_b > 0$, fiber volume fraction V_f decreases. For a small incremental change, we have

$$\Delta \epsilon_b \approx -\Delta A_f / A_f \approx -\Delta V_f / V_f \qquad (3\text{-}9)$$

where A_f or V_f refers to the reference state.

In the following discussion, we present our study on evaluating the three compliance terms and the experiment verifications.

3-4-1. Estimation of the transverse compliance

Here we discuss the term S_{bb}, which measures how much the transverse deflection would be if the bundle is under the transverse compression. This is the typical stress state during the compression or autoclave

90

molding processes. In [33,34] Gutowski and coworkers gave a detailed dis-
cussion of the deformation behavior of a fiber bundle in these cases. The
basic assumption was that the fiber bundle responded to the transverse load
by bending between multiple contact points which resulted from either the
waviness or misalignment of fibers during earlier processing. The study
showed that S_{bb} was a function of the fiber volume fraction V_f, and
decreased substantially with the increase of V_f. Extensive experimental
data supported the analytical constitutive relation. Here we summarize the
main points in the derivation.

Fig. 3-8 shows a conceptual "fiber in a box" model. For a curved
fiber beam in the figure, we can use the bending beam calculation for the
stress and deflection

$$\sigma_f = \frac{F}{DL} = \frac{\pi\ Ed^4\delta}{64\ \alpha DL^4} \tag{3-10}$$

where terms F, D, L, d are shown in the Fig. 3-8, σ_f is the average fiber
stress, which is positive for compression in this expression, δ is the dis-
placement under force F, and α reflects the end conditions. Also we have

$$V_f = V_a\ \frac{d}{h}\frac{d}{D}\frac{l}{L} \tag{3-11}$$

where d and l are fiber diameter and length respectively, h, D, L are
dimensions of the "box", and V_a is the available fiber volume fraction, or
maximum packing efficiency. We assume that l/L is very close to one. Fur-
thermore a linear relationship is assumed for the deflection and beam span

91
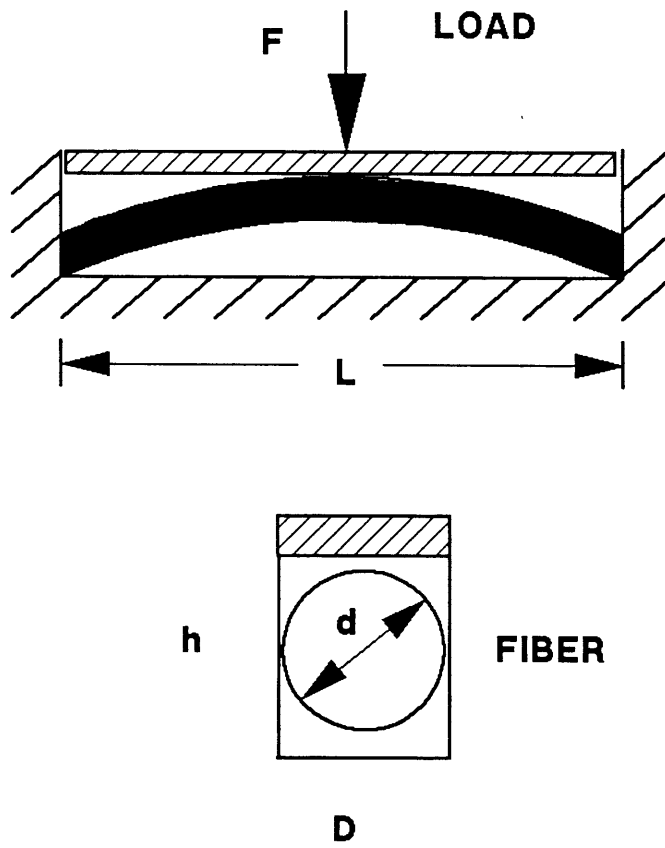
Fig. 3-8: "Fiber in a box" model for calculating compliance
term S_{bb}

$$L = \beta (h-d) \qquad\qquad (3\text{-}12)$$

where β is assumed to be constant. The physical meaning of β is the ratio of the span length to the span height. The geometry condition also gives

$$\delta = -(h_o - h) \qquad\qquad (3\text{-}13)$$

where h_o is the reference height corresponding to V_o which is the reference fiber volume fraction. The assumption is that when V_f is below V_o, fibers carry no load. Combining relations (3-10) to (3-13), we have

$$\sigma_f = A_s \; \frac{\dfrac{\sqrt{V_f}}{\sqrt{V_o}} - 1}{\left(\dfrac{\sqrt{V_a}}{\sqrt{V_f}} - 1\right)^4} \qquad\qquad (3\text{-}14)$$

where σ_f is the average fiber stress, A_s is the spring constant, which is determined experimentally, and V_a is the available fiber volume fraction or packing efficiency, which is the maximum V_f under practical conditions. By definition of the compliance, we have the expression for S_{bb}

$$S_{bb} = \Delta\epsilon_b/\Delta\sigma_b = (\Delta\epsilon_b/\Delta V_f)/(\Delta\sigma_b/\Delta V_f) \qquad\qquad (3\text{-}15)$$

In our tests fibers were constrained in the mold. There was no gross fiber movement in the y direction, so that $-\sigma_f \approx \sigma_b$ which, in the physical sense, was a "cylindrical" compression stress state. The minus sign here takes into account for the difference in definition of σ_f and σ_b. Combining (3-8), (3-14), and (3-15), we obtain

$$S_{bb} = \frac{(\frac{\sqrt{V_a}}{\sqrt{V_f}} - 1)^5}{A_s \frac{\sqrt{V_a}}{\sqrt{V_o}} [\ 2.5 - 0.5 \frac{\sqrt{V_f}}{\sqrt{V_a}} - 2 \frac{\sqrt{V_o}}{\sqrt{V_f}}\ ]} \qquad (3\text{-}16)$$

S_{bb} decreases with the increase of V_f, and reaches zero as V_f approaches V_a. This expression is plotted in Fig. 3-9, where parameters in (3-16) are chosen as V_a=0.85, V_o=0.5, and A_s=0.06 (psi) [64].

3-4-2. Estimation of the longitudinal compliance

Here we discuss the term S_{11}, which reflects the longitudinal or axial deformation when load is applied in the same direction. According to the micro-structure mechanics of the composite material, under the ideal condition where the fibers are perfectly aligned and straight, S_{11} is equal to $1/(E_f V_f)$, where E_f is the elastic modulus of the fiber [65]. Because of the imperfections of the fiber bundle, such as waviness and misalignment of fibers, the axial bundle stiffness is reduced. We analyze this reduction factor by using a statistical approach to the waviness and misalignment.

To simplify the analysis, we use a single fiber with some small waviness as an example. This is shown in Fig. 3-10, but in the figure the curvature is exaggerated. If we apply a tensile load to this fiber, the extension comes not only from the fiber elongation but also from the geom- etry change due to the change of the curvature. The force-extension rela- tion can be easily derived by using the energy method. According to exper- imental observations, the ratio a/L, which is shown in the figure, is less
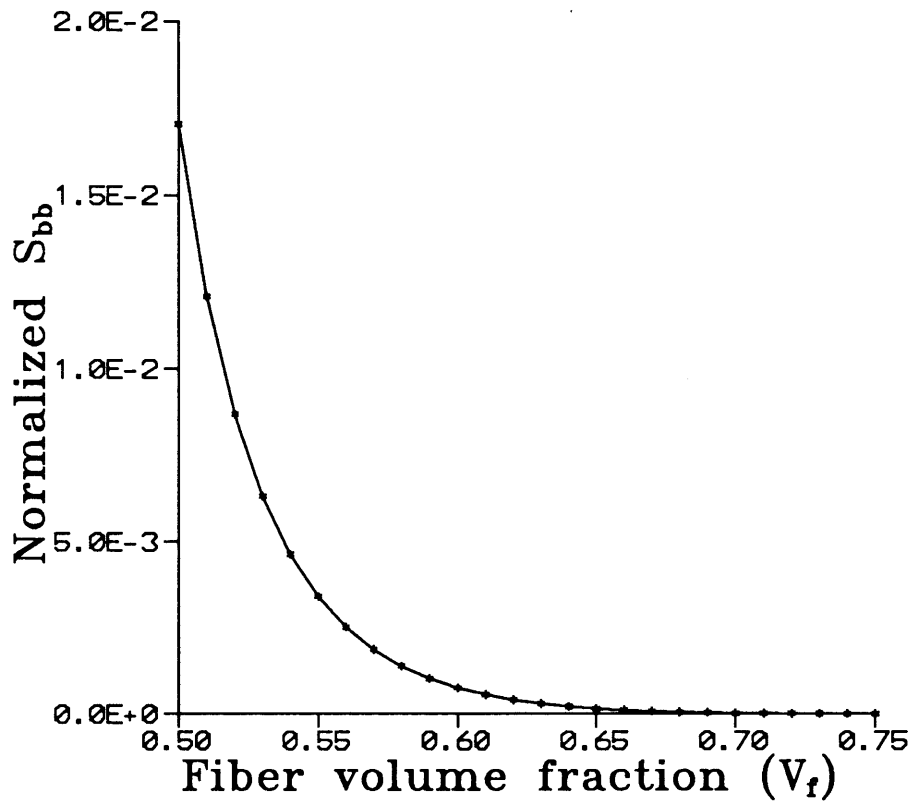
Fig. 3-9: Transverse fiber bundle compliance versus fiber
volume fraction (normalized by $S_{bb}*A_s$)
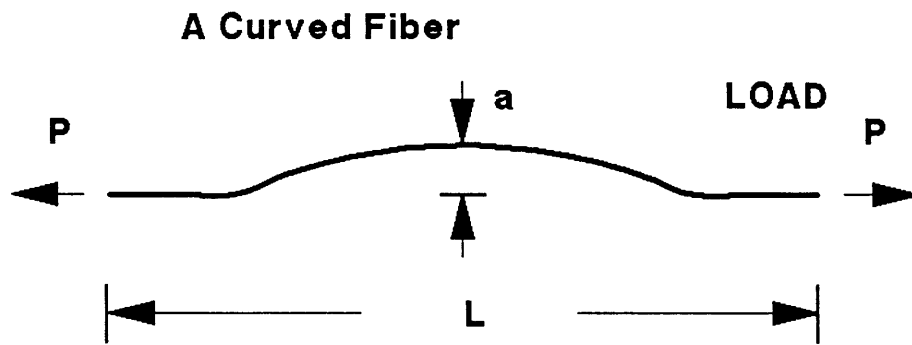
A Curved Fiber

Fig. 3-10: Example of a curved fiber under the longitudinal
tension load (curvature exaggerated)

or much less than 0.01 [50]. The bending stiffness of this fiber is $E_fI = E_f(\pi r^4/4)$, and the tensile stiffness is $E_fA = E_f(\pi r^2)$, where E_f is the fiber stiffness, and r is the fiber radius. If we apply a force P to the fiber in the longitudinal direction and measure the elongation ΔL by using the unit-load approach [66], we have

$$\Delta L = \int_0^L \frac{M_u M_L}{E_f I} \, dx + \int_0^L \frac{N_u N_L}{E_f A} \, dx \qquad (3\text{-}17)$$

where subscripts L refers to the real load and u refers to the unit-load, M_u and M_L are bending moments, and N_u and N_L are tension forces. Clearly $M_L = -Py$, $N_L = P$ with the real load P applied as shown in the figure, and $M_u = -y$, $N_u = 1$ with a unit-load applied. By using these relations we have

$$\Delta L = \frac{PL}{E_f A} \left(1 + \frac{4}{Lr^2} \int_0^L y^2 \, dx \right) \qquad (3\text{-}18)$$

where the second term in the parentheses is the contribution due to the waviness. We can use E_{eq} to express the equivalent bundle stiffness as

$$E_{eq} = \frac{E_f}{1 + \dfrac{4}{Lr^2} \displaystyle\int_0^L y^2 \, dx} \qquad (3\text{-}19)$$

In the expression the term y is used to express the curve shape of a fiber, which could be arbitrary for a single fiber. If we use *a* as the magnitude of the waviness, we can write $y = a \, f(x)$ and thus

$$E_{eq} = \frac{E_f}{1 + b(a^2/r^2)} \qquad (3\text{-}20)$$

where b is a dimensionless shape factor of the waviness and we have

$$b = \frac{4}{L} \int_0^L [f(x)]^2 \, dx \qquad (3\text{-}21)$$

We have to find some way to estimate this shape factor. With boundary conditions x=0, y=0 and y'=0; x=L, y=0 and y'=0, which are necessary for a continuous fiber, and the condition f(x=L/2)=1, we can choose some approximate expressions for f(x) to estimate values of b, as listed in the following table.

Table 3-1: Shape factor and curve shape of a single fiber

1) $f(x) = (1/2) \times [1\text{-}\cos(2\pi x/L)]$;   b=1.5

2) $f(x) = 16 \times (x/L)^2 \times (1\text{-}x/L)^2$;   b=1.625

3) $f(x) = 64 \times (x/L)^3 \times (1\text{-}x/L)^3$;   b=1.364

From the table we conclude that the value of b is close to 1.5. If the value of a is known, E_{eq} can be estimated.

The above analysis is only valid for a single curved fiber. To apply this analysis to a fiber bundle, we assume that some kind of distribution exists for the curvature or waviness parameters a/r and b. To simplify the problem, we assume b is constant, since the tabulation shows only small differences for different approximations. We treat the term a/r as a random variable with uniform distribution between [0, c], where c is a constant. This accounts for the fact that some of the fibers in the bundle are straight or almost straight, as observed in the previous experiments [50]. According to this definition c=max(a/r), but c can vary from sample

to sample. If c is small, the reduction of the stiffness is small. Previous test data showed that c can be around 1 [67].

We can use a statistical average method to derive the stiffness of a fiber bundle in the longitudinal direction. We define two random variables as follows

$$x = (a/r) \qquad\qquad\qquad (3-22)$$

$$z = 1/[1 + b(a/r)^2]. \qquad\qquad\qquad (3-23)$$

Physically, x reflects the curvature of the fiber, and z is the reduction factor, as shown in (3-20). The probability distributions of these variables are [68]

$$f_x(x) = 1/c \qquad\qquad [0 \leq x \leq c] \qquad (3-24)$$

$$f_z(z) = \frac{1}{2cb^{1/2}z^2(1/z-1)^{1/2}} \qquad [1/(1+bc^2) \leq z \leq 1] \qquad (3-25)$$

The expectation of z can be derived

$$E(z) = \frac{1}{2cb^{1/2}}[\ \sin^{-1}(1) - \sin^{-1}(\frac{1-bc^2}{1+bc^2})\ ] \qquad\qquad (3-26)$$

E(z) is also the reduction factor for a fiber bundle. For a bundle of fibers, the equivalent stiffness is

$$E_{eq} = V_f E_f E(z) \qquad\qquad\qquad (3-27)$$

Evidently, E(z) is smaller than 1 and is a function of b and c. Following is a table of E(z) values for selected b and c values.

Table 3-2: Stiffness reduction factor E(z) versus curvature
parameter b and c

	c=1.0	c=0.8	c=0.6	c=0.4	c=0.2	c=0.1
b=1.364	0.739	0.804	0.872	0.935	0.983	0.996
b=1.5	0.723	0.791	0.862	0.929	0.981	0.995
b=1.625	0.712	0.779	0.853	0.924	0.979	0.995

This tabulation shows that the reduction of the stiffness can be
over 20% for some extreme cases, and that the parameter c, which is used as
the index of the imperfections of the bundle and defined the maximum (a/r),
is important in evaluating this stiffness reduction.

According to observations made in [67], the max(a/r) is about one
and only about half of the fibers are curved in the AS4/3501-6 prepreg tape
with the fiber volume fraction around 0.5. The calculation of E(z) gives
result of about 0.86 in this case. Test data presented in Chapter 5 sup-
port this analysis. For the higher fiber volume fraction, the parameter c
will decrease. Thus the reduction factor would be larger, and in the ex-
treme case when V_f reaches V_a, this factor would be very close to 1. Com-
pared to the variation of S_{bb} term at different V_f values, the variation in
S_{11} is rather small. To simplify calculation, a constant of 0.9 is proba-
bly a good approximation for E(z) for fiber volume fraction between 0.5 to
0.7. Therefore the expression for S_{11} can be written as

$$S_{11} = \frac{1}{E(z)E_f V_f} \tag{3-28}$$

with E(z) is approximately equal to 0.9.

3-4-3. Estimation of the coupling term

As mentioned before, this term measures the deformation of a fiber bundle in the axial direction while load is applied in the transverse direction, or vise versa. Knowing of this coupling term is important in some cases. Fig. 3-11 shows an example where transverse load is applied to a fiber bundle which is restricted into a rigid wall box. In this case if some of the fibers are curved, compressive force can be induced against the wall. Since the stiffness of the fiber in the longitudinal direction is very high, the induced force could be large enough to buckle fibers. This could happen in closed shape structures, where fibers are restricted in motion in the longitudinal direction. In the case where all of the fibers were perfectly straight, this term would be zero until the available fiber volume fraction V_a was reached and the Poisson ration effect of each fiber had to be considered.

For the case of "fiber in a box", when a transverse load is applied within the fiber curvature plane and the fiber is restricted to move within the plane, fiber will extend in the axial direction. If the fiber is also restricted from extending in its axial direction, a compressive stress will be induced in the fiber. However, if the applied force is out of the plane of which the fiber curvature resides, the fiber may just be pushed to a new balance state without introducing any effect in the axial direction. In the discussion of the transverse compliance term, relation (3-12) shows that as the force applied to the fiber bundle becomes larger and larger, more and more contact points will develop between fibers, and the fiber
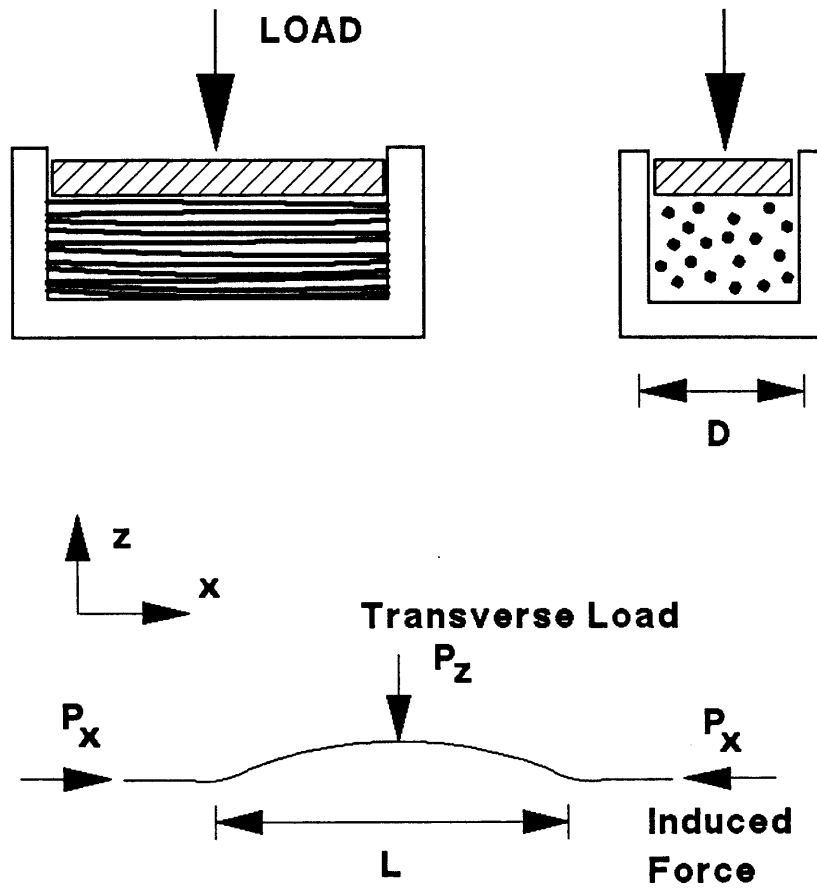
Fig. 3-11: Example of induced longitudinal load in fiber bundle
under the transverse compression

beam span becomes shorter and shorter. This is probably true even if the force applied to a single fiber is not within the curvature plane, since the fiber rearrangement may cause more contacts between fibers. For the coupling term, only a small portion of the force transmitted to a single fiber will induce an axial response. Now we consider the case of "fiber bundle in a box" such as in Fig. 3-11. Since all fibers are restricted in the axial direction, we have

$$S_{1b} = -(\sigma_1/\sigma_b)S_{11} \qquad\qquad (3\text{-}29)$$

For a single fiber curved in the x-z plane as shown in Fig. 3-11, we assume the curvature of the fiber can be expressed as

$$z = (a/2)*[1-\cos(2\pi x/L)] \qquad\qquad (3\text{-}30)$$

where L is the span length, and a is the span height. This expression satisfies the boundary conditions stated before. Under the given boundary conditions and with the restriction that the fiber can only move within the plane, the relation between the reacting axial force P_x and the acting transverse force P_z is

$$P_z/P_x = (a\pi^2)/(2L) \qquad\qquad (3\text{-}31)$$

P_x and P_z are shown in the figure. By using relation (3-11) we can write

$$D \approx d\ (V_a/V_f)^{1/2} \qquad\qquad (3\text{-}32)$$

where d is the fiber diameter, V_a is the available fiber volume fraction, and D is shown in the figure. From Fig. 3-11 we also have

$$P_z \approx \sigma_z\ L\ d\ (V_a/V_f)^{1/2} \qquad\qquad (3\text{-}33)$$

103

where σ_z is the average fiber stress component, and L is the curve span length as shown in the figure. For each fiber we can obtain the stress in the axial direction from (3-31) and (3-33) as

$$(\sigma_f)_x = (P_x)/(\pi d^2/4) = \sigma_z \ (8/\pi^3) \ (L^2/ad) \ (V_a/V_f)^{1/2} \qquad (3\text{-}34)$$

For a bundle of fibers the situation is more complicated. The span height a and length L are random variables with some kind of distributions. Only force components acting within the fiber curvature plane will cause the axial elongation. In other words only a small portion of the stress in the transverse direction causes the fiber to extent in the axial direction. The other portion of the stress just pushes the fiber to a new equilibrium state. How much is the portion of the stress which contributes to the axial elongation is closely related to the fiber volume fraction. As in the low fiber volume fraction state, fibers tend to move and rearrange themselves under the transverse compression stress. When fibers are more compacted, they tend to extend in the axial direction when transverse load is applied. This shows that S_{1b} term is strongly related to the fiber bundle deformation state V_f. For a bundle containing n fibers, from (3-34) we can summarize the fiber stress induced in the axial direction as

$$\sigma_1 = \sigma_z \ (V_a/V_f)^{1/2} \ (8/\pi^3) \ C(V_f) \ [(1/n)\sum_{i=1}^{n}(L_i^2/a_i d)] \qquad (3\text{-}35)$$

where σ_z is the transverse fiber stress which is in compression, n is the number of fibers in a fiber bundle, a_i is the span height, L_i is the span length, and the term $C(V_f)$ takes into account that only portion of the transverse load contributes to the induced force.

By combining (3-28), (3-29), and (3-35), we can write an expression for S_{1b}

$$S_{1b} = - \frac{B}{E_f} \frac{\sqrt{V_a}}{\sqrt{V_f}} C(V_f) \left[(1/n) \sum_{i=1}^{n} (L_i^2/a_i d) \right] \qquad (3\text{-}36)$$

where B is a constant, E_f is the fiber elastic modulus. To simplify the problem, we assume that within a range of V_f in the discussion, S_{1b} is a power function of V_f as

$$S_{1b} = C (V_f)^m / E_f \qquad (3\text{-}37)$$

where C and m are considered as constants which can be determined experimentally.

The detailed test device and measurements are given in Chapter 5. In the test the induced longitudinal force from the fiber bundle was monitored while the transverse load was applied to the bundle. Then non-linear least square curve fitting was performed. The estimations of constants C and m are, C=-0.0156, and m=-5.94. Therefore we have

$$S_{1b} = -0.0156 (V_f)^{-5.94} / E_f \qquad (3\text{-}38)$$

where E_f is the fiber axial stiffness and is equal to 34×10^6 *psi* for the graphite fibers used in the experiments. This relation is plotted in Fig. 3-12.
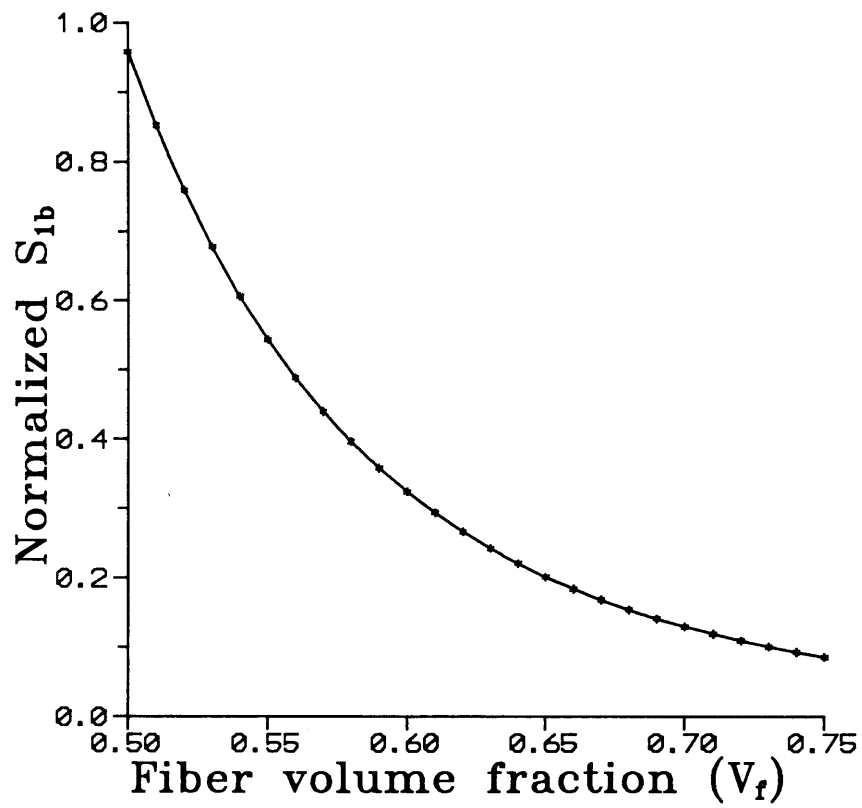
Fig. 3-12: Compliance term S_{1b} (coupling term) versus fiber
volume fraction (normalized by $S_{1b}*E_f$)

3-5. Viscoelastic Behavior of the Fiber Bundle

Although we treat the fiber bundle deformation in the material principal directions as elastic, there are other effects observed in the experiments. The assumption we made for the elastic analysis is that there is no gross movement of fibers in the deformation process. In other words, the internal friction loss due to relative motions of fibers can be excluded. This condition is probably true if the fiber stress is small in the transverse direction, or if the process time is relatively short. In general, non-elastic fiber deformation behavior was observed in the experiments. In some of measurements of transverse fiber bundle stiffness made by Kingery in this group, fiber bundles were pressed and released, and then pressed again. It was found that the stiffness curves of the fiber bundle for different runs were shifted [67]. Clearly there was irreversible fiber rearrangement in these runs. Since the fiber shape is cylindrical, this can be easily understood. Under the transverse compression pressure applied to the fiber bundle, fibers make contact with each other. A lot of these contact points and lines, or even small surfaces are in unstable states. Any small disturbance could cause fibers to move to a new equilibrium state, which is usually still an unstable state. This was especially true for unidirectional and aligned fiber bundles.

Viscoelastic analysis is one way of including the non-elastic effect. The compliance terms of the fiber bundle could be considered not only a function of the deformation state, which is parametrized by the fiber volume fraction V_f, but also a function of time. Also we assume these two functions can be separated and equation (3-7) can be rewritten as

$$\Delta \epsilon_i = [S_{ij}(\sigma_o, \epsilon_o) J_{ij}(t)] \; \Delta \sigma_j \qquad (i,j = 1,b) \qquad (3\text{-}39)$$

where J_{ij} terms are introduced for the creep or stress relaxation effect and are functions of time. In other words, even when stress terms do not change (i.e. $\Delta \sigma_j$ is zero), the changes in strains $\Delta \epsilon_i$ are not necessarily zero because the J_{ij} terms can change over a period of time. For example if we put a constant load on a fiber bundle, the fiber volume fraction may change with time. Consequently if $\Delta \epsilon_i$ is zero, over a period of time $\Delta \sigma_j$ may not be zero. For instance, if we hold the fiber bundle at certain volume fraction, the required transverse load would decrease with time. Since we assume the bundle stiffness is time dependent, the stress rate will affect the deformation behavior. If we apply load at a high stress rate, fiber motion is more limited than that with a lower stress rate.

In the real process, the situation is more complicated. At any instant of time, both S_{ij} terms and J_{ij} terms could change. As already derived, S_{ij} terms are nonlinear functions of fiber volume fraction V_f. The change of V_f depends on the process conditions. Usually V_f is some nonlinear function of time. Although we did not derive an explicit form of $J_{ij}(t)$, it can be thought of as some kind exponentially decaying function of time as used widely in the viscoelastic analysis. Experimental evaluation of these terms is difficult since it is almost impossible to "freeze" one variable and measure the other. In (3-39) we use the separation of variable, but this may not be true.

We have briefly discussed the complexity of the fiber bundle deformation problems encountered in the fabrication processes. This might

become a field for future research work.

3-6. Summary

The deformation of an aligned and lubricated continuous fiber bundle in composite manufacturing processes was discussed and a continuum mechanics model for the deformation was proposed. The deformation was considered as a combination of shear deformation and elastic modes. For some processes, such as molding, pultrusion, and winding, elastic deformation in the principal directions is dominant. A compliance matrix was presented and the compliance terms were evaluated to describe the elastic deformation modes. The analyses show that, in the longitudinal direction, the fiber bundle behaves linearly since the deformation is small and the elastic modulus is high, whereas in the transverse direction the bundle showed non-linear and quick stiffening behavior under compressive load. These compliance terms were found to be functions of the deformation state, which was represented by the fiber volume fraction V_f. Quantitative evaluation of these compliance terms was made by using statistical approaches.

The relationship derived in this discussion can be used for many composite manufacturing processes. In this project we applied the deformation relationship to the winding and consolidation process, as discussed in Chapter 2. In Chapter 5 we present experimental results on evaluating compliance terms and applying this fiber bundle deformation model to the winding and consolidation experiments.

4. NUMERICAL FORMULATION AND COMPUTER SIMULATION

4-1. Introduction

The process model presented in Chapter 2 includes nonlinear partial differential equations for consolidation and temperature distribution. The boundary conditions for these equations are also functions of time and various process parameters. Therefore the calculation can only be solved by using numerical techniques. Since we deal with a regular cylindrical structure, and assume the problem is axial-symmetric, the finite difference method is used in the numerical formulation. One difficulty in the calculation is that the temperature equation is coupled with the consolidation equation, which includes the fiber deformation and resin flow. The temperature profile determines the change of resin viscosity, which then determines the resin flow state. When the fiber volume fraction changes because of the resin flow, the material thermal conductivity as well as the material density changes. These in turn affect the temperature calculation. In the formulation of the computer simulation program, iterative loops are devised for performing the calculation. In this chapter we will discuss the finite difference scheme for consolidation and temperature calculation, and the computer program structure.

4-2. Formulation of the Consolidation Calculation

As discussed in Chapter 2, in the winding and consolidation calculations we have variables V_f, p_r, ξ, u, ϵ_r, ϵ_θ, σ_r, σ_θ, $(\sigma_f)_r$, and $(\sigma_f)_\theta$.

However, in the partial differential equation for flow and fiber deformation, the two primary variables we have chosen are V_f and p_r. These two variables directly reflect the consolidation and flow state of the material. We use λ as the index for the time step, and Δt as the time interval. Assuming we already know values of all these variables at the time $t=\lambda(\Delta t)$, we try to solve for new values at the time $t=(\lambda+1)(\Delta t)$. The calculation uses (2-6) to obtain new values of V_f at the new time. Then we obtain other process variables through equilibrium and other constitutive relations of displacement, strain, and stress. We assume that the temperature distribution at the new time step is already solved, so that parameters related to the temperature, such as resin viscosity or thermal expansion coefficient are known. This will be discussed further in the following section on the temperature calculation.

In this finite difference formulation, subscript λ is used for the time step, and k for the space step in the radial direction. We count the composite layers outwards, so that layer 1 is the layer on top of the mandrel. There are two kinds of space step variables. Some of the variables are evaluated at nodes or interfaces, so that they run from 0 to n. Others are averaged over the space step interval so that they run from 1 to n. Here n is the total number of space steps. For example, node 0 is always at the inner most boundary, and interval 1 is the inner most space step interval next to the inner most boundary.

For the flow and continuity equation (2-6), we first write all the terms explicitly as

$$\frac{1}{V_f}\frac{\partial V_f}{\partial t} = -\frac{1}{\xi}\frac{S}{\mu}\frac{\partial p_r}{\partial \xi} - \frac{\partial S}{\partial V_f}\frac{1}{\mu}\frac{\partial V_f}{\partial \xi}\frac{\partial p_r}{\partial \xi} + \frac{S}{\mu^2}\frac{\partial \mu}{\partial \xi}\frac{\partial p_r}{\partial \xi}$$

$$-\frac{S}{\mu}\frac{\partial^2 p_r}{\partial \xi^2} \qquad\qquad (4\text{-}1)$$

In this equation, the unknown variable is V_f at the new time step. By using the forward finite difference for the time variable, and central finite difference for the space variable, we have

$$(V_f)_{\lambda+1,k} = (V_f)_{\lambda,k}\ \{1 - \frac{1}{(\xi)_{\lambda,k}}(\frac{S}{\mu})_{\lambda,k}\frac{\Delta t}{2(\Delta\xi)_{\lambda,k}}[(p_r)_{\lambda,k+1} - (p_r)_{\lambda,k-1}]$$

$$- (\frac{S'}{\mu})_{\lambda,k}\frac{\Delta t}{4(\Delta\xi)^2}[(V_f)_{\lambda,k+1} - (V_f)_{\lambda,k-1}][(p_r)_{\lambda,k+1} - (p_r)_{\lambda,k-1}]$$

$$+ (\frac{S}{\mu^2})_{\lambda,k}\frac{\Delta t}{4(\Delta\xi)^2}[(\mu)_{\lambda,k+1} - (\mu)_{\lambda,k-1}][(p_r)_{\lambda,k+1} - (p_r)_{\lambda,k-1}]$$

$$- (\frac{S}{\mu})_{\lambda,k}\frac{\Delta t}{(\Delta\xi)^2}[(p_r)_{\lambda,k+1} - 2(p_r)_{\lambda,k} + (p_r)_{\lambda,k-1}]\ \}$$

$$(k=1,\ 2,\ \ldots,\ n\text{-}1) \qquad\qquad (4\text{-}2)$$

This relation is used to solve $(V_f)_k$ at the new time step since other variables at time step λ are all known. Variable V_f is an interface or node variable. The boundary values of V_f at new time step, $(V_f)_0$ and $(V_f)_n$, are related to the boundary conditions and will be discussed later. After solving V_f for the new time step, we can proceed to solve for ξ by using the continuity relation (2-4), which is a nonlinear ordinary differential equation for variable ξ. The finite difference form of (2-4) can be written as

$$\left[\frac{(V_f)_\lambda}{(V_f)_{\lambda+1}}\right]_0 = \frac{\xi_0}{r_0} \frac{\xi_1 - \xi_0}{(\Delta r)_1}$$

$$\left[\frac{(V_f)_\lambda}{(V_f)_{\lambda+1}}\right]_k = \frac{\xi_k}{r_k} \frac{\xi_{k+1} - \xi_{k-1}}{2(\Delta r)_k} \qquad (k=1, 2, \ldots, n-1)$$

$$\left[\frac{(V_f)_\lambda}{(V_f)_{\lambda+1}}\right]_n = \frac{\xi_n}{r_n} \frac{\xi_n - \xi_{n-1}}{(\Delta r)_{n-1}} \qquad (4\text{-}3)$$

where r_k's and $(\Delta r)_k$'s are known for the current time step, and ξ_k's are unknown for the new time step. ξ is also a interface variable. When V_f's are solved for the new time step, this becomes a set of equations for unknown ξ's.

This is a set of nonlinear algebraic equations so that iteration schemes must be used in the calculation. Newton's iteration method can be used to solve these equations [69]. We rewrite these equations in the form of

$$g_0(x_0, x_1, \ldots, x_n) = 0$$
$$g_1(x_0, x_1, \ldots, x_n) = 0$$
$$g_2(x_0, x_1, \ldots, x_n) = 0$$
$$\ldots\ldots \qquad \ldots\ldots$$
$$g_n(x_0, x_1, \ldots, x_n) = 0$$

$$(4\text{-}4)$$

The iteration equations are

$$\begin{bmatrix} (\dfrac{\partial g_0}{\partial x_0})_j & \cdots & (\dfrac{\partial g_0}{\partial x_n})_j \\ \cdots & & \cdots \\ (\dfrac{\partial g_n}{\partial x_0})_j & \cdots & (\dfrac{\partial g_n}{\partial x_n})_j \end{bmatrix} \begin{bmatrix} (x_0)_{j+1} \\ \cdots \\ (x_n)_{j+1} \end{bmatrix} = \begin{bmatrix} (\dfrac{\partial g_0}{\partial x_0})_j & \cdots & (\dfrac{\partial g_0}{\partial x_n})_j \\ \cdots & & \cdots \\ (\dfrac{\partial g_n}{\partial x_0})_j & \cdots & (\dfrac{\partial g_n}{\partial x_n})_j \end{bmatrix} \begin{bmatrix} (x_0)_j \\ \cdots \\ (x_n)_j \end{bmatrix} - \begin{bmatrix} (g_0)_j \\ \cdots \\ (g_n)_j \end{bmatrix}$$

$$(4\text{-}5)$$

where x_k's are the unknowns and in this case $x_k = \xi_{\lambda+1,k}$, ($k=0, 1, \ldots, n-1,$ n). Subscript j refers to the j-th iteration so that for each iteration we calculate the (j+1)-th new values from the known j-th values. In equation (4-5), $(x_k)_j$, $(g_k)_j$, and $(\partial g_k/\partial x_i)_j$ are all known, so that the iteration can be performed for $(x_k)_{j+1}$. This is repeated until $\max|(x_k)_{j+1} - (x_k)_j| < \epsilon$, where ϵ is the convergence error for the calculation.

The explicit forms of equation (4-4) and terms of $(\partial g_k/\partial x_i)$ in (4-5) are as follows (we omit the time subscripts $\lambda+1$ for some of the variables for simplicity)

$$g_0 = \xi_0 \, (\xi_1 - \xi_0) - r_0 \, (\Delta r)_1 \, [(V_f)_\lambda / (V_f)_{\lambda+1}]_0$$

$$g_k = \xi_k \, (\xi_{k+1} - \xi_{k-1}) - 2r_k \, (\Delta r)_k \, [(V_f)_\lambda / (V_f)_{\lambda+1}]_k$$

$$(k=1,2,\ldots,n-1)$$

$$g_n = \xi_n \, (\xi_n - \xi_{n-1}) - r_n \, (\Delta r)_{n-1} \, [(V_f)_\lambda / (V_f)_{\lambda+1}]_n$$

$$(4\text{-}6)$$

$$\frac{\partial g_0}{\partial \xi_0} = -2\xi_0 + \xi_1$$

$$\frac{\partial g_0}{\partial \xi_1} = \xi_0$$

114

$$\frac{\partial g_k}{\partial \xi_{k-1}} = -\xi_k$$

$$\frac{\partial g_k}{\partial \xi_k} = \xi_{k+1} - \xi_{k-1}$$

$$\frac{\partial g_k}{\partial \xi_{k+1}} = \xi_k$$

$$(k=1, 2, \ldots, n-1)$$

$$\frac{\partial g_n}{\partial \xi_{n-1}} = -\xi_n$$

$$\frac{\partial g_n}{\partial \xi_n} = 2\xi_n - \xi_{n-1}$$

$$(4-7)$$

The calculation scheme was constructed in an iterative way. Assuming that we already knew ξ_k at the time λ, we can estimate a new ξ_k at time $\lambda+1$ simply by using $\xi_{k,\lambda}$ since the difference between the two was very small. By using equations (4-6) and (4-7), we can calculate terms $g_i(\xi_j)$ and $\partial g_i / \partial \xi_j$. Then we can solve matrix equation (4-5) and obtain new values of $\xi_{k,\lambda+1}$. We repeated this kind of calculation until we reached the condition that $\max |[\xi_{k,\lambda+1}]_{j+1} - [\xi_{k,\lambda+1}]_j| < \epsilon$, where $k=0,1,\ldots,n$.

The $\partial g_i / \partial x_j$ matrix in (4-5) is a sparse matrix so that the amount of calculation can be greatly reduced. For each time step, we have the matrix form

$$
\begin{bmatrix}
\dfrac{\partial g_0}{\partial x_0} & \dfrac{\partial g_0}{\partial x_1} & 0 & & \cdots, & & 0 \\[2ex]
\dfrac{\partial g_1}{\partial x_0} & \dfrac{\partial g_1}{\partial x_1} & \dfrac{\partial g_1}{\partial x_2} & 0 & & \cdots, & 0 \\[2ex]
0 & \dfrac{\partial g_2}{\partial x_1} & \dfrac{\partial g_2}{\partial x_2} & \dfrac{\partial g_2}{\partial x_3} & 0 & \cdots, & 0 \\[2ex]
& & \cdots, & & \cdots, & & \\[1ex]
0 & & \cdots, & 0 & \dfrac{\partial g_{n-1}}{\partial x_{n-2}} & \dfrac{\partial g_{n-1}}{\partial x_{n-1}} & \dfrac{\partial g_{n-1}}{\partial x_n} \\[2ex]
0 & & \cdots, & & 0 & \dfrac{\partial g_n}{\partial x_{n-1}} & \dfrac{\partial g_n}{\partial x_n}
\end{bmatrix}
\tag{4-8}
$$

In doing Gauss elimination, a large amount of calculation can be saved because of these 0 elements. For a full n x n matrix, the Gauss elimination takes $(1/3)(n+1)^3$ operations. For matrix (4-8), only about $4(n+1)$ operations are needed [70]. Thus, even with large values of n, the increase of the amount of calculation is still limited.

When ξ_k's are solved for the new time step, the displacement u_k, and strains $(\epsilon_r)_k$ and $(\epsilon_\theta)_k$ can be derived directly from (2-7), (2-11), and (2-12)

$$
u_{k,\lambda+1} = \xi_{k,\lambda+1} - r_{k,\lambda+1} = \xi_{k,\lambda+1} - \xi_{k,\lambda}
\tag{4-9}
$$

$$
(\epsilon_r)_{k,\lambda+1} = (\Delta\xi)_{k,\lambda+1}/(\Delta r)_{k,\lambda+1} - 1 = (\Delta\xi)_{k,\lambda+1}/(\Delta\xi)_{k,\lambda} - 1
$$
$$
\tag{4-10}
$$

$$
(\epsilon_\theta)_{k,\lambda+1} = \xi_{k,\lambda+1}/r_{k,\lambda+1} - \xi_{k,\lambda+1}/\xi_{k,\lambda}
\tag{4-11}
$$

116

In the calculation, terms $\Delta\xi$ and Δr are evaluated over each space step, while ξ and r are evaluated at each node. From (4-10) ϵ_r's are obtained for each space step, but from (4-11) ϵ_θ's are for each space node or interface. Since in the calculation we use the interface or node values for stress and fluid pressure, we need to transform ϵ_r's into interface values. This is done by taking the average value over the adjacent space intervals as

$$(\epsilon_r)^*_0 = (\epsilon_r)_1$$
$$(\epsilon_r)^*_k = 0.5\ [(\epsilon_r)_k + (\epsilon_r)_{k+1}] \qquad (k=1,2,\ldots,n-1)$$
$$(\epsilon_r)^*_n = (\epsilon_r)_n$$

$$(4\text{-}12)$$

where ϵ_r^*'s are values at the interfaces. We also need interface values for $\Delta\xi$ terms in some formulation. This can be obtained in the same way as

$$(\Delta\xi)^*_0 = (\Delta\xi)_0 = \xi_1 - \xi_0$$
$$(\Delta\xi)^*_k = 0.5\ [(\Delta\xi)_k + (\Delta\xi)_{k+1}] = 0.5\ [(\xi_{k+1} - \xi_{k-1})]$$
$$(k=1,2,\ldots,n-1)$$
$$(\Delta\xi)^*_n = (\Delta\xi)_{n-1} = \xi_n - \xi_{n-1}$$

$$(4\text{-}13)$$

where $(\Delta\xi)^*$'s are values at the interfaces. Later we just drop the $*$ for simplicity. We obtain the stress terms $(\sigma_f)_r$ and $(\sigma_f)_\theta$ from (2-13) and (2-14)

$$[(\sigma_f)_\theta]_k = [\frac{S_{rr}(\epsilon_\theta - \alpha_\theta \Delta T) - S_{\theta r}(\epsilon_r - \alpha_r \Delta T)}{S_{\theta\theta}S_{rr} - S_{r\theta}S_{\theta r}}]_k \qquad (4\text{-}14)$$
$$(k=0,\ 1,\ 2,\ \ldots,\ n)$$

117

$$[(\sigma_f)_\theta]_k = [\frac{S_{\theta\theta}(\epsilon_r - \alpha_r \Delta T) - S_{r\theta}(\epsilon_\theta - \alpha_\theta \Delta T)}{S_{\theta\theta}S_{rr} - S_{r\theta}S_{\theta r}}]_k \qquad (4\text{-}15)$$

$$(k=0, 1, 2, \ldots, n)$$

We also rewrite (2-8) as

$$\frac{(\sigma_f)_r - (\sigma_f)_\theta}{r} + \frac{\partial(\sigma_f)_r}{\partial r} - \frac{\partial p_r}{\partial r} = 0 \qquad (4\text{-}16)$$

This equation combined with (2-9) and (2-10) gives a relation for the fluid pressure p_r

$$\frac{\partial p_r}{\partial \xi} = \frac{\partial r}{\partial \xi} \frac{1}{r} \frac{1}{S_{\theta\theta}S_{rr} - S_{r\theta}S_{\theta r}} [(S_{\theta\theta}+S_{\theta r})(\frac{\partial \xi}{\partial r} - 1 - \alpha_r \Delta T) + (S_{r\theta}+S_{rr})$$

$$(\frac{\xi}{r} - 1 - \alpha_\theta \Delta T)] + \frac{\partial}{\partial \xi} \{ \frac{1}{S_{\theta\theta}S_{rr} - S_{r\theta}S_{\theta r}} [S_{\theta\theta}(\frac{\partial \xi}{\partial r} - 1 - \alpha_r \Delta T)$$

$$- S_{r\theta}(\frac{\xi}{r} - 1 - \alpha_\theta \Delta T)]\} \qquad (4\text{-}17)$$

This illustrates the relationship for the equilibrium condition between p_r and other variables V_f and ξ. We can simply write (4-17) as

$$\frac{\partial p_r}{\partial \xi} = F(V_f, \xi, \xi') \qquad (4\text{-}17a)$$

where

$$\xi' = \frac{\partial \xi}{\partial r} \qquad (4\text{-}18)$$

Here we note that S_{ij} terms are all functions of V_f as discussed in Chapter 3. Therefore when V_f values for the new time step are obtained, these S_{ij}

118

terms can be calculated. The finite difference equations for p_r become

$$\frac{(p_r)_k - (p_r)_{k-1}}{(\Delta\xi)_k} = F_k(V_f, \xi, \xi') \qquad (k=1,2,\ldots,n)$$

(4-19)

To solve for p_r values we still need to use the boundary condition. At the interface of bleeder and composite, both resin pressure and resin flow must be continuous. Therefore we have

$$q = \frac{S_b}{(\mu)_n} \frac{(p_r)_n}{h_r} = -\frac{(S)_n}{(\mu)_n} \frac{(p_r)_n - (p_r)_{n-1}}{(\Delta\xi)_n}$$

(4-20)

This gives us the relation between $(p_r)_n$ and $(p_r)_{n-1}$ as

$$\left[\frac{S_b}{h_r} + \frac{(S)_n}{(\Delta\xi)_n}\right](p_r)_n - \frac{(S)_n}{(\Delta\xi)_n} (p_r)_{n-1} = 0$$

(4-21)

where q is the flow rate, S_b is the permeability of the bleeder, S is the permeability of the composite layer, h_r is the height of the fluid accumulated in the bleeder. The subscript n refers to the node at the top surface of the layer, or the composite and bleeder interface. The fluid height h_r can be calculated as

$$h_r = \sum_{i=1}^{\lambda} q_i (\Delta t)/\epsilon_b$$

(4-22)

where

$$q_i = -\left(\frac{S}{\mu}\right)_n \frac{(p_r)_n - (p_r)_{n-1}}{(\Delta\xi)_n}$$

(4-23)

which is the flow rate at the interface of the bleeder and composite at each time step, and ϵ_b is the bleeder porosity. Other boundary conditions

119

are also used here for the process variable V_f and ξ. We assume that at the bleeder and composite interface, which is also the top surface of the wound layers, the load must be balanced by fiber and resin. This introduces the relation

$$- p = (\sigma_f)_r - p_r \qquad (4\text{-}24)$$

where p is the boundary pressure, which could be either consolidation pressure or applied pressure. At the interface of mandrel and composite, there is no radial flow, therefore we have

or
$$[\partial p_r / \partial \xi]_0 = 0 \qquad (4\text{-}25)$$

$$(p_r)_1 = (p_r)_{-1} \qquad (4\text{-}25a)$$

By substituting this relation into (4-1), we can obtain the other boundary condition for V_f as

$$(V_f)_{\lambda+1,0} = (V_f)_{\lambda,0} - (\frac{S'}{\mu})_0 \frac{2\Delta t}{(\Delta\xi)^2} (V_f)_{\lambda,0} [(p_r)_1 - (p_r)_0] \qquad (4\text{-}26)$$

At this interface we also have continuity conditions

$$\xi_0 = b_m + (u_m)_o \qquad (4\text{-}27)$$

$$(\sigma_r)_0 = - (p_m)_o \qquad (4\text{-}28)$$

where b_m is the external radius of the mandrel, and $(p_m)_o$ is the external radial pressure on the mandrel.

In the iteration loops for the flow calculation, these boundary conditions are coupled so that we estimate some values first, then do the

120

calculation and use these equations to check if the calculated values con-
verge to the estimation values. Here we first estimate the value of ξ_0,
then use (4-2) and (4-26) to obtain new values of V_f except at the top
boundary. To obtain the top boundary $(V_f)_n$ value we estimate it by using
$(p_r)_n$ at time λ. Then (4-17) and (4-21) are used to derive p_r values.
$(V_f)_n$ is checked again by using new p_r values. This is repeated until the
calculation converges. The same procedures are applied to the ξ_0 term in
another loop. This flow calculation loop is illustrated in Fig. 4-1.

This flow and consolidation calculation is still within a larger
loop for the temperature calculation. This will be presented later after
the discussion of temperature calculation formulation.

4-3 Formulation of the Temperature Calculation

The basic equations for the temperature calculation are (2-61), (2-
62), and (2-63). These are nonlinear partial differential equations. The
difficulty here is the coupling between the thermal and consolidation cal-
culation. The way we proceed is to assume a temperature distribution for
the new time step based on the information of temperature distribution at
the previous time step and the applied temperature conditions. Then we
solve the consolidation equations to obtain variables V_f, p_r, ξ, and others
for the new time step. From these solutions we can solve temperature dis-
tribution by using (2-61), (2-62), and (2-63). This temperature distribu-
tion, of course, is usually different from our assumptions, and we use it
to repeat the consolidation calculation. This kind of iteration is
repeated until the temperature distribution calculation converges, which

```
                 ENTER FROM CONSO
                        |
        INITIALIZATION FOR FLOW SUBROUTINE
                        |
            BEGIN LOOP 1 (B.C. FOR ξ) ←─────────────────┐
                        |                                |
          BEGIN LOOP 2 (B.C. FOR Vf & pr) ←────────┐    |
                        |                           |    |
              CALCULATION FOR NEW Vf                |    |
                        |                           |    |
                CALCULATION FOR ξ                   |    |
                        |                           |    |
          LOOP 3 (NEWTON'S METHOD FOR ξ)            |    |
                        |                           |    |
               CALCULATION FOR εr, εθ               |    |
                        |                           |    |
                CALCULATION FOR σf                   |    |
                        |                           |    |
                CALCULATION FOR pr                   |    |
                        |                           |    |
             CHECK B.C. FOR Vf & pr  ── no ─────────┘    |
                        |                                |
                       yes                               |
                        |                                |
                  END LOOP 2                             |
                        |                                |
              CHECK B.C. FOR ξ  ── no ──────────────────┘
                        |
                       yes
                        |
                  END LOOP 1
                        |
              GO BACK TO CONSO
```
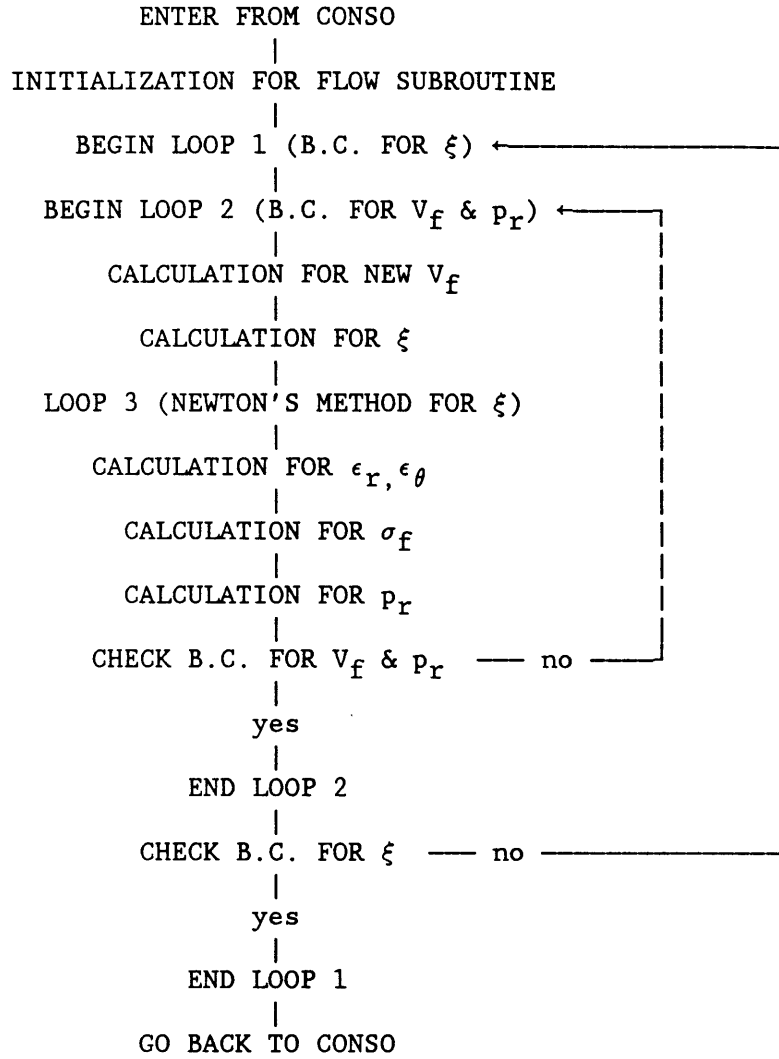
Fig. 4-1: Calculation scheme of flow and consolidation

means that the proposed temperature distribution for the new time step is close enough to the calculated results. Since we proceed incrementally, this convergence is usually guaranteed.

In this iteration scheme, when we solve for the new temperature, other variables such as V_f, p_r, or ξ, are already known. Therefore it is possible to use the implicit scheme for the temperature calculation. The advantage of the implicit scheme is the unconditional stability regardless of the time step used.

We first write out (2-61) explicitly as

$$
\frac{\xi}{V_f}\frac{\partial T}{\partial t} = \frac{\xi T}{V_f^2}\frac{\partial V_f}{\partial t} + \frac{\xi k_T}{V_f\rho c}\frac{\partial^2 T}{\partial \xi^2} + \frac{k_T}{V_f\rho c}\frac{\partial T}{\partial \xi} + \frac{TS}{\mu V_f}\frac{\partial p_r}{\partial \xi} + \frac{\xi S}{V_f\mu}\frac{\partial T}{\partial \xi}\frac{\partial p_r}{\partial \xi}
$$

$$
+ \frac{\xi T}{V_f\mu}\frac{\partial S}{\partial V_f}\frac{\partial V_f}{\partial \xi}\frac{\partial p_r}{\partial \xi} - \frac{\xi TS}{V_f\mu^2}\frac{\partial \mu}{\partial \xi}\frac{\partial p_r}{\partial \xi} + \frac{\xi TS}{V_f\mu}\frac{\partial^2 p_r}{\partial \xi^2} + \frac{\xi \rho H'}{V_f} \qquad (4\text{-}29)
$$

This combined with (2-62) for the mandrel, and (2-63) for the bleeder, will be used for the formulation. As we have done for the variable ξ, here we still use the form $g_j(T_j)=0$ such as in the expression (4-4) and (4-5). To simplify the expression, we omit the time subscript $\lambda+1$, and use T_{j0} and $(V_f)_{k0}$ to represent these variables at the time step λ. We also assume that we have nm space intervals for the mandrel, n space intervals for composite layer, and nb space intervals for the bleeder. In these expressions, we use two sets of subscripts because the temperature is solved for the mandrel, composite layers, and the bleeder material, while other variables, such as V_f, P_r, or μ, etc., are only for the composite layers. The

123

temperature variable T_j has a total of *nm+n+nb+1* nodes. Other variables with subscript k have only *n+1* nodes.

For the mandrel we have

$$
(\frac{k_T}{\rho c})_m \frac{\Delta t}{2(\Delta r_m)(r_m)_k} [T_{j+1} - T_{j-1}] + (\frac{k_T}{\rho c})_m \frac{\Delta t}{(\Delta r_m)^2} [T_{j+1} - 2T_j + T_{j-1}]
$$

$$
- T_j + T_{j0} = 0 \qquad (k=1,2,\ldots,nm-1; \; j=1,2,\ldots,nm-1)
$$

$$(4\text{-}30)$$

where Δr_m is the space step for the mandrel and $\Delta r_m = h_m/nm = (b_m - a_m)/nm$. These are equations $g_j = 0$, $j=1,2,\ldots,nm-1$. Then we use the mandrel and composite interface condition to obtain equation $g_{nm} = 0$. Clearly the temperature and the heat flow must be continuous at this interface. Therefore we have [71]

$$
K_L \frac{T_{nm+1} - T_{nm}}{(\Delta\xi)_1} = K_m \frac{T_{nm} - T_{nm-1}}{(\Delta r)_m} \qquad (4\text{-}31)
$$

Here the subscript L refers to the composite layer. From (4-31), we can derive equation $g_{nm} = 0$ as

$$
- T_{nm} + \frac{k_L(\Delta r_m)}{k_m(\Delta\xi)_1 + k_L(\Delta r)_m} T_{nm+1} + \frac{k_m(\Delta\xi)_1}{k_m(\Delta\xi)_1 + k_L(\Delta r)_m} T_{nm-1} = 0
$$

$$(4\text{-}32)$$

For the composite layer, we can derive similar equations $g_j = 0$ by using (4-29)

$$\frac{T_j}{(V_f)_k} [(V_f)_k - (V_f)_{k0}] + (\frac{k_T}{\rho c})_k \frac{\Delta t}{(\Delta\xi)^2}[T_{j+1} - 2T_j + T_{j-1}]$$

$$+ (\frac{k_T}{\rho c})_k\frac{\Delta t}{2(\Delta\xi)\xi_k} [T_{j+1} - T_{j-1}] + \frac{S_k T_j}{\xi_k \mu_k} \frac{\Delta t}{2(\Delta\xi)} [(p_r)_{k+1} - (p_r)_{k-1}]$$

$$+ \frac{S_k}{\mu_k} \frac{\Delta t}{4(\Delta\xi)^2} [T_{j+1} - T_{j-1}] [(p_r)_{k+1} - (p_r)_{k-1}] + \frac{S_k' T_j}{\mu_k} \frac{\Delta t}{4(\Delta\xi)^2}$$

$$[(p_r)_{k+1} - (p_r)_{k-1}] [(V_f)_{k+1} - (V_f)_{k-1}] - \frac{S_k T_j}{\mu_k^2} \frac{\Delta t}{4(\Delta\xi)^2}[\mu_{k+1} - \mu_{k-1}]$$

$$[(p_r)_{k+1} - (p_r)_{k-1}] + \frac{S_k T_j}{\mu_k} \frac{\Delta t}{(\Delta\xi)^2} [(p_r)_{k+1} - 2(p_r)_k + (p_r)_{k-1}]$$

$$+ (\rho H')_k (\Delta t) - T_j + T_{j0} = 0$$

$$(k=1,2,\ldots,n-1; \; j=nm+1,nm+2,\ldots,nm+n-1) \qquad (4\text{-}33)$$

Then for the bleeder and composite interface, the temperature and heat flow must be continuous. Similar to the composite and mandrel interface, we have [71]

$$K_b \frac{T_{nm+n+1} - T_{nm+n}}{(\Delta r)_b} = K_L \frac{T_{nm+n} - T_{nm+n-1}}{(\Delta\xi)_{n-1}} \qquad (4\text{-}34)$$

where $(\Delta r)_b$ is the space interval of the bleeder and $(\Delta r)_b = h_b/nb = (b_b - a_b)/nb$. The equation $g_{nm+n} = 0$ becomes

$$- T_{nm+n} + \frac{k_L(\Delta r)_b}{k_b(\Delta\xi)_{n-1} + k_L(\Delta r)_b} T_{nm+n+1}$$

$$+ \frac{k_b(\Delta\xi)_{n-1}}{k_b(\Delta\xi)_{n-1} + k_L(\Delta r)_b} T_{nm+n-1} = 0 \qquad (4\text{-}35)$$

For the bleeder material, the equation $g_j = 0$ becomes

125

$$(k_{eq})_b \, \frac{\Delta t}{2(\Delta r_b)(\xi_b)_k} \, [T_{j+1} - T_{j-1}] + (k_r')_b \, \frac{\Delta t}{(\Delta r_b)^2} \, [T_{j+1} - 2T_j + T_{j-1}]$$

$$- T_j + T_{j0} = 0$$

$$(j = nm+n+1, \ nm+n+2, \ \ldots, \ nm+n+nb-1; \ k=1,2,\ldots,nb-1) \qquad (4\text{-}36)$$

where $(k_{eq})_b$ is the equivalent thermal diffusivity for the bleeder material, which includes the effect of the fluid accumulated in the bleeder. For the bleeder, ξ_b changes when layers are consolidated, but Δr_b remains unchanged since we neglect the deformation of the bleeder material. Here we only consider the heat conduction. We assume that the bleeder porosity does not change, or there is no deformation for the bleeder material. Therefore although there is heat convection because of the resin flow, the contribution due to convection is small compared to the conduction. However, the fluid accumulated in the bleeder will change the thermal property and density of the material, which cannot be neglected.

To calculate the equivalent thermal diffusivity, we need to consider three different cases, a bleeder layer without fluid, a bleeder layer partially filled with fluid, and a bleeder layer filled with fluid. This is shown in Fig.4-2. We will discuss these situations separately.

We use k_b, ρ_b and c_b for thermal conductivity, density, and specific heat for the bleeder material, and k_r, ρ_r, and c_r for fluid resin. Also e_b is the porosity of the bleeder material. For bleeder layer without fluid resin, the heat transfer equation is

126

WITHOUT FLUID

BLEEDER

WITH PARTIAL FLUID
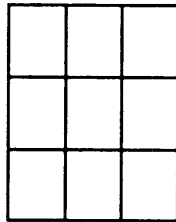
BLEEDER

BLEEDER   FLUID
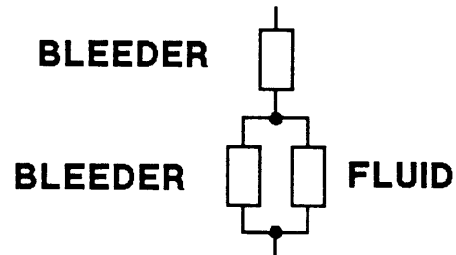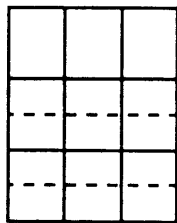
WITH FLUID
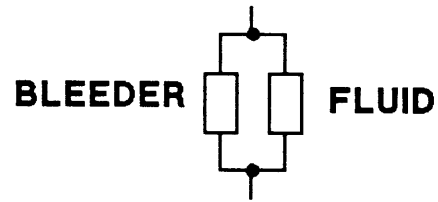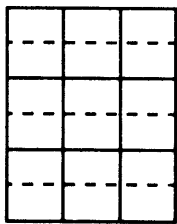
BLEEDER   FLUID

Fig. 4-2: Heat transfer modes of bleeder without fluid, partially
filled with fluid, and with fluid

127

$$(1 - e_b) \; \rho_b c_b \; \frac{\partial T_b}{\partial t} = (1 - e_b) \; k_b \; (- \frac{1}{\xi_b} \frac{\partial T_b}{\partial \xi_b} + \frac{\partial^2 T_b}{\partial \xi_b{}^2}) \qquad (4\text{-}37)$$

where T_b is the temperature distribution. For this case we have

$$(K_{eq})_b = \frac{k_b}{\rho_b c_b} \qquad (4\text{-}38)$$

where $(K_{eq})_b$ is the equivalent thermal diffusivity of the bleeder layer. For the bleeder layer filled with fluid, the fluid and the porous bleeder material act like parallel heat conductors as shown in Fig. 4-2. The heat transfer equation in this case becomes

$$[e_b \rho_r c_r + (1\text{-}e_b) \rho_b c_b] \; \frac{\partial T_b}{\partial t} = [e_b k_r + (1\text{-}e_b) k_b] \; (- \frac{1}{\xi_b} \frac{\partial T_b}{\partial \xi_b} + \frac{\partial^2 T_b}{\partial \xi_b{}^2})$$

$$(4\text{-}39)$$

Therefore in this case we have

$$(K_{eq})_b = \frac{e_b k_r + (1\text{-}e_b) k_b}{e_b \rho_r c_r + (1\text{-}e_b) \rho_b c_b} \qquad (4\text{-}40)$$

For the bleeder layer partially filled with fluid, the situation is more complicated. The portion with fluid and the portion without fluid act like two different heat conductors, and then these two conductors are connected in series. This is also shown in Fig. 4-2. The heat transfer equation is

$$[e_b \rho_r c_r \; \frac{\Delta h_r}{\Delta r_b} + (1\text{-}e_b) \rho_b c_b] \; \frac{\partial T_b}{\partial t} = K' (- \frac{1}{\xi_b} \frac{\partial T_b}{\partial \xi_b} + \frac{\partial^2 T_b}{\partial \xi_b{}^2}) \qquad (4\text{-}41)$$

where

$$K' = \cfrac{1}{(1 - \cfrac{\Delta h_r}{\Delta r_b})\,\cfrac{1}{k_b} - + \cfrac{\Delta h_r}{\Delta r_b}\,\cfrac{1}{e_b k_r + (1-e_b)k_b}} \qquad (4\text{-}42)$$

where Δh_r is the height of the fluid accumulated in the bleeder layer which is partially filled with fluid. In this case the equivalent thermal diffusivity is

$$(K_{eq})_b = \cfrac{K'}{e_b \rho_r c_r (\Delta h_r / \Delta r_b) + (1-e_b)\rho_b c_b} \qquad (4\text{-}43)$$

In the calculation we have the total bleeder thickness h_b and total space steps nb for the bleeder. For each space interval of the bleeder, the thickness is $(\Delta r)_b$. The height of the fluid accumulated in the bleeder is h_r, which is calculated for each time step. By comparing h_r with Δr_b, we can determine how many space intervals of the bleeder material are filled with fluid, and which space interval is partially filled with fluid. Then the equivalent thermal diffusivity $(K_{eq})_b$ for each space interval is determined.

To solve these equations $g_j(T_j)=0$ by using Newton's iteration method, we need to know terms $\partial g_j / \partial T_j$, which we list as follows

1) Mandrel part:

$$\frac{\partial g_j}{\partial T_{j-1}} = - (\frac{k_T}{\rho c})_m \frac{\Delta t}{2(\Delta r_m)(r_m)_k} + \frac{\Delta t}{(\Delta r_m)^2} (\frac{k_T}{\rho c})_m$$

$$(j=2,\ 3,\ \ldots,\ nm\text{-}1;\ k=2,\ 3,\ \ldots,\ nm\text{-}1)$$

$$\frac{\partial g_j}{\partial T_j} = -2\,(\frac{k_T}{\rho c})_m \frac{\Delta t}{(\Delta r_m)^2} - 1$$

$$(j=1,\ 2,\ \ldots,\ nm-1)$$

$$\frac{\partial g_j}{\partial T_{j+1}} = (\frac{k_T}{\rho c})_m \frac{\Delta t}{2(\Delta r_m)(r_m)_k} + \frac{\Delta t}{(\Delta r_m)^2}\,(\frac{k_T}{\rho c})_m$$

$$(k=1,\ 2,\ \ldots,\ nm-2;\ k=1,\ 2,\ \ldots,\ nm-2) \qquad (4\text{-}44)$$

2) Mandrel/composite interface:

$$\frac{\partial g_{nm}}{\partial T_{nm-1}} = \frac{k_m \Delta \xi}{k_m \Delta \xi + k_L \Delta r_m}$$

$$\frac{\partial g_{nm}}{\partial T_{nm}} = -1$$

$$\frac{\partial g_{nm}}{\partial T_{nm+1}} = \frac{k_L \Delta r_m}{k_m \Delta \xi + k_L \Delta r_m}$$

$$(4\text{-}45)$$

3) Composite layer:

$$\frac{\partial g_j}{\partial T_{j-1}} = (\frac{k_T}{\rho c})_k \frac{\Delta t}{(\Delta \xi)^2} - (\frac{k_T}{\rho c})_k \frac{\Delta t}{2(\Delta \xi)\xi_k} - \frac{S_k}{\mu_k} \frac{\Delta t}{4(\Delta \xi)^2} [(p_r)_{k+1} - (p_r)_{k-1}]$$

$$+ \frac{S_k T_j}{\mu_k^2} \frac{\Delta t}{4(\Delta \xi)^2}\,\mu'_{k-1}\,[(p_r)_{k+1} - (p_r)_{k-1}]$$

$$(k=2,\ 3,\ \ldots,\ n-1;\ j=nm+k)$$

$$\frac{\partial g_j}{\partial T_j} = \frac{[(V_f)_k - (V_f)_{k0}]}{(V_f)_k} - 2(\frac{k_T}{\rho c})_k \frac{\Delta t}{(\Delta \xi)^2} + \frac{S_k}{\xi_k \mu_k} \frac{\Delta t}{2(\Delta \xi)} [(p_r)_{k+1} - (p_r)_{k-1}]$$

$$- \frac{S_k}{\xi_k} \frac{\Delta t}{2(\Delta \xi)} \frac{\mu_k'}{\mu_k^2} [(p_r)_{k+1} - (p_r)_{k-1}] - \frac{S_k \mu_k'}{\mu_k^2} \frac{\Delta t}{4(\Delta \xi)^2} [T_{j+1} - T_{j-1}]$$

$$[(p_r)_{k+1} - (p_r)_{k-1}] + \frac{S_k'}{\mu_k} \frac{\Delta t}{4(\Delta \xi)^2} [(p_r)_{k+1} - (p_r)_{k-1}][(V_f)_{k+1} - (V_f)_{k-1}]$$

$$- \frac{S_k' \mu_k'}{\mu_k^2} \frac{\Delta t}{4(\Delta\xi)^2} [(V_f)_{k+1} - (V_f)_{k-1}][(p_r)_{k+1} - (p_r)_{k-1}] - \frac{S_k}{\mu_k^2} \frac{\Delta t}{4(\Delta\xi)^2}$$

$$[(p_r)_{k+1} - (p_r)_{k-1}][\mu_{k+1} - \mu_{k-1}] + \frac{S_k T_j}{\mu_k^3} \frac{\Delta t}{4(\Delta\xi)^2} [\mu_{k+1} - \mu_{k-1}]$$

$$[(p_r)_{k+1} - (p_r)_{k-1}] + \frac{S_k}{\mu_k} \frac{\Delta t}{(\Delta\xi)^2} [(p_r)_{k+1} - 2(p_r)_k + (p_r)_{k-1}]$$

$$- \frac{S_k T_j \mu_k'}{\mu_k^2} \frac{\Delta t}{(\Delta\xi)^2} [(p_r)_{k+1} - 2(p_r)_k + (p_r)_{k-1}] - 1$$

$$(k=1, 2, \ldots, n-1; \ j=nm+k)$$

$$\frac{\partial g_j}{\partial T_{j+1}} = (\frac{k_T}{\rho c})_k \frac{\Delta t}{(\Delta\xi)^2} + (\frac{k_T}{\rho c})_k \frac{\Delta t}{2(\Delta\xi)\xi_k} + \frac{S_k}{\mu_k} \frac{\Delta t}{4(\Delta\xi)^2} [(p_r)_{k+1} - (p_r)_{k-1}] \cdot$$

$$- \frac{S_k T_j}{\mu_k^2} \frac{\Delta t}{4(\Delta\xi)^2} \mu'_{k-1} [(p_r)_{k+1} - (p_r)_{k-1}]$$

$$(k=1, 2, \ldots, n-2; \ j=nm+k)$$

$$(4-46)$$

4) Composite/bleeder interface:

$$\frac{\partial g_{nm+n}}{\partial T_{nm+n-1}} = \frac{k_L (\Delta_r)_b}{k_b (\Delta\xi)_{n-1} + k_L (\Delta r)_b}$$

$$\frac{\partial g_{nm+n}}{\partial T_{nm+n}} = -1$$

$$\frac{\partial g_{nm+n}}{\partial T_{nm+1+n}} = \frac{k_b (\Delta\xi)_{n-1}}{k_b (\Delta\xi)_{n-1} + k_L (\Delta r)_b}$$

$$(4-47)$$

5) Bleeder part:

$$\frac{\partial g_j}{\partial T_{j-1}} = - [(K_{eq})_b]_k \frac{\Delta t}{2(\Delta r_b)(r_b)_k} + [(K_{eq})_b]_k \frac{\Delta t}{(\Delta r_b)^2}$$

$$(k=2, 3, \ldots, nb-1; \ j=nm+n+k)$$

$$\frac{\partial g_j}{\partial T_j} = -2 \ [(K_{eq})_b]_k \ \frac{\Delta t}{(\Delta r_b)^2} - 1$$

$$(k=1, \ 2, \ \ldots, \ nb\text{-}1; \ j=nm+n+k)$$

$$\frac{\partial g_j}{\partial T_{j+1}} = [(K_{eq})_b]_k \ \frac{\Delta t}{2(\Delta r_b)(r_b)_k} + [(K_{eq})_b]_k \ \frac{\Delta t}{(\Delta r_b)^2}$$

$$(k=1, \ 2, \ \ldots, \ nb\text{-}2; \ j=nm+n+k)$$

(4-48)

These are the terms we need to solve temperature distribution T_j (j=1, 2, ..., nm, nm+1, ..., nm+n, nm+n+1, ..., nm+n+nb-1). We assume the boundary temperature T_0 and $T_{nm+n+nb}$ are known from the applied conditions. We also use terms of S' and μ' in the formulation, which represent $\partial S/\partial V_f$ and $\partial \mu/\partial T$ respectively, since the permeability S is a function of V_f, and resin viscosity μ is a function of temperature and degree of cure. From the discussion in Chapter 2, we know the analytical forms of these functions so that their derivatives can be obtained.

This set of equations for temperature distribution can be solved in the same way as the calculation for ξ in the consolidation calculation, which we discussed in detail in the previous section. After the temperature distribution is derived, further calculation of resin viscosity and degree of cure can be carried out as discussed in section 2-4.

4-4. Computer Simulation Program Structure

The computer simulation program was developed on a Micro-VAX system with FORTRAN language. The program structure is illustrated in Fig. 4-3,

132
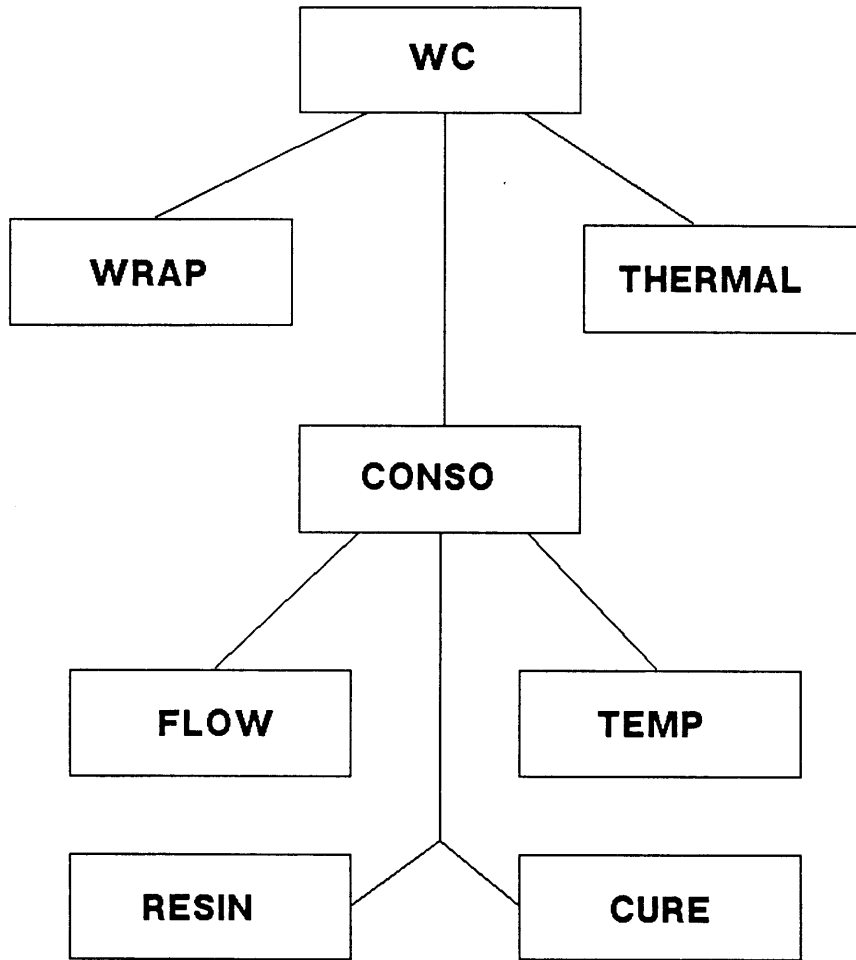
Fig. 4-3: Block diagram of WC simulation program

where each block represents a main program or subroutine. This program consists of main program WC, which stands for the winding calculation, and several subroutines for winding, consolidation, cure, and post-cure stages. For example, WRAP is the subroutine for the winding operation calculation, CONSO is the subroutine for the consolidation calculation, FLOW is the iteration subroutine for the resin flow, and TEMP is the iteration subroutine for the temperature. The basic process variables in the calculation are fiber stress, fiber deformation state or fiber volume fraction, resin pressure, and product dimensions. The input for the program includes applied winding tension, applied pressure, applied temperature, resin viscosity properties, fiber or prepreg tape properties, mandrel dimension, etc. The program then does the simulation and yields the variations of the process variables and the final state of the product. These relations are shown in Fig. 4-4.

As stated in the previous sections, there are several iteration loops in the program for temperature and flow calculations because of the coupling between the thermal effect and consolidation of the composite material, and because of the coupled boundary conditions. This is illustrated in Fig. 4-5. The main variables used in the calculation are V_f, p_r, T, and ξ. All of them appear in the partial differential equations and the boundary conditions. The way we proceed is to assume some boundary values for these variables for the new time step. This is based on the solutions of current time step and the applied conditions so that the estimations are close to the real solution, which bounds the convergence of the iteration. This is summarized in Fig. 4-6. For each new time step, we first estimate the new temperature distributions based on the previous

```
INPUT                                                   OUTPUT

┌─────────────────┐                              ┌─────────────────┐
│  MANDREL        │        ┌──────────┐          │                 │
│    DIMENSION    │        │          │          │    WINDING      │
│  WINDING        │───────▶│ WINDING  │─────────▶│    STRESS       │
│    TENSION      │        │          │          │    DIMENSIONS   │
│  MATERIAL       │        └──────────┘          │                 │
│    PROPERTY     │             │                └─────────────────┘
└─────────────────┘             │
                                ▼
┌─────────────────┐        ┌──────────┐          ┌─────────────────┐
│  APPLIED        │        │          │          │  LAYER STRESS   │
│    PRESSURE     │        │ CONSO-   │          │  DIMENSIONS     │
│  DEBULKING      │───────▶│ LIDATION │─────────▶│  RESIN PRESSURE │
│    TEMPERATURE  │        │          │          │  FIBER VOLUME   │
│  RESIN          │        └──────────┘          │    FRACTION     │
│    VISCOSITY    │             │                └─────────────────┘
└─────────────────┘             │
                                ▼
┌─────────────────┐        ┌──────────┐          ┌─────────────────┐
│  APPLIED        │        │          │          │  LAYER STRESS   │
│    PRESSURE     │        │  CURE    │          │  DIMENSIONS     │
│  CURE           │───────▶│          │─────────▶│  FIBER VOLUME   │
│    TEMPERATURE  │        └──────────┘          │    FRACTION     │
│                 │             │                └─────────────────┘
└─────────────────┘             │
                                ▼
┌─────────────────┐        ┌──────────┐          ┌─────────────────┐
│  COOLING        │        │  POST    │          │                 │
│    RATE         │───────▶│  CURE    │─────────▶│  LAYER STRESS   │
│  APPLIED        │        │          │          │  DIMENSIONS     │
│    PRESSURE     │        └──────────┘          │                 │
└─────────────────┘                              └─────────────────┘
```

Fig. 4-4: Simulation program structure
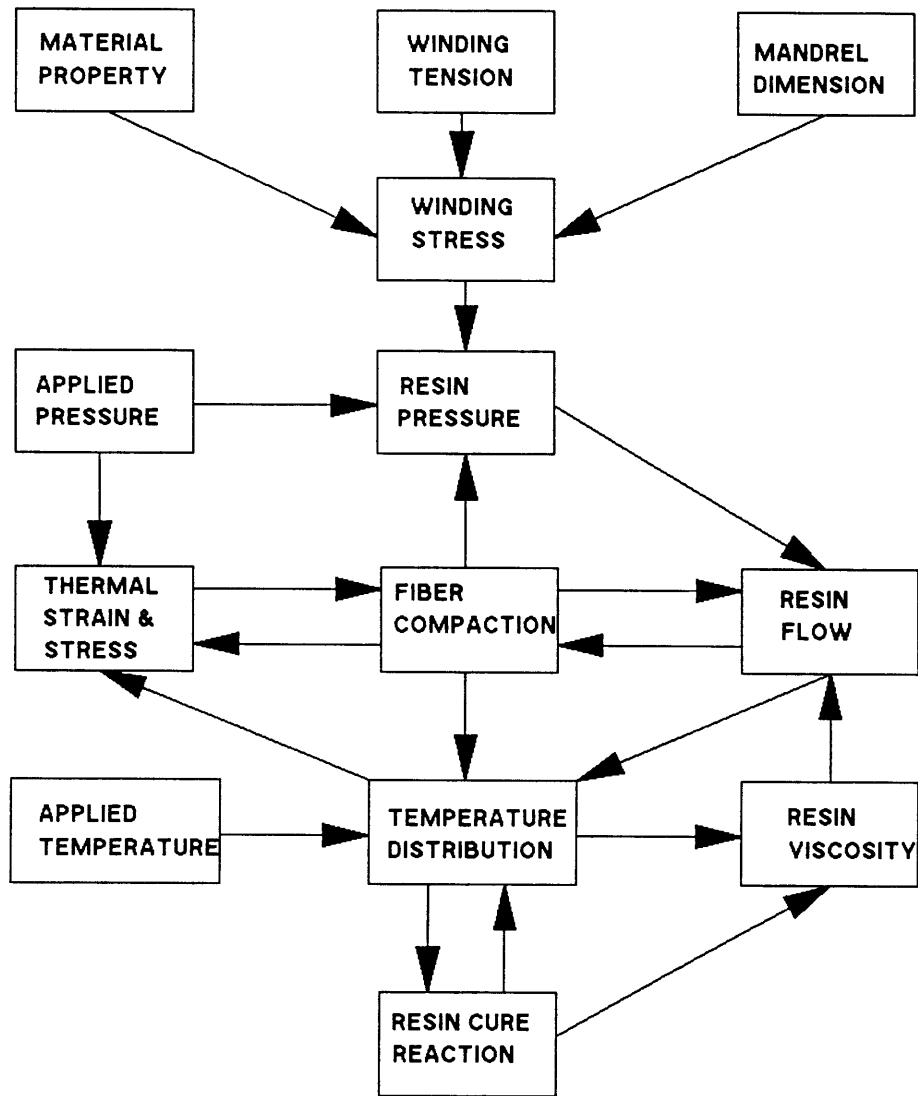
Fig. 4-5: Illustration of coupling between heat transfer and
consolidation calculation

```
                    READ INPUT DATA
                          |
                    INITIALIZATION
                          |
                 WINDING SUBROUTINE
                          |
            BEGIN LOOP 1 (NEW TIME)  ←──────────────────────────┐
                          |                                      |
            INPUT APPLIED CONDITIONS                             |
                          |                                      |
             BEGIN LOOP 2 (NEW TEMP)  ←──────────────────┐       |
                          |                               |      |
                 TRIAL T_x (NEW TEMP)                      |      |
                          |                               |      |
                CALCULATION FOR μ, α                       |      |
                          |                               |      |
        GO TO FLOW SUBROUTINE (WITH T_x)                   |      |
                          |                               |      |
            BEGIN LOOP 3 (HEAT TRANSFER)  ←──┐             |      |
                          |                   |            |      |
                 TRIAL T_1 (NEW TEMP)          |            |      |
                          |                   |            |      |
                CALCULATION FOR T_2            |            |      |
                          |                   |            |      |
                  CHECK T_1=T_2?  ── no ──────┘            |      |
                          |                                |      |
                         yes                               |      |
                          |                                |      |
                    END LOOP 3                             |      |
                          |                                |      |
                  CHECK T_2=T_x?  ── no ───────────────────┘      |
                          |                                       |
                         yes                                      |
                          |                                       |
                    END LOOP 2                                    |
                          |                                       |
              CALCULATION TIME?  ── no ────────────────────────────┘
                          |
                         yes
                          |
               POST CURE SUBROUTINE
                          |
                         END
```
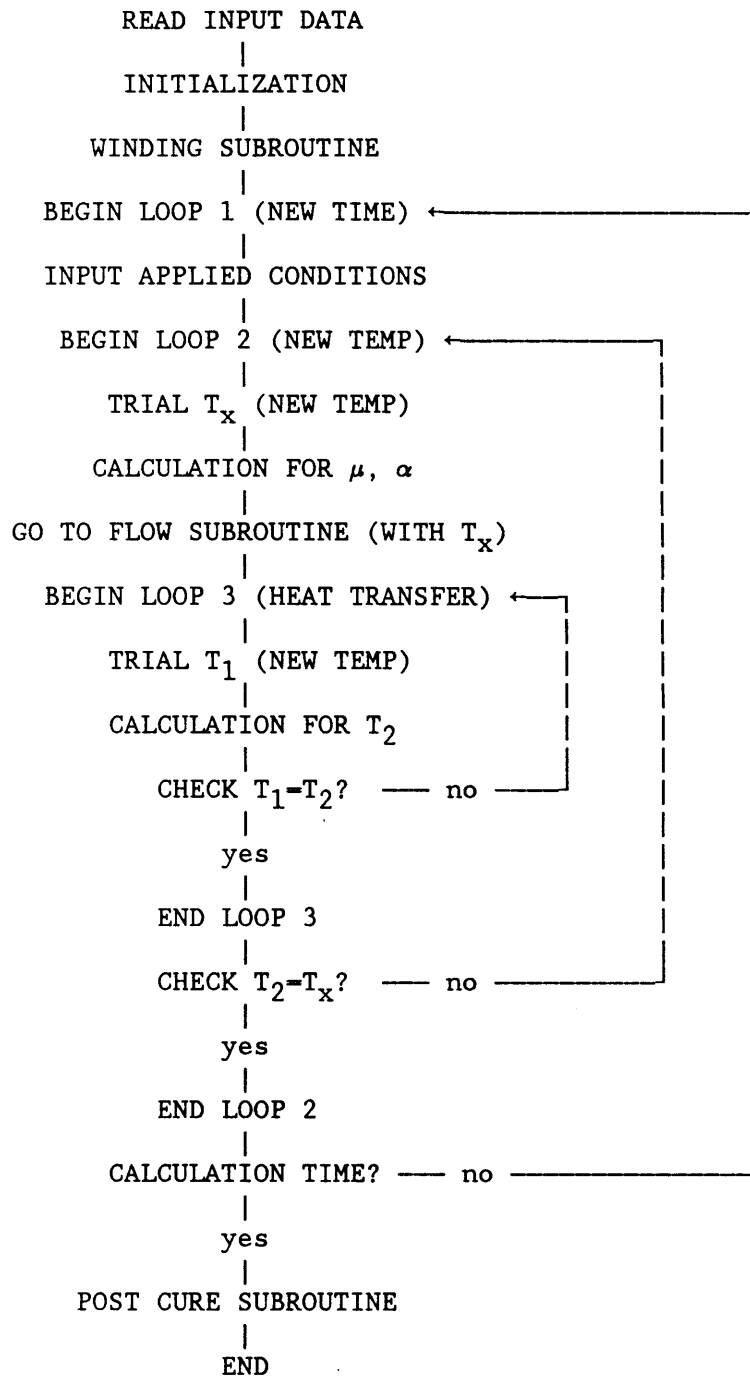
Fig. 4-6: Illustration of numerical iteration loops in
computer simulation program

values and the applied temperature conditions in this time step. We express these estimations as T_x's. Then we proceed with the flow and consolidation calculation, and continue to the temperature cycle. In the temperature cycle, in which we use the Newton's method for iteration, we need to estimate the temperature distribution. We express them as T_1's. Then we calculate a new temperature distributions, which we express as T_2's, by using iteration. These are equivalent to the j-th and (j+1)-th values in the iteration equation (4-5). If T_1's and T_2's are not close enough, we use T_2's to replace T_1's as new estimations and repeat the calculation. This calculation continues until T_1's and T_2's are close enough. Since this is still within the temperature loop, we use new T_2's to update the T_x's, and repeat the calculation until T_x's and T_2's converge. This kind of iteration is repeated for each time step.

Since the temperature calculation used the implicit finite difference formulation, there was no time step requirement for the stability, which was a serious restriction for the explicit formulation. Newton's method showed very good convergence rate so that iteration times were very limited. The flow and consolidation formulation involved the explicit finite difference method so that the time step was restricted by the stability requirement. Since the equations were nonlinear, the time step limitation was not only determined by the linear term but also the nonlinear effect. This limitation was the main factor in determining the simulation time required.

The consolidation calculation ends when the resin cures. After this point, the material is considered as solid composite which exhibits

transversely isotropic properties. The stress existing in the material is assumed to be retained, and used as initial condition for the post cure calculation, which involves solving algebraic equations discussed in Section 2-5. The input data here includes applied pressure and temperature, and post-cure process time. The block diagram in Fig. 4-7 shows the calculation procedures, which are based on the manufacturing process design. Usually the calculation starts with the winding operation. If the winding operation can be simplified, the calculation of the winding and consolidation can be separated. Otherwise we must do the winding and consolidation calculation at the same time. If there are debulking procedures between several winding stages, the calculation is performed accordingly between the winding and consolidation. The cure process calculation involves the temperature change and cure reaction, in which Springer's model developed in [2] is used as a subroutine. The final step is the post cure thermal stress calculation, in which the final stress state and dimensions are obtained.

The simulation program is used to compare with various experimental results, as discussed in the following chapter. The applied experimental parameters are used as the simulation program input, and the test results are compared with the model predictions. Since our work focuses on the consolidation part of the problem, the main process variables in our study are the fiber volume fraction V_f, and resin pressure p_r, which we use as basic variables in the formulation and experiment design.
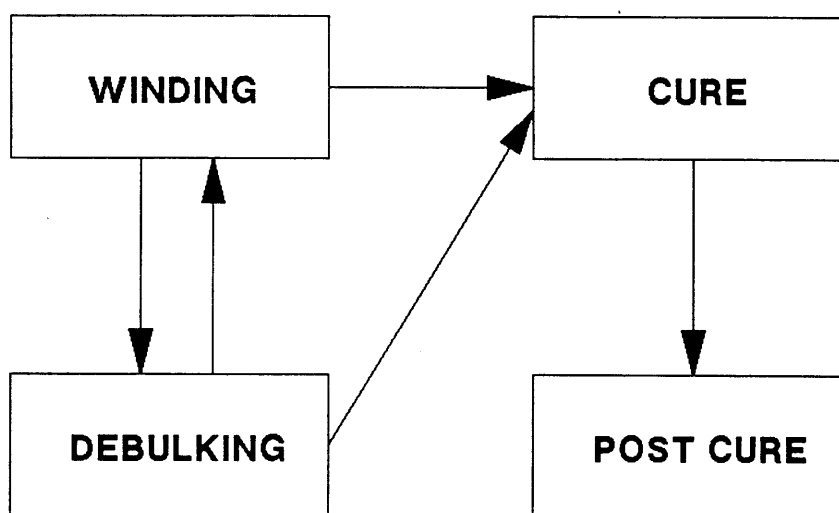
Fig. 4-7: Block diagram of calculation procedures

4-5. Summary

In this chapter we presented the formulation of the numerical simulation schemes. The key issue in this formulation was to design iteration loops and to choose appropriate initial estimations for better convergence rate. In our formulation we separated the temperature calculation and consolidation calculation by assuming initial temperature distributions. Then we proceeded with the flow and consolidation calculation, and continued with a calculation on the new temperature distribution. This iteration continued until the convergence was reached. This simulation successfully included different operation stages and yielded a time history of process variables.

This numerical simulation of the process, combined with the experiment investigation which will be discussed in the following chapter, helps to understand better the process physics and to design and control fabrication processes.

5. EXPERIMENTS

5-1. Introduction

The purpose of the series of experiments conducted in this study was to improve understanding of the process physics and to verify the computer simulation results. There were two categories of experiments, the study of the basic material properties and behaviors, and the simulation of the manufacturing processes. The first category studied the fiber bundle deformation behavior in detail. One example of verification of this fiber bundle model was the fiber distribution measurement in the laminate molding process. The second category simulated the wet filament winding operation and the consolidation of cylindrical parts. This was to verify the winding and consolidation model developed in this study. These experiments will be discussed in detail in the following sections.

5-2. Experiments on Fiber Bundle Deformation

As we presented in Chapter 3, fiber bundle elastic deformation behavior during the process can be summarized by using three compliance terms and the incremental form of stress-deformation matrix. Experiments were designed and performed to estimate these compliance terms and to determine some of the constants used in deriving these expressions. Three compliance terms, S_{11}, S_{1b}, and S_{bb} will be discussed separately in the following sections. In this study, only S_{11} and S_{1b} were measured in experiemtns. For completeness, the experiment on measuring S_{bb}, which was done in the pre-

142

vious study in this group on consolidation of laminate composites and was presented in the form of the transverse fiber stiffness [33,34,35,67], is summarized here.

5-2-1. Experiments on Measuring Longitudinal Compliance

This term determines how much a fiber bundle deforms in the longitudinal direction when load is applied to the bundle in the same direction. The difficulty in measuring this term is attaching a displacement or strain measuring device to the fiber bundle without disturbing the fiber bundle state. Prepreg tape was chosen for the test because the uncured epoxy resin effectively held fibers together and, at the same time, made a negligible contribution to the material stiffness. The fiber conditions within the prepreg tape were also very close to the manufacturing processing conditions.

AS4/3501-6 graphite fiber/epoxy prepreg tapes supplied from Hercules were used. The tape had fiber volume fraction about 0.5 and average thickness about 0.007 inch. Test specimens were obtained by cutting the tape to pieces of 0.75 inch wide and 6 inches long in the fiber direction. Then these pieces of prepreg tapes were laid up unidirectionally to 2 and 4 ply thickness. Inspection of the prepreg tapes showed that fibers were well aligned within the tape. The cutting and lay-up operations were done carefully to avoid introducing any significant disturbance.

Because the prepreg tape did not provide the hard surface necessary for attaching strain gages, a special treatment was devised. Both ends of

the tape layup of about 1 inch in the fiber direction were cured on a hot press by using special molds, while the middle part of the specimen was kept at room temperature by forced air convection. The arrangement is shown in Fig. 5-1. The cure temperature of the ends of the specimen was kept at 350°F for about two hours via the heated mold on a hot press. Thermocouples were inserted into the mold to monitor temperature. Room temperature air was forced through middle part of the specimen, maintaining the temperature of the middle part at 90-100°F. This became a typical fin type heat transfer problem, which can be solved analytically, as summarized in Appendix A. The temperature distribution is also shown in Fig 5-1. After the cure, the middle part of the tape was checked and found still un-cured, which confirmed that the uncured resin would not affect fiber deformation when tension load was applied.

A special strain gage EA-06-40CBY-120 with 4 inch long effective length, which was made by Micro-Measurements Group, was bonded to each specimen. This strain gage was used as an extensometer to obtain an aver-age strain over the 4 inch length. The cured region was hard enough to al-low the specimen to be gripped at both ends. The test was done on an In-stron 1125 test machine at a constant crosshead speed of 0.01 in/min, and the load-deformation curve was recorded for each specimen. Fig. 5-2 il-lustrates the test specimen and strain gage arrangement.

The load-deformation relation for this case is

$$F_x = R_x\, A_x\, E_f\, V_f\, \epsilon_x \tag{5-1}$$

HOT PRESS
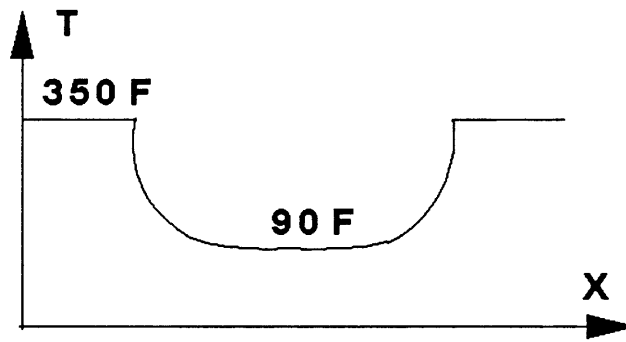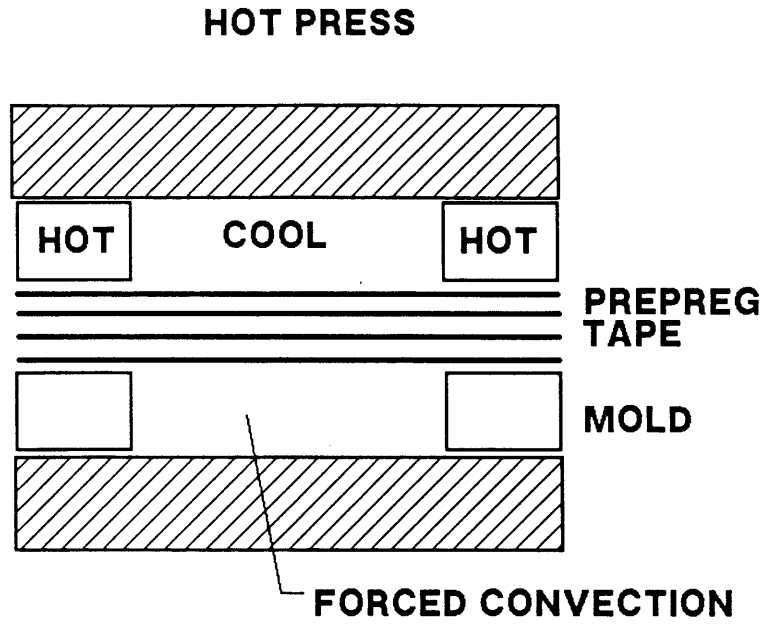
Fig. 5-1: Curing ends of test specimen for measuring compliance
term S_{11}
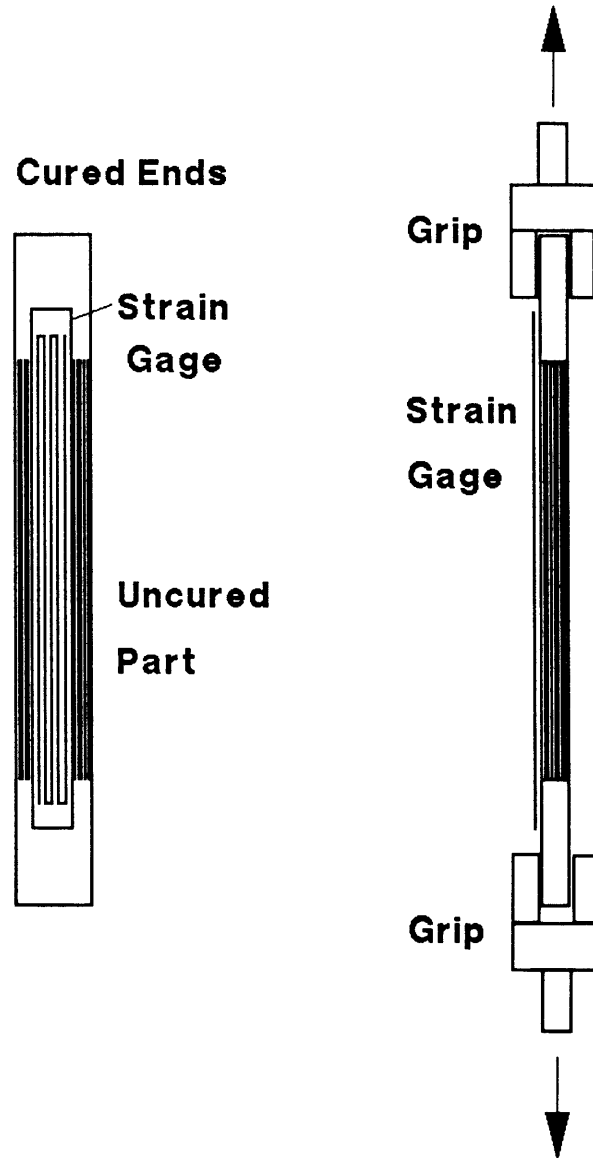
Fig. 5-2: Test specimen and strain gage arrangement for
measuring compliance term S_{11}

where F_x is the total load in the x direction obtained from the Instron load cell output, A_x is the cross section area, E_f is the fiber stiffness, V_f is the fiber volume fraction, and ϵ_x is the average strain obtained from the strain gage output. R_x is the reduction factor to be determined, which was equivalent to the term E(z) in (3-27). Since the strains were small in the test, A_x and V_f were treated as constant. A_x, V_f, and E_f were determined from the measurement of the prepreg tape.

Test results show that the stress-strain curve is almost linear. Least square curve fitting was used to obtain the stiffness of the fiber bundle. The stiffness reduction was within the range of the analytical solution. The reduction factor on stiffness calculated from the test data was around 0.83. Fig. 5-3 shows one set of experimental data on stress-strain relations. Test data are summarized in Appendix B.

Since the deformation of fibers in the longitudinal direction was very small, the fiber volume fraction was almost constant in the test. Thus the reduction factor data from the tests was for the case of about 0.5 fiber volume fraction. Similar test results of stress-strain relation of a fiber bundle in longitudinal direction were also reported in [56], although test data showed larger sample to sample scatter.

According to observations made in [67], the maximum *a/r*, which was the ratio of curve span to the fiber radius, was about one, and only about half of the fibers were curved. The theoretical estimation of E(z), which was the stiffness reduction factor, gave 0.86 for this case. Therefore the analytical result is in good agreement with the test data. These data were
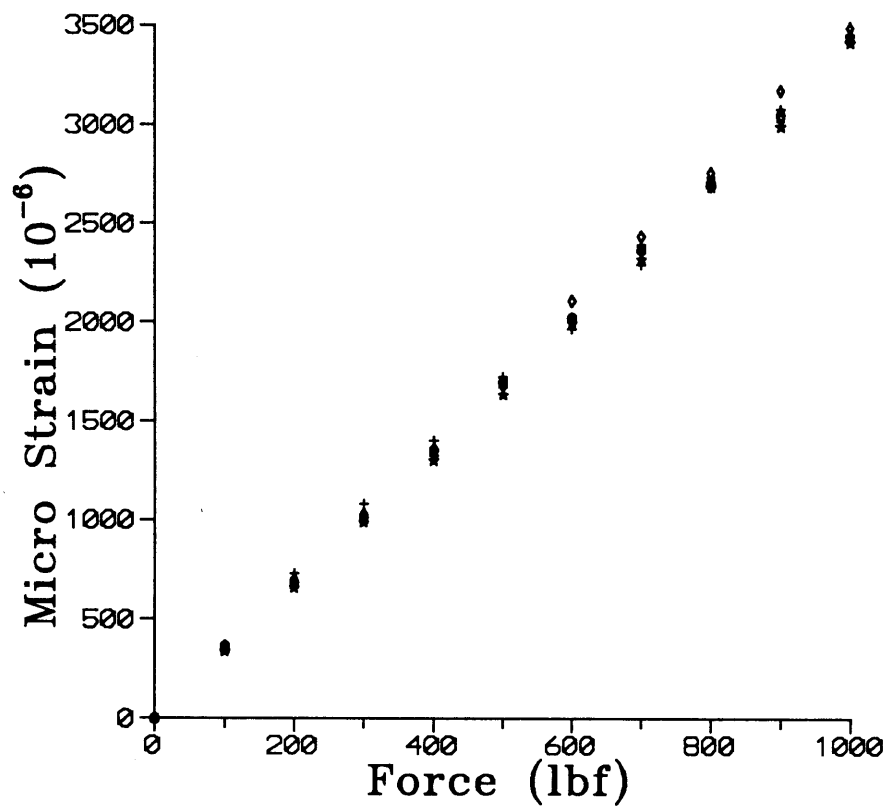
147

Prepreg tape: AS4/3501-6 Fiber volume fraction: 0.5
Length: 6 inches Width: 0.75 inch
Ply thickness: 0.007 inch. Ply number: 4

Fig. 5-3: Experiment data on measuring compliance term S_{11}

all for a fiber volume fraction of about 0.5. For the higher fiber volume fraction, this factor would be larger which means smaller stiffness reduction. In the extreme case when V_f reached V_a, which was the available fiber volume fraction or the maximum packing efficiency, this factor would be very close to one. Compared with S_{bb} term, which is the compliance of the fiber bundle in the transverse direction, the variation in S_{11} for different V_f values is rather small. To simplify calculation, a constant of 0.9 is probably a good approximation for $E(z)$ for fiber volume fraction at the range between 0.5 to 0.7, which is the range used in various advanced composite processing techniques.

5-2-2. Experiments on Measuring Transverse Compliance

This term determines the deflection of a fiber bundle in the transverse direction while compressive load is applied in that direction. As mentioned before, this was measured in the previous experiments in this group [35,67]. In order to complete the description of the fiber deformation experiments, a short summary is given here.

The experimental arrangement is shown in Fig. 5-4. Graphite fiber bundles were made from Hercules AS4/3501-6 prepreg tape by washing out the uncured resin. These fibers were then put into a mold which restricted motion of fibers in transverse directions. The transverse load was applied by an Instron test machine. Both the applied transverse load and the deflection of the fiber bundle were measured in the test. The experiments were discussed in detail and the results were reported in [35,67]. These original measurements of stress-deflection relation were reported in terms

LOAD CELL

**FIBERS
(LUBRICATED)**   **DISPLACEMENT
TRANSDUCER**

FIBERS

CLAMP

MOLD
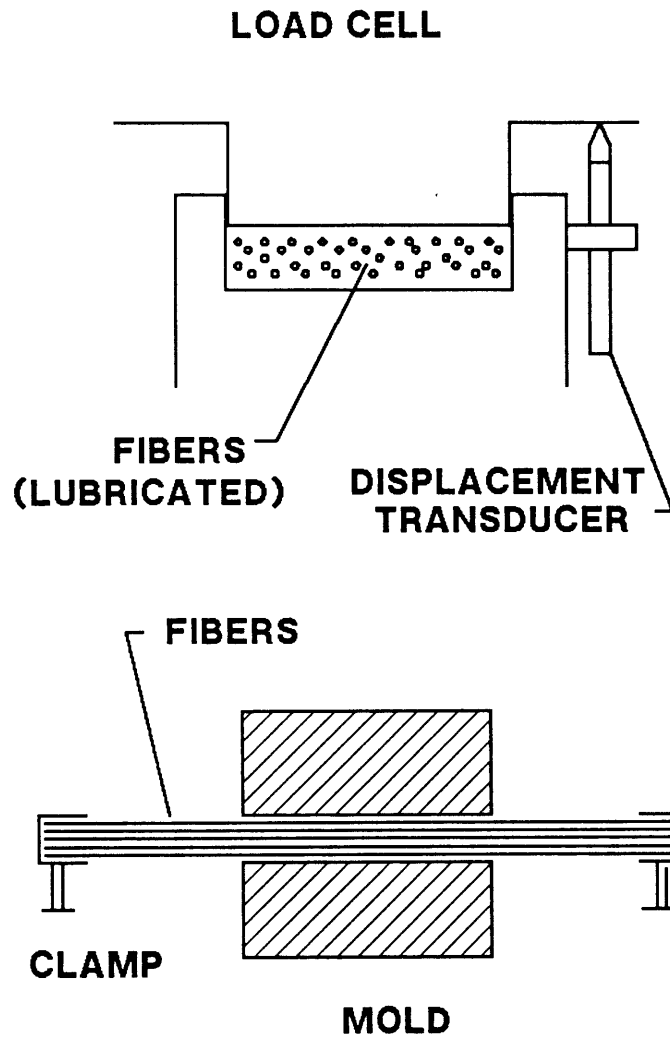
Fig. 5-4: Test set-up for measuring compliance term S_{bb}

of σ_f and V_f, where σ_f was defined as the average transverse fiber bundle compression stress. Then the least square curve fitting was used to determine the constants in expression (3-14). By using relation (3-15), we can recalculate for the S_{bb} term by using the experimental data presented in [67]. Selected experimental data and the analytical expression of S_{bb} versus V_f are shown in Fig. 5-5, where the constants in expression (3-16) are chosen as $V_a=0.85$, $V_o=0.5$, and $A_s=0.06$ (psi) according to the discussions in [35].

5-2-3. Experiments on Measuring the Coupling Term

The coupling term measures the response of the fiber bundle in the transverse direction when load is applied in the longitudinal direction, or the bundle response in the longitudinal direction when transverse load is applied. Physically this term is similar to the material Poisson ratio. Because of the difficulty in measurement, several test methods were devised and tried. One direct method was to measure the longitudinal deformation of the fiber bundle when transverse load was applied, as used in determining the Poisson ratio of other materials. Several test arrangements were tried but failed because of the difficulty in distinguishing the very small displacement of the fiber bundle extension from other noise signals. Then an indirect method was developed which measured the compressive force induced in the longitudinal direction as the transverse load was applied. Although there was scattering in the measurement data, this approach was proved successful.
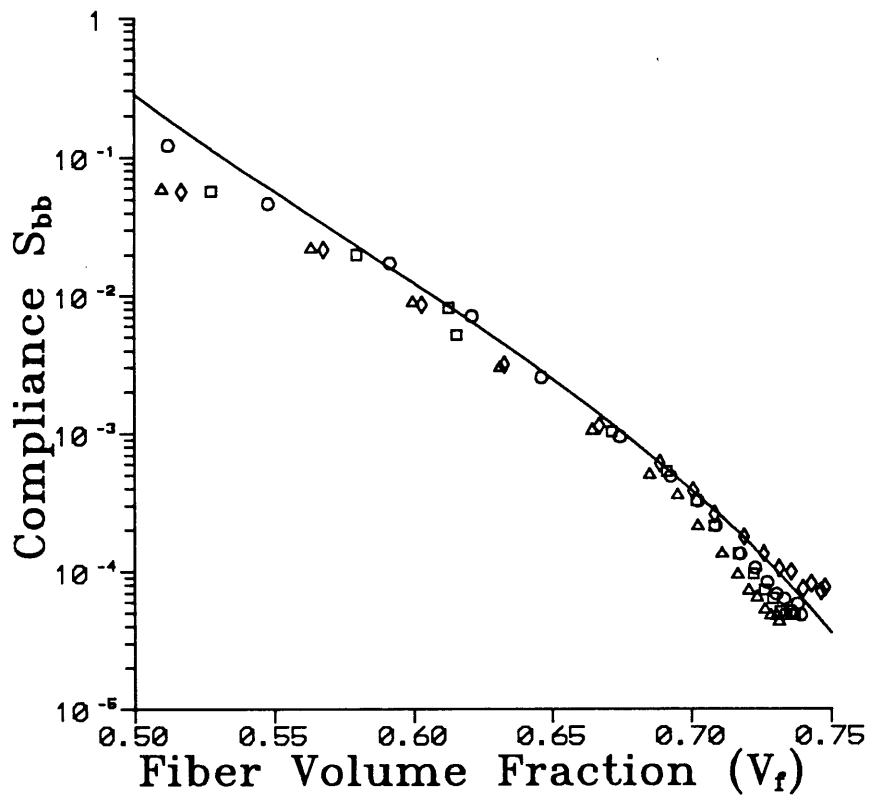
Fig. 5-5: Experiment data versus model prediction on S_{bb} measurement

Fig. 5-6 shows the test arrangement, in which the force induced in the longitudinal direction is monitored while a transverse compression load is applied. Ideally we would have the test arrangements shown in Fig. 5-7. However, it was almost impossible to obtain an aligned fiber bundle with thousands of fibers exactly even on both ends, despite great attention in the cutting process. If we had used the test arrangements shown in Fig. 5-7, we would have obtained the induced force signal only by part of the fibers contacting with the transducer surface. It was impossible to know how many fibers or what portion of the bundle would be in contact with the transducer surface. To avoid this uncertainty in fiber end condition, the test arrangement shown in Fig. 5-6 was used. The well aligned fiber bundle was obtained by using the same prepreg tape and by washing out the uncured resin as in the S_{bb} measurement. The bundle was then soaked with clean corn oil of viscosity of 0.057 *Pa*sec*. The fiber bundle length was about 5 inches, and the original bundle cross section area was about 0.02 in^2. The critical aspect of the experiment was obtaining uniform fiber ends to transfer the force signal to the flat surface of the transducer. In the experimental preparation, the force transducer was pushed very slowly against one end of the fiber bundle. Since the bundle was well lubricated, fibers were able to move longitudinally relative to each other. The other end of the bundle was clamped about 2 inches away from the mold to allow the fibers to move freely up and down with the mold in the transverse direction. The transverse load was applied through the Instron Test Machine load cell and the longitudinally induced force was measured by the force transducer, which was made up of the strain gage bridge as shown in Fig. 5-8.

LOAD CELL

FIBERS

DISPLACEMENT
TRANSDUCER

FIBERS
(LUBRICATED)

CLAMP

MOLD
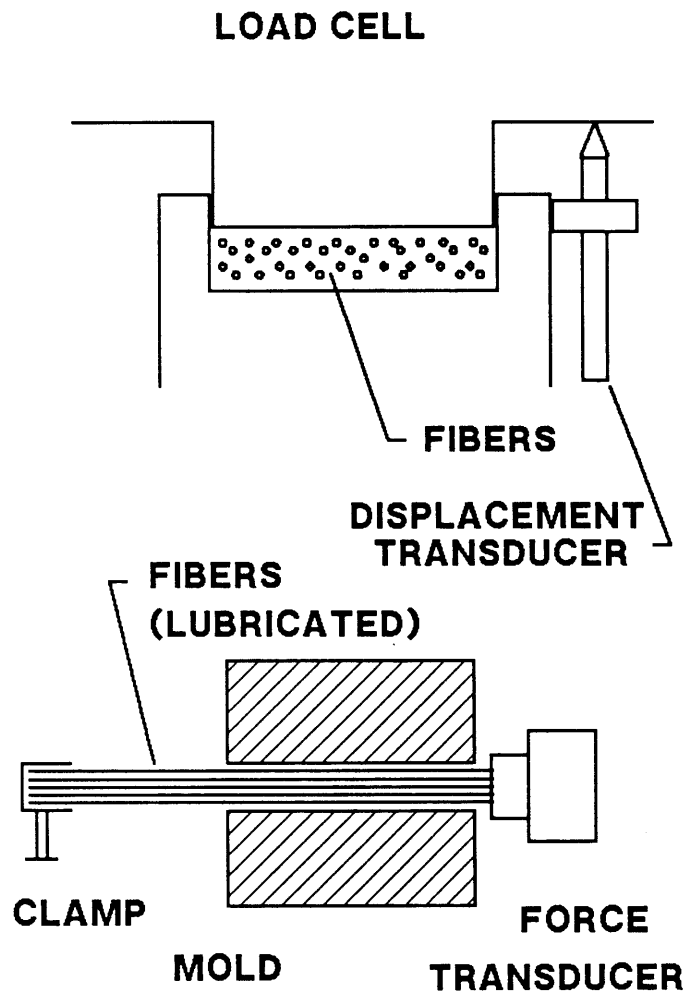
FORCE
TRANSDUCER

Fig. 5-6: Test arrangement for measuring the compliance term S_{1b}
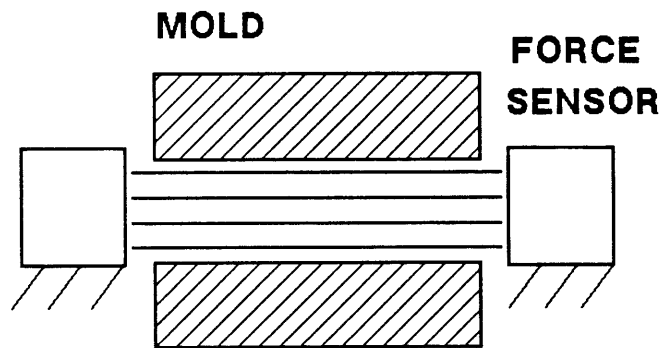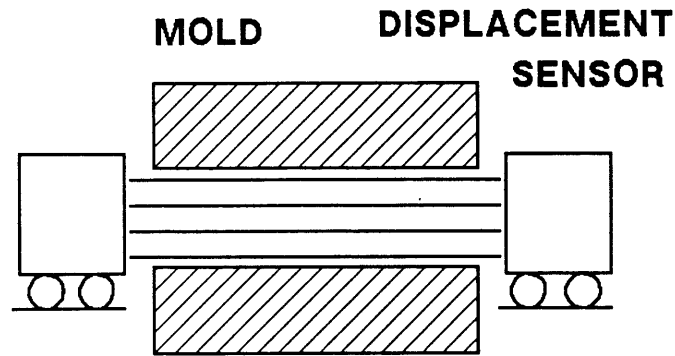
Fig. 5-7: "Ideal" test condition for measuring the compliance
term S_{1b}

TOP VIEW

MOLD
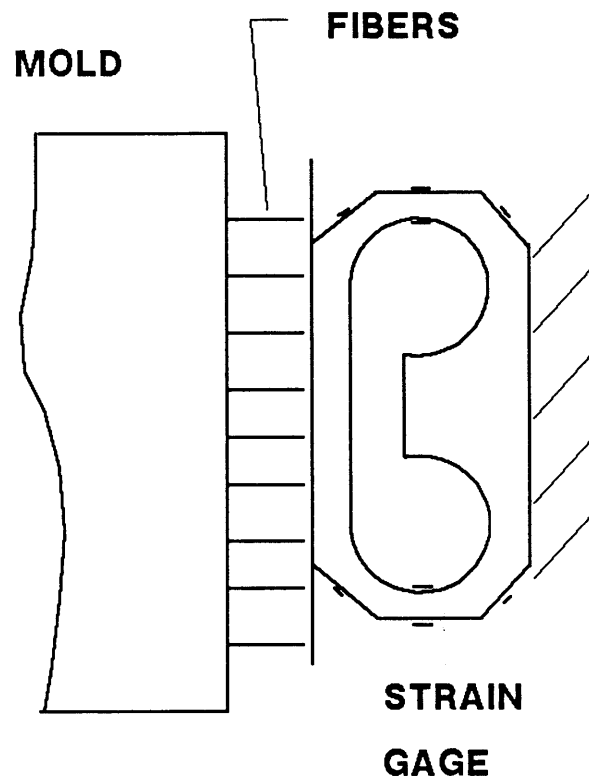
FIBERS

STRAIN

GAGE

Fig. 5-8: High sensitivity force transducer made by strain gage
bridge for the measurement of S_{1b}

The total force acting on this transducer is

$$F_t = A_x V_f (\sigma_f)_x \qquad\qquad (5\text{-}2)$$

where F_t is the total force and A_x is the cross sectional area of the fiber

bundle. From (3-29), we can relate $(\sigma_f)_x$ and $(\sigma_f)_z$ as

$$(\sigma_f)_x/(\sigma_f)_z = - S_{12}/S_{11} \qquad\qquad (5\text{-}3)$$

We already obtained an estimate of the S_{11} term in the previous section as

a function of V_f. In the experiment F_t was measured directly by the force

transducer, σ_z was obtained by monitoring the transverse load over the mold

area on the Instron machine, A_x and V_f were derived by measuring the dis-

placement of the mold part. F_t was expected to increase as the transverse

load became larger and V_f became higher. The measurement data of F_t are

shown in Fig. 5-9. From (5-2), (5-3), and (3-37), we have

$$C (V_f)^m/E_f = -[F_t/(A_x\sigma_z)] S_{11} \qquad\qquad (5\text{-}4)$$

This was used to estimate constants C and m. Other variables in

(5-4) were either measured data or material constants. Nonlinear least

square curve fitting was used to obtain values of C and m as

$$S_{1b} = -0.0156 (V_f)^{-5.94} / E_f \qquad\qquad (5\text{-}5)$$

where E_f is the fiber stiffness which is 34×10^6 *psi* for the fibers used

here. This relation is plotted with the test data in Fig. 5-10.

The test data show some variations from sample to sample. In the

force measurement experiments, errors could result from two sources. The

first was that some fibers in the bundle might still not touch the surface
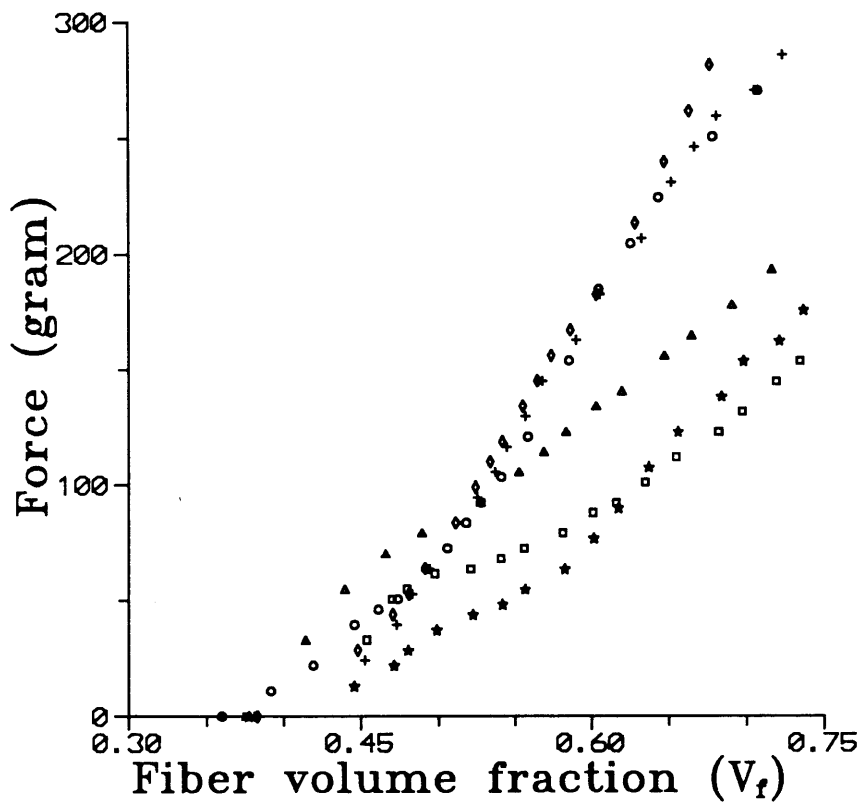
Fig. 5-9: Data of induced longitudinal force measured in the
test of S_{1b} term
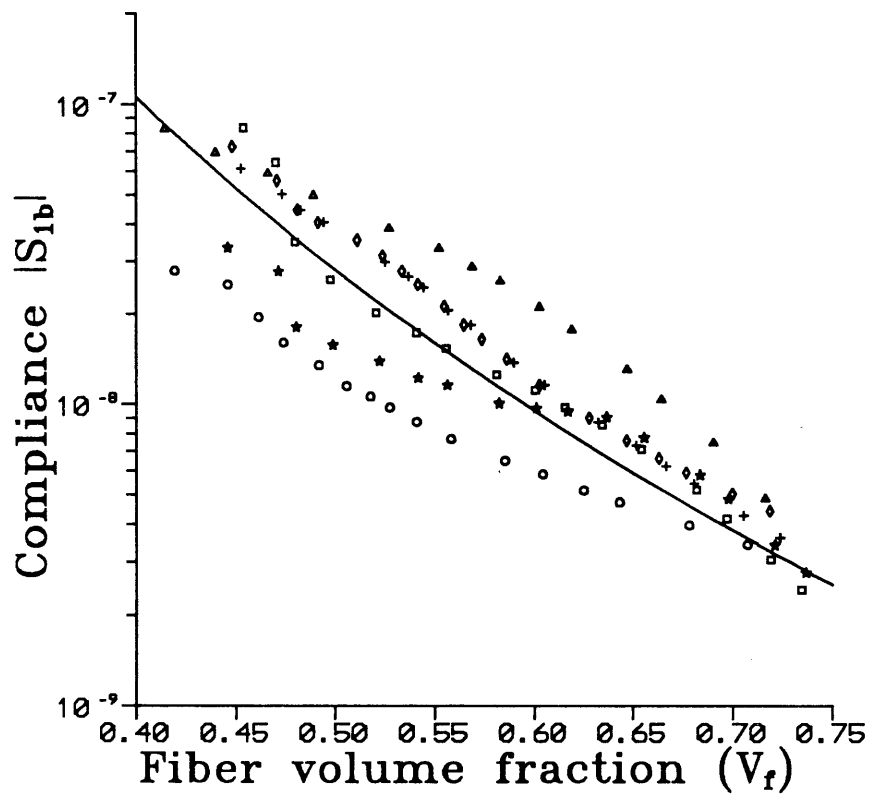
Fig. 5-10: Comparison of test data and the least square curve
fitting of the model for the S_{1b} term

159

of the force transducer. In this case the force measured would be smaller than the real value under the ideal condition. The second was that, by pushing the fiber ends against the transducer surface, more waviness might be introduced in some fibers. In this case the force measured would be higher than the real value. The condition of each fiber bundle was different so that in any individual test one or the other source of error could dominate. This probably caused the data scattering among different test runs.

5-3. Experiments on Micro-structure Development in Molding

These experiments were performed as a means of applying the fiber deformation model to a real process, and obtaining a better understanding of the process mechanisms. The process of molding a composite laminate on the hot press is similar to the process of filament winding in the sense of consolidation and resin flow. In both cases, the transverse flow is dominant. Both processes involve the application of heat and pressure. The study of the micro-structure development in laminate molding thus is helpful to the understanding of the consolidation process in the fabrication of closed shape products.

The mechanism of consolidation or fiber compaction in the molding process, which includes resin flow and fiber movement, has been discussed in several papers. Process models were constructed to describe the consolidation process [1,35,72,73]. Various simulation experiments were performed to investigate the process mechanisms. The direct continuous measurement of the laminate compaction, in which the total laminate thick-

ness was monitored as a function of process time, was reported in a recent paper [74]. However, the micro-structure development of the composite laminate during this consolidation process, such as fiber motion and the resin content gradients within the laminate, was still not fully understood, especially in molding with a bleeder where transverse resin flow was dominant. The objective of our experiments, therefore, is to provide an alternative way of monitoring micro-structure development of the composite laminate as a function of process time. This measurement provides a better understanding of the compaction mechanism and helps to determine the optimum cure profile.

The key items in the experiments were selecting a special cure profile to obtain an incomplete resin flow state, and embedding non-stick porous teflon coated sheets within the laminate so that changes in individual plies could be measured without disturbing the flow field. The ply thickness of the composite material used in this study was only about 0.18 mm (0.007 inch). It was impossible to monitor the micro-structure development by placing sensors within individual plies without disturbing the flow field because available sensors were too large. The study of the resin viscosity during the cure process showed that viscosity decreased to a minimum and then increased rapidly until the resin gel point. This resin behavior required selection of a pressure profile to obtain the certain resin flow time period. In our experiments, we utilized this resin viscosity behavior and designed a set of special pressure and temperature profiles so that we can simulate the cure process but "freeze" the resin flow states corresponding to different time windows. In other words, we intentionally

obtained incomplete compaction of the specimen then measured the micro-
structure development as a function of time.

AS4/3501-6 graphite/epoxy prepreg tapes supplied by Hercules were
used in these experiments. The initial resin content of the prepreg was
about 50% in volume percent, and the uncompacted thickness was about 0.18
mm (0.007 in). The viscosity of the this kind of resin was studied by
Springer in [2] and was model as a function of temperature and time. Fig.
5-11 shows the viscosity change with a certain temperature profile, which
is calculated according to the formula given in [2]. The viscosity
decreases as temperature rises and reaches a minimum. It then increases
rapidly as the cure reaction progresses. Pressure is usually applied be-
fore this minimum in resin viscosity in order to obtain full compaction.
In our experiments, however, we applied the pressure after this viscosity
minimum was passed. The rapidly increased resin viscosity therefore
stopped resin flow at a specific time. In this way we obtained a "frozen"
flow field with an incomplete compaction state, which was equivalent to an
opening of time window in a normal cure cycle.

In order to measure the micro-structure development in the
laminate, we had to determine the resin flow state of each individual ply
quantitatively. We embedded sheets of very thin, porous, teflon coated
glass fabric between plies. This made it possible to measure the fiber
volume fraction and resin content for each individual ply because it was
possible to separate and measure the individual layers after the cure pro-
cess. The teflon coated glass fabric sheet (TCGF 400-2A) was supplied by
American Durafilm Inc. The nominal thickness of the sheet was only about

162
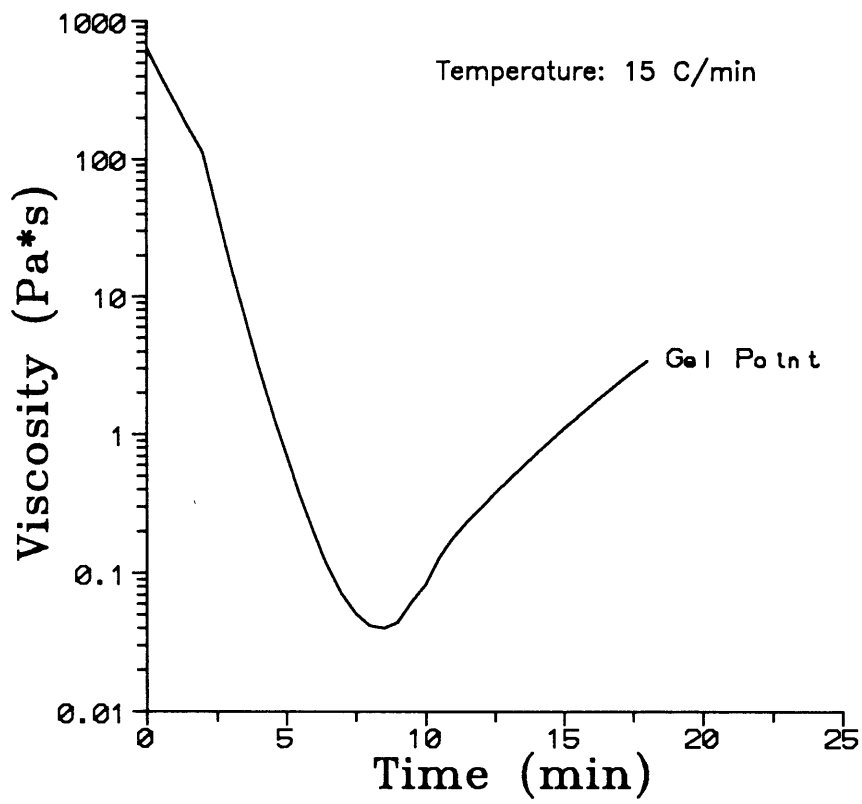
Fig. 5-11: Viscosity change of the 3501-6 resin system
calculated from [2]

0.025 mm (0.001 in). The porosity was over 60% and the sheet was in plain

woven structure, so that its permeability was well beyond that of the fiber

network. This assured that the flow field was undisturbed. This was

verified by comparing of resin amounts for specimens with and without em-

bedded teflon sheets.

A schematic of the experimental setup is shown in Fig. 5-12. The

laminate consisted of 4 plies, 114 mm (4.5 in) by 102 mm (4 in), with

unidirectional lay up. These dimensions were determined according to the

available molding equipment and the consideration of obtaining the dominant

transverse flow, which limited the total number of layers or the layer

thickness otherwise the edge flow could not be neglected. The porous

teflon coated sheets were cut to the same size and embedded during the lay-

up operation. The thickness of the teflon coated sheets was on the order

of the prepreg surface roughness so that careful lay-up operation can avoid

trapping air. The laminate was surrounded by cork dams, bonded to the bot-

tom steel plate, to prevent the resin flow within the prepreg ply plane.

Bleeder paper was put on top of the laminate to permit the resin flow in

the upward direction. The top and bottom tool plates were used to conduct

heat and to transfer load to the laminate. The whole assembly was placed

on a laboratory hot press made by Carver Inc. The press was controlled by

an IBM PC/XT computer and an ANDS 4400 data acquisition system made by

Analogic Inc. Thermocouples were embedded in the tool plates to monitor

the temperature. Pressure transducers were connected to the press

hydraulic line to measure the load. The computer sent out control signals

via the data acquisition system, activating the heaters and the pressure

pump, thus obtaining the programmed temperature and pressure profile. The
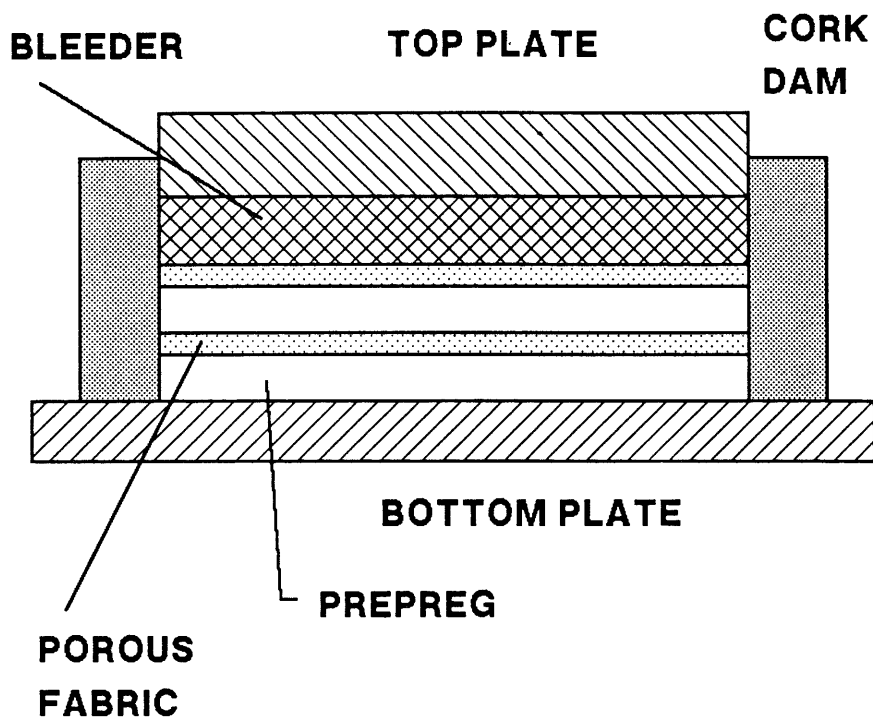
Fig. 5-12: Micro-structure development experiment set up

laminate structure was studied before and after the process. Since it is difficult to measure the prepreg thickness directly because of the surface contour of the tape, each prepreg ply as well as each teflon-coated sheet, and the bleeder paper were all weighed before the cure cycle. The unique non-stick property of teflon coated sheets made it possible to separate each individual composite ply after the cure cycle. Then each of them was weighed again to determine resin content and fiber volume fraction for each ply. The formula used in the calculation is

$$V_f = \frac{M_o V_i \rho_r}{M_o V_i (\rho_r - \rho_f) + M[(1-V_i)\rho_r + V_i \rho_f]} \qquad (5-6)$$

where V_f is the fiber volume fraction, V_i is the initial fiber volume fraction, ρ_f is the fiber density, ρ_r is the resin density, M_o is the original ply weight, and M is the final ply weight. The measurement of weight changes in all specimens showed that the bleeder absorbed over 90% percent of the resin flowing out of the composite. Therefore the flow process could be considered as one dimensional, in the upward direction only.

The pressure and temperature profile was determined according to the resin viscosity function. The heating rate of the hot press, which was set at the maximum heating rate, was about 15 °C/min (27 °F/min). After the cure temperature was reached, which was 177 °C (350 °F), the temperature was held for about 20 minutes. The minimum resin viscosity was reached about 12 to 13 minutes after the heater was turned on. The resin viscosity then increased rapidly and a few minutes later the resin was solidified. The pressure profile was very close to a step function of 1.4×10^5 *Pa* (20 psi) and was applied right after the low viscosity period.

The ideal pressure-temperature profile would have no pressure applied until the load was activated. In that way the initial fiber volume fraction, which was about 0.5, would be maintained until the load was applied. However, in the experiments it was necessary to apply a small pressure to close the mold for the heat transfer process. This initial pressure was about 1.4×10^4 Pa (2 psi), and varied somewhat due to the friction in the press mechanisms. Since this pressure was applied from the beginning, it was enough to compact the fiber to a fiber volume fraction of about 0.55. There was no way to maintain the laminate at the initial fiber volume fraction when the 1.4×10^5 Pa (20 psi) pressure was applied. This pressure profile was used in the computer simulation to account for the first part of the flow process due to this small pressure. This applied temperature and pressure profile is plotted in Fig. 5-13.

The computer simulation was performed and the results were compared with experimental measurements. The computer program was developed based on the fiber deformation/resin flow model developed in this group, which was discussed in detail in [35]. In the model the fiber network was treated as a nonlinear elastic porous medium and the resin flow was assumed to obey Darcy's law. To establish the physical model and mathematical equations, the coordinates of the laminate are chosen as shown in Fig. 5-14. For our bleeder molding case, we only considered the transverse resin flow and fiber movement. The continuity equation for this fiber and resin mixture is

$$\frac{V_i^2}{V_f^2} \frac{\partial V_f}{\partial t} = -\frac{\partial}{\partial z} \left(\frac{V_f S_{zz}}{\mu} \frac{\partial p_r}{\partial z} \right) \tag{5-7}$$

167
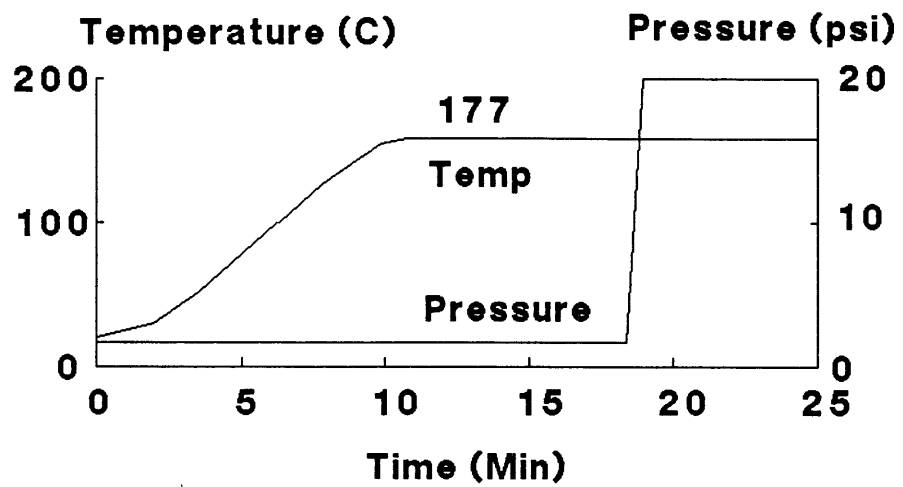
Fig. 5-13: Temperature and pressure cycle used in molding test
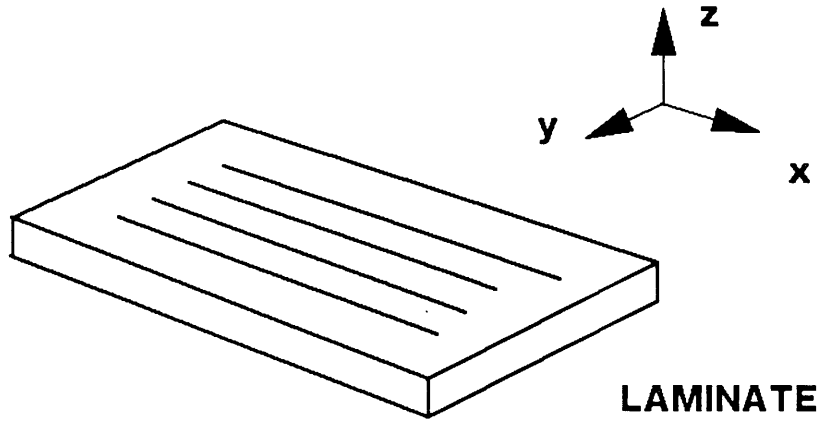
Fig. 5-14: Illustration of a laminate and coordinates

where V_f is the fiber volume fraction, V_i is the initial fiber volume fraction and equal to 0.5 from the prepreg tape data, p_r is the resin pressure, μ is the resin viscosity, and S_{zz} is the permeability of the fiber network. This is a second order nonlinear diffusion equation with unknowns V_f and p_r. The boundary conditions for this equation are that, if we neglect the flow resistance of bleeder material, on top of the laminate the resin pressure is equal to the atmospheric pressure, and at the bottom interface there is no resin flow.

The force balance condition is that the applied load is shared by the resin and the fiber

$$p_a = p_r + \sigma_f \tag{5-8}$$

where p_a is the applied load and σ_f is the average fiber stress. These boundary conditions for equation (5-7) entered the calculation through this equation.

Two constitutive relations were necessary to solve these equations. One was the fiber bundle permeability, and the other was the transverse fiber bundle stiffness. The transverse permeability of the fiber bed was the same as in the filament winding case, which was given in (2-18) and was derived from the original Carman-Kozeny equation by taking into account the geometry of the transverse flow paths of the fiber network. The transverse stiffness of the bundle was given in (3-14), which showed σ_f was a nonlinear function of V_f and the thus fiber stress increased rapidly when V_f became high.

The numerical simulation program was written in FORTRAN on a Micro VAX system. The experimental data of the pressure and temperature profile were used as the input of the computer simulation program. The temperature distribution monitored by thermocouples inserted into molds was used in the viscosity calculation, in which we used the viscosity model developed in [2] which was summarized in section 2-4, but neglect the spatial variation of the temperature. The fiber volume fraction and resin content were calculated as program output and compared with the experimental results. The comparison of the data and the model prediction is shown in Fig. 5-15, in which the curve is the computer simulation output, and different data marks represent different runs. Test data are listed in Appendix D. The test data show good agreement with the computer output. The total amount of the resin flowing out from the laminate is consistent with the calculation based on the permeability relations (2-18). This also verifies the value of Kozeny constant k_z obtained from the previous experiments [35].

5-4. Wet Filament Winding Simulation Experiments

The first part of the winding and consolidation experiments was a simulation of wet filament winding. This was to study fiber bundle deformation and stress behavior in a cylindrical closed shape structure. In this "wet" process, the applied material was a mixture of the fiber bundle and fluid resin matrix. When the winding tension was applied to the material, the consolidation pressure was established and there existed a pressure gradient over layers. This pressure gradient caused fluid resin to be squeezed out from the layers. This was a dynamic flow and consolidation process, as shown in Fig. 5-16.

171
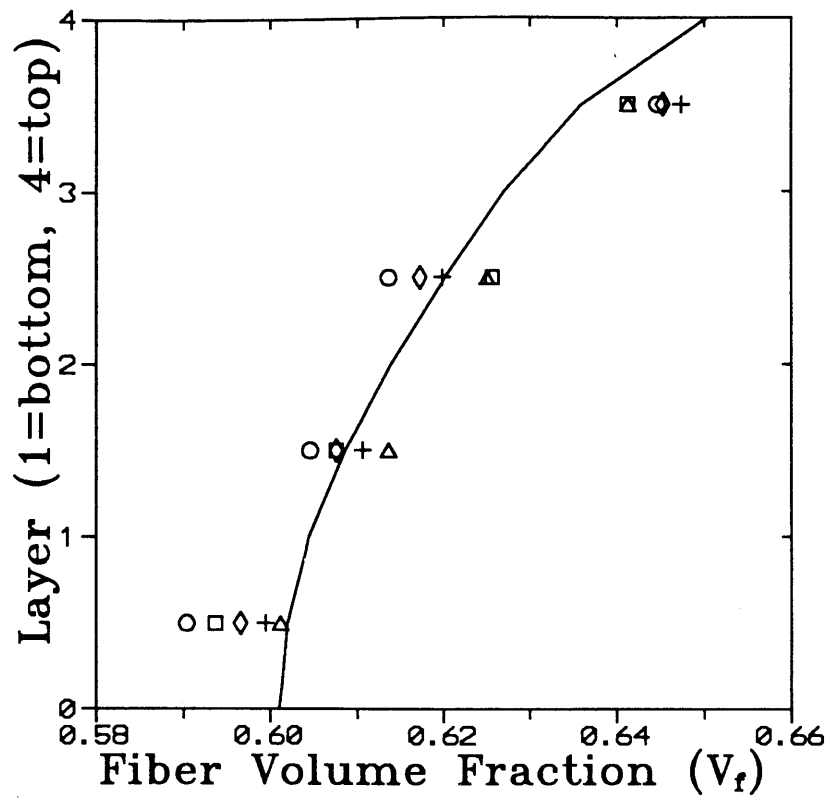
Fig. 5-15: V_f distribution over layers in the molding process

WINDING TENSION

MANDREL

RESIN FLOW

FIBER STRESS
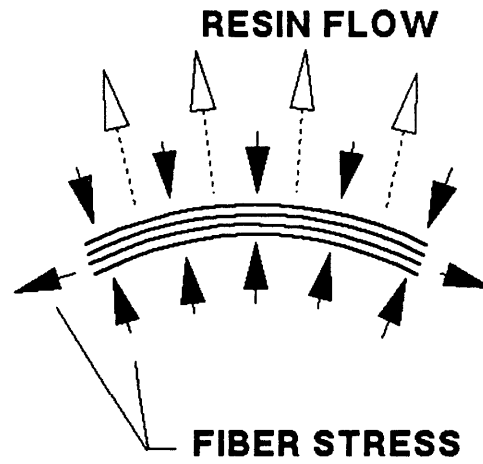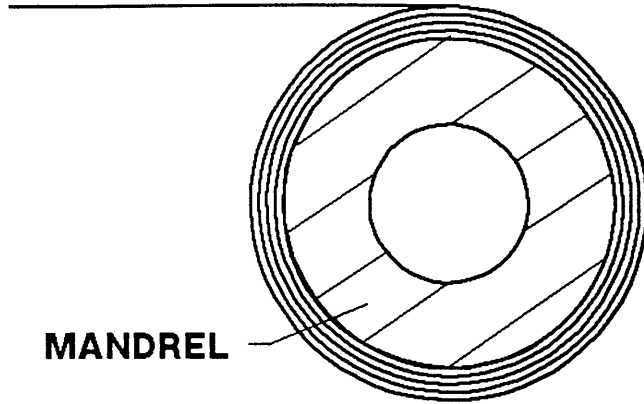
Fig. 5-16: Flow and consolidation in wet filament winding

In our simulation test, we simplified the problem by using constant viscosity silicone fluids to replace the real epoxy resin, thus eliminating temperature-time effects. Silicone fluids were obtained from Dow Corning, and the viscosities were 10,000 and 100,000 centistokes (cst) respectively for different cases. AS4 3k fiber tows from Hercules and RK 30-40k fiber tows from RK Fiber were used in different runs. The properties of these fibers, as given by the suppliers, are listed in Table 5-1.

Table 5-1. AS4 3k and RK 30-40k Fiber Properties

	AS4 3k	RK 30-40k
Tensile strength	4071 MPa	Min. 3000 MPa
Tensile modulus	248 GPa	220-240 Gpa
Ultimate elongation	1.65%	1.25-1.60%
Density	1.80 g/cm^3	1.78 g/cm^3
Carbon content	94.0%	95%
Filament diameter	7 μm	6.8 μm
Tow cross-section area	0.12 mm^2	1.47 mm^2

The impregnation and tension control device are shown in Fig. 5-17. The fiber tow was fed through cylindrical shape rollers and changed directions when passed these rollers, which forced the fiber tow to spread and contract to effectively pick up the fluid. This enhanced the wetting process of the fiber bundle. After the fiber tow ran through the fluid bath, a pair of rubber rollers were placed to help the mixing process. The tow then passed a tension monitoring device, which was built by using an extended octagonal ring force sensor and was capable of separating the parallel and transverse force components. This force sensor continuously recorded the tension of the fiber tow. A brief discussion of this kind of force sensor is given in Appendix E. The winding device was built by using a lathe as the winder to obtain both axial rotation and axial feeding.
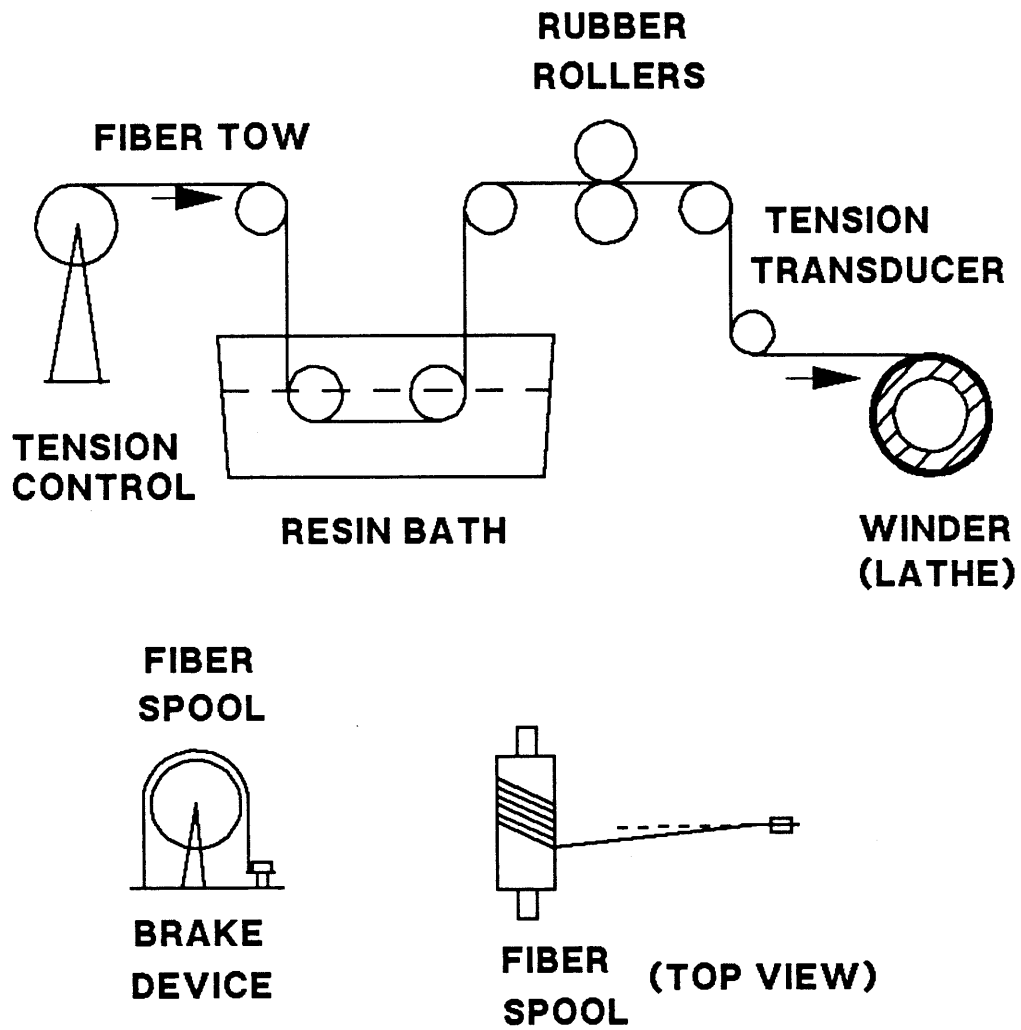
Fig. 5-17: Wet filament winding simulation test set up

However, the feed of the lathe was slow so that the winding angles in all experiments were close to 0 degree, or in the hoop direction.

The mandrel was made of aluminum. The size was about 3 inches long, 2 inches of external radius and 1.5 inches of internal radius. There were removable flanges on both sides to restrict the fiber sliding motion. Several measuring devices were mounted on to the mandrel to obtain the radial pressure and force during operation. Fluid pressure at the interface of the mandrel and composite was measured by using a small size pressure transducer, which was supplied by Entran Device with dimensions of 0.14 inch in diameter and 0.44 inch in length. This transducer was embedded into the mandrel with a recess from the mandrel surface, which eliminated the fiber contact with the transducer surface. Initially strain gages were bonded to the inner surface of the mandrel to measure the total radial pressure resulting from the winding tension force. However, it was found that the effects of bending and torsion during the winding were much larger than that of the radial pressure. Later small size flat shape force sensor resistors made by Interlink Electronics were bonded on to the mandrel external surface to measure the total radial stress, which was transverse to the sensor surface. The size of the force sensor resistor was about 0.25 inch by 0.25 inch with a thickness of only 0.01 inch, which made possible to avoid any geometric distortion to the force signals. The principle of using this kind of force sensor resistor was the change of the resistance when a transverse load was applied. A brief discussion of this kind of force sensor resistor was given in Appendix F. Since the mandrel was in rotation in the winding, a slip ring device made by Litton Poly-Scientific was used to transfer the signals from the rotating part to the

stationary part. These signals were then fed to a data acquisition system

for real time data processing. MetraByte data acquisition boards DAS-16

and DAS-20, which were mounted on a Hyundai 286C AT computer, were used for

the processing. This measurement and data processing set up is shown in

Fig. 5-18.

The tension applied to the fiber tow was controlled by a brake-like

friction device, as shown in Fig. 5-17. However, in the winding a minimum

tension was needed to pull the fiber tow through the wetting device. This

minimum tension came from two main sources: the friction between fibers and

rollers, and within the rollers and bearings themselves; and the induced .

shear force when fibers were pulled through a high viscosity fluid bath.

The available range of the tension on the tow was between this minimum

value and the maximum force the fiber tow can stand. For a 3k size AS4

fiber tow, the minimum force was about 3 lbf/tow, and the maximum force was

about 10 lbf/tow at which some of the fibers were already broken in some

runs. For a 40k size RK fiber tow, the minimum force was about 15 lbf/tow.

Since the tension control device was placed at the spool side which was the

beginning of the fiber tow path, total tension control was not very effec-

tive. On the fiber tow path there were many uncontrolled factors, such as

bearing friction variation, roller surface condition, and fluid flow mo-

tion. The way fibers were fed to the wetting device also contributed to

tension variation. The spool length was about 10 inches, and the spool

axis was perpendicular to the fiber path center line. When fibers were un-

wound from the spool, they moved from one side to the other, back and

forth, as shown in Fig. 5-17. The angle between the fiber path and the

center line thus changed all the time. In order to reduce this systematic

MANDREL

TENSION
SENSOR

SLIP RING

AMPLIFIER

DATA
ACQUISITION
SYSTEM
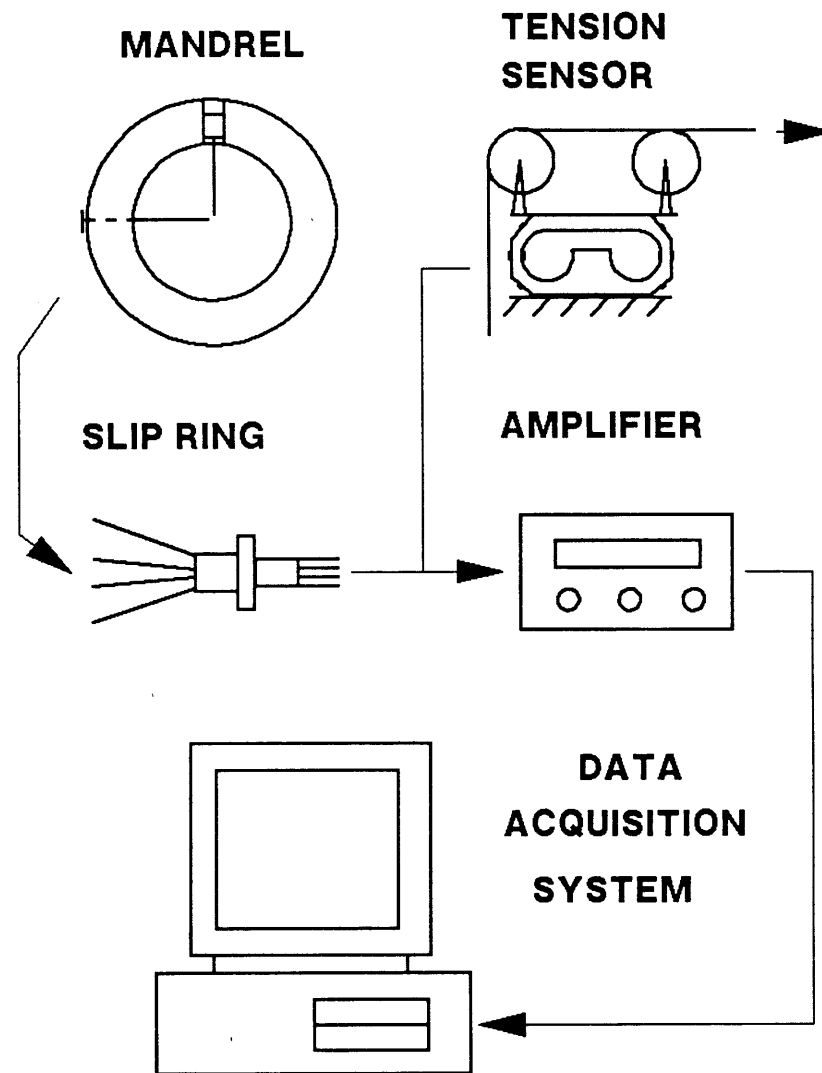
Fig. 5-18: Test measurement and data processing set up in
wet filament winding simulation experiments

178

angle variation, the fiber spool was put as far away from the fluid bath, which was about 4 feet as allowed by the room space. It was also found that longer distance between the spool and the fluid bath would cause undesired dynamic response of the tow motion such as periodic lateral vibration of the fiber tow, which would increase the tension variation. For the arrangement we used now we calculated the tension variation only due to this geometry factor, the results showed that the contribution was less than one percent.

The tension of the fiber tow was monitored continuously via a special force sensor built with 8 strain gages, as shown in Fig. 5-19. This sensor was capable of separating the horizontal and vertical force components. A brief discussion of this kind of force sensor is given in Appendix E. Fiber tows were guided through the sensor from the vertical direction and then forced to the horizontal direction. In this way the tension signal was generated by a strain bridge circuit and was transferred to the amplifier and the data acquisition system simultaneously. The measurement showed that on the average there was about 15 percent variation in the tension. In a few cases about 20 percent variation was detected. A typical tension history with winding of RK 40k size fiber tow is shown in Fig. 5-20.

In order to check the effect of the wetting process, fiber volume fraction measurement was taken for the wetted fiber tows. The silicone fluid was very sticky so that by handling the fluid mixture carefully we can avoid the spontaneous flow. The fiber tow was cut right before it reached the winder. Therefore this was the initial fiber volume fraction

STRAIN
GAGE

FIBER TOW   TENSION

PULLEY
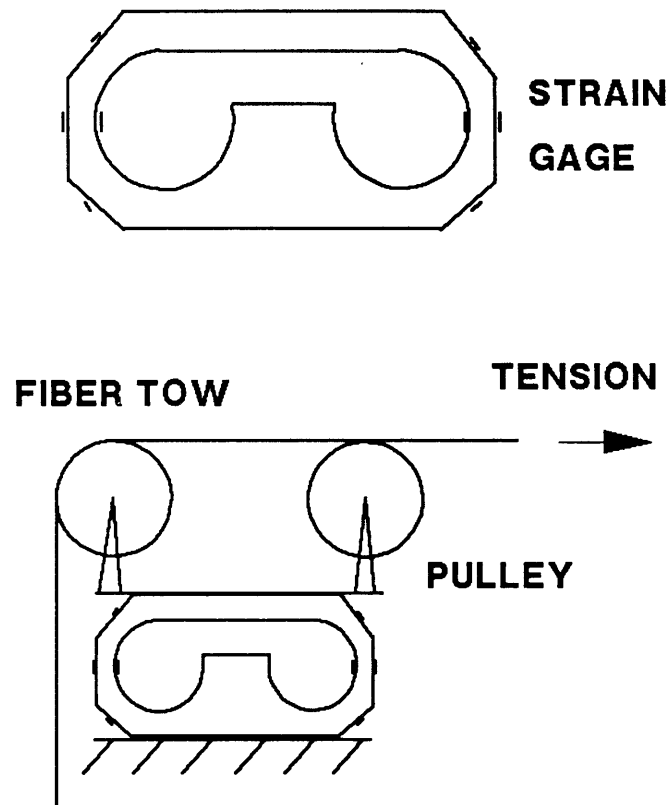
Fig. 5-19: Force sensor used to monitor winding tension force
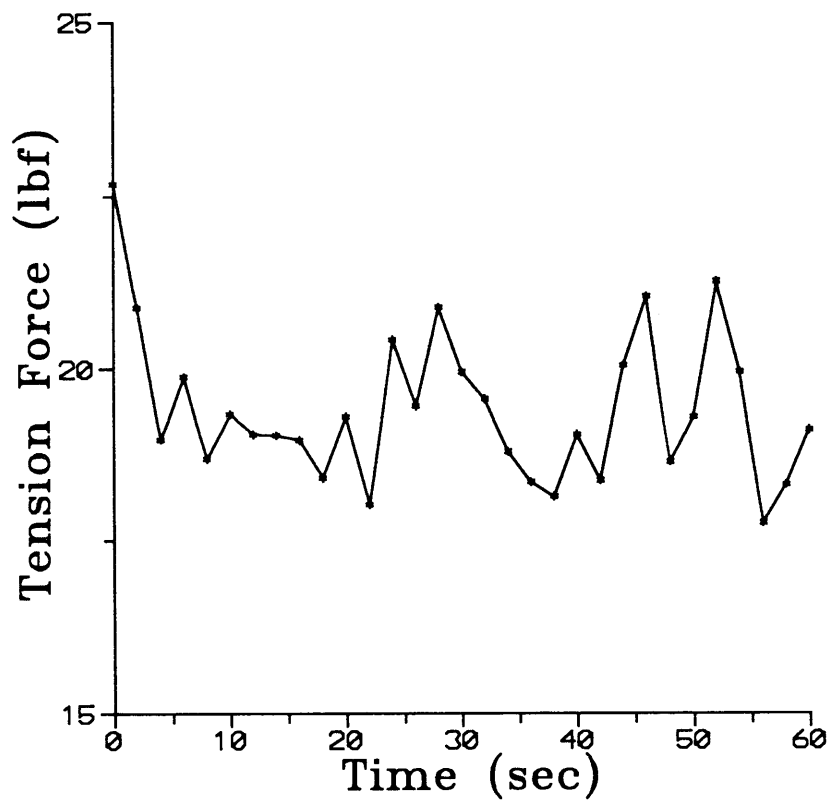
Fig. 5-20: Tension fluctuation during winding

of the tow in the winding process. After the sample was cut, the fiber and
fluid mixture was weighed first. The mixture was then immersed into
methylene chloride solution to dissolve the fluid, which took about 6 to 8
hours. Then the sample was put into an acetone solution bath for 2 to 3
hours. After the fiber tows were taken out from the solvent, they were
checked for cleanliness, then dried for over an hour. The dried fibers
were weighed again. The fiber volume fraction was then calculated as fol-
lows

$$V_f = \frac{1}{\dfrac{w_t - w_f}{w_f} \dfrac{\rho_f}{\rho_r} + 1} \qquad (5\text{-}9)$$

where w_t is the total weight of the fiber and fluid mixture, w_f is the
fiber weight, ρ_f is the density of fiber, and ρ_r is the fluid density. For
materials used in our experiments, ρ_f was 1.79 kg/m^3, and ρ_r was 0.971
kg/m^3. Therefore (5-9) can be simplified to

$$V_f = \frac{1}{1 + 1.84[(w_t/w_f) - 1]} \qquad (5\text{-}10)$$

This kind of weighing method is also recommended for measurement of fiber
volume fraction in composites [75].

Measurements showed that the wetting process was very effective,
but there were variations in the fiber volume fraction over the tow length.
This was due to the very little control after the fiber tow went through
the fluid bath. If more pairs of squeezing rollers had been used, varia-

tion probably would have been reduced. Experimental data were summarized in Appendix G.

As mentioned in Chapter 2, the wet filament winding process can be thought of as a fiber behavior dominated process as long as the flow time constant is much shorter compared to the winding process time. When AS4 3k high strength fiber tows were used with silicone fluid of 10,000 cst viscosity in the winding, the process was indeed dominated by fiber deformation. This will also be discussed in the following section. The process thus became fiber bundle deformation under the consolidation pressure established by the applied winding tension. The nonlinear elastic analysis presented in section 2-2-5 can be applied to this case. As more and more layers were wound onto the mandrel, the inner layers were increasingly squeezed in the transverse direction. This resulted in relaxation of the tensile stress in fiber tows in the hoop direction, and changed fiber compaction state throughout the layers. By using calculations given in section 2-2-5 we were able to calculate the final equilibrium state of the wound layers.

The use of the high viscosity silicone fluid also made it possible to measure fiber volume fraction for each individual layers. In the experiments it was found that the silicone fluid stuck to fibers in the winding operation. When we tried to unwound layer by layer, the fiber and fluid mixture was in good condition, and there was no spontaneous fluid flow. In order to obtain a clear picture of fiber volume fraction distribution throughout layers, fiber tows were unwound carefully and samples were cut from each individual layer. The fiber and fluid mixture was then weighed,

cleaned, and weighed again, as described in the measurement of initial

fiber volume fraction of the tow. The comparison of the weight difference

then determined the fiber volume fraction for each individual layer as

shown in (5-10).

The experimental measurements of the fiber volume fraction distri-

bution were then compared with the computer model predictions. It was

found that in this case the winding tension was the dominant factor. As we

can visualize, higher tension would result in a higher fiber volume frac-

tion. However, the increase in fiber volume fraction was balanced by the

increased transverse stiffness of the fiber bundle, which resisted further

compaction of the fiber bundle. At the constant winding tension, the inner

layers were squeezed the most, so that there was a V_f distribution through-

out the composite layers. A typical comparison between the model predic-

tion and measured data is shown in Fig. 5-21, which is the case of winding

the AS4 3k fiber tow with a constant tension. Although there are varia-

tions in the measurements for different layers, there is good agreement be-

tween the model and data. There is a deviation of the V_f value for the

outmost layer. It was found that a thin fluid layer accumulated on the top

surface of the structure, so that the measured fluid content was higher for

this layer even though the fluid squeezed out from the layer was removed

during the winding. More experimental data and plots are in Appendix G.

Variation in the measurement came from several possible sources and

showed some random effects. One source was the variation of initial V_f in

the fiber tow, which is given in Appendix G. Another was tension fluctua-

tion during the winding operation, as shown in Fig. 5-20. In unwinding
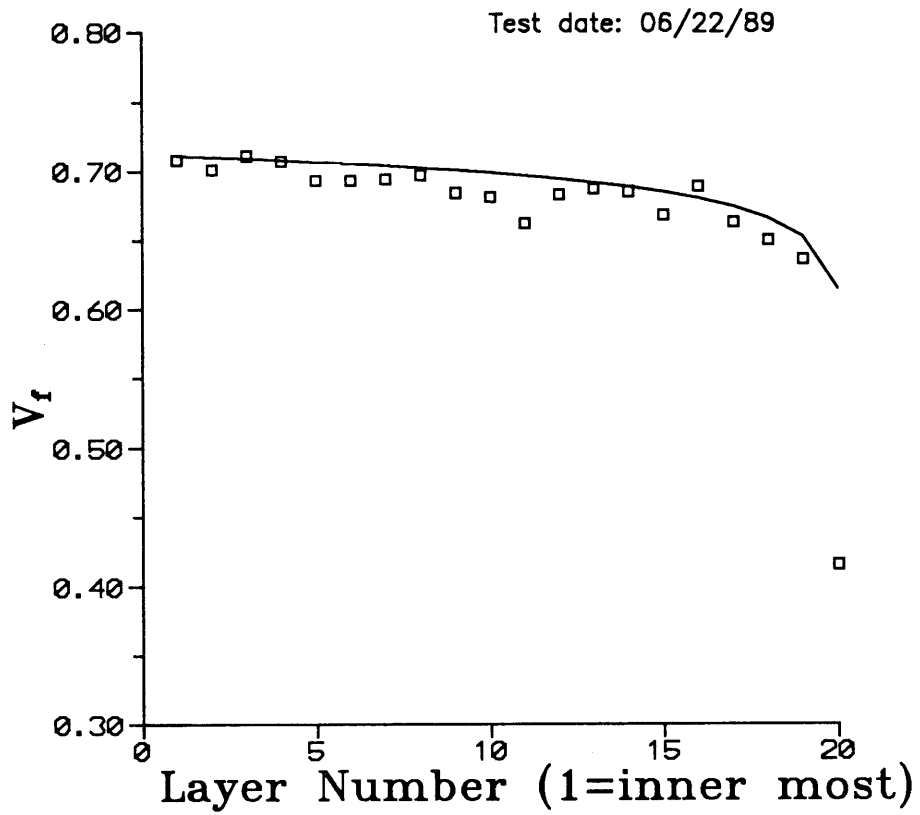
Fig. 5-21: V_f distribution over layers after winding

there was also some disturbance of the fiber tow, such as entanglement or fiber breakage. For the fluid between two adjacent layers, it was a random effect to which layer the fluid would stick to. All these factors contributed to the measurement variations.

This wet filament winding simulation by using fiber tows with silicone fluid was successful. Experimental data verified the process model analysis and showed the strong relation between winding tension and fiber volume fraction distribution.

5-5. Winding Process Time Constant Evaluation

As we found in the wet filament winding simulation experiments, flow was substantial in the winding. We then used the nonlinear elastic analysis to model the fiber bundle deformation and obtained good agreement between model predictions and experimental data. This showed that the flow time constant must be very small compared with the winding operation time. As discussed in Chapter 2, the comparison of flow time constant with operation cycle time determines whether the process can be simplified as fiber bundle behavior dominated. Here we will use our winding and consolidation data to evaluate the process.

As we mentioned in section 2-2-3, there are two process time constants. One is the flow or consolidation time constant and the other is the winding or process time constant. The flow time constant is a function of fluid viscosity, layer thickness, and fiber radius, as shown in (2-23). This time constant is also related to the consolidation pressure, which is

determined by the winding tension force. In our winding simulation tests, we varied fiber tow size, fluid viscosity, and winding tension, to change the flow time constant.

The fiber tows used in the experiments were AS4 3k tow from Hercules, and RK 30-40k tow from RK Fibers. Both were graphite fibers. The fluids used in the experiments were Dow Corning silicone fluid with viscosities of 10,000 and 100,000 centistokes (cst) respectively. Winding tension and speed were also varied in different test runs. Two sets of experimental data are listed in Table 5-2.

Table 5-2. Experimental Data of Time Constant Evaluation

	Case 1	Case 2
Fiber tow	AS4 3k	RK 30-40k
Layer thickness (h_o)	0.006 in	0.01 in
Viscosity (μ)	10 $Pa*s$	100 $Pa*s$
Number of tows	65 tow/layer	8 tow/layer
Winding time (t_w)	90 sec	10 sec
Fiber radius (r_f)	3.5 μm	3.4 μm
Kozeny constant (k_z)	0.2	0.2
Fiber spring constant (A_s)	0.06 psi	0.06 psi
Flow time constant (t_f)	36.7 sec	1079 sec
Dimensionless time $t^*=t_w/t_f$	2.45	0.0093

Two types of measurements were made. One was the total layer thickness, which reflected the compaction of the wound layers. The other was fluid pressure, which gave out information on the fluid flow. The wet winding process was very messy since the flow usually was substantial. When the number of wound layers increased, massive amount of fluid accumulated on top of the structure. It was hard to determine whether the flow process was complete merely from visual observation. The two measurements were used as indices of the flow process.

For the thickness measurement, a linear differential variable transducer (LVDT) made by Schaevitz was mounted on the winder. The moving spindle of the LVDT was kept in touch with the outer wound layer surface continuously. This is shown in Fig. 5-22. Since the center line of the lathe chuck and the center line of the mandrel were not exactly colinear due to the assembly tolerances, the maximum and minimum values of each revolution were used to determine the increase of the total thickness of layers. These values were taken manually from the continuous reading of the transducer. When winding was finished, the spindle of the LVDT would be at a random location on the mandrel. This position was used as the reference for the consolidation measurement. The settlement of the wound layers was calculated relative to this point. The previous data on layer thickness increase in the winding was then superimposed to the settling data. The tip of the LVDT spindle was always in contact with fibers during these measurements, so that fluid accumulated on top of the structure did not interfere with the thickness readings. The measurement of the thickness continued after the winding was finished, and until the thickness readings showed that settling of the layers was complete. For the fluid pressure measurement, a pressure transducer was embedded into the mandrel, as explained in the previous section.

This thickness measurement was successfully conducted in the winding of 3k size fiber tow experiments, in which automatic axial feeding was used and the thickness data were recorded manually. For winding of the 40k size fiber tow, axial feeding was done manually. Only the fluid pressure,

PRESSURE TRANSDUCER

LVDT

MANDREL

FORCE SENSOR RESISTOR
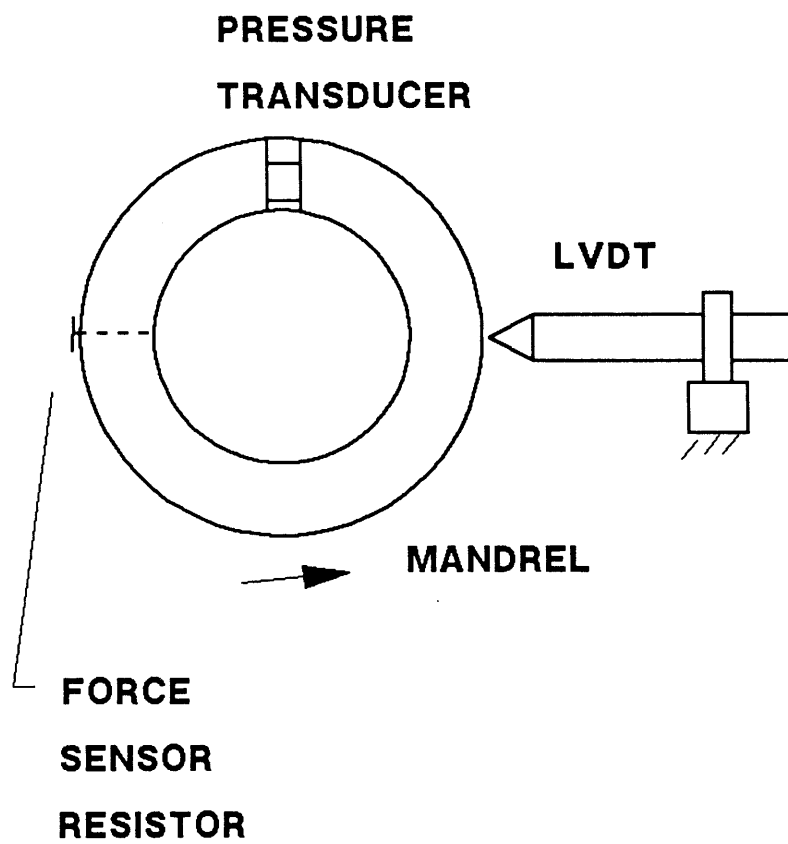
Fig. 5-22: Layer thickness measurement in winding

total pressure, and winding tension were recorded automatically via the data acquisition system.

As discussed in the previous section, wet filament winding of 3k-size fiber tow with relatively low viscosity fluid can be thought of as a fiber dominated process, which meant that the fluid pressure was low and the time for settling of wound layers was short. The measurements of the fluid pressure and layer thickness verified this assumption. An example of the thickness data is shown in Fig. 5-23. More data and plots are given in Appendix H. The result showed that the layer thickness change was stopped almost immediately after the end of the winding operation. Fluid pressure history data, as given in Appendix H, show that the fluid pressure at the interface of the layer and mandrel never exceeded 2 psi. This proves that fibers carried most of the consolidation pressure, and the flow process was very rapid.

To change the flow time constant of the process, high viscosity fluid as well as thicker fiber tows were used. From expression (2-23) we knew that the heavy tow size would have more effect on the flow time constant than the viscosity change. This was verified by the use of 40k size fiber tows. When 40k fiber tows were wound with the higher viscosity silicone fluid, the fluid pressure build up was substantial. The peak resin pressure in some runs was as high as over 50 psi. The settling time was also much longer than that in the previous case. An example of the experimental data on fluid pressure build up in the winding is shown in Fig. 5-24. More data and plots are given in Appendix H.
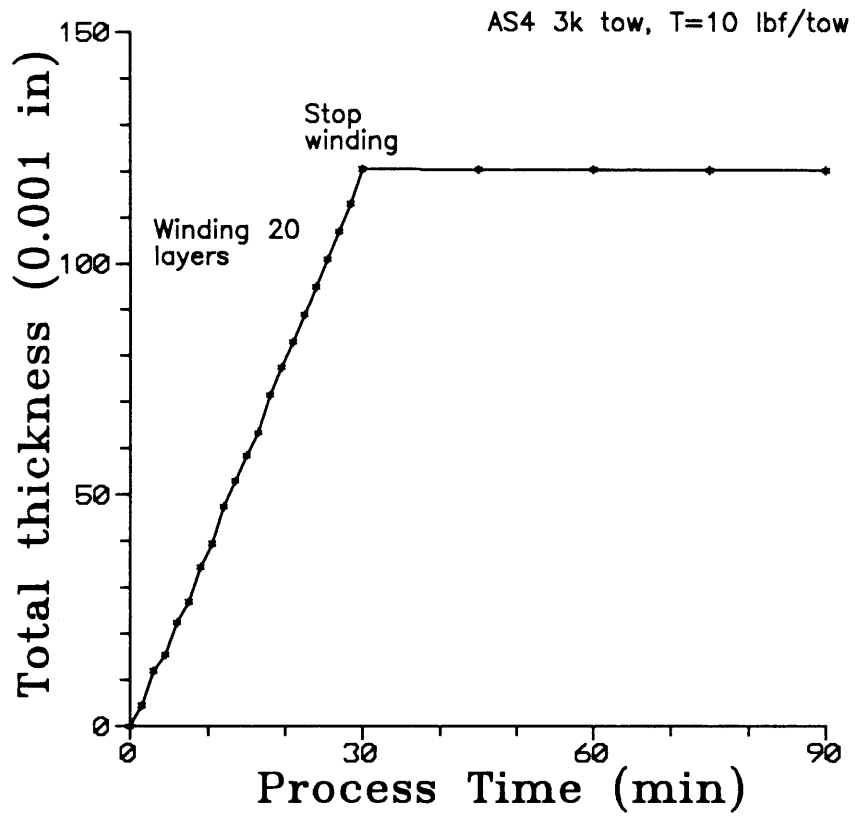
Fig. 5-23: Test data on fiber deformation dominated winding process

191
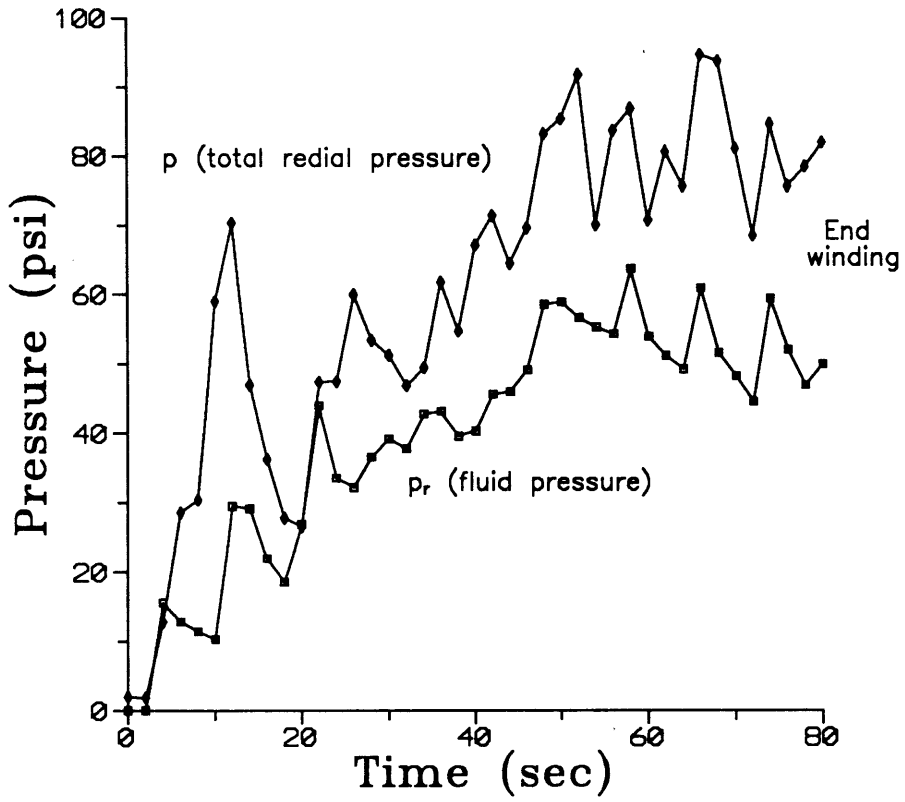
Fig. 5-24: Test data of winding with heavy fiber tows

Compared to the discussion in Chapter 2 on the process time constant evaluation, the settling time in the experiments was shorter than the model prediction. This was due to the difference between the ideal condition assumed in the model and the real experimental conditions. In the computer calculation, resin flow was modelled as one dimensional radially outward and uniform over the whole structure. However, in the winding process fiber tows were wound continuously so that side flow from the tow, which was in the axial direction of the cylindrical structure, was inevitable. This difference in flow conditions produced the discrepancy between the experimental data and model prediction.

This part of the experiments successfully verified the relation between the flow time constant and the winding process time. The relation for flow time constant estimation as shown in (2-23) was verified by the experiments. Fiber tow size proved to be the most effective factor in changing the flow time constant, which agreed with the analytical solution given in Chapter 2.

5-6. Consolidation Experiments on Cylindrical Shaped Parts

The consolidation experiments were to study fiber deformation and resin flow for cylindrical shaped parts. This was considered similar to the prepreg tape winding process, in which there was no substantial flow in winding so that a consolidation stage after the winding was necessary to improve the microstructure of the product. We tried to avoid using prepreg tapes in our test because the viscosity of the epoxy resin in the prepreg tape changed dramatically in the process and it was hard to determine the

exact viscosity at certain point in the test. We used the same kind of

silicone fluid to replace the real resin in these consolidation experi-

ments.

To make the consolidation after the winding possible, fluid flow in

the winding stage must be reduced to a minimum. As discussed in the pre-

vious section, several factors can affect the flow process. These are

fiber tow size, fluid viscosity, winding speed, and winding tension ap-

plied. The heavy size fiber tow RK 30-40k was chosen for these experi-

ments. Silicone fluid of viscosity 100,000 cst was used, although higher

viscosity fluid was also available. This was in consideration that the

wetting process of the fiber tow may be difficult for higher viscosity

fluid. Faster winding speed can only reduce the flow in the winding stage.

However, there was a time interval between the completion of winding and

the start of the consolidation because of the equipment set up. Faster

winding could not appreciably reduce the total amount of flow before the

consolidation, because this set up time could not be shortened very much.

Reducing the winding tension showed substantial effect on the flow process

and the fiber volume fraction of the layer after the winding. As stated in

the previous discussion, in addition to the winding tension applied to the

fiber tow by the friction brake-like device, both the friction of rollers

and bearings, and the viscous shearing force from the fluid when fiber tows

ran through it, contributed to the tension in the fiber bundle. We can

reduce the applied friction force in the tension control device, but we

cannot reduce other friction effects substantially. When we increased the

fiber tow size, the shearing force exerted by the fluid also increased, but

the friction effects from the rollers and bearings did not change much. In

other words, the tension needed to pull a fiber tow was not proportional to the tow size, so that it was possible to pull the heavy fiber tow with lower average tensile stress. The minimum tension to pull a fiber tow increased from about 3 lbf for 3k fiber tow to about 15 lbf for 40k fiber tow, thus the average tensile stress in the fiber tow was greatly reduced. As the tensile stress was lower, the driving force for flow in the winding operation was also smaller. When finished with winding, we could still maintain a relatively low fiber volume fraction. This made it possible to conduct the consolidation experiments after the winding, and thus to approximate the prepreg tape winding process.

The pressure device in the consolidation test must be able to apply radial pressure evenly over the whole structure, and at the same time allow an easy pressure measurement. A simple hose clamp device was designed and used at first. Later when an autoclave became available, it was used as a pressure chamber for the consolidation experiments.

The hose clamp type squeezing flow device is shown in Fig. 5-25. After the winding was complete, bleeder paper with its width equal to the axial length of the mandrel was wrapped on to the wound layers. Then a thin sheet of steel of the same width was wound on the top, which helped to spread load evenly over the whole area underneath. Four hose clamps were then put on the outside of the whole assembly. Consolidation pressure was applied by tightening these clamps gradually and in turns to obtain the better control of the pressure distribution. As was done in the winding experiments, the total radial pressure was measured by flat shape force sensor resistors bonded onto the mandrel, and the fluid pressure was
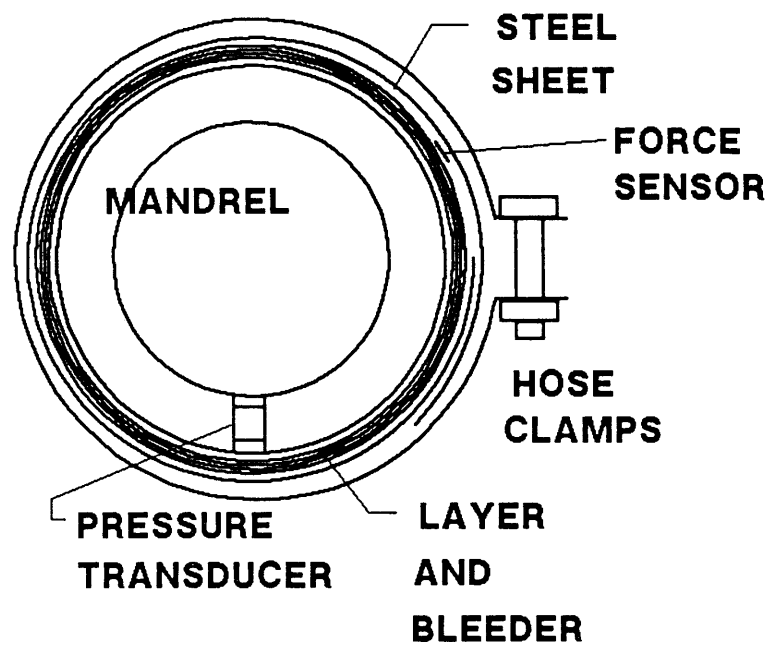
Fig. 5-25: Hose clamp device for consolidation experiment

measured by an embedded pressure transducer. The applied pressure was measured by inserting another flat shape force sensor resistor at the steel sheet and bleeder interface. These measurement devices are also shown in Fig. 5-25. Bonding of strain gages on to the surface of the clamps was also tried, but the signal from the circumferential extension strain of the clamp was overwhelmed by the signals from other effects since the bending deformation of the clamp was large. After the applied pressure reached maximum, which was limited by the clamp tightening force, the clamp was left in position. The applied pressure dropped gradually because of the fiber rearrangement and layers settling under the radial pressure. These test data and plots are given in Appendix I.

Later when a used autoclave was obtained, the consolidation tests were repeated in the autoclave with better control of the applied pressure. The autoclave was used just as a pressure chamber without applying heat. In the autoclave consolidation experiments, the assembly of wound layers and bleeder paper, and the mandrel was put onto a tool plate and sealed in a vacuum bag. Pressure was applied to the bag. This is shown in Fig. 5-26. After completing the winding operation, bleeder paper was wrapped onto the wound structure. The whole part was then put onto a aluminum tool plate designed with a vacuum port and the instrumentation penetrator. A vacuum bag was then placed over the assembly, and sealing tapes were care-fully inserted around the edge of the plate and bag. After this assembly was sealed, the port on the tool plate was then connected to a vacuum pump, and seals were checked for leaks. Then the assembly was placed into the autoclave. The autoclave was then gradually pressurized. Measurements taken from the assembly included the total radial pressure on the mandrel
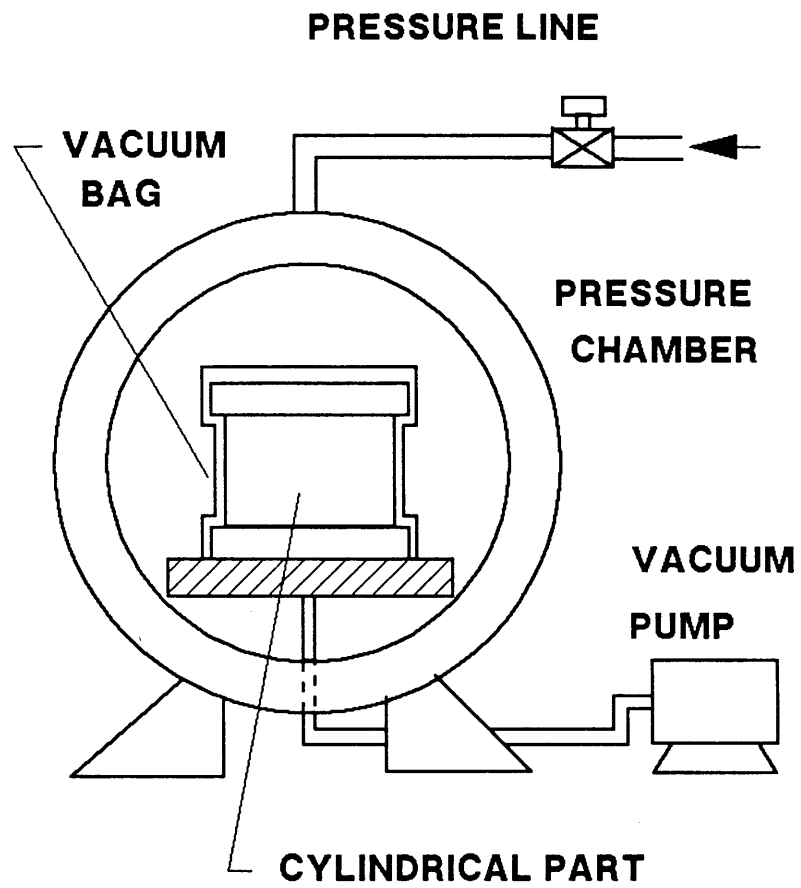
Fig. 5-26: Autoclave set up in consolidation experiments

surface, and the fluid pressure at the layer/mandrel interface. These signals were transferred via the penetrator through the tool plate, and then through the penetrator on the autoclave door, to the data acquisition system. Pressure in the autoclave was also measured by another pressure transducer connected to the autoclave pressure line, which gave a direct reading of the applied pressure and was more accurate than the applied pressure data in the earlier clamp pressure device. The applied pressure appeared more uniform too. After the desired pressure was reached, the pressure was held until the fluid pressure dropped, which indicated the flow process was complete.

The autoclave consolidation experiments were repeated for seven times but only three of them were successfully finished. In other runs either the vacuum bag seals were ripped off, or the data acquisition system was out of order, so that the experiments had to be stopped. The results of these three successful runs were consistent. Data are listed in Appendix I.

Results for both setups showed the load transfer from the fluid to the fiber bundles. When pressure was first applied to the structure, the fluid pressure increased with the applied load. Then as applied pressure was maintained at a fixed level, the fluid pressure dropped gradually over time. This showed that flow decreased and the fiber bundle was squeezed to a more compacted state.

The computer simulation program used the experimental data as input to calculate the fluid pressure response. When incorporating the computer

simulation output with the experimental data, the parameter V_a' in the permeability expression (2-18), which was the available fiber volume fraction for the transverse flow, was adjusted to obtain the best fit. This approach was also used in the previous study of laminate molding, where the transverse flow experiments were conducted [35,64]. The value of V_a' was 0.79 for all three successful runs. The experimental data showed some variations between different runs. These variations may come from differences in wound structure states, applied pressure profiles, vacuum seal conditions, etc. Although great effort was expended in controlling these parameters, the results still showed variations because of various random factors. One of the experimental data with computer simulation results are plotted in Fig. 5-27. Other two cases of test data and plots are given in Appendix I.

In general, the experimental data on consolidation of cylindrical parts show good agreement with the computer model analysis. This verifies the process analysis presented in Chapter 2. The experiments also help understanding of consolidation process mechanisms, which is the combination of the fiber rearrangement and resin squeezing flow. The load transfer phenomenon observed in the flat laminate molding process also appeared in the cylindrical part experiments. Since the fiber bundle carries part of the transverse load, and gradually most of the transverse load in these cases, fiber bundle deformation behavior is important to the final microstructure of the product.
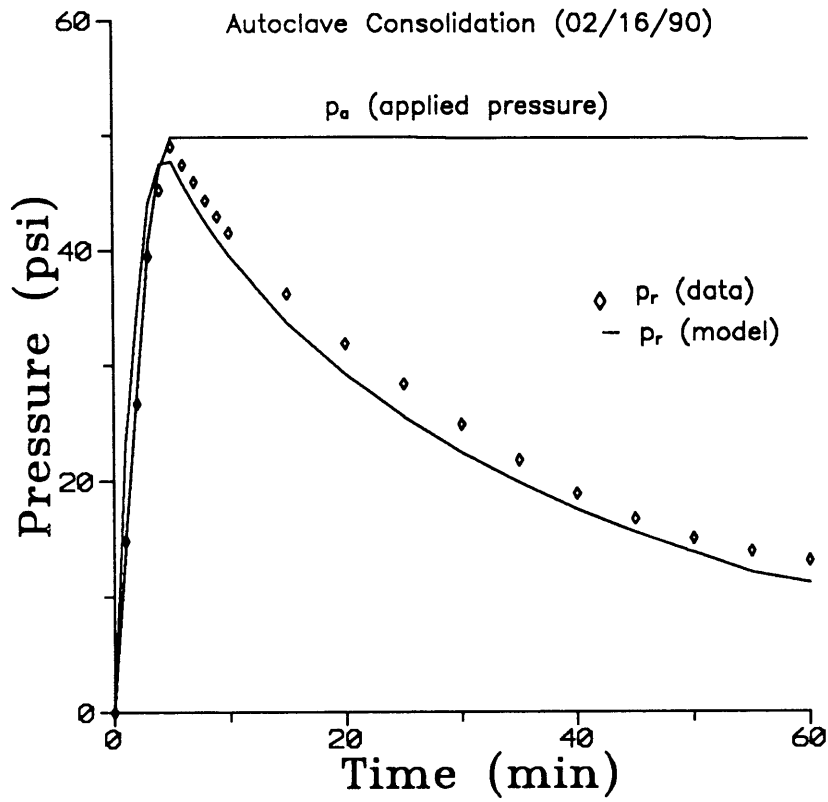
Fig. 5-27: Experimental data with computer simulation results
          for consolidation of cylindrical parts

5-7. Summary

A series of experiments were performed successfully on investigating material deformation behaviors and on simulating the winding and consolidation processes. Experimental results verified the fiber bundle deformation model and the winding and consolidation process model. Experimental data were also used to determine or verify some of the constants in various expressions and relations. The fiber bundle deformation data are useful not only for the analysis of closed shape composite structures, but also for study of other manufacturing processes. Experimental data on winding and consolidation simulation helped the understanding of the fiber motion and resin flow processes, which then can be used in the design and control of process variables.

6. CONCLUSIONS AND SUGGESTIONS

6-1. Conclusions

In this project we developed a computer simulation model for the manufacturing of a thick-wall composite cylinder. We also studied fiber bundle deformation in the composite manufacturing process and presented a continuum mechanics model to describe the deformation behaviors. A series of experiments were designed and carried out to clarify the process physics, and to verify the process model predictions.

From previous discussions we can derive following conclusions:

a) The process analysis for manufacture of a thick-walled cylindrical composite structure was successfully performed. In the analysis, fiber bundle deformation and its effect on the process mechanisms were studied in detail. Emphasis in this study was on the winding and consolidation process, which involved material deformation, mass flow, and force equilibrium with a closed shape structure. A general process model based on these analyses was then proposed. This consisted of winding and consolidation, debulking and cure, and post-cure stages. Mathematical equations were derived for these physical processes.

b) A computer simulation program WC was developed by using FORTRAN language on a Micro-VAX system. Calculation of the process variables involved solving the coupled nonlinear partial differential equations of

203

resin flow and temperature distribution, with changing boundary conditions. Iteration schemes were therefore constructed by using Newton's method for nonlinear equations and by employing prediction-correction iterative loops. The simulation program calculated the time history of various process variables, such as fiber volume fraction, resin pressure, product dimensions, and temperature distribution. These can be used in the design and control of the fabrication processes.

c) A continuum mechanics model for the deformation of an aligned, lubricated, and continuous fiber bundle was proposed. From experimental observations, deformation of such a fiber bundle showed elastic deformation as well as viscous responses in various processing conditions. This fiber bundle model separated these two responses by assuming the "cylindrical" and the "deviatoric" stress components, which can represent the deformation behaviors of the fiber bundle for many applications.

d) The fiber bundle elastic responses in the material principal directions were analyzed by using a compliance matrix and an incremental form of stress and deflection relations. This approximated many manufacturing processes, such as autoclave molding, filament winding, and pultrusion, in which the fiber bundle underwent transverse compression and there was no gross fiber movement. There were three independent compliance terms under this condition. These terms were analyzed by assuming statistical distributions for fiber bundle imperfections, such as small waviness, misalignment, and fiber cross-over. It was found that all these compliance terms were related to the fiber bundle deformation state which in our study was the fiber volume fraction. Analytical relations were derived and ex-

periments were performed. The results showed that in the transverse direction, fiber bundles behaved like a nonlinear and quickly stiffening spring, while in the longitudinal direction, they behaved linearly but the bundle stiffness was reduced because of the imperfections of the fiber bundle. This fiber bundle model was applicable to various manufacturing processes.

e) As one application of the fiber bundle model, experiments and computer simulation were performed for compression molding of composite laminates. Flow and consolidation of the composite material in this case were very close to that in the filament winding process since in both cases flow was transverse to the fiber bundle axial direction. A special applied pressure and temperature profile was designed to intentionally obtain the incomplete flow status in order to study the intermediate fiber distribution states. Then computer simulation was performed by using the experiment data. The results showed good agreement between them, thus the fiber motion proposed in the fiber deformation/resin flow model was verified.

f) Wet filament winding simulation was performed by using continuous fiber tows with constant viscosity silicone fluids. It was found that flow was substantial and consolidation time was very short. The process was then modeled as a fiber bundle deformation dominated process and nonlinear elastic analysis was used in the calculation. Fiber distribution after the winding was found closely related to the winding force applied, and inner layers were at a higher fiber volume fraction state. Computer calculation was also carried out and showed good agreement with the experimental measurements.

g) Process time evaluation was done for the winding and consolidation processes. The time constant study of the laminate transverse flow was adapted in the analysis. Fiber tow size and fluid viscosity were proven to be the most important factors in determining the flow process time constant. By using different fiber tow sizes and fluid viscosities, process time constants were evaluated. The relationship between the process variables and the process time constant was verified.

h) Consolidation experiments were designed and carried out to study the deformation behavior of the fiber bundle and fluid mixture in a closed shape structure. Fluid pressure and radial stress were measured in the experiments and the results were compared with the computer simulation outputs. It was found that the load transfer as reported in the previous study on laminate molding case also appeared here. As the fiber bundle underwent more and more compaction, fluid pressure dropped gradually and fibers carried most of the load. This consolidation study confirmed the proposed process model.

In short, this process model and a series of experiments successfully analyzed the manufacturing process and provided a tool for the process design and control.

6-2. Suggestions

There are several areas in which further study on the composite manufacturing could be conducted. This study only considered the cylindrical shape structure, there are much more complicated geometric shapes which

will be used more and more in different industrial applications. For the fiber bundle deformation, only the state where fibers were under the transverse compressive stress was studied in detail. As we listed in the experimental observations in Chapter 3, there were many other deformation modes in composite manufacturing processes. For the process modeling work presented in this study, experiments were carried out only with constant viscosity fluids. This simplified the problem but also deviated from real processing conditions. These problems will be discussed briefly here.

The basic difference between a cylindrical tube structure and other closed shape structures, such as an elliptical tube with the major axis much larger than the minor axis, is the flow and consolidation conditions. In the former case, flow and consolidation can be simplified as one dimensional and only in the radial direction, whereas in the latter case this advantage is not available. In the winding operation, the applied winding tension induces uniformly distributed consolidation pressure for a cylindrical structure, whereas for other geometries, there will be a varying pressure distribution over the structure. Therefore the consolidation of the layers by this pressure would be different at different locations. The other problem in the winding operation is the fiber placement. For structures such as cylinder or sphere, the fiber placement is realized by following the geodesic paths of the geometry. Usually the designed winding pattern by considering the structural performance can be combined with the consideration of the geodesic paths of the structure. For other closed shape structure, these two considerations could be in conflict with each other in many cases. A compromise solution must be found for these cases. This also implies that a process model would be very helpful in the analy-

sis of more complicated structures. Further development of the process
model is necessary if these structures are used more frequently in various
applications.

For the fiber bundle deformation modeling, we omitted the non-
elastic responses in the analysis. As we discussed in Chapter 3, the ex-
perimental observations showed that in some cases this had to be included
in the analysis. In general the overall deformation of the fiber bundle in
the material principal directions is viscoelastic. Only if the process
time is relatively short, which was the assumption in our analysis, can
this viscous effect be neglected. A complete model for the fiber deforma-
tion therefore must include the viscoelastic effect. The other part which
was not discussed in detail was the shear mode deformation of the bundle.
This appears in the forming process, which is used more and more in various
applications. Shear motion was undesirable in the various processes dis-
cussed in this study, such as molding and winding. However, shear motion
can also be used for a specific purpose. A new development in the com-
posite material processing area is the long discontinuous fibrous composite
sheet which can be formed by using conventional press or die equipment for
the metal material. In this processing technique, fiber deformation behav-
ior is the main concern. Fiber placement and shear deformation are the
main physical processes in forming. A good process model is necessary to
the analysis and development of this kind of new technique and material.

The application of the computer simulation model to the real pro-
duction of composite structures is still a new field. Although verifica-
tions of the computer simulation models by applying them to the thick wall

composite cylinders were reported in [23,26], applications of the computer simulation model in this field is still very limited. To expand the role of the computer simulation in the manufacturing process, more work needs to be done in the area of quality engineering and real time measurement and data processing. Closed-loop control technique is one method of applying computer model to the processes, but this requires more accurate and extensive modeling and the development of measuring devices and instrumentations for the real monitoring. This is also a promising new field as the development of composite materials and structures enters a new era in 1990s.

APPENDIX A

Heat Transfer Solution for Curing Specimen Ends

The heat transfer problem of curing ends of the specimen for measuring the compliance term S_{11} can be simplified as a typical fin structure, as shown in Fig. A-1. Because of the symmetric condition, only half of the piece needs to be considered. The hot ends are considered to be at a constant cure temperature during the process. There is forced air convection at both top and bottom surfaces of the specimen. Therefore the boundary temperature at these surfaces is considered as at room temperature. We consider only the steady state heat flow for this problem, so that the heat transfer equation becomes

$$k_x \frac{\partial^2 T}{\partial x^2} + k_y \frac{\partial^2 T}{\partial y^2} = 0 \qquad\qquad (A-1)$$

where k_x and k_y are the thermal conductivities in x and y directions respectively, and directions x and y are shown in Fig. A-1. By using the reference temperature T_2 as shown in Fig. A-1, we can define the temperature variable T' as

$$T' = (T - T_2) \qquad\qquad (A-2)$$

For simplicity we just use T in the following discussion. We have temperature boundary condition for boundaries x=0, y=0, and y=b, and heat flow boundary condition at x=a. These can be written as
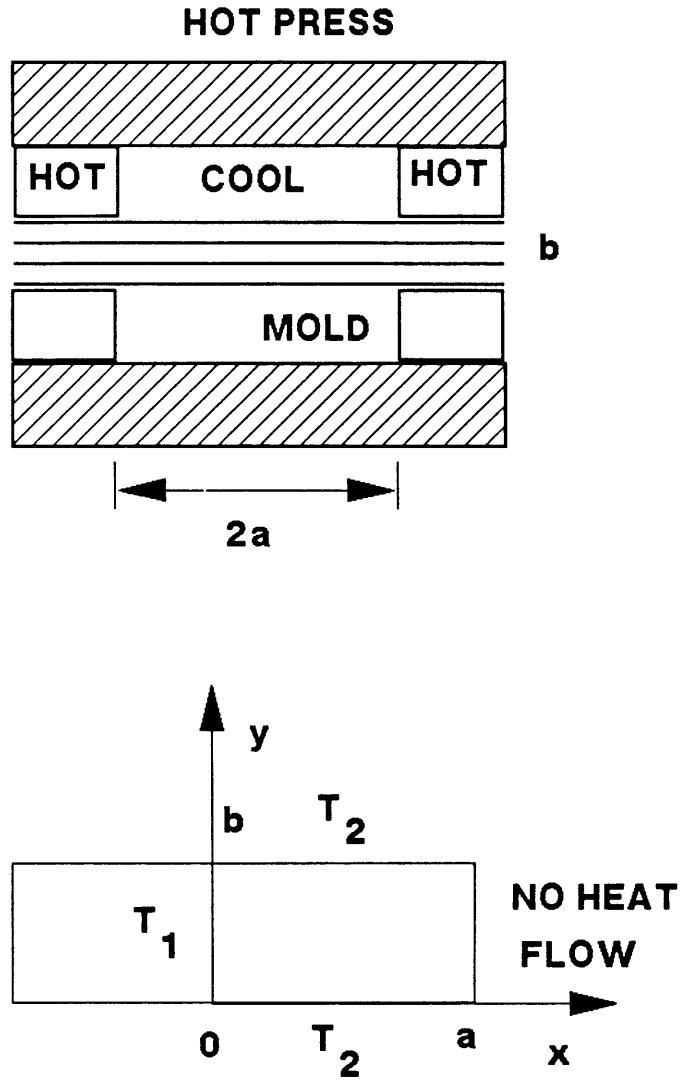
Fig. A-1: Heat transfer problem of curing specimen ends

$$x = 0, \quad T = T_0 = T_1 - T_2$$
$$x = a, \quad dT/dx = 0$$
$$y = 0, \quad T = 0$$
$$y = b, \quad T = 0 \tag{A-3}$$

where T_1 is the cure temperature as shown in Fig. A-1. By using separation of variables, we can express the solution form of T as

$$T = X(x) * Y(y) \tag{A-4}$$

By substituting (A-4) into (A-1), we have

$$\frac{k_x}{k_y} \frac{X''}{X} + \frac{Y''}{Y} = 0 \tag{A-5}$$

We can rewrite (A-5) as

$$\frac{k_x}{k_y} \frac{X''}{X} = - \frac{Y''}{Y} = \alpha^2 \tag{A-6}$$

From (A-6) we can separate equations for X and Y as

$$X'' - \beta^2 X = 0 \tag{A-7}$$

$$Y'' + \alpha^2 Y = 0 \tag{A-8}$$

where

$$\beta = \alpha \, (k_x/k_y)^{1/2} \tag{A-9}$$

Solutions for (A-7) and (A-8) are

$$X = C_1 \, e^{\beta x} + C_2 \, e^{-\beta x} \tag{A-10}$$

$$Y = C_3 \, \cos(\alpha y) + C_4 \, \sin(\alpha y) \tag{A-11}$$

212

where C_i's are constants to be determined by boundary conditions. For the boundary condition at x=0, $T=T_0$, we can use Fourier expansion

$$T = T_0 = \sum_{n=0}^{\infty} A_n \sin \frac{n\pi y}{b} \qquad (A-12)$$

In order to obtain A_n, we can multiply both sides of (A-12) by $\sin(m\pi y/b)$, then integrate

$$\int_0^b T_0 \sin \frac{m\pi y}{b} \, dy = \int_0^b \sum_{n=0}^{\infty} A_n \sin \frac{n\pi y}{b} \sin \frac{m\pi y}{b} \, dy$$

$$= \int_0^b A_m \sin^2 \frac{m\pi y}{b} \, dy = \frac{b}{2} A_m \qquad (A-13)$$

Therefore, we have

$$A_m = \frac{4T_0}{m\pi} \qquad (m=1,3,5,\ldots)$$

$$A_m = 0 \qquad (m=2,4,6,\ldots) \qquad (A-14)$$

By substituting this back to (A-12), we have the boundary condition at x=0

$$T = \sum_{n=1,3,\ldots}^{\infty} \frac{4T_0}{n\pi} \sin \frac{n\pi y}{b} \qquad (A-15)$$

Since the solution of T can be written as

$$T = XY = (C_1 e^{\beta x} + C_2 e^{-\beta x})[C_3 \cos(\alpha y) + C_4 \sin(\alpha y)] \qquad (A-16)$$

At y=0, T=0, and C_3=0. At y=b, T=0, and $C_4 \sin(\alpha b)$=0, so we have

$$\alpha_n = n\pi/b \qquad (n=1,2,3,\ldots) \qquad (A-17)$$

At x=0, T=T$_0$

$$T = (C_1 + C_2) \sin(\alpha_n y) \sum_{n=1,3,..}^{\infty} \frac{4T_0}{n\pi} \sin \frac{n\pi y}{b} \qquad (A-18)$$

At x=a, dT/dx=0

$$C_1 exp(\beta_n a) - C_2 exp(-\beta_n a) = 0 \qquad (A-19)$$

where

$$\beta_n = \alpha_n \; (k_x/k_y)^{1/2} \qquad (A-20)$$

From (A-19), we can rewrite (A-16) as

$$T = \sum_{n=1,3,..}^{\infty} C_n \; [exp(\beta_n x) - exp(2\beta_n a) exp(-\beta_n x)] \; \sin \frac{n\pi y}{b} \qquad (A-21)$$

From the boundary condition at x=0, we can solve for C$_n$

$$C_n = \frac{4T_0}{[1-exp(2\beta_n a)]n\pi} \qquad (A-22)$$

We can use the dimensionless expression by assuming $T^* = T/T_0$, $x^* = x/a$, $y^* = y/b$. and $\gamma = (a/b)(K_y/k_x)^{1/2}$

$$T^* = \sum_{n=1,3,...}^{\infty} C_n^* [exp(n\pi\gamma x^*) - exp(2n\pi\gamma) exp(-n\pi\gamma x^*)] \sin(n\pi y^*) \qquad (A-23)$$

where

$$C_n^* = \frac{4}{[1-exp(2\pi n\gamma)]n\pi} \qquad (A-24)$$

Since the most sensitive part is the center line at $y = b/2$ or $y^* = 1/2$, we just check temperature distribution along this line

$$T^* = \sum_{n=1,3,\ldots}^{\infty} C_n^* [exp(n\pi\gamma x^*) - exp(2n\pi\gamma)exp(-n\pi\gamma x^*)]sin(n\pi/2) \quad (A-25)$$

In (A-25) the only parameter is γ which is determined by material properties. For a fibrous composite material, we have the relation: $k_y/k_x = k_T/k_L$, which is approximately equal to 1/50 [A-1]. We can choose some values of a and b for extreme cases, $a=1$ (in), and $b=0.1$(in), so that the test sample has 2 inch effective length and is about 14 plies (each ply is about 0.007 inch thick). In this case, $\gamma = 1.4142$. We also assume $T_1 = 350°F$, and $T_2 = 50°F$, so that $T_0 = 300°F$. We assume that for $T < 100°F$ or $T^* < 1/6$, the material would not be affected. The temperature distribution of the center line is plotted in Fig. A-2 by using dimensionless parameters T^* and x^*. From the figure we find that if $\gamma = 1.4142$, the solution for $T^* < 1/6$ is approximately $x^* > 0.45$. Therefore the heat affected zone is only about a half inch in this case. In our test for measuring S_{11} compliance term, the effective length was about 4 inch long, and the ply number was 4 or 6, so that the heat affected zone was even shorter.

Reference

A-1. Agrarwal, B.D., and Broutman, L.J., <u>Analysis and Performance of Fiber Composites</u>," Wiley, New York, 1980, pp. 62.
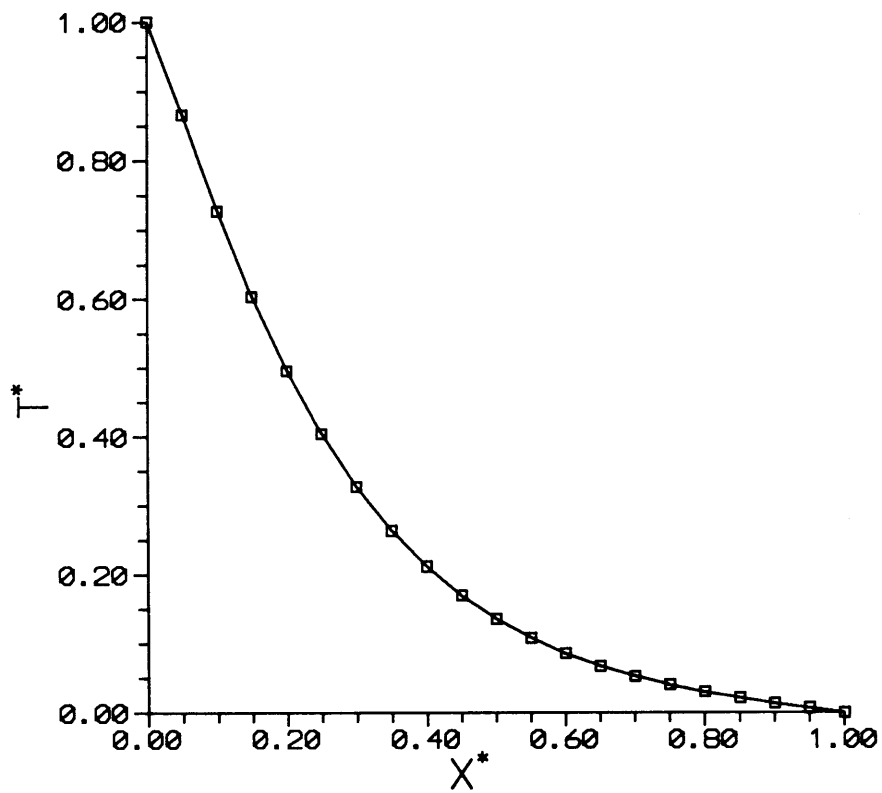
Fig. A-2: Temperature distribution at the specimen center line

APPENDIX B

Data of Measuring the Longitudinal Compliance

Batch B-1 (Data of Fig. 5-3)   Date files: 6

Sample Data:

Prepreg tape: AS4/3501-6   Fiber volume fraction: 0.5
Length: 6 inches   Width: 0.75 inch
Ply thickness: 0.007 inch.   Ply number: 4

1) DATA FILE: JUL30-1.DAT   DATE: 07/30/87

LOAD   STRAIN   (Load: lbf;   Strain: 10^{-6})
0   0
100   365
200   688
300   1019
400   1351
500   1694
600   2023
700   2364
800   2711
900   3051
1000   3430

Stiffness reduction factor by using linear curve fitting: 0.826

2) DATA FILE: JUL30-2.DAT   DATE: 07/30/87

LOAD   STRAIN   (Load: lbf;   Strain: 10^{-6})
0   0
100   345
200   674
300   1008
400   1343
500   1692
600   2017
700   2378
800   2724
900   3039
1000   3447

Stiffness reduction factor by using linear curve fitting: 0.820

3) DATA FILE: AUG01-1.DAT   DATE: 08/01/87

LOAD   STRAIN   (Load: lbf;   Strain: 10^{-6})
0   0
100   352
200   678
300   1004
400   1339
500   1687
600   2030
700   2373
800   2719
900   3076
1000   3466

Stiffness reduction factor by using linear curve fitting: 0.816

4) DATA FILE: AUG01-2.DAT   DATE: 08/01/87

LOAD   STRAIN   (Load: lbf;   Strain: 10^{-6})
0   0
100   361
200   698
300   1029
400   1359
500   1678
600   2108
700   2434
800   2759
900   3177
1000   3496

Stiffness reduction factor by using linear curve fitting: 0.801

5) DATA FILE: AUG03-1.DAT   DATE: 08/03/87

LOAD   STRAIN   (Load: lbf;   Strain: 10^{-6})
0   0
100   339
200   659
300   988
400   1301
500   1633
600   1995
700   2321
800   2687
900   2997
1000   3422

Stiffness reduction factor by using linear curve fitting: 0.829

6) DATA FILE: AUG03-2.DAT   DATE: 08/03/87

LOAD   STRAIN   (Load: lbf; Strain: 10^{-6})
0   0
100   371
200   730
300   1079
400   1402
500   1722
600   1965
700   2294
800   2683
900   3084
1000   3459

Stiffness reduction factor by using linear curve fitting: 0.833

Batch B-2 (Data of Fig. B-1)   Date files: 4

Sample Data:

Prepreg tape: AS4/3501-6   Fiber volume fraction: 0.5
Length: 6 inches   Width: 0.75 inch
Ply thickness: 0.007 inch.   Ply number: 2

1) DATA FILE: AUG12-1.DAT   DATE: 08/12/87

LOAD   STRAIN   (Load: lbf; Strain: 10^{-6})
0   0
50   368
100   697
150   1005
200   1304
250   1674
300   1898
350   2319
400   2547
450   2924
500   3270

Stiffness reduction factor by using linear curve fitting: 0.872

2) DATA FILE: AUG12-2.DAT   DATE: 08/12/87

```
LOAD     STRAIN     (Load: lbf;  Strain: 10⁻⁶)
0        0
50       356
100      713
150      1120
200      1441
250      1742
300      2045
350      2366
400      2675
450      2941
500      3299
```

Stiffness reduction factor by using linear curve fitting: 0.860

3) DATA FILE: AUG14-1.DAT   DATE: 08/14/87

```
LOAD     STRAIN     (Load: lbf;  Strain: 10⁻⁶)
0        0
50       343
100      735
150      1124
200      1443
250      1856
300      2168
350      2469
400      2766
450      3071
500      3386
```

Stiffness reduction factor by using linear curve fitting: 0.825

4) DATA FILE: AUG14-2.DAT   DATE: 08/14/87

```
LOAD     STRAIN     (Load: lbf;  Strain: 10⁻⁶)
0        0
50       385
100      766
150      1093
200      1392
250      1673
300      1961
350      2280
400      2659
450      3001
500      3275
```

Stiffness reduction factor by using linear curve fitting: 0.869
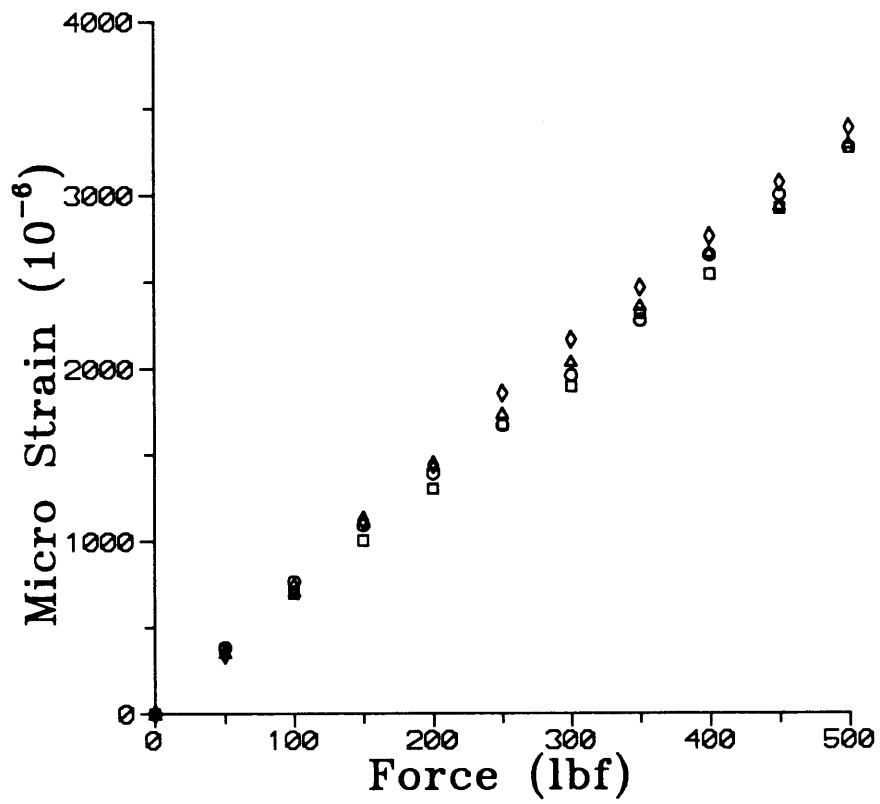
Fig. B-1: Experimental data of measuring the S_{11} term

APPENDIX C

Data of Measuring the Coupling Term

Experiment data: (Data of Fig. 5-9 and Fig. 5-10)

Mold area (A_z): 9.003 in*in   Mold width (W): 3.00 in
Gage factor (GF): 1 reading = 2.20 grams   LVDT: 1 in = 40.735 V

Data reduction formula:

$$\Delta F_x = GF \; \Delta reading \qquad\qquad (C-1)$$

$$\Delta \sigma_z = \Delta F_z / A_z \qquad\qquad (C-2)$$

$$A_x = W \; H \qquad\qquad (C-3)$$

$$S_{1b} = (\Delta F_x \; S_{11})/(A_x \; \Delta \sigma_z) \qquad\qquad (C-4)$$

where GF, A_z, and W are constants, H was from LVDT, $\Delta reading$ was from force sensor, and ΔF_z was from Instron load cell.

1) Data File: Nov22-1.dat

LOAD	LVDT	[COMPLIANCE DATA FOR MOLD]	[LOAD:LBF; LVDT:V]
0	9.481		
5	9.490		
10	9.502		
25	9.516		
50	9.527		
100	9.542		
150	9.556		
200	9.566		
250	9.574		
300	9.579		
400	9.588		
500	9.593		
600	9.597		
750	9.601		
1000	9.605		
1500	9.610		
2000	9.612		
2500	9.614		
3000	9.616		
4000	9.617		
5000	9.618		

```
LOAD      LVDT      GAGE      [TEST DATA]   [LOAD:LBF; LVDT:V; GAGE: GAGE READING]
0         6.003     -25
2.5       6.291     -30
5         6.505     -35
10        6.695     -43
15        6.794     -46
20        6.870     -48
30        6.974     -54
40        7.048     -58
50        7.110     -63
60        7.157     -67
75        7.220     -72
100       7.299     -80
150       7.417     -95
200       7.495     -109
250       7.572     -118
300       7.633     -127
400       7.742     -139
500       7.823     -148
750       7.978     -166
1000      8.078     -175


PARA1     PARA2     PARA3     PARA4     [1:AREA; 2:LVDT; 3:WEIGHT; 4:GAGE]
9.003     40.735    8.164     2.20
ISCL      IDT       [ISCL: 1=AUTO; -2=INPUT.  IDT: 1014=POINTS; 14=CURVE]
-2        1014
XSCL(4)   [X1,X2; Y1,Y2]
0.3       0.8       0.0       400.0
L         [SHAPE OF PLOT POINTS]
6
XL
'VF'
YL
'FORCE (gram)'
```

2) Data File: Nov22-2.dat

```
LOAD    LVDT        [COMPLIANCE DATA FOR MOLD]    [LOAD:LBF; LVDT:V]
0       9.481
5       9.490
10      9.502
25      9.516
50      9.527
100     9.542
150     9.556
200     9.566
250     9.574
300     9.579
400     9.588
500     9.593
600     9.597
750     9.601
1000    9.605
1500    9.610
2000    9.612
2500    9.614
3000    9.616
4000    9.617
5000    9.618


LOAD    LVDT    GAGE    [TEST DATA]    [LOAD:LBF; LVDT:V; GAGE: GAGE READING]
0       6.148   -57
2.5     6.465   -72
5       6.643   -82
7.5     6.811   -89
10      6.944   -93
15      7.133   -99
20      7.245   -105
25      7.315   -109
30      7.371   -113
40      7.446   -118
50      7.506   -121
75      7.600   -128
100     7.658   -132
150     7.743   -138
250     7.826   -145
500     7.936   -150
750     7.992   -150
1000    8.025   -151
1500    8.059   -152
2000    8.081   -154
2500    8.095   -155
```

```
PARA1   PARA2   PARA3   PARA4    [1:AREA; 2:LVDT; 3:WEIGHT; 4:GAGE]
9.003   40.735  8.161   2.20
ISCL    IDT     [ISCL: 1=AUTO; -2=INPUT.  IDT: 1014=POINTS; 14=CURVE]
-2      1014
XSCL(4) [X1,X2; Y1,Y2]
0.3     0.8     0.0     400.0
L       [SHAPE OF PLOT POINTS]
7
XL
'VF'
YL
'FORCE (gram)'
```

3) Data File: Nov25-1.dat

LOAD	LVDT	[COMPLIANCE DATA FOR MOLD] [LOAD:LBF; LVDT:V]
0	9.481	
5	9.490	
10	9.502	
25	9.516	
50	9.527	
100	9.542	
150	9.556	
200	9.566	
250	9.574	
300	9.579	
400	9.588	
500	9.593	
600	9.597	
750	9.601	
1000	9.605	
1500	9.610	
2000	9.612	
2500	9.614	
3000	9.616	
4000	9.617	
5000	9.618	

LOAD	LVDT	GAGE	[TEST DATA] [LOAD:LBF; LVDT:V; GAGE: GAGE READING]
0	6.154	-30	
2.5	6.728	-45	
5	6.828	-53	
10	6.894	-55	
15	6.992	-58	
20	7.108	-59	
25	7.201	-61	
30	7.266	-63	
40	7.368	-66	
50	7.443	-70	
60	7.497	-72	
75	7.562	-76	
100	7.629	-81	
150	7.720	-86	
200	7.770	-90	
300	7.838	-96	
400	7.884	-100	
600	7.942	-105	
800	7.975	-108	
1000	7.997	-110	
1500	8.028	-115	
2000	8.047	-118	
2500	8.056	-120	
3000	8.064	-123	

PARA1	PARA2	PARA3	PARA4	[1:AREA; 2:LVDT; 3:WEIGHT; 4:GAGE]
9.003	40.735	8.156	2.20	

ISCL	IDT	[ISCL: 1=AUTO; -2=INPUT. IDT: 1014=POINTS; 14=CURVE]
-2	1014	

XSCL(4) [X1,X2; Y1,Y2]
0.3	0.8	0.0	400.0

L   [SHAPE OF PLOT POINTS]
8
XL
'VF'
YL
'FORCE (gram)'

4) Data File: Nov30-1.dat

LOAD	LVDT	[COMPLIANCE DATA FOR MOLD] [LOAD:LBF; LVDT:V]
0	9.481	
5	9.490	
10	9.502	
25	9.516	
50	9.527	
100	9.542	
150	9.556	
200	9.566	
250	9.574	
300	9.579	
400	9.588	
500	9.593	
600	9.597	
750	9.601	
1000	9.605	
1500	9.610	
2000	9.612	
2500	9.614	
3000	9.616	
4000	9.617	
5000	9.618	

LOAD	LVDT	GAGE	[TEST DATA] [LOAD:LBF; LVDT:V; GAGE: GAGE READING]
0	6.214	-36	
2.5	6.693	-49	
5	6.831	-56	
7.5	6.894	-60	
10	6.955	-65	
15	7.058	-74	
20	7.122	-81	
25	7.170	-86	
30	7.207	-90	
40	7.266	-97	
50	7.310	-102	
60	7.348	-107	
75	7.399	-112	
100	7.465	-119	
150	7.563	-133	
200	7.631	-145	
250	7.686	-155	
300	7.729	-164	
400	7.799	-181	
500	7.851	-195	
750	7.936	-221	
1000	7.986	-238	
1500	8.046	-260	

```
PARA1    PARA2   PARA3   PARA4    [1:AREA; 2:LVDT; 3:WEIGHT; 4:GAGE]
9.003    40.735  8.166   2.20
ISCL     IDT     [ISCL: 1=AUTO; -2=INPUT.  IDT: 1014=POINTS; 14=CURVE]
-2       1014
XSCL(4) [X1,X2; Y1,Y2]
0.3      0.8     0.0     400.0
L        [SHAPE OF PLOT POINTS]
9
XL
'VF'
YL
'FORCE (gram)'
```

5) Data File: Nov30-2.dat

LOAD	LVDT	[COMPLIANCE DATA FOR MOLD]	[LOAD:LBF; LVDT:V]
0	9.481		
5	9.490		
10	9.502		
25	9.516		
50	9.527		
100	9.542		
150	9.556		
200	9.566		
250	9.574		
300	9.579		
400	9.588		
500	9.593		
600	9.597		
750	9.601		
1000	9.605		
1500	9.610		
2000	9.612		
2500	9.614		
3000	9.616		
4000	9.617		
5000	9.618		

LOAD	LVDT	GAGE	[TEST DATA] [LOAD:LBF; LVDT:V; GAGE: GAGE READING]
0	6.165	-29	
2.5	6.678	-35	
5	6.835	-39	
10	6.897	-42	
15	6.998	-46	
20	7.115	-49	
25	7.205	-51	
30	7.268	-54	
40	7.373	-58	
50	7.445	-64	
60	7.502	-70	
75	7.569	-78	
100	7.633	-85	
150	7.725	-92	
200	7.772	-99	
300	7.843	-103	
400	7.889	-109	
600	7.947	-114	
800	7.981	-119	
1000	8.002	-125	
1500	8.034	-131	
2000	8.056	-136	
2500	8.062	-140	
3000	8.071	-145	

PARA1	PARA2	PARA3	PARA4	[1:AREA; 2:LVDT; 3:WEIGHT; 4:GAGE]
9.003	40.735	8.163	2.20	

ISCL	IDT	[ISCL: 1=AUTO; -2=INPUT. IDT: 1014=POINTS; 14=CURVE]
-2	1014	

XSCL(4) [X1,X2; Y1,Y2]

0.3	0.8	0	400

L   [SHAPE OF PLOT POINTS]
5
XL
'VF'
YL
'FORCE (gram)'

6) Data File: Nov30-3.dat

LOAD	LVDT	[COMPLIANCE DATA FOR MOLD] [LOAD:LBF; LVDT:V]
0	9.481	
5	9.490	
10	9.502	
25	9.516	
50	9.527	
100	9.542	
150	9.556	
200	9.566	
250	9.574	
300	9.579	
400	9.588	
500	9.593	
600	9.597	
750	9.601	
1000	9.605	
1500	9.610	
2000	9.612	
2500	9.614	
3000	9.616	
4000	9.617	
5000	9.618	

LOAD	LVDT	GAGE	[TEST DATA] [LOAD:LBF; LVDT:V; GAGE: GAGE READING]
0	6.195	-27	
2.5	6.720	-38	
5	6.845	-45	
7.5	6.904	-51	
10	6.970	-56	
20	7.128	-70	
25	7.185	-75	
30	7.219	-80	
40	7.274	-86	
50	7.323	-93	
75	7.412	-101	
100	7.474	-110	
150	7.577	-121	
200	7.645	-132	
250	7.696	-139	
300	7.740	-145	
400	7.813	-150	
500	7.863	-157	
750	7.952	-163	
1000	7.999	-170	
1500	8.055	-178	
2000	8.099	-184	
2500	8.136	-189	

```
PARA1    PARA2    PARA3    PARA4    [1:AREA; 2:LVDT; 3:WEIGHT; 4:GAGE]
9.003    40.735   8.159    2.20
ISCL     IDT      [ISCL: 1=AUTO; -2=INPUT.  IDT: 1014=POINTS; 14=CURVE]
-2       1014
XSCL(4)  [X1,X2; Y1,Y2]
0.3      0.8      0        400
L        [SHAPE OF PLOT POINTS]
4
XL
'VF'
YL
'FORCE (gram)'
```

Program for data reduction of coupling term measurement

```
C          PROGRAM TEST-S12.FOR (ON VAX MACHINE)
C
C          [ FOR TEST DATA REDUCTION OF S12 TERM ]
C
           DIMENSION C1(100), C2(100), C3(100), C4(100), C5(100), C6(100),
          1       H(100), E(100), FORCE(100),FIG(9,100), XSCL(4), VF(100),
          1       AX(100), AD(100), S11(100), S12(100)
C
           CHARACTER*40 XL, YL
C
           DATA XSCL/ 0.0, 0.14, 0.0, 350.0/  DEN/ 1.8E6/ PI/ 3.14159/
C                                      [ DENSITY: KG/M*3) ]
C
C          [DEN: DENSITY OF FIBERS (GRAM/M**3) ]
C
           OPEN (UNIT=15, FILE='TEST.DAT', STATUS='OLD')
           READ(15,*)
           READ(15,*)
           READ(15,*)
C          READ COMPLIANCE DATA [LOAD,LVDT]
           I=1
110        READ(15,*)C1(I),C2(I)
           I=I+1
           IF(C1(I-1).GE.0.0) GOTO 110
           N1=I-2
           READ(15,*)
           READ(15,*)
C          READ TEST DATA [LOAD,LVDT,GAGE]
           I=1
120        READ(15,*)C3(I),C4(I),C5(I)
           I=I+1
           IF(C3(I-1).GE.0.0) GOTO 120
           N2=I-2
C          READ TEST PARAMETERS
           READ(15,*)
           READ(15,*)
           READ(15,*)PARA1,PARA2,PARA3,PARA4
           READ(15,*)
C          READ PLOT PARAMETERS
           READ(15,*)ISCL,IDT
           READ(15,*)
           READ(15,*)XSCL(1),XSCL(2),XSCL(3),XSCL(4)
           READ(15,*)
           READ(15,*)L
           READ(15,*)
           READ(15,*)XL
           READ(15,*)
           READ(15,*)YL
           CLOSE(UNIT=15)
C
           AREA=PARA1
```

```
C                                          AREA: SAMPLE AREA (IN**2)
        TLVDT=PARA2
C                                          TLVDT: TRANSFORM V TO IN
        WF=PARA3
C                                          WF: WEIGHT OF FIBERS (GRAM)
        GAGE=PARA4
C                                          GAGE: TRANSFORM READING TO FORCE
C                                                (GRAM)
        DO 130 I=1,N1
        C1(I)=C1(I)/AREA
130     CONTINUE
C                                          TRANSFORM LOAD FROM LBF TO PSI
        DO 140 I=1,N2
        C3(I)=C3(I)/AREA
140     CONTINUE
C                                          TRANSFORM LOAD FROM LBF TO PSI
        JP=1
        X11=C1(1)
        X22=C1(2)
        Y11=C2(1)
        Y22=C2(2)
C                                          LINEAR INTERPOLATION FOR MOLD
C                                          COMPLIANCE DATA
        Z11=C5(1)
C                                          BASE READING FOR INDUCED FORCE
        DO 150 I=1,N2
        J=1
180     CONTINUE
        IF((C3(I).GE.C1(J)).AND.(C3(I).LT.C1(J+1))) THEN
        X11=C1(J)
        X22=C1(J+1)
        Y11=C2(J)
        Y22=C2(J+1)
        ELSE
        J=J+1
        GOTO 180
        END IF
C
        C6(I)=Y11+(Y22-Y11)/(X22-X11)*(C3(I)-X11)
C                                          C6: MOLD COMPLIANCE
        H(I)=(C6(I)-C4(I))/TLVDT
C                                          H: HEIGHT (IN)
        AX(I)=3.0*H(I)
C                                          AX: AREA IN X DIRECTION (IN*IN)
C                                                (MOLD LENGTH: 3.0 IN)
        VF(I)=(WF/DEN)/(H(I)*AREA*0.0254**3)
C                                          [VOLUME FROM IN*3 TO M*3]
        FORCE(I)=(Z11-C5(I))*GAGE
C                                          FORCE: TOTAL FORCE IN X DIRECTION
C                                          (IN GRAMS!)
        S11(I)=1.0/EF/VF(I)/0.9
C                                          S11: COMPLIANCE IN X DIRECTION
        IF(I.NE.1) THEN
```

```
                  S12(I)=FORCE(I)/453.6/AX(I)/C3(I)*S11(I)
          ELSE
                  S12(I)=1.0E10
          END IF
C                                         C3: FORCE IN TRANSVERSE DIRECTION
C         --- PLOTTING OUTPUT ---
C
          FIG(1,I)=H(1)-H(I)
          FIG(2,I)=VF(I)
          FIG(L,I)=FORCE(I)
          WRITE(7,*)I,VF(I),LOG(VF(I)),S12(I),LOG(S12(I))
150       CONTINUE
C
c         DO 250 I=40,80
c         I1=I-39
c         FIG(1,I1)=0.01*FLOAT(I)
c         FIG(2,I1)=0.0156/34.0E6/(FIG(1,I1))**5.94
250       CONTINUE
C
C         ISCL=-2
          CALL QPICTR(FIG,9,N2,QY(L),QX(2),QLABEL(IDT),QISCL(ISCL),
          1        QXSCL(XSCL),QXLAB(XL),QYLAB(YL))
C
c         CALL QPICTR(FIG,9,I1,QY(2),QX(1),QLABEL(IDT),QISCL(ISCL),
c         1        QXSCL(XSCL),QXLAB(XL),QYLAB(YL))
800       CONTINUE
C
          STOP
          END
```

APPENDIX D

Data of Micro-structure Development in Molding

Test data for Fig. 5-15

LAMINATE CONSOLIDATION EXPERIMENT DATA (1)

Data File: lami-1.dat   Date: 12-16-1988

Note: All weights are in grams!

Layer 1: Bottom layer; Layer 4: Top layer

Layer	Initial Weight	Final Weight	Vf
1	4.11	3.71	.5904449
2	4.12	3.67	.6045778
3	4.12	3.64	.6136338
4	4.14	3.56	.6445775

Material constants:

$(V_f)_o$ = 0.495 ρ_f = 1.78 (g/cm^3) ρ_r = 1.26 (g/cm^3)
W_b = 1.13 (g) [Weight of backing paper]

Other Weights:

	Initial	Final
Peel Ply	0.78	0.78
Teflon	1.20	1.20
Bleeder	5.10	6.95

Initial total weight:	23.57
Final total weight:	23.51
Total resin loss in composite:	1.91
Total resin gain in peel ply, bleeder & teflon sheets:	1.85

Total Weight Loss or Gain: -.255 %

LAMINATE CONSOLIDATION EXPERIMENT DATA (2)

Data File: lami-2.dat   Date: 12-19-1988

Note: All weights are in grams!

Layer 1: Bottom layer; Layer 4: Top layer

Layer	Initial Weight	Final Weight	Vf
1	4.10	3.69	.5937018
2	4.12	3.66	.6075666
3	4.13	3.61	.6255868
4	4.14	3.57	.6412366

Material constants:

$(V_f)_o = 0.495$ $\rho_f = 1.78$ (g/cm^3) $\rho_r = 1.26$ (g/cm^3)
$W_b = 1.13$ (g) [Weight of backing paper]

Other Weights:

	Initial	Final
Peel Ply	0.78	0.78
Teflon	1.20	1.20
Bleeder	5.11	6.93

Initial total weight:	23.58
Final total weight:	23.44
Total resin loss in composite:	1.96
Total resin gain in peel ply, bleeder & teflon sheets:	1.82

Total Weight Loss or Gain: -.594 %

236

LAMINATE CONSOLIDATION EXPERIMENT DATA (3)

Data File: lami-3.dat   Date: 12-20-1988

Note: All weights are in grams!

Layer 1: Bottom layer; Layer 4: Top layer

Layer	Initial Weight	Final Weight	Vf
1	4.13	3.69	.6011868
2	4.12	3.64	.6136338
3	4.14	3.62	.625039
4	4.14	3.57	.6412366

Material constants:

$(V_f)_o = 0.495$ $\rho_f = 1.78$ (g/cm^3) $\rho_r = 1.26$ (g/cm^3)
$W_b = 1.13$ (g) [Weight of backing paper]

Other Weights:

	Initial	Final
Peel Ply	0.78	0.78
Teflon	1.20	1.20
Bleeder	5.11	6.96

Initial total weight:	23.62
Final total weight:	23.46
Total resin loss in composite:	2.01
Total resin gain in peel ply, bleeder & teflon sheets:	1.85

Total Weight Loss or Gain: -.677 %

LAMINATE CONSOLIDATION EXPERIMENT DATA (4)

Data File: lami-4.dat   Date: 12-23-1988

Note: All weights are in grams!

Layer 1: Bottom layer;   Layer 4: Top layer

Layer	Initial Weight	Final Weight	Vf
1	4.10	3.68	.5966031
2	4.12	3.66	.6075666
3	4.11	3.62	.6172226
4	4.13	3.55	.6452273

Material constants:

$(V_f)_o = 0.495$ $\rho_f = 1.78$ (g/cm^3) $\rho_r = 1.26$ (g/cm^3)
$W_b = 1.13$ (g) [Weight of backing paper]

Other Weights:

	Initial	Final
Peel Ply	0.78	0.78
Teflon	1.20	1.20
Bleeder	5.09	6.94

Initial total weight:	23.53
Final total weight:	23.43
Total resin loss in composite:	1.95
Total resin gain in peel ply, bleeder & teflon sheets:	1.85

Total Weight Loss or Gain: -.425 %

LAMINATE CONSOLIDATION EXPERIMENT DATA (5)

Data File: lami-5.dat   Date: 12-27-1988

Note: All weights are in grams!

Layer 1: Bottom layer;   Layer 4: Top layer

Layer	Initial Weight	Final Weight	Vf
1	4.10	3.67	.5995333
2	4.12	3.65	.6105851
3	4.12	3.62	.6198235
4	4.15	3.56	.647291

Material constants:

$(V_f)_o$ = 0.495 ρ_f = 1.78 (g/cm^3) ρ_r = 1.26 (g/cm^3)
W_b = 1.13 (g) [Weight of backing paper]

Other Weights:

	Initial	Final
Peel Ply	0.78	0.78
Teflon	1.20	1.20
Bleeder	5.09	6.96

Initial total weight:	23.56
Final total weight:	23.44
Total resin loss in composite:	1.99
Total resin gain in peel ply, bleeder & teflon sheets:	1.87

Total Weight Loss or Gain: -.509 %

BASIC Program for V_f Calculation

```
10 'PROGRAM: VF.BAS '
20 ' '
30 '    THIS PROGRAM CALCULATES THE VF VALUE FROM THE MEASURED WEIGHT AND '
40 '  OTHER VALUES FROM THE DATA OF THE LAMINATE CONSOLIDATION EXPERIMENT.'
50 ' '
60 '  PARAMETERS OF THE LAMINATE CONSOLIDATION EXPERIMENT: '
70 '  PLY NUMBER: 1 AT BOTTOM & N AT TOP      MOLD AREA: 4(IN)*4.5(IN) '
80 '  PREPREG: AS4/3501-6  [RESIN WEIGHT PERCENT: 42%] '
90 ' '
100    VF0=.495 : LUF=1.78 : LUR=1.26 : BP=1.13
110 '  LUF: GRAM/CM^3;   LUR: GRAM/CM^3;   BP: GRAM '
120 INPUT"INPUT DATA FILE NAME";FILE$
130 ' '
140 OPEN FILE$ FOR OUTPUT AS #1
150 PRINT #1,"EXPERIMENT DATA:","(";FILE$;")",DATE$
160 PRINT #1,
170 PRINT #1,"Note: All weights are in grams!"
180 PRINT #1,
190 PRINT #1,"Layer     Initial Weight     Final Weight     Vf"
200 CLS : INPUT "HOW MANY LAYERS";N
210 PRINT
220 PRINT "THE AVERAGE WEIGHT OF BACK PAPER IS 1.13 (g)."
230 INPUT"IF YOU WANT TO CHANGE, INPUT Y";A$
240 IF A$="y" OR A$="Y" THEN INPUT"INPUT BACK PAPER WEIGHT (g)";BP
250 PRINT
260 SUM1=0 : SUM2=0
270 FOR I=1 TO N
280 PRINT "LAYER";I
290 INPUT "INITIAL WEIGHT (INCLUDING BACKING PAPER)";M0(I)
300 INPUT "FINAL WEIGHT (INCLUDING BACKING PAPER)";M(I)
310 'M & M0 ARE IN GRAMS '
320 SUM1=SUM1+M0(I) : SUM2=SUM2+M(I)
330 MF=(M0(I)-BP)*VF0*LUF/((1!-VF0)*LUR+VF0*LUF)
340 VF(I)=MF*LUR/(MF*LUR+(M(I)-BP-MF)*LUF)
350 PRINT "VF=";VF(I) : PRINT
360 PRINT #1,I,M0(I),M(I),VF(I)
370 NEXT I
380 PRINT #1,
390 PRINT "NOTE: VF0=";VF0;"   LUF=";LUF;"(G/CM^3)    LUR=";LUR;"(G/CM^3)"
400 PRINT #1,"Note: Vf0=";VF0;"    Luf=";LUF;"(g/cm^3)
Lur=";LUR;"(g/cm^3)"
410 PRINT "BP=";BP;"(G)" : PRINT
420 PRINT #1,"Bp=";BP;"(g)" : PRINT #1,
430 INPUT"INITIAL WEIGHT OF THE PEEL PLY";PEEL1
440 INPUT"FINAL WEIGHT OF THE PEEL PLY";PEEL2
450 PRINT
460 INPUT"INITIAL WEIGHT OF THE POROUS TEFLON SHEETS";TEF1
470 INPUT"FINAL WEIGHT OF THE POROUS TEFLON SHEETS";TEF2
480 PRINT
490 INPUT"INITIAL WEIGHT OF THE BLEEDERS";BLEE1
500 INPUT"FINAL WEIGHT OF THE BLEEDERS";BLEE2
```

```
510 PRINT
520 PRINT #1,"Weight","Initial","Final"
530 PRINT #1,"Peel Ply",PEEL1,PEEL2
540 PRINT #1,"Teflon",TEF1,TEF2
550 PRINT #1,"Bleeder",BLEE1,BLEE2
560 PRINT #1,
570 SUM3=PEEL1+TEF1+BLEE1
580 SUM4=PEEL2+TEF2+BLEE2
590 TOTAL1=SUM1+SUM3
600 TOTAL2=SUM2+SUM4
610 PRINT "INITIAL TOTAL WEIGHT=";TOTAL1,"FINAL TOTAL WEIGHT=";TOTAL2
620 PRINT #1,"INITIAL TOTAL WEIGHT=";TOTAL1,"FINAL TOTAL WEIGHT=";TOTAL2
630 PRINT
640 PRINT "TOTAL RESIN LOSS IN COMPOSITE=";SUM1-SUM2
650 PRINT #1,"TOTAL RESIN LOSS IN COMPOSITE=";SUM1-SUM2
660 PRINT "TOTAL RESIN GAIN IN PEEL PLY, BLEEDER & TEFLON SHEETS=";SUM4-
SUM3
670 PRINT #1,"TOTAL RESIN GAIN IN PEEL PLY, BLEEDER & TEFLON SHEETS=";SUM4-
SUM3
680 PRINT : PRINT #1,
690 PRINT #1,"WEIGHT LOSS (OR GAIN): ";(TOTAL2-TOTAL1)/TOTAL1*100!;"%"
700 PRINT #1,
710 CLOSE #1 : END
```

APPENDIX E

Force Sensor Made with Strain Gages in Experiments

As shown in Fig. E-1, the force sensor used for measuring the S_{1b} term and for monitoring the winding tension was made with 2 sets of 4 strain gages mounted on an extended octagonal ring. These two sets of strain gages were mounted at specific positions for measuring loads parallel and transverse to the sensor surface separately. Two different wiring diagrams are also shown in Fig. E-1. Detailed discussion of this kind of force sensor was given in [E-1]. We will briefly discuss the sensitivity and force component separation here.

In the experiment for measuring the S_{1b} term, fiber induced load was transverse to the sensor top plane, as shown in Fig. 5-8. There were thousands of fibers in contact with the sensor surface. In the test the total load induced by fiber bundle was measured. This required that the sensor not only provided high sensitivity in the loading direction, but would also gave out correct load reading even when the total load was not exactly centered.

In the wet filament winding simulation experiments, fiber tows were guided through rollers mounted on the sensor, and the tow moving direction was changed from vertical to horizontal. This sensor can separate the vertical load from the horizontal load, which made possible the winding tension monitoring. This set up is shown in Fig. 5-19.
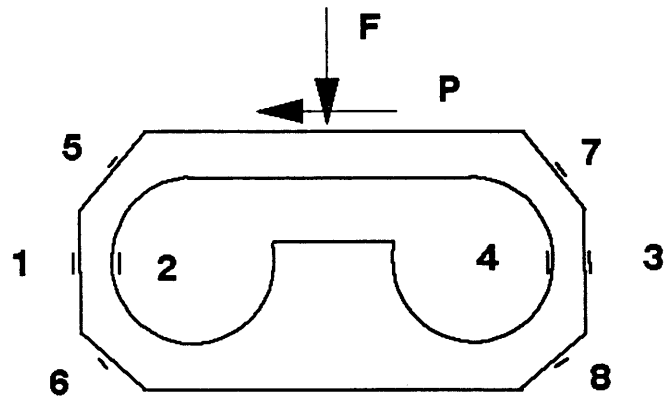
EXTENDED OCTAGONAL RING
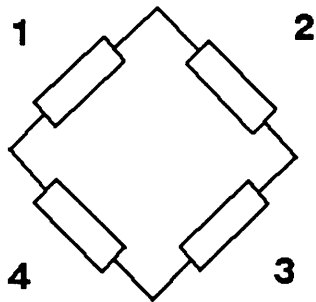
F CIRCUIT
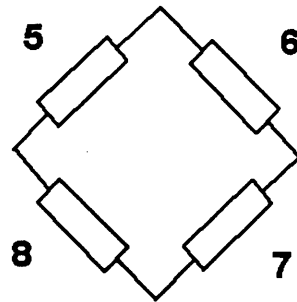
P CIRCUIT

Fig. E-1: Force sensor made with strain gages

The sensitivity of the strain gage circuit is defined in [E-2] as

$$S_c = \Delta E / \epsilon \tag{E-1}$$

where ΔE is the output voltage, and ϵ is the strain. For a Wheatstone bridge circuit, as shown in Fig. E-1, we can calculate ΔE as

$$\Delta E = \frac{V}{4} \left(\frac{\Delta R_1}{R_1} - \frac{\Delta R_2}{R_2} + \frac{\Delta R_3}{R_3} - \frac{\Delta R_4}{R_4} \right) \tag{E-2}$$

where V is the excitation voltage, and all resistors are 120 Ω in our set up. This relation is true if the change of resistance is small, which is satisfied in our experiments. The arrangement of strain gages in the force sensor ensured that gages 1 and 3 were on the tension stress side, and gages 2 and 4 were on the compression stress side, when the transverse load was applied. Thus maximum sensitivity was achieved.

For force component separation, we first consider a ring device such as shown in Fig. E-2. The top and the bottom of the ring are restrained from rotation. Force components F and P are applied to the ring. Consider one-half of the ring with load as shown. The bending moment M_θ at any point of the ring is

$$M_\theta = M_o + \frac{Fr}{2} \sin \theta + \frac{Pr}{2} (1 - \cos \theta) \tag{E-3}$$

where r is the radius of the ring, θ is shown in the figure, and M_o is the moment at $\theta = 0$. The total strain energy due to bending is

$$U = \frac{1}{2EI} \int_0^\pi M_\theta^2 \, r \, d\theta \tag{E-4}$$
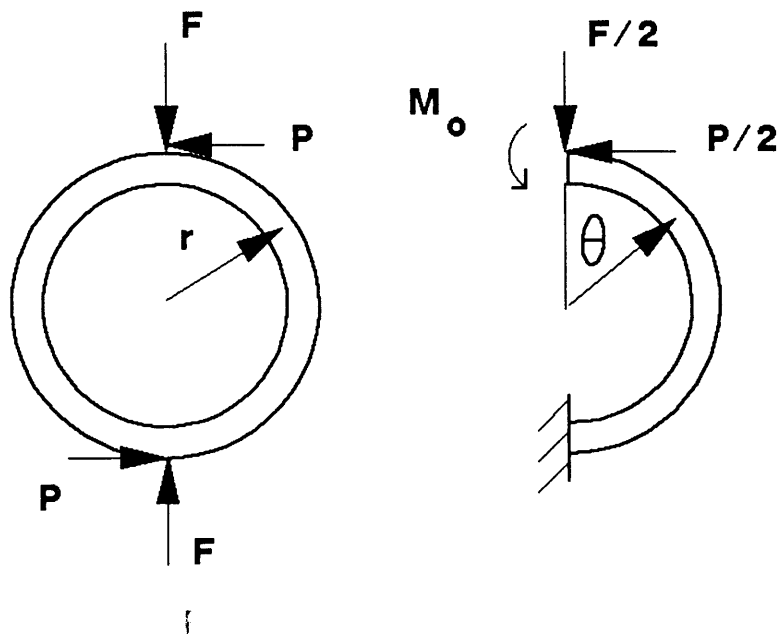
Fig. E-2: Analysis of the ring device

The angular rotation of the ring at $\theta=0$ is 0. This gives

$$\left(\frac{\partial U}{\partial M_o}\right)_{\theta=0} = 0 = \frac{1}{EI} \int_0^\pi M_\theta \frac{\partial M_\theta}{\partial M_o} r \, d\theta \qquad (E\text{-}5)$$

By substituting (E-3) into (E-5), we can solve for M_o as

$$M_o = -\frac{Fr}{\pi} - \frac{Pr}{2} \qquad (E\text{-}6)$$

The bending moment can be solved as

$$M_\theta = \frac{Fr}{2}\left(\sin \theta - \frac{2}{\pi}\right) - \frac{Pr}{2}\cos \theta \qquad (E\text{-}7)$$

From this expression we find that for certain θ values the contribution of either F or P can be eliminated. If we let $\sin \theta = 2/\pi$, or $\theta = 39.6°$, the moment due to F is zero. If we let $\cos \theta = 0$, or $\theta = 90°$, the moment due to P is zero. Therefore these two points are special strain nodes for each component. If we mount strain gages at these points, we can measure these force components separately.

The extended octagonal ring used in these experiments increased the stability but still kept the same function to separate force components as a simple ring. In the measurement, the output is independent of the location of the force. For example, if the transverse load was not centered in the S_{1b} measurement, the total load was still the same although the load carried by the left half or the right half would change. Since the Wheat-

stone bridge circuit used all four strain gages, the output was propor-
tional to the sum of all strains, or the total load.

In the experiments, this extended octagonal ring force sensor was
first calibrated by applying known forces to it in two different direc-
tions. The calibration data are shown in Fig. E-3 and E-4 respectively.
Since the output voltage from the strain gage circuit was very small, an
amplifier or strain gage indicator was used in different experiments. In
both directions the voltage responses to the input force showed good linear
relations.

References

E-1. Cook, N.H., and Rabinowicz, E., Physical Measurement and Analysis,
Addison-Wesley, Reading, Mass., 1963, pp. 160-165.

E-2. Dally, J.W., and Riley, W.F., Experimental Stress Analysis, McGraw-
Hill, New York, 1978, pp. 229-235.
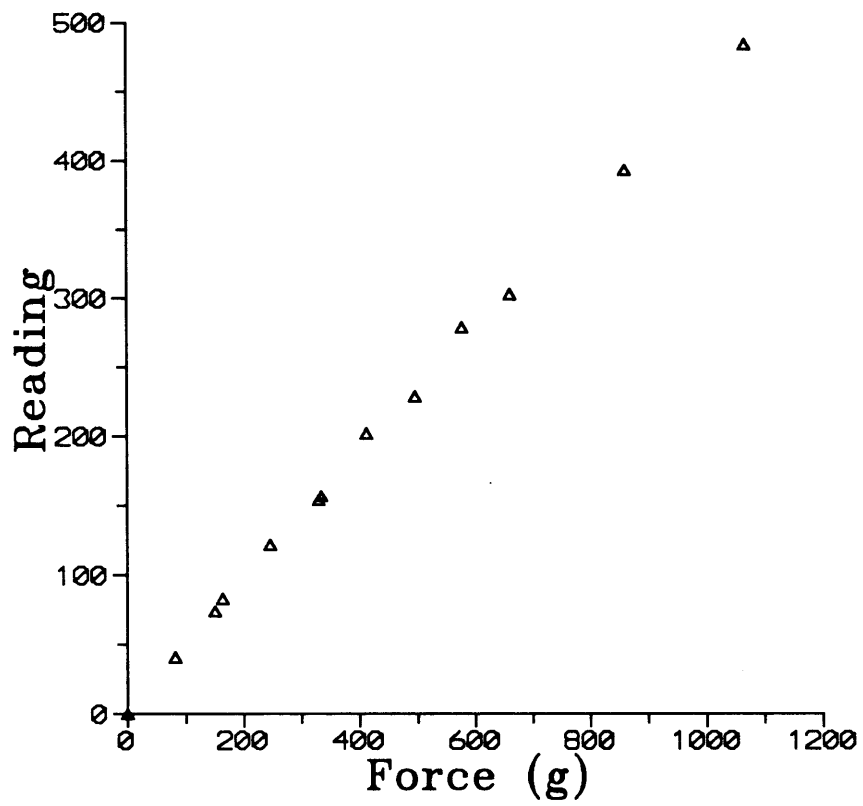
Fig. E-3: Calibration data in the transverse direction
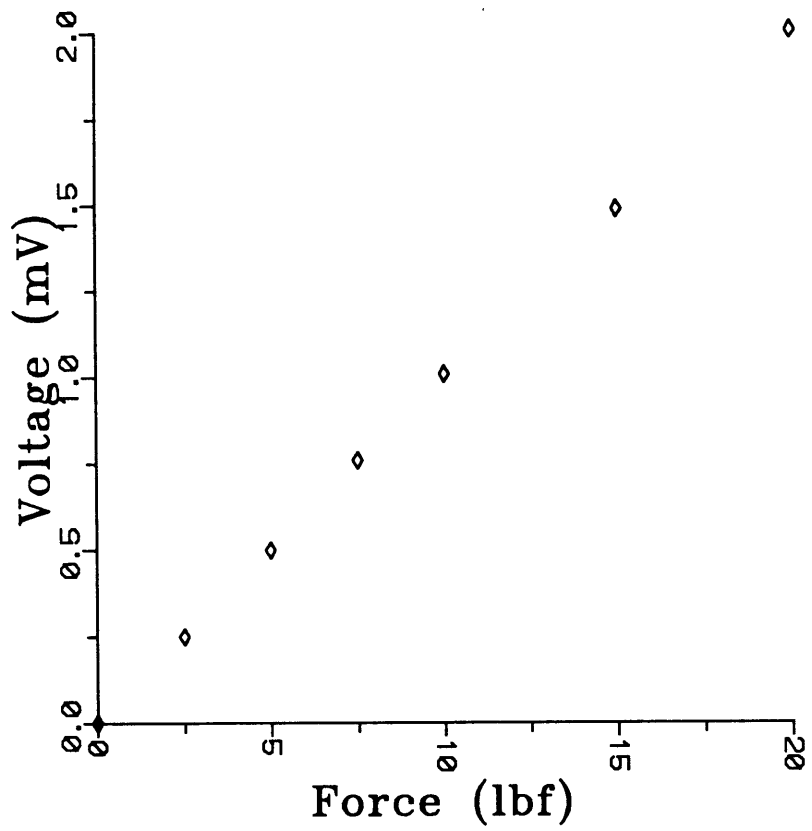
Fig. E-4: Calibration data in the parallel direction

APPENDIX F

Force Sensor Resistor for Transverse Load Measurement

In the winding and consolidation simulation experiments, flat shape force sensor resistors were used for measuring the load which was transverse to the layer surface. They were supplied by Interlink Electronics. Fig. F-1 shows the structure of these sensor resistors. These sensors were bonded onto the mandrel surface to measure the total radial pressure. The size of the sensor was 0.25 inch by 0.25 inch with the thickness of only 0.01 inch. Therefore the embedded sensors did not disturb the wound structure. The no-load resistance of the sensor was very high and on the order of tens of megohms. When a small load was applied transverse to the sensor surface, the resistance dropped dramatically. The sensor can have a varying resistance over three decades depending on the applied force. By using this unique characteristics of the sensor, we can build a circuit for the transverse load measurement, as shown in Fig. F-1.

One problem in using this kind of sensor was the nonlinearity of the sensor response. Thus there were more and less sensitive regions in the measurement. An example of the calibration data of the sensor is shown in Fig. F-2. In the calibration the circuit as shown in Fig. F-1 was used. From this calibration curve we can see that the sensitivity of the sensor, $\Delta F/\Delta V$, changed dramatically. In the low-load region a small change in the load would cause a large change in the output voltage. Thus calibration of this region became very difficult. On the other hand, in the high-load

250

FORCE SENSOR RESISTOR
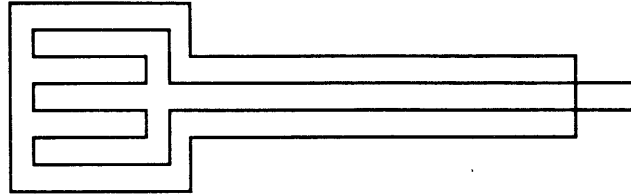
APPLICATION CIRCUIT
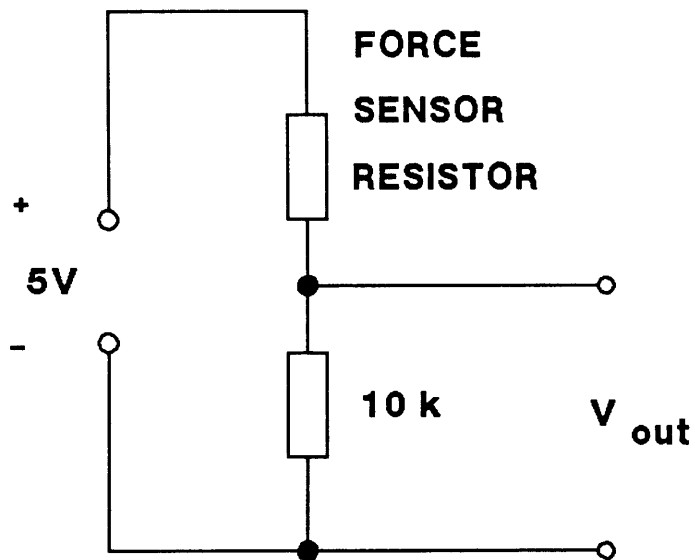
Fig. F-1: Force sensor resistor and application circuit
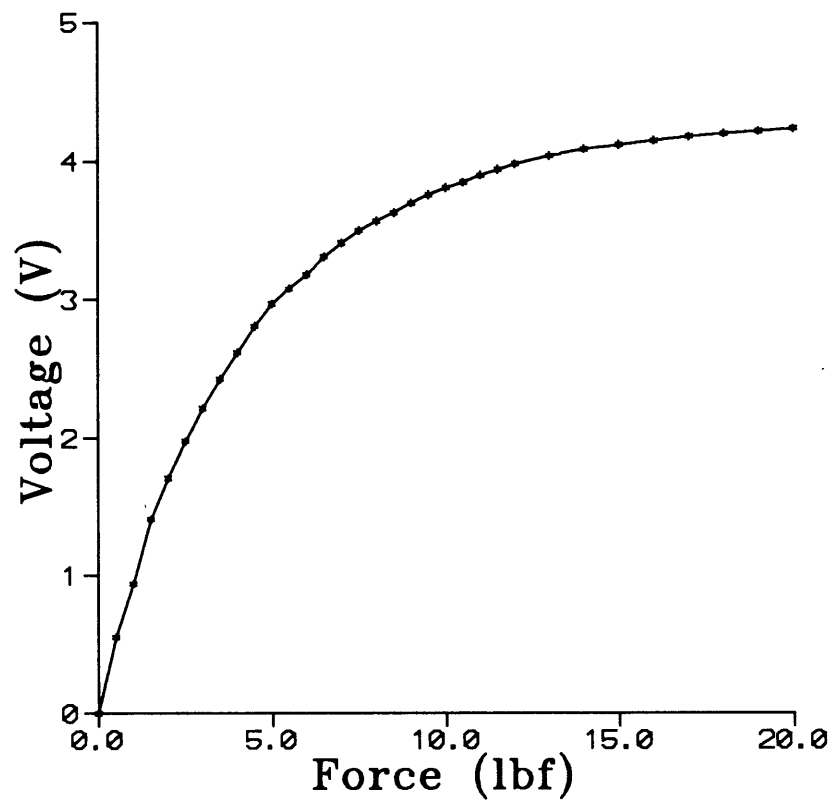
Fig. F-2: Calibration data of the force sensor resistor

region, it was difficult to interpret the measured force from the voltage signal, since any small noise signal in the voltage reading would introduce large errors in calculating the load.

The other problem in using this kind of sensor was the load distribution over the sensor surface. With a pressure transducer, the media to which the measurement was taken was fluid, so that the fluid pressure was uniformly distributed over the sensor surface. For the force sensor resistor used in the experiments, the total pressure was applied by both the fluid and the fiber tows. There were thousands of fibers in contact with the sensor surface. It could not be guaranteed that load was uniformly distributed. In the calibration it was found that the sensor was sensitive to the load distribution. When the load was applied slightly off center, the response of the sensor changed, especially in the low-load region where the resistance of the sensor changed the most. Since there was no way to predict the real loading condition in different experiments, repeated calibrations were made, and the calibration curve was determined by a nonlinear least square curve fitting over these calibration data, which was a compromise between different loading conditions.

Creep was also observed in the use of these force sensor resistors, although the effect was only a few percent. As suggested by the manufacturer, preloading was an effective way to minimize or eliminate this problem. In the calibration, force was applied repeatedly until the reading showed very stable. In other words the two consequent calibration readings showed good agreement. Usually four or five runs were needed, and conducted over a time period of about 20 to 30 minutes. Then experiments were

carried out right after these calibrations. Since the time interval be-
tween each winding or consolidation experiments was one day or a few days,
the calibration procedures of the sensor were repeated before each experi-
ment to eliminate this creep problem. Fig. F-3 shows an example of
repeated calibration data of the sensor.

Although there were shortcomings in using this kind of force sensor
resistors, the small size of the sensor, especially the thickness, was
still a unique advantage for the real time measurement of the total radial
pressure without introducing geometrical disturbance to the composite
structures.
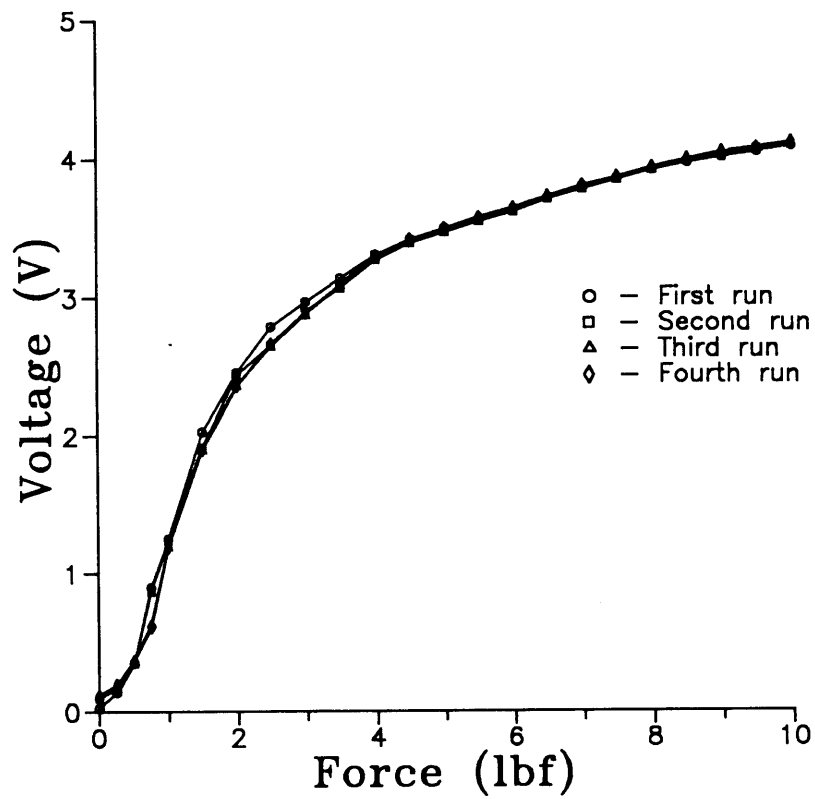
Fig. F-3: Repeated calibration data of the force sensor resistor

APPENDIX G

Fiber Volume Fraction Measurement in Winding Experiments

As mentioned in Chapter 5, two types of fiber volume fraction measurement were conducted in the winding simulation experiments, in which fiber tows and silicone fluid were used to replace the real composites. One was the initial fiber volume fraction of the tow after it went through the wetting device. This was to check the wetting effect. The other was the fiber volume fraction of each wound layer after the wet filament winding process, which would verify the relationship between the winding ten- . sion and the fiber compaction state. For the initial fiber volume fraction measurement, fiber tow samples were cut before they reached the winder. For the measurement after the winding, fiber tows were carefully unwound from the mandrel, layer by layer. Since the fluid was so viscous, there was no flow or fluid motion when the tows were unwound. After the sample was cut, the tow and fluid mixture was weighed first. The fluid was then washed off and fibers were dried and weighed again. The initial and final weight were then used to calculate the fiber volume fraction.

The calculation formula was given in (5-10), which assumed the densities of the fluid and fiber were known quantities. The formula was given as

$$V_f = \frac{1}{1 + 1.84[(w_t/w_f) - 1]} \qquad \text{(G-1)}$$

where w_t was the total weight of the fiber and fluid mixture, w_f was the fiber weight. The known fiber density ρ_f was 1.79 kg/m^3, and fluid density ρ_r was 0.971 kg/m^3. The ratio of them gave out the constant 1.84 in the expression. In the experiments we always used aluminum foils to handle the samples. These samples were weighed with the aluminum foils and then the foils were weighed again. Therefore the weight calculation was

$$w_t = w_{to} - w_{al} \tag{G-2}$$

$$w_f = w_{fo} - w_{a2} \tag{G-3}$$

where w_{to} was the initial total weight including the aluminum foil, w_{fo} was the weight including dry fibers and aluminum foil, and w_{al} and w_{a2} were the foil weights. Combining these relations, we have

$$V_f = \frac{1}{1 + 1.84 \ \{[(w_{to}-w_{al})/(w_{fo}-w_{a2})] - 1\}} \tag{G-4}$$

A short BASIC program was written based on this formula to calculate V_f for each individual layer.

<u>Initial fiber volume fraction measurement</u>

(Data of Fig. G-1)

(All weights are in grams.)

1) Data file: VF-0530A.DAT   Test date: 05-30-89

Sample	w_{to}	w_{fo}	V_f
1	0.4454	0.4382	0.497
2	0.4499	0.4406	0.475
3	0.4448	0.4385	0.536
4	0.4455	0.4381	0.488
5	0.4506	0.4417	0.503

($w_{a1}=w_{a2}=0.4253$)

2) Data file: VF-0531A.DAT   Test date: 05-31-89

Sample	w_{to}	w_{fo}	V_f
1	0.4499	0.4440	0.498
2	0.4555	0.4465	0.459
3	0.4570	0.4483	0.488
4	0.4537	0.4452	0.451
5	0.4587	0.4461	0.485

($w_{a1}=0.4253$, $w_{a2}=0.4281$)

3) Data file: VF-0531B.DAT   Test date: 05-31-89

Sample	w_{to}	w_{fo}	V_f
1	0.5074	0.4912	0.384
2	0.4971	0.4881	0.460
3	0.4956	0.4847	0.378
4	0.5068	0.4921	0.413
5	0.5011	0.4885	0.402

4) Data file: VF-0531C.DAT   Test date: 05-31-89

Sample	w_{to}	w_{fo}	w_a	V_f
1	0.6655	0.6538	0.6320	0.503
2	0.5170	0.5020	0.4805	0.438
3	0.5500	0.5403	0.5196	0.537
4	0.6184	0.6091	0.5891	0.539
5	0.6587	0.6452	0.6205	0.499

5) Data file: VF-0601A.DAT   Test date: 06-01-89

Sample	w_{to}	w_{fo}	w_a	v_f
1	0.6319	0.6222	0.6016	0.536
2	0.5393	0.5280	0.5068	0.505
3	0.5769	0.5661	0.5505	0.440
4	0.5480	0.5170	0.4786	0.402
5	0.5927	0.5580	0.5192	0.378

6) Data file: VF-0601B.DAT   Test date: 06-01-89

Sample	w_{to}	w_{fo}	w_a	v_f
1	0.5971	0.5824	0.5552	0.501
2	0.5422	0.5238	0.5029	0.382
3	0.4712	0.4514	0.4287	0.384
4	0.4600	0.4397	0.4174	0.374
5	0.4776	0.4617	0.4316	0.507
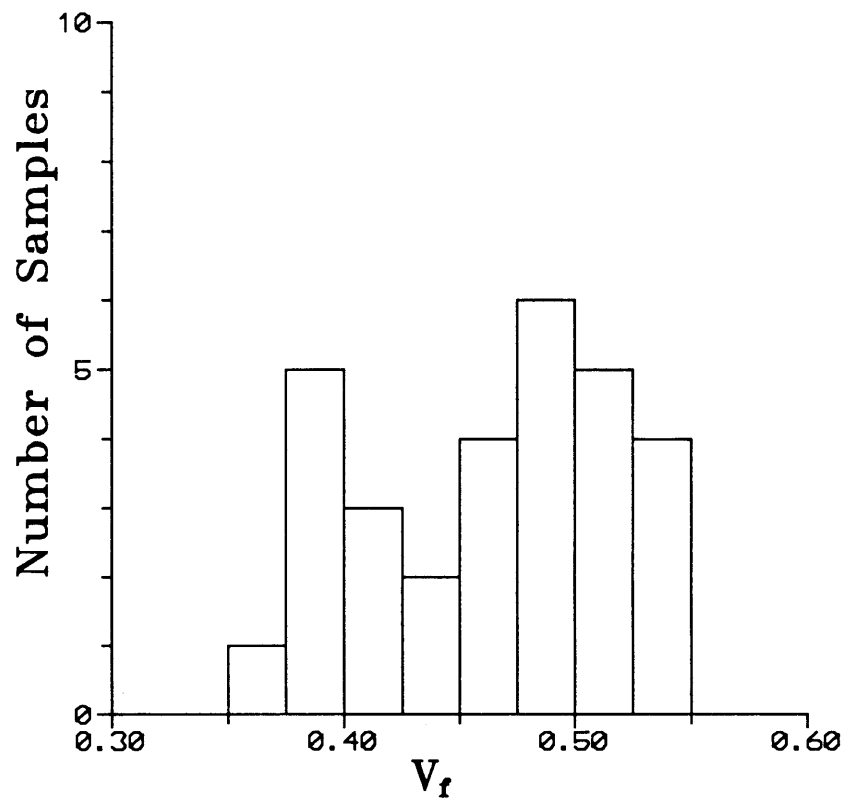
Fig. G-1: Data of initial fiber volume fraction measurement

Fiber volume fraction measurement for wound layers

(All weights are in grams.)

(Layer 1 is the inner most layer on top of the mandrel)

1) Data file: VF-0606.DAT   Test date: 06-06-89

(Test data for Fig. G-2)

Fiber: AS4 3k tow   Tension: 3 lbf/tow
Winding parameters: 45 turns/min, 65 turns/layer, 20 layers

Layer	w_{to}	w_{fo}	w_a	V_f (data)	V_f (model)
1	0.9537	0.9071	0.7303	0.673	0.6902
2	0.9441	0.8905	0.7007	0.658	0.6891
3	0.9324	0.8752	0.6837	0.645	0.6878
4	0.9380	0.8763	0.6896	0.622	0.6865
5	0.9653	0.9037	0.7267	0.610	0.6851
6	0.8539	0.7893	0.6065	0.606	0.6835
7	0.9115	0.8490	0.6675	0.612	0.6819
8	0.8421	0.7815	0.5982	0.617	0.6801
9	0.9215	0.8574	0.6730	0.610	0.6782
10	1.0277	0.9694	0.7903	0.625	0.6761
11	0.9169	0.8619	0.6929	0.625	0.6737
12	0.8873	0.8282	0.6344	0.641	0.6711
13	0.9584	0.8975	0.7069	0.630	0.6681
14	0.9617	0.8998	0.7048	0.631	0.6646
15	0.9785	0.9084	0.7285	0.582	0.6604
16	0.8578	0.8048	0.6379	0.631	0.6553
17	0.9001	0.8378	0.6579	0.611	0.6488
18	0.9160	0.8557	0.6828	0.609	0.6397
19	0.9132	0.8584	0.6993	0.612	0.6253
20	1.0110	0.8889	0.7310	0.413	0.5868
Sum of 1-19	17.5801	16.4509	13.0119	0.623	
Sum of 1-20	18.5911	17.3398	13.7429	0.610	

Fig. G-2: Data of fiber volume fraction over wound layers

2) Data file: VF-0608.DAT   Test date: 06-08-89

(Test data for Fig. G-3)

Fiber: AS4 3k tow   Tension: 10 lbf/tow
Winding parameters: 45 turns/min, 65 turns/layer, 20 layers

Layer	w_{to}	w_{fo}	w_a	V_f (data)	V_f (model)
1	1.0505	0.9971	0.7287	0.732	0.7150
2	0.8987	0.8655	0.7003	0.730	0.7141
3	0.8910	0.8528	0.6826	0.708	0.7131
4	0.9238	0.8787	0.6885	0.696	0.7120
5	0.9421	0.9003	0.7263	0.693	0.7108
6	0.8011	0.7635	0.6052	0.696	0.7096
7	0.7841	0.7474	0.5961	0.691	0.7082
8	0.8630	0.8212	0.6661	0.669	0.7067
9	0.8765	0.8333	0.6704	0.672	0.7051
10	0.9987	0.9597	0.7898	0.703	0.7033
11	0.9178	0.8712	0.6922	0.676	0.7013
12	0.8572	0.8117	0.6330	0.681	0.6990
13	0.9202	0.8763	0.7060	0.678	0.6965
14	0.9346	0.8810	0.7040	0.642	0.6934
15	0.9138	0.8705	0.7278	0.642	0.6898
16	0.8529	0.8092	0.6367	0.682	0.6854
17	0.8631	0.8207	0.6573	0.677	0.6796
18	0.8946	0.8502	0.6824	0.673	0.6716
19	0.9096	0.8606	0.6987	0.642	0.6586
20	1.0119	0.8898	0.7311	0.414	0.6212
Sum of 1-19	17.0933	16.2709	12.9921	0.684	
Sum of 1-20	18.1052	17.1607	13.7232	0.664	

263
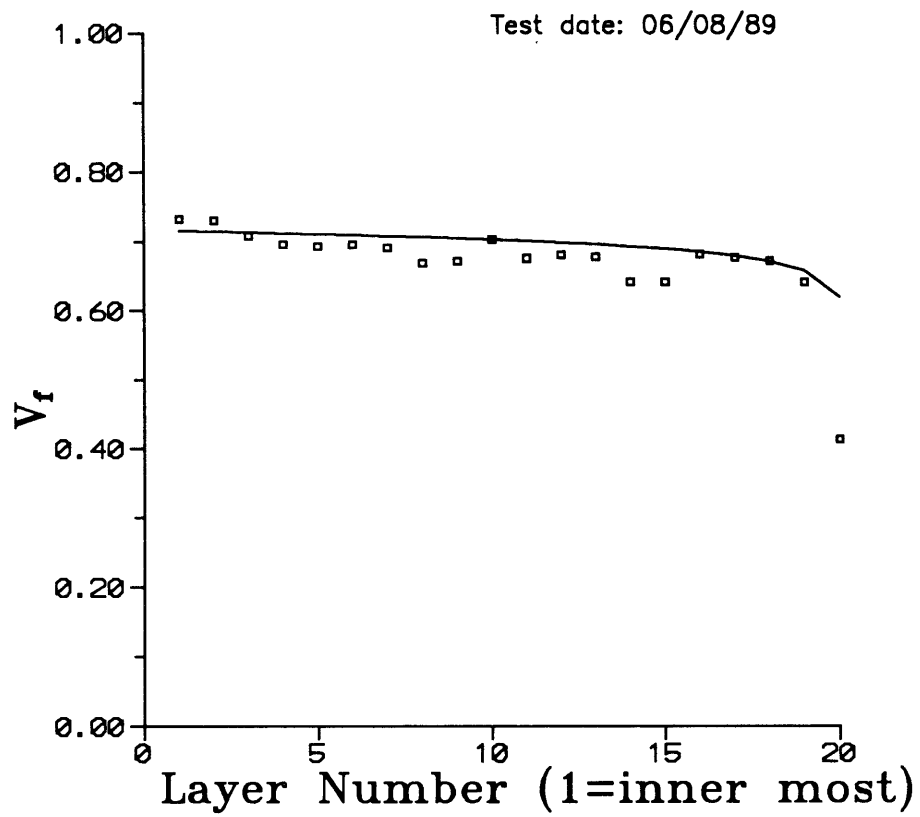
Fig. G-3: Data of fiber volume fraction over wound layers

3) Data file: VF-0616.DAT   Test date: 06-16-89

(Test data for Fig. G-4)

Fiber: AS4 3k tow   Tension: 5 lbf/tow
Winding parameters: 45 turns/min, 65 turns/layer, 20 layers

Layer	w_{to}	w_{fo}	w_a	V_f (data)	V_f (model)
1	0.9749	0.9218	0.7297	0.663	0.7015
2	0.9824	0.9207	0.7012	0.659	0.7004
3	0.9174	0.8651	0.6839	0.653	0.6993
4	0.9388	0.8864	0.6898	0.671	0.6980
5	0.9693	0.9165	0.7270	0.661	0.6967
6	0.8470	0.7951	0.6055	0.665	0.6953
7	0.8490	0.7964	0.5967	0.673	0.6938
8	0.9206	0.8687	0.6716	0.673	0.6921
9	0.9186	0.8673	0.6668	0.680	0.6904
10	1.0510	0.9959	0.7904	0.670	0.6884
11	0.9228	0.8758	0.6927	0.679	0.6861
12	0.8826	0.8302	0.6338	0.670	0.6837
13	0.9308	0.8833	0.7067	0.669	0.6808
14	0.9279	0.8817	0.7046	0.676	0.6775
15	0.9592	0.9081	0.7285	0.656	0.6736
16	0.8760	0.8244	0.6375	0.663	0.6687
17	0.8953	0.8423	0.6575	0.655	0.6625
18	0.9363	0.8782	0.6827	0.646	0.6538
19	0.9470	0.8858	0.6989	0.624	0.6399
20	1.0435	0.9129	0.7314	0.430	0.6013
Sum of 1-19	17.6469	16.6437	13.0055	0.663	
Sum of 1-20	18.6904	17.5566	13.7369	0.647	

265
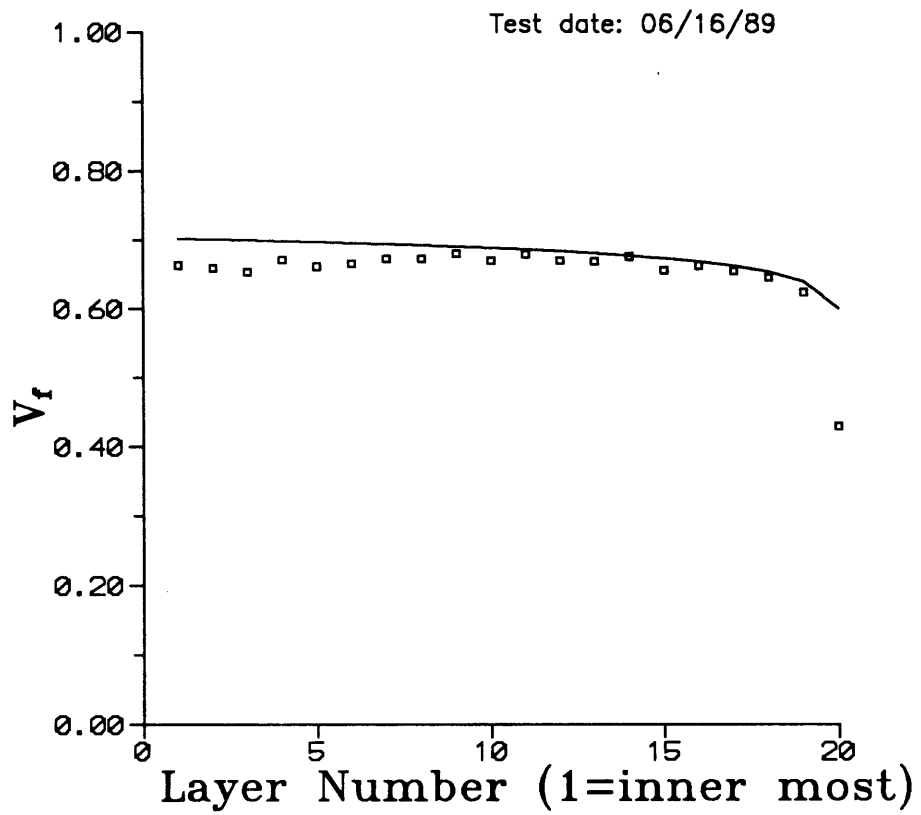
Fig. G-4: Data of fiber volume fraction over wound layers

4) Data file: VF-0620.DAT   Test date: 06-20-89

(Test data for Fig. G-5)

Fiber: AS4 3k tow   Tension: 7 lbf/tow
Winding parameters: 45 turns/min, 65 turns/layer, 20 layers

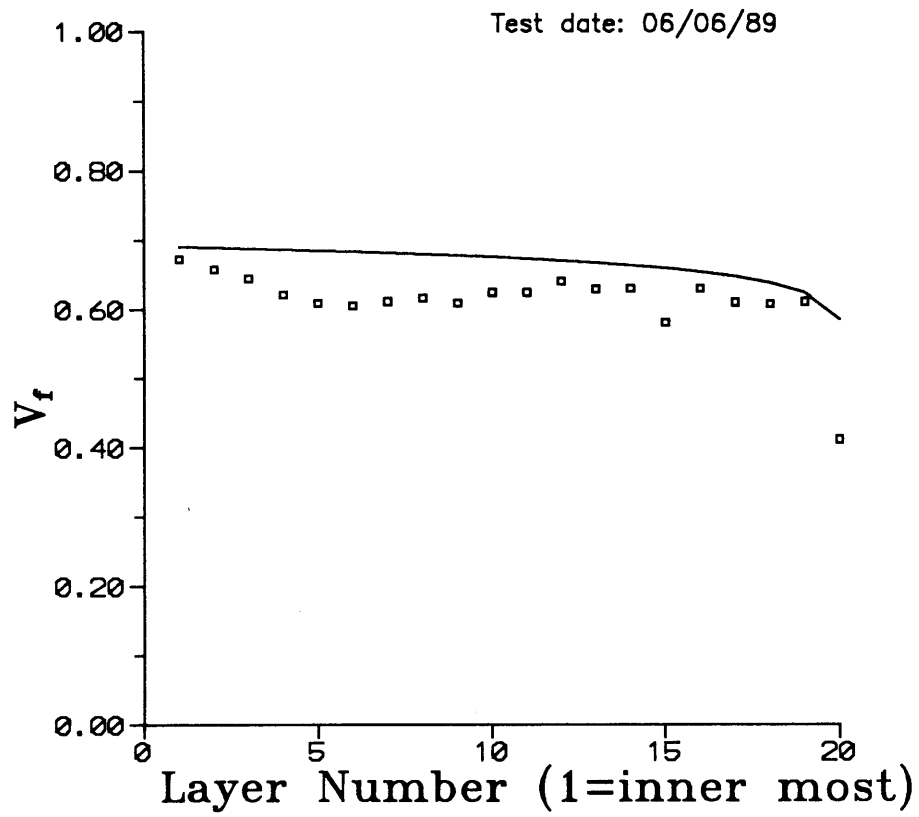| Layer	w_{to}	w_{fo}	w_a	V_f (data)	V_f (model)
1	0.9521	0.9091	0.7298	0.694	0.7083
2	0.9224	0.8815	0.7012	0.706	0.7073
3	0.9187	0.8766	0.6839	0.713	0.7062
4	0.9304	0.8858	0.6899	0.705	0.7050
5	0.9828	0.9312	0.7271	0.683	0.7038
6	0.8313	0.7887	0.6051	0.701	0.7025
7	0.8860	0.8397	0.6667	0.670	0.7010
8	0.8318	0.7823	0.5966	0.671	0.6995
9	0.8674	0.8271	0.6714	0.677	0.6977
10	1.0230	0.9745	0.7904	0.674	0.6958
11	0.9279	0.8809	0.6928	0.685	0.6937
12	0.8807	0.8307	0.6339	0.681	0.6914
13	0.9561	0.9055	0.7064	0.681	0.6886
14	0.9409	0.8925	0.7045	0.678	0.6855
15	0.9633	0.9167	0.7285	0.687	0.6817
16	0.8674	0.8184	0.6374	0.668	0.6770
17	0.8906	0.8411	0.6575	0.668	0.6710
18	0.8907	0.8475	0.6829	0.674	0.6626
19	0.9503	0.8928	0.6993	0.647	0.6491
20	1.0243	0.9135	0.7312	0.472	0.6109
Sum of 1-19	17.4140	16.5226	13.0053	0.682	
Sum of 1-20	18.4383	17.4361	13.7365	0.667	
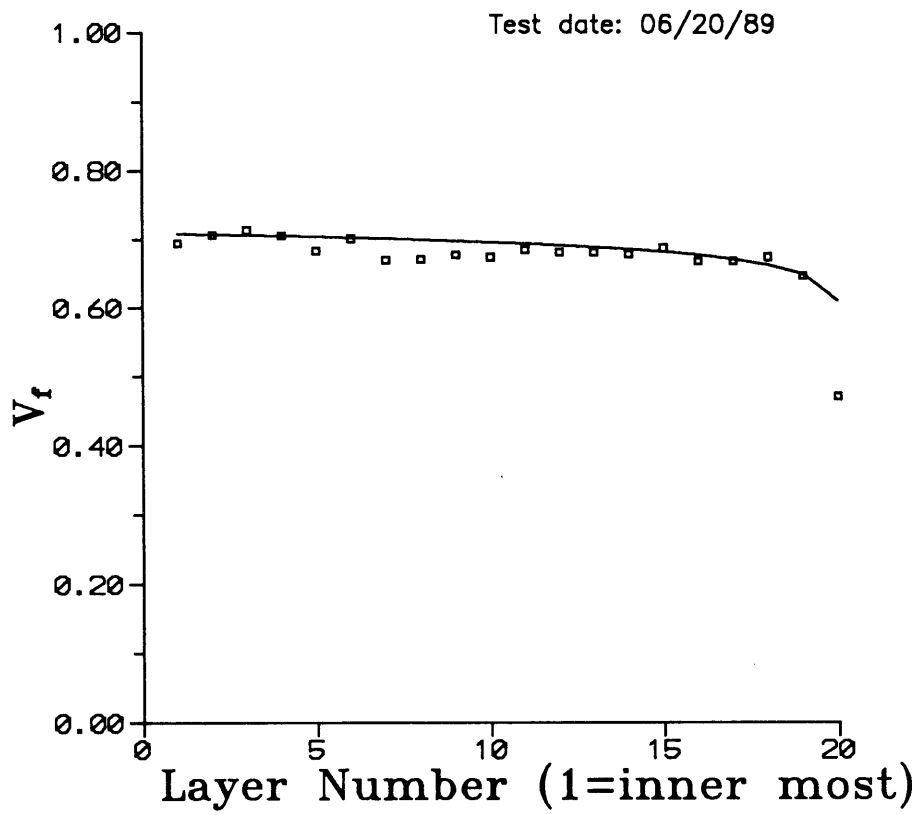
Fig. G-5: Data of fiber volume fraction over wound layers

5) Data file: VF-0622.DAT   Test date: 06-22-89

(Test data for **Fig.** 5-21)

Fiber: AS4 3k tow   Tension: 8 lbf/tow
Winding parameters: 45 turns/min, 65 turns/layer, 20 layers

Layer	w_{to}	w_{fo}	w_a	V_f (data)	V_f (model)
1	0.9592	0.9173	0.7306	0.708	0.7109
2	0.9223	0.8775	0.6842	0.701	0.7099
3	0.9449	0.9013	0.7039	0.711	0.7088
4	0.9321	0.8877	0.6907	0.707	0.7077
5	0.9450	0.9027	0.7272	0.693	0.7065
6	0.8371	0.7921	0.6052	0.693	0.7052
7	0.8379	0.7913	0.5968	0.694	0.7038
8	0.9020	0.8559	0.6671	0.697	0.7022
9	0.9107	0.8627	0.6716	0.684	0.7006
10	1.0369	0.9869	0.7907	0.681	0.6987
11	0.8741	0.8220	0.6341	0.662	0.6966
12	0.9305	0.8826	0.6927	0.683	0.6943
13	0.9586	0.9087	0.7070	0.687	0.6916
14	0.9384	0.8917	0.7048	0.685	0.6885
15	0.9743	0.9221	0.7286	0.668	0.6848
16	0.8654	0.8206	0.6375	0.689	0.6802
17	0.9043	0.8509	0.6580	0.663	0.6743
18	0.9323	0.8759	0.6828	0.650	0.6660
19	0.9437	0.8857	0.6993	0.636	0.6527
20	1.0413	0.9070	0.7313	0.416	0.6148
Sum of 1-19	17.5497	16.6356	13.0128	0.683	
Sum of 1-20	18.5910	17.5426	13.7441	0.663	

BASIC Program to calculate fiber volume fraction

```
100 'PROGRAM: VF_WIND.BAS
110 '(FOR VF CALCULATION)
120 '
130 DIM WT(50), WF(50), WTO(50), WFO(50), WAL(50), VF(50)
140 INPUT "INPUT LAYER NUMBER";NUM
150 FOR I=1 TO NUM
160 GOSUB 400
170 NEXT I
180 PRINT "NUMBER","W(BEFORE)","W(AFTER)","W(FOIL)","VF"
190 FOR I=1 TO NUM
200 PRINT I,WTO(I),WFO(I),WAL(I),VF(I)
210 NEXT I
220 PRINT
230 INPUT "DATA ALL RIGHT (Y/N)";Z$
240 IF Z$="N" OR Z$="n" THEN 270
250 IF Z$="Y" OR Z$="y" THEN 300
260 GOTO 230
270 INPUT "WHICH LAYER IS WRONG";L
280 I=L : GOSUB 400
290 GOTO 190
300 INPUT"DATA FILE";DF$
310 OPEN "O", 1,DF$
320 PRINT #1, "DATA FILE:";DF$,"DATE:";DATE$ : PRINT #1,
330 PRINT #1,"NUMBER","W(BEFORE)","W(AFTER)","W(FOIL)","VF" : PRINT #1,
340 FOR I=1 TO NUM
350 PRINT #1,I,WTO(I),WFO(I),WAL(I),VF(I)
360 NEXT I
370 CLOSE #1
380 END
390 '
400 '--- CALCULATION ---'
410 PRINT "NUMBER";I
420 INPUT "INPUT WEIGHT: W(BEFORE), W(AFTER), W(FOIL)";WTO(I),WFO(I),WAL(I)
430 WT(I)=WTO(I)-WAL(I)
440 WF(I)=WFO(I)-WAL(I)
450 VF(I)=1!/(1!+1.84*(WT(I)/WF(I)-1!))
460 PRINT "VF=";VF(I) : PRINT
470 RETURN
```

APPENDIX H

Experimental Data of Time Constant Evaluation

Batch 1: Data of winding with AS4 3k tows

a) Date: 06/05/89 (Test data of Fig. H-1 and Fig. H-2)

Tension: 3 lbf/tow   65 tows/layer   45 turns/min
Silicone fluid: 10,000 cst

Layer	Fluid Pressure (mV) (1 psi = 0.857 mV)	Thickness (0.001 in) (min)	(max)
0	11.904	9	19
1	11.938	12	22
2	12.008	20	30
3	12.085	26	36
4	12.162	33	43
5	12.251	40	50
6	12.284	46	56
7	12.315	53	63
8	12.342	60	70
9	12.368	65	75
10	12.393	72	82
11	12.403	79	89
12	12.411	87	97
13	12.419	93	103
14	12.426	101	111
15	12.434	106	116
16	12.445	112	122
17	12.458	118	130
18	12.471	125	136
19	12.485	131	142
20	12.495	138	149

Stop winding at 3:00 pm.

Time		Fluid pressure (mV)	Thickness (0.001 in)
3:05	pm	12.511	141
3:10		12.533	139
3:15		12.562	137
3:20		12.583	136
3:25		12.594	135.6
3:30		12.613	135.1
3:45		12.636	134.7
4:00		12.640	134.3
4:15		12.629	134.2
4:30		12.594	134.1
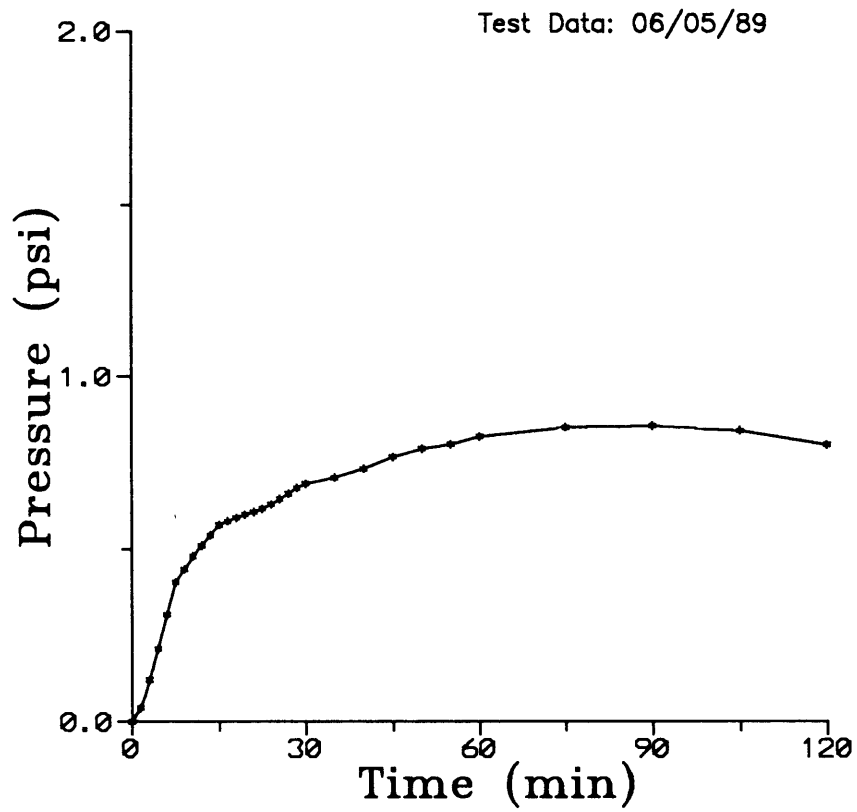
Fig. H-1: Fluid pressure data in winding of 3k size fiber tow

Fig. H-2: Layer thickness data in winding of 3k size fiber tow

b) Date: 06/08/89 (Test data of Fig. H-3 and Fig. 5-23)

Tension: 10 lbf/tow   65 tows/layer   45 turns/min
Silicone fluid: 10,000 cst

Layer	Fluid Pressure (mV) (1 psi = 0.857 mV)	Thickness (0.001 in) (min)	(max)
0	12.000	22	34
1	12.018	27	38
2	12.047	34	46
3	12.081	38	49
4	12.117	45	56
5	12.151	49	61
6	12.184	56	69
7	12.207	61	74
8	12.230	69	82
9	12.247	74	86
10	12.266	81	92
11	12.285	86	97
12	12.305	93	106
13	12.322	99	112
14	12.337	105	117
15	12.354	111	123
16	12.369	117	129
17	12.388	123	135
18	12.399	129	141
19	12.411	135	147
20	12.427	142	155

Stop winding at 11:00 am.

Time		Fluid pressure (mV)	Thickness (0.001 in)
11:10	am	12.435	146.6
11:20		12.472	146.5
11:30		12.542	146.5
11:45		12.661	146.4
12:00	pm	12.734	146.4
1:00		12.974	146.3
1:30		13.021	146.3
2:00		13.050	146.2
2:30		13.072	146.2
3:00		13.082	146.1
3:30		13.061	146.1
4:00		13.031	146.1
4:30		13.024	146.1
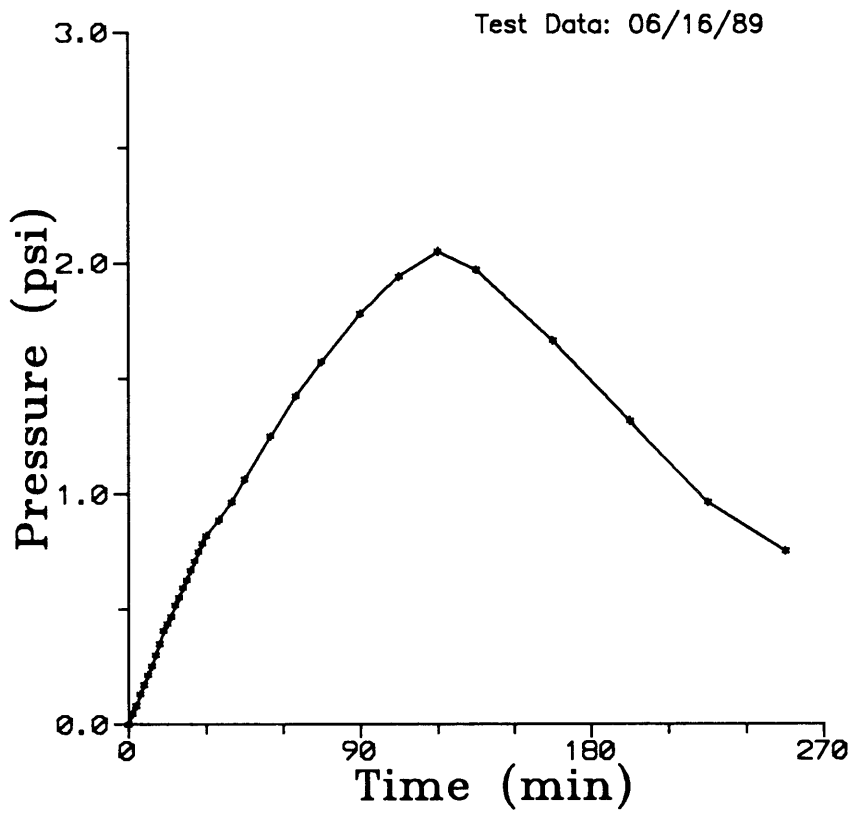
Fig. H-3: Fluid pressure data in winding of 3k size fiber tow

c) Date: 06/16/89 (Test data of Fig. H-4 and Fig. H-5)

Tension: 5 lbf/tow   65 tows/layer   45 turns/min
Silicone fluid: 10,000 cst

Layer	Fluid Pressure (mV) (1 psi = 0.857 mV)	Thickness (0.001 in) (min)	(max)
0	11.908	50	62
1	11.948	57	68
2	11.978	66	78
3	12.021	71	82
4	12.056	78	88
5	12.093	84	96
6	12.126	90	101
7	12.168	100	110
8	12.209	105	116
9	12.257	110	122
10	12.283	116	127
11	12.311	123	135
12	12.353	130	140
13	12.381	137	149
14	12.416	142	154
15	12.446	148	160
16	12.481	153	166
17	12.514	160	172
18	12.550	167	179
19	12.582	174	185
20	12.611	179	191

Stop winding at 11:15 am.

Time		Fluid pressure (mV)	Thickness (0.001 in)
11:15	am	12.611	179.5
11:20		12,670	178.2
11:25		12.737	177.6
11:30		12.821	177.5
11:40		12.981	177.1
11:50		13.130	177.0
12:00	pm	13.257	177.0
12:15		13.435	177.0
12:30		13.572	177.0
12:45		13.665	176.9
13:00		13.597	176.9
13:30		13.336	176.9
14:00		13.038	176.9
14:30		12.736	176.8
15:00		12.554	176.8
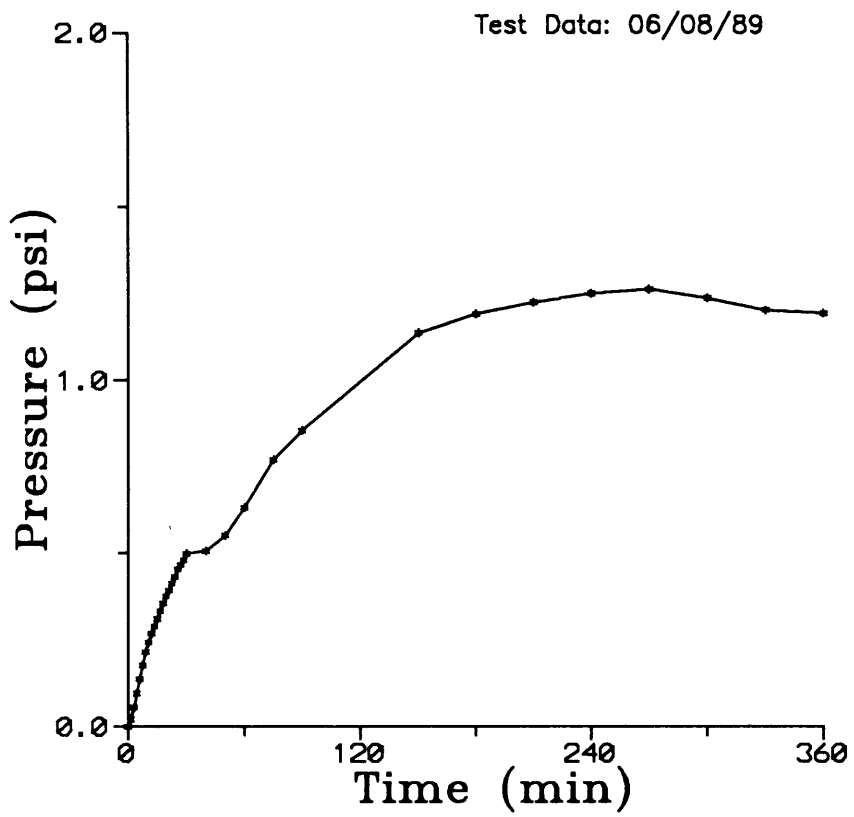
Fig. H-4: Fluid pressure data in winding of 3k size fiber tow
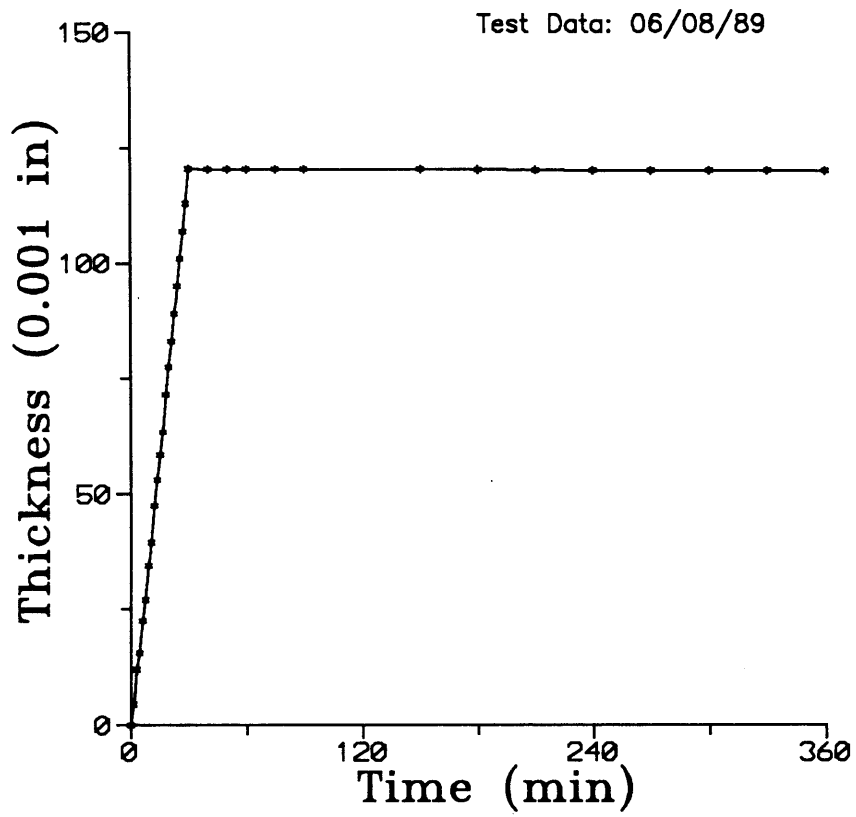
Fig. H-5: Layer thickness data in winding of 3k size fiber tow

d) Date: 06/20/89 (Test data of Fig. H-6 and Fig. H-7)

Tension: 7 lbf/tow   65 tows/layer   45 turns/min
Silicone fluid: 10,000 cst

Layer	Fluid Pressure (mV) (1 psi = 0.857 mV)	Thickness (0.001 in) (min)	(max)
0	11.878	30	41
1	11.895	34	45
2	11.941	43	54
3	11.970	46	59
4	12.201	53	65
5	12.056	60	71
6	12.089	66	77
7	12.122	70	82
8	12.148	78	90
9	12.173	84	96
10	12.199	91	102
11	12.220	96	108
12	12.242	105	116
13	12.270	112	122
14	12.295	118	129
15	12.321	124	136
16	12.351	129	140
17	12.380	136	145
18	12.411	142	153
19	12.439	146	158
20	12.468	154	165

Stop winding at 8:00 pm.

| Time		Fluid pressure (mV)	Thickness (0.001 in)
8:00	pm	12.470	163.6
8:20		12.773	162.9
8:40		13.011	162.8
9:00		13.193	162.7
9:20		13.328	162.6
9:40		13.440	162.6
10:00		13.291	162.6
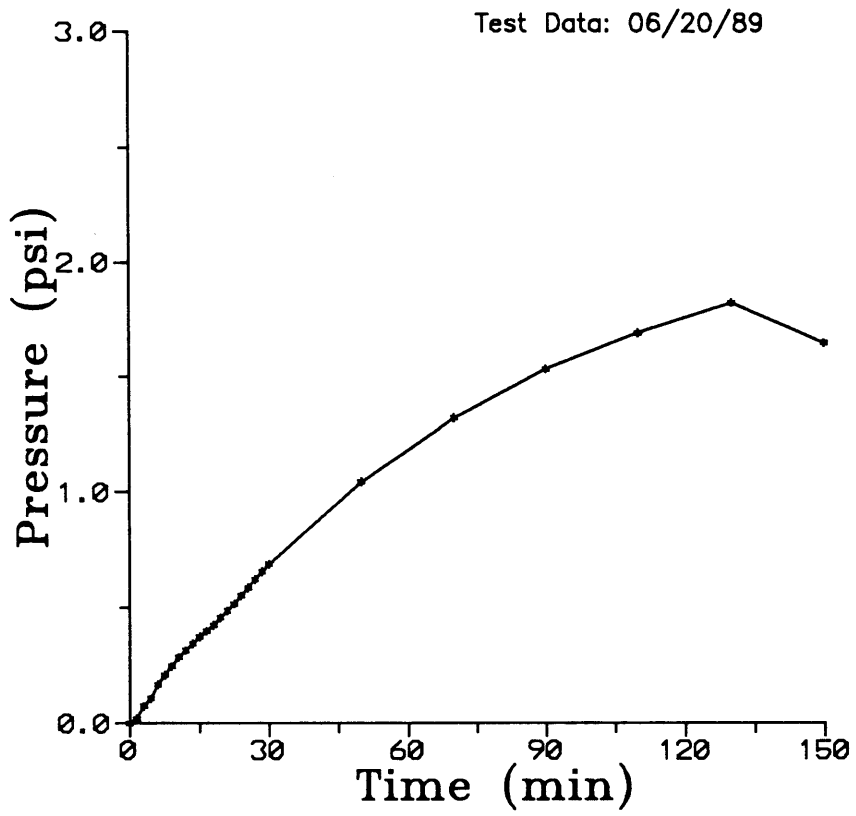
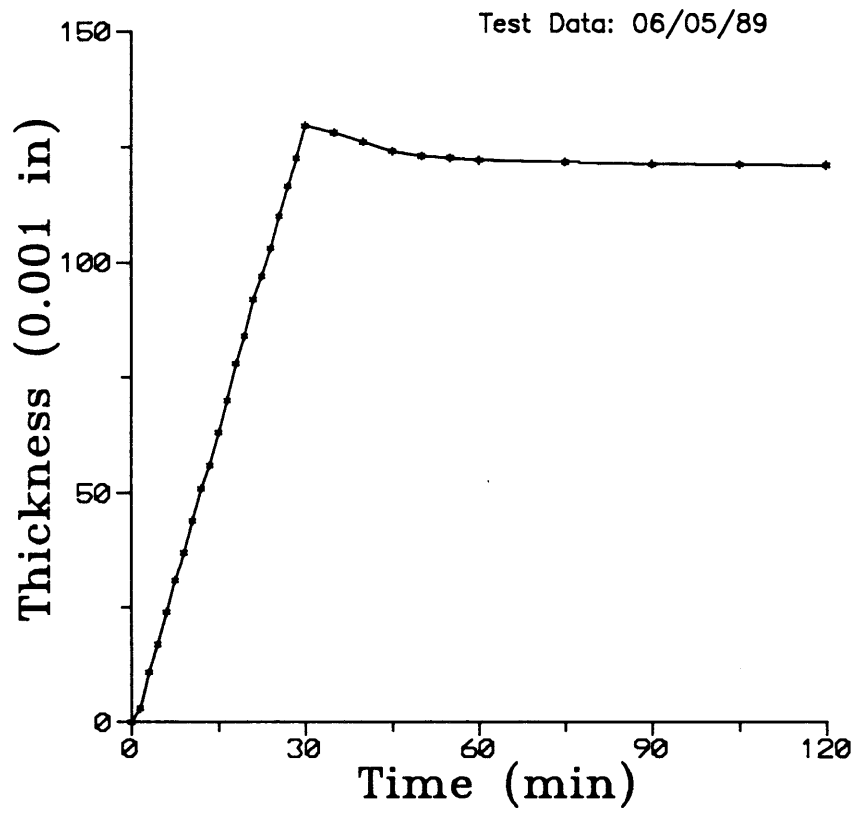Fig. H-6: Fluid pressure data in winding of 3k size fiber tow
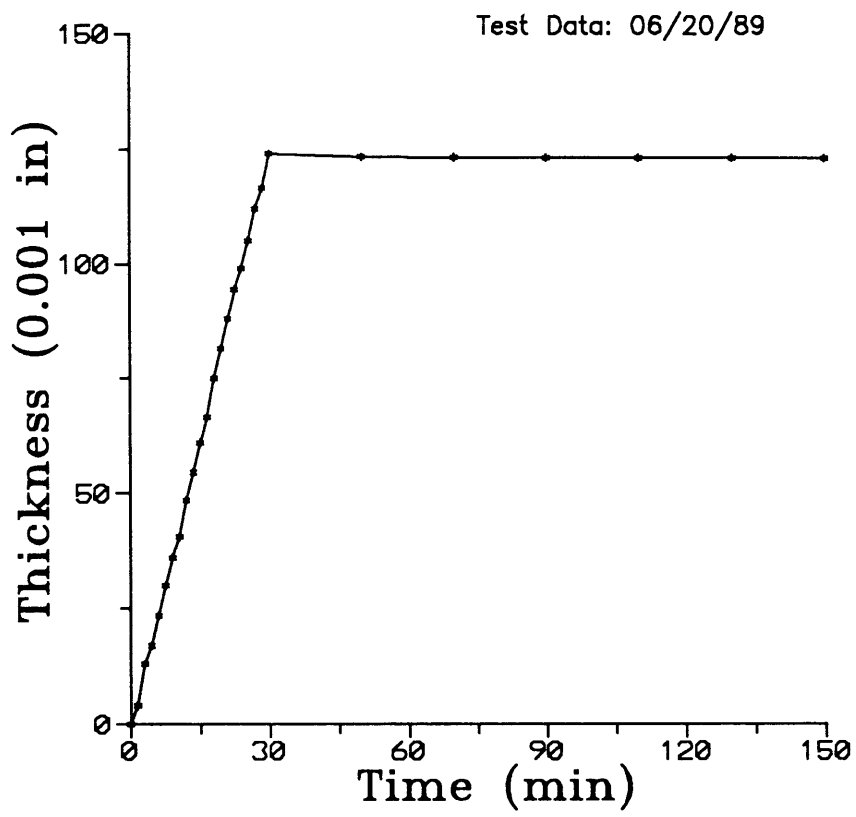
Fig. H-7: Layer thickness data in winding of 3k size fiber tow

e) Date: 06/22/89 (Test data of Fig. H-8 and Fig. H-9)

Tension: 8 lbf/tow   65 tows/layer   45 turns/min
Silicone fluid: 10,000 cst

Layer	Fluid Pressure (mV) (1 psi = 0.857 mV)	Thickness (0.001 in) (min)	(max)
0	12.187	77	86
1	12.222	81	91
2	12.260	89	99
3	12.306	97	107
4	12.354	103	112
5	12.391	110	118
6	12.427	117	126
7	12.457	121	131
8	12.490	129	139
9	12.514	134	143
10	12.537	140	150
11	12.554	146	156
12	12.579	153	163
13	12.600	160	169
14	12.631	169	179
15	12.652	173	183
16	12.673	179	189
17	12.693	185	195
18	12.713	195	203
19	12.733	203	211
20	12.756	208	216

Stop winding at 8:15 pm.

Time		Fluid pressure (mV)	Thickness (0.001 in)
8:15	pm	12.758	211.2
8:20		12.805	210.1
8:30		12.894	209.8
8:45		12.997	209.4
9:00		13.065	209.2
9:15		13.123	209.1
9:30		13.188	208.6
10:00		13.281	208.1
10:30		13.325	208.1
11:00		13.356	208.1
11:30		13.378	208.1
12:00	am	13.393	208.1
12:30		13.379	208.1
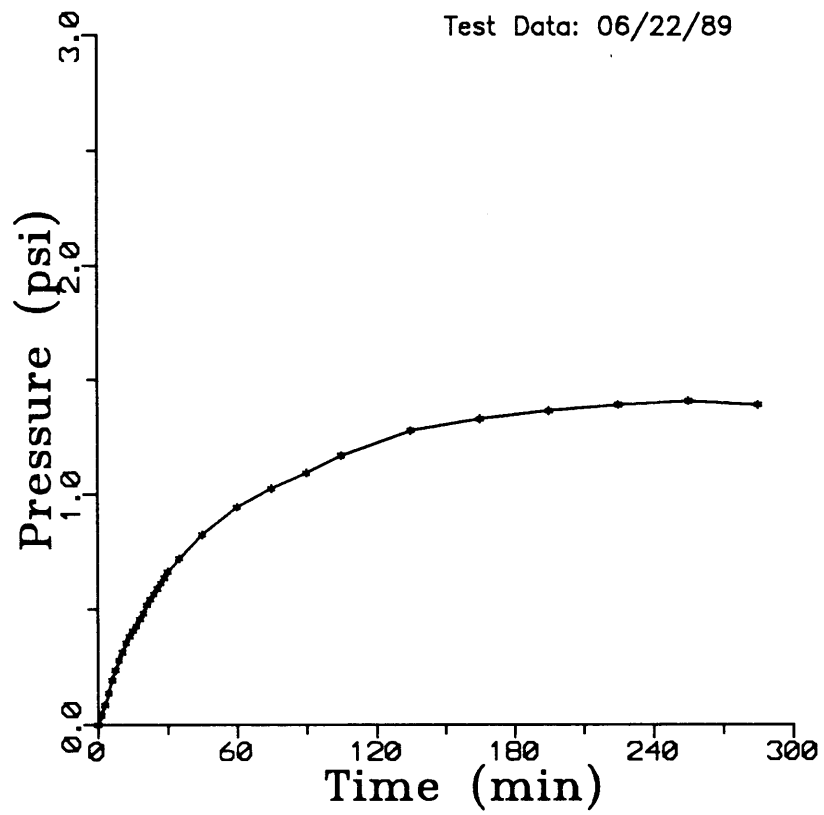
Fig. H-8: Fluid pressure data in winding of 3k size fiber tow
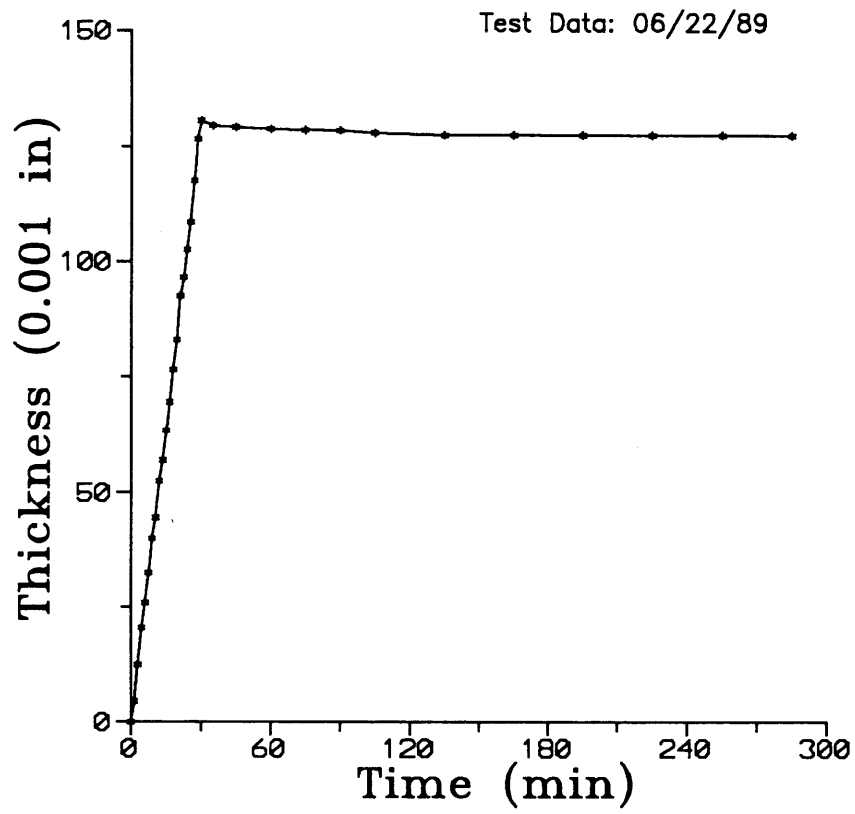
Fig. H-9: Layer thickness data in winding of 3k size fiber tow

Batch 2: Data of winding with RK 30-40k tows

a) Date: 12-21-89 (Test data of Fig. 5-24)   Data File: WF-1221A.DAT

Data: RK 30-40k fiber tow   Tension=20 lbf/tow
         8 tows/layer   10 layers
         Dow Corning silicone fluid, Viscosity=100,000 cst

Pressure measurement during winding: p_r=fluid pressure, p_t=total pressure.

Time (sec)	p_r (psi)	p_t (psi)	
0	0.07	1.99	
2	0.07	1.92	
4	15.53	12.78	
6	12.84	28.63	
8	11.43	30.44	
10	10.31	59.02	
12	29.53	70.30	
14	29.16	46.98	
16	21.97	36.27	
18	18.55	27.81	
20	26.94	26.60	
22	44.00	47.43	
24	33.54	47.53	
26	32.21	59.95	
28	36.58	53.44	
30	39.18	51.28	
32	37.85	46.91	
34	42.82	49.52	
36	43.19	61.76	
38	39.63	54.79	
40	40.37	67.12	
42	45.71	71.42	
44	46.08	64.47	
46	49.20	69.67	
48	58.62	83.14	
50	58.92	85.30	
52	56.69	91.71	
54	55.36	70.14	
56	54.39	83.61	
58	63.74	86.82	
60	54.02	70.77	
62	51.28	80.64	
64	49.35	75.70	
66	61.00	94.65	
68	51.72	93.75	
70	48.38	81.08	
72	44.67	68.60	
74	59.51	84.58	
76	52.17	75.70	
78	47.05	78.49	
80	50.16	81.98	(Stop winding)

b) Date: 12-22-89 (Test data of Fig. H-10)   Data File: WF-1222A.DAT

Data: RK 30-40k fiber tow   Tension=20 lbf/tow
        8 tows/layer   10 layers

        Dow Corning silicone fluid, Viscosity=100,000 cst

Pressure measurement during winding: p_r-fluid pressure, p_t-total pressure.

Time (sec)	p_r (psi)	p_t (psi)	
0	0.0	8.64	
2	10.31	5.37	
4	9.50	32.04	
6	5.86	21.77	
8	16.47	54.30	
10	37.40	44.60	
12	26.12	29.50	
14	20.93	23.83	
16	25.01	22.02	
18	26.79	25.86	
20	37.18	68.15	
22	29.98	67.12	
24	35.17	68.91	
26	39.85	67.12	
28	40.67	56.93	
30	44.75	57.90	
32	44.82	58.91	
34	41.18	78.09	
36	43.49	73.24	
38	48.90	94.35	
40	53.80	84.32	
42	49.20	79.98	
44	48.68	78.30	
46	50.76	79.34	
48	56.40	92.56	
50	49.94	107.71	
52	50.61	82.67	
54	62.33	107.32	
56	63.97	92.86	
58	51.57	78.09	
60	52.54	83.61	
62	60.03	96.83	
64	67.38	112.10	
66	61.67	112.93	
68	58.70	88.66	
70	59.88	88.92	
72	73.32	103.25	
74	66.71	92.56	
76	61.67	91.71	
78	66.56	101.83	
80	40.00	59.25	(Stop winding)
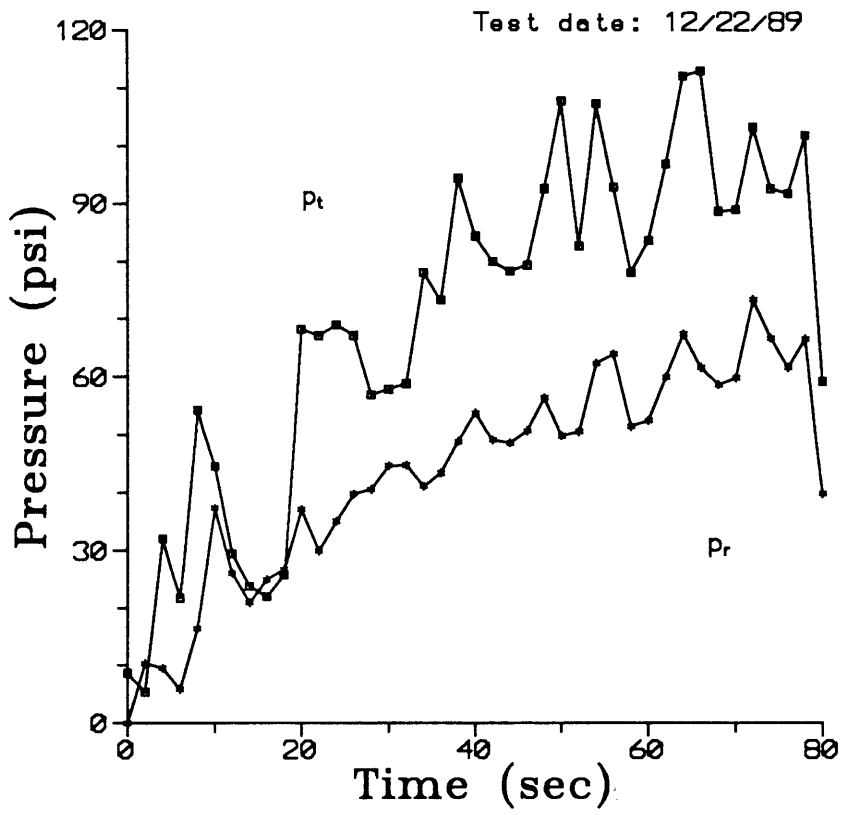
Fig. H-10: Fluid pressure data in winding of 40k size fiber tow

c) Date: 12-26-89 (Test data of Fig. H-11)   Data File: WF-1226A.DAT

Data: RK 30-40k fiber tow   Tension=20 lbf/tow
        8 tows/layer   10 layers

        Dow Corning silicone fluid, Viscosity=100,000 cst

Pressure measurement during winding: p_r=fluid pressure, p_t=total pressure.

Time (sec)	p_r (psi)	p_t (psi)	
0	0	2.52	
2	0.30	2.71	
4	14.25	15.73	
6	7.12	22.40	
8	5.19	16.87	
10	4.53	96.67	
12	29.91	84.39	
14	34.36	57.47	
16	26.57	39.49	
18	23.89	28.30	
20	33.02	23.23	
22	42.30	61.59	
24	40.96	77.21	
26	42.22	91.47	
28	48.01	75.92	
30	47.79	57.06	
32	42.08	50.40	
34	38.96	76.30	
36	45.71	94.52	
38	42.45	109.59	
40	43.86	97.83	
42	48.90	113.04	
44	53.06	80.40	
46	49.12	88.80	
48	46.53	85.25	
50	48.38	90.37	
52	53.21	109.36	
54	54.99	90.88	
56	57.44	100.80	
58	59.29	113.61	
60	61.00	93.74	
62	50.76	92.98	
64	55.80	112.58	
66	53.35	104.97	
68	54.84	118.40	
70	47.57	99.93	
72	58.40	104.13	
74	62.63	114.14	
76	65.52	112.54	
78	56.77	106.41	
80	58.62	109.93	(Stop winding)
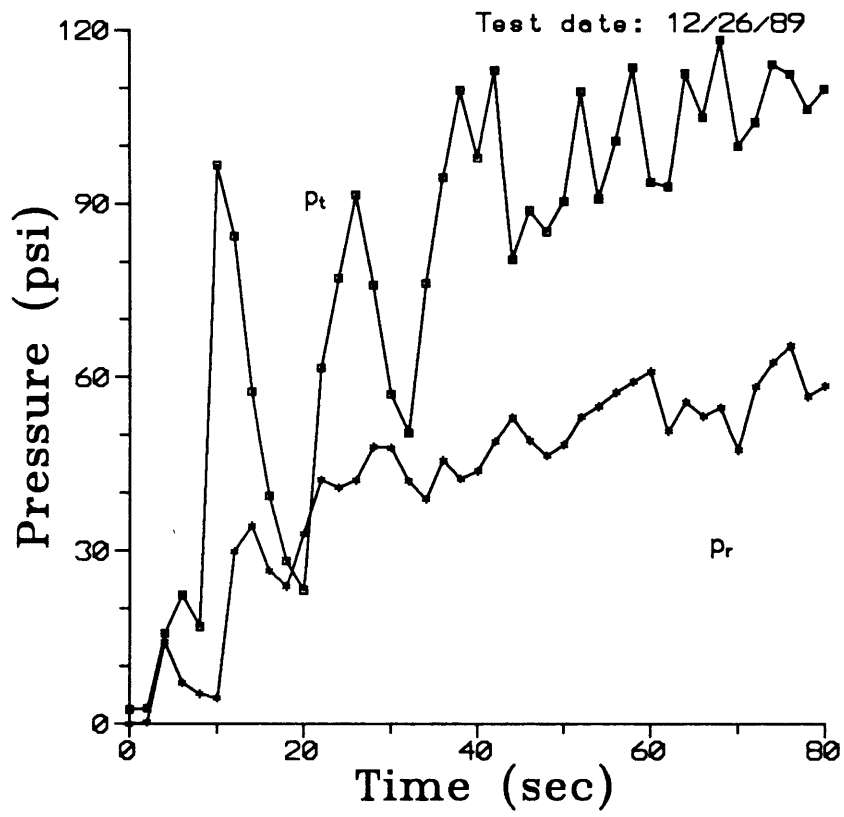
Fig. H-11: Fluid pressure data in winding of 40k size fiber tow

d) Date: 12-27-89 (Test data of Fig. H-12)   Data File: WF-1227A.DAT

Data: RK 30-40k fiber tow   Tension=20 lbf/tow
        8 tows/layer   10 layers

        Dow Corning silicone fluid, Viscosity=100,000 cst

Pressure measurement during winding: p_r=fluid pressure, p_t=total pressure.

| Time (sec)	p_r (psi)	p_t (psi)	
0	0	2.63	
2	0	3.78	
4	21.74	10.70	
6	13.36	19.78	
8	9.87	15.18	
10	11.06	72.69	
12	46.68	93.20	
14	33.17	45.73	
16	26.86	28.30	
18	26.64	23.29	
20	31.69	32.23	
22	45.56	42.91	
24	41.11	73.70	
26	40.37	69.72	
28	46.68	64.13	
30	40.67	51.86	
32	38,81	84.39	
34	43.11	77.61	
36	48.83	73.39	
38	49.57	88.15	
40	52.61	82.10	
42	60.40	83.40	
44	45.49	96.43	
46	49.42	100.40	
48	58.55	108.58	
50	67.68	117.74	
52	55.06	118.51	
54	58.85	100.88	
56	61.96	114.74	
58	72.13	110.71	
60	59.22	103.99	
62	56.77	109.72	
64	62.04	101.41	
66	82.44	129.91	
68	69.38	123.99	
70	63.37	103.23	
72	70.13	106.22	
74	73.61	103.97	
76	64.56	100.96	
78	54.76	94.13	
80	60.78	103.07	(Stop winding)

Fig. H-12: Fluid pressure data in winding of 40k size fiber tow

e) Date: 12-28-89 (Test data of Fig. H-13)   Data File: WF-1228A.DAT

Data: RK 30-40k fiber tow   Tension=20 lbf/tow
         8 tows/layer   10 layers

         Dow Corning silicone fluid, Viscosity=100,000 cst

Pressure measurement during winding: p_r=fluid pressure, p_t=total pressure.

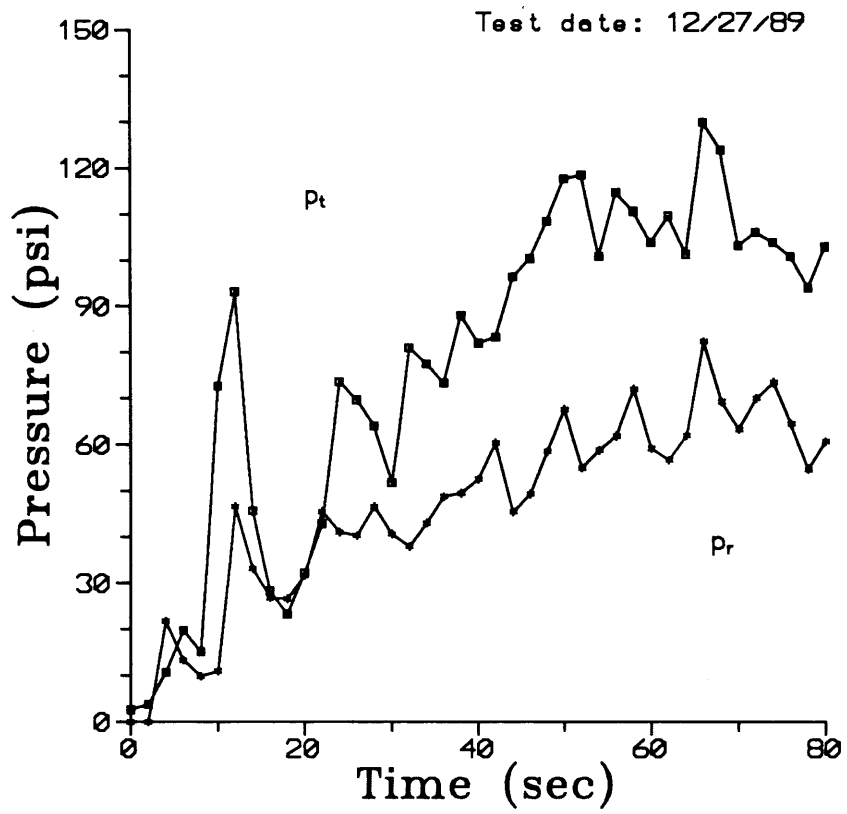| Time (sec)	p_r (psi)	p_t (psi)	
0	0	2.71	
2	13.36	14.49	
4	12.32	36.32	
6	6.75	24.10	
8	7.57	83.77	
10	29.46	53.38	
12	20.63	29.93	
14	15.73	17.24	
16	14.92	12.54	
18	35.03	29.88	
20	42.82	54.49	
22	35.77	48.53	
24	39.03	59.42	
26	50.16	55.92	
28	46.82	67.43	
30	42.15	71.64	
32	48.01	87.95	
34	50.02	77.45	
36	46.68	75.21	
38	47.86	76.70	
40	58.62	81.65	
42	53.06	84.88	
44	47.64	77.58	
46	48.38	77.06	
48	55.36	84.13	
50	51.72	95.92	
52	48.98	88.39	
54	52.39	77.60	
56	61.67	97.40	
58	56.17	81.31	
60	51.05	91.86	
62	58.03	86.70	
64	68.42	94.74	
66	60.48	78.19	
68	53.65	70.72	
70	60.33	70.72	
72	65.82	78.01	
74	58.40	68.53	
76	52.61	76.34	
78	60.55	90.72	
80	52.17	89.36	(Stop winding)
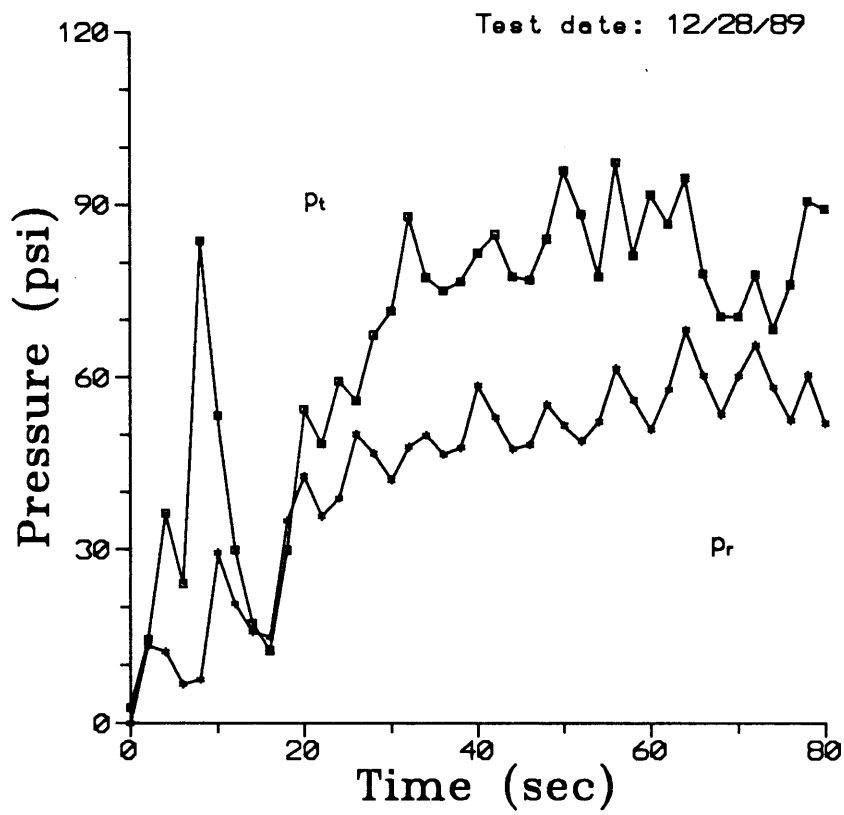
Fig. H-13: Fluid pressure data in winding of 40k size fiber tow

f) Date: 12-29-89 (Test data of Fig. H-14)   Data File: WF-1229A.DAT

Data: RK 30-40k fiber tow   Tension=20 lbf/tow
        8 tows/layer   10 layers
        Dow Corning silicone fluid, Viscosity=100,000 cst

Pressure measurement during winding: p_r=fluid pressure, p_t=total pressure.

Time (sec)	p_r (psi)	p_t (psi)	
0	0	2.67	
2	8.01	4.02	
4	15.66	14.26	
6	7.79	22.45	
8	5.86	23.52	
10	29.24	57.76	
12	27.60	38.56	
14	19.81	17.66	
16	17.66	19.10	
18	27.31	26.95	
20	39.48	44.56	
22	33.91	50.08	
24	33.17	61.86	
26	38.66	74.13	
28	41.63	68.39	
30	36.73	64.08	
32	38.74	79.61	
34	43.86	92.38	
36	47.64	88.02	
38	44.90	80.00	
40	53.13	90.13	
42	50.98	82.87	
44	40.22	77.60	
46	43.11	71.50	
48	50.91	91.64	
50	54.76	92.73	
52	50.24	99.61	
54	50.24	88.02	
56	55.73	86.32	
58	54.91	83.52	
60	48.38	78.74	
62	48.98	86.27	
64	53.21	93.61	
66	55.66	99.46	
68	41.78	89.59	
70	50.24	90.80	
72	67.83	109.29	
74	59.81	98.91	
76	52.39	93.04	
78	53.80	90.45	
80	44.60	82.60	(Stop winding)
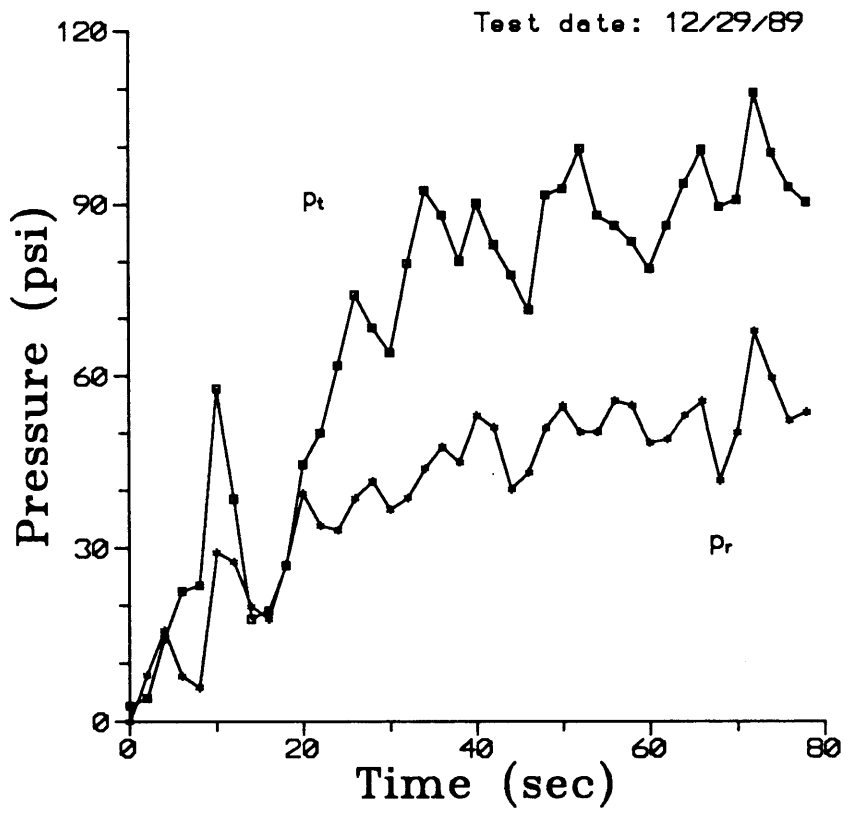
Fig. H-14: Fluid pressure data in winding of 40k size fiber tow

APPENDIX I

Experimental Data of Consolidation of Cylindrical Parts

<u>Batch 1: Consolidation with hose clamp device (4 clamps)</u>

a) Date: 01-26-90 (Test data of Fig. I-1)   Data File: WF-0126A.DAT

Data: Rk 30-40k fiber tow, Dow Corning silicone fluid (100,000 cst).
         10 wound layers, 8 tows/layer.

Time (min)	p_r (psi)	p_a (psi)
0	0	0
1	4.8	3.59
2	16.7	15.23
3	35.8	35.63
4	32.4	30.76
5	29.1	28.77
6	25.9	26.78
7	22.8	25.79
8	19.9	24.81
9	17.6	23.96
10	15.8	23.25
11	14.5	22.72
12	13.1	22.24
13	11.8	21.81
14	10.8	21.45
15	9.9	21.20
16	9.3	20.98
17	8.7	20.84
18	8.2	20.73
19	7.7	20.61
20	7.2	20.49
21	6.8	20.37
22	6.5	20.25
23	6.2	20.16
24	5.9	20.07
25	5.6	19.88
26	5.4	19.82
27	5.2	19.75
28	5.1	19.71
29	5.0	19.68
30	4.9	19.65
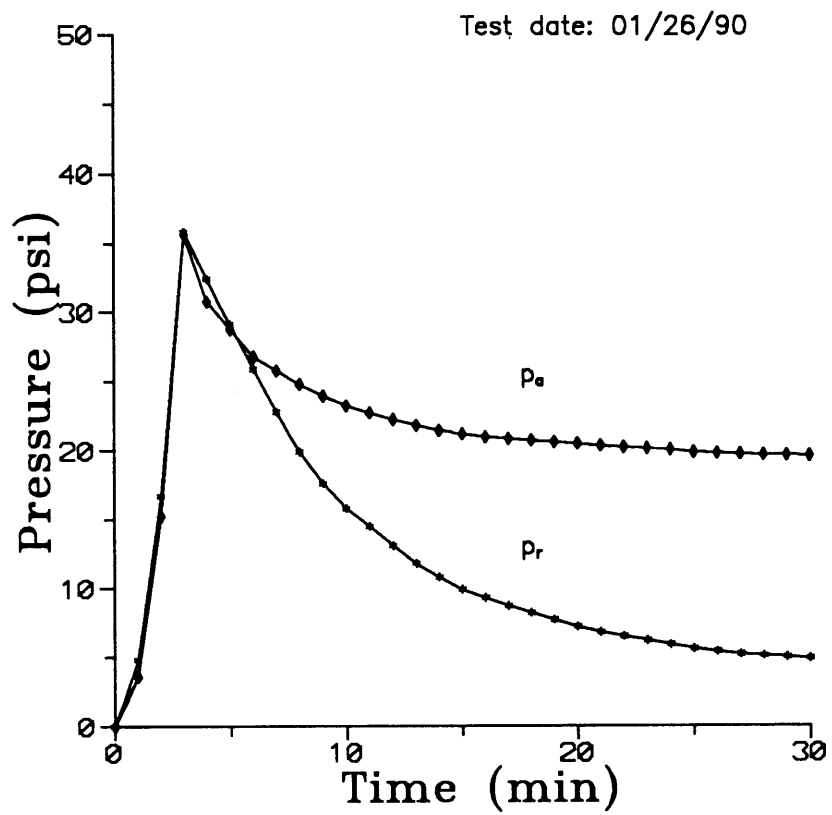
Fig. I-1: Experiment data of consolidation of cylindrical parts
(hose clamp device)

b) Date: 01-27-90 (Test data of Fig. I-2)   Data File: WF-0127A.DAT

Data: Rk 30-40k fiber tow, Dow Corning silicone fluid (100,000 cst).
        10 wound layers, 8 tows/layer.

Time (min)	p_r (psi)	p_a (psi)
0	0	0
1	4.9	4.6
2	18.0	17.2
3	37.5	38.4
4	33.2	33.5
5	29.9	30.2
6	27.4	29.3
7	25.2	28.4
8	23.3	27.6
9	21.6	26.9
10	20.0	26.2
11	18.5	25.6
12	17.2	25.1
13	15.9	24.5
14	14.8	24.0
15	13.7	23.5
16	12.6	23.1
17	11.4	22.7
18	10.3	22.3
19	9.4	21.9
20	8.6	21.6
21	7.9	21.3
22	7.3	21.1
23	6.8	20.8
24	6.4	20.6
25	6.0	20.4
26	5.7	20.2
27	5.5	20.1
28	5.4	19.9
29	5.2	19.8
30	5.1	19.6
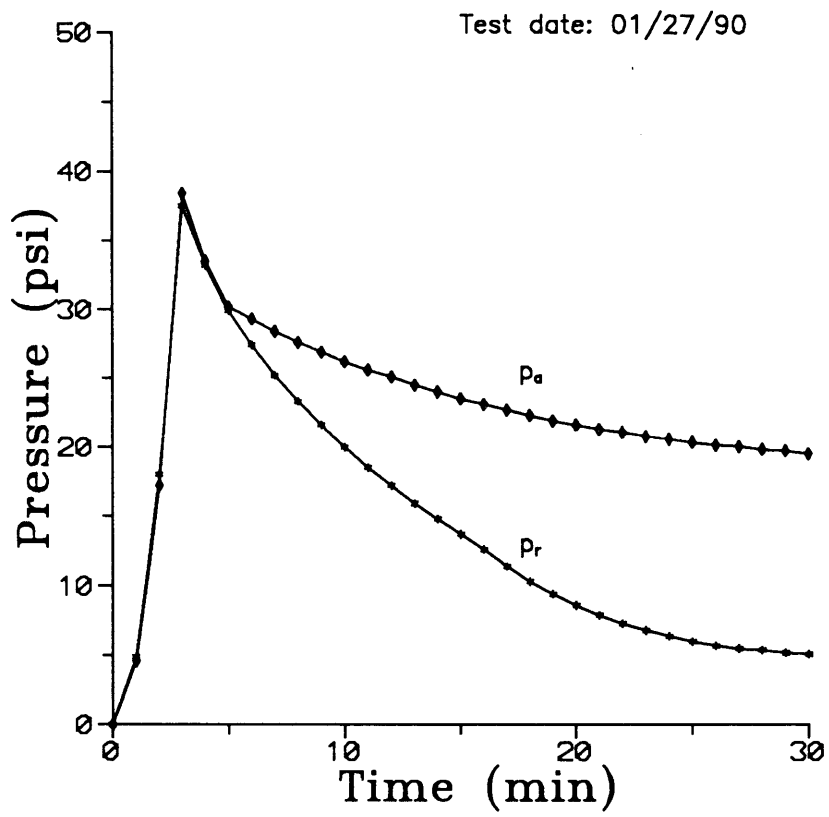
Fig. I-2: Experiment data of consolidation of cylindrical parts
(hose clamp device)

c) Date: 01-30-90 (Test data of Fig. I-3)   Data File: WF-0130A.DAT

Data: Rk 30-40k fiber tow, Dow Corning silicone fluid (100,000 cst).
        10 wound layers, 8 tows/layer.

Time (min)	p_r (psi)	p_a (psi)
0	0	0
1	5.2	4.2
2	18.5	19.0
3	35.6	36.6
4	32.3	32.7
5	29.6	30.4
6	27.1	29.0
7	25.0	28.3
8	23.2	27.7
9	21.7	27.1
10	20.3	26.6
11	19.0	26.1
12	17.9	25.7
13	16.9	25.3
14	16.0	24.9
15	15.2	24.6
16	14.4	24.3
17	13.6	23.9
18	12.9	23.6
19	12.2	23.3
20	11.5	22.9
21	10.9	22.6
22	10.3	22.4
23	9.7	22.1
24	9.0	21.9
25	8.4	21.7
26	7.9	21.6
27	7.4	21.4
28	6.9	21.2
29	6.5	21.0
30	6.0	20.9
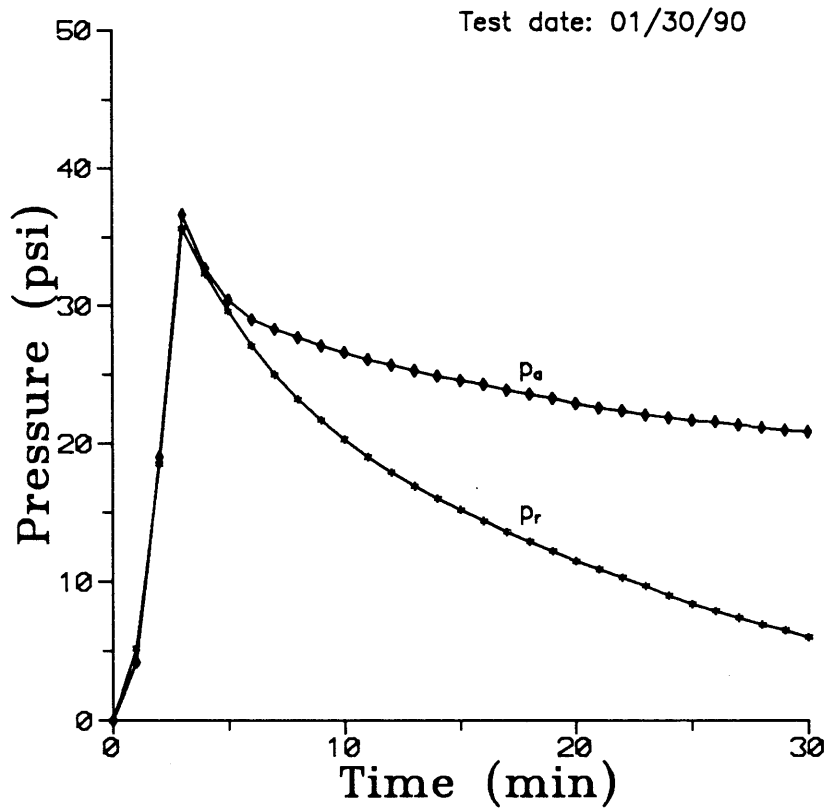
Fig. I-3: Experiment data of consolidation of cylindrical parts
         (hose clamp device)

Batch 2: Autoclave consolidation

a) Date: 02-16-90   Data File: WFP0216A.DAT

Data: Rk 30-40k fiber tow, Dow Corning silicone fluid (100,000 cst).
            10 wound layers, 8 tows/layer.

Simulation data:

        Fiber constants: V_o=0.5, V_a=0.85, A_s=0.06.
        Flow constants: V_a'=0.79, K_z=0.2.
        Simulation program: WC (with constant viscosity)

Time (min)	p_r (psi) (data)	p_a (psi)	p_r (psi) (model)
0	0	0	0
1	14.8	14.7	23.34
2	26.7	27.8	34.51
3	39.5	40.6	44.05
4	45.2	47.1	47.46
5	49.0	49.8	47.68
6	47.4	49.8	45.74
7	45.9	49.8	43.99
8	44.3	49.8	42.39
9	42.9	49.8	40.90
10	41.5	49.8	39.52
15	36.2	49.8	33.69
20	31.9	49.8	29.25
25	28.4	49.8	25.56
30	24.9	49.7	22.49
35	21.8	49.7	19.83
40	18.9	49.7	17.54
45	16.7	49.7	15.54
50	15.0	49.7	13.78
55	13.9	49.6	12.07
60	13.1	49.6	11.21

This set of test data and computer simulation is plotted in Fig. 5-27.

b) Date: 02-19-90   Data File: WFP0219A.DAT

Data: Rk 30-40k fiber tow, Dow Corning silicone fluid (100,000 cst).
        10 wound layers, 8 tows/layer.

Simulation data:

    Fiber constants: V_o=0.5, V_a=0.85, A_s=0.06.
    Flow constants: V_a'=0.79, K_z=0.2.
    Simulation program: WC (with constant viscosity)

Time (min)	p_r (psi) (data)	p_a (psi)	p_r (psi) (model)
0	0	0	0
1	12.7	12.5	20.79
2	25.0	24.3	31.22
3	33.8	34.1	38.37
4	42.8	43.0	44.32
5	48.3	48.9	47.43
6	46.9	48.9	45.45
7	45.2	48.8	43.68
8	43.5	48.8	42.06
9	42.0	48.7	40.56
10	40.6	48.7	39.16
15	36.0	48.7	33.30
20	31.7	48.6	28.86
25	27.8	48.6	25.20
30	24.3	48.6	22.11
35	21.2	48.6	19.46
40	18.8	48.5	17.18
45	16.9	48.5	15.19
50	15.4	48.5	13.46
55	14.1	48.5	11.94
60	13.0	48.5	10.60

This set of test data and computer simulation is plotted in Fig. I-4.
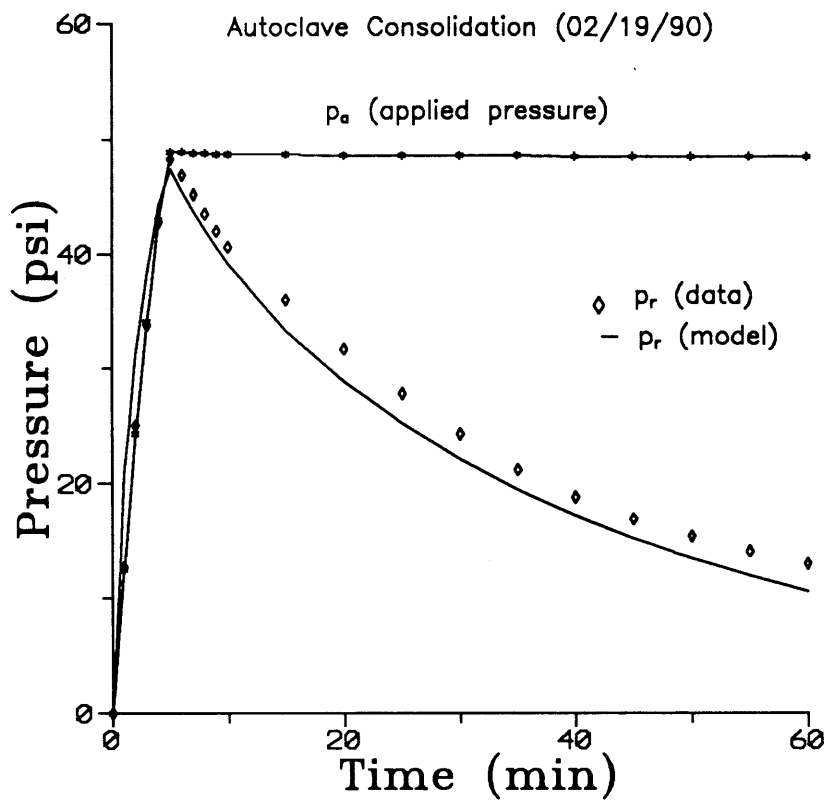
Fig. I-4: Experimental data with computer simulation results of
consolidation of cylindrical parts (autoclave set up)

c) Date: 02-20-90   Data File: WFP0220A.DAT

Data: Rk 30-40k fiber tow, Dow Corning silicone fluid (100,000 cst).
         10 wound layers, 8 tows/layer.

Simulation data:

    Fiber constants: V_o=0.5, V_a=0.85, A_s=0.06.
    Flow constants: V_a'=0.79, K_z=0.2.
    Simulation program: WC (with constant viscosity)

Time (min)	p_r (psi) (data)	p_a (psi)	p_r (psi) (model)
0	0	0	0
1	13.4	13.1	21.50
2	26.5	26.7	33.59
3	40.7	41.5	45.05
4	46.7	47.1	47.57
5	49.9	49.7	47.68
6	48.7	49.6	45.74
7	47.1	49.5	43.99
8	45.4	49.5	42.38
9	43.6	49.5	40.89
10	42.0	49.4	39.50
15	37.0	49.4	33.65
20	32.4	49.4	29.21
25	28.2	49.4	25.54
30	24.5	49.4	22.44
35	21.3	49.3	19.78
40	18.8	49.3	17.48
45	16.8	49.3	15.48
50	15.1	49.3	13.73
55	13.8	49.2	12.19
60	12.7	49.2	10.83

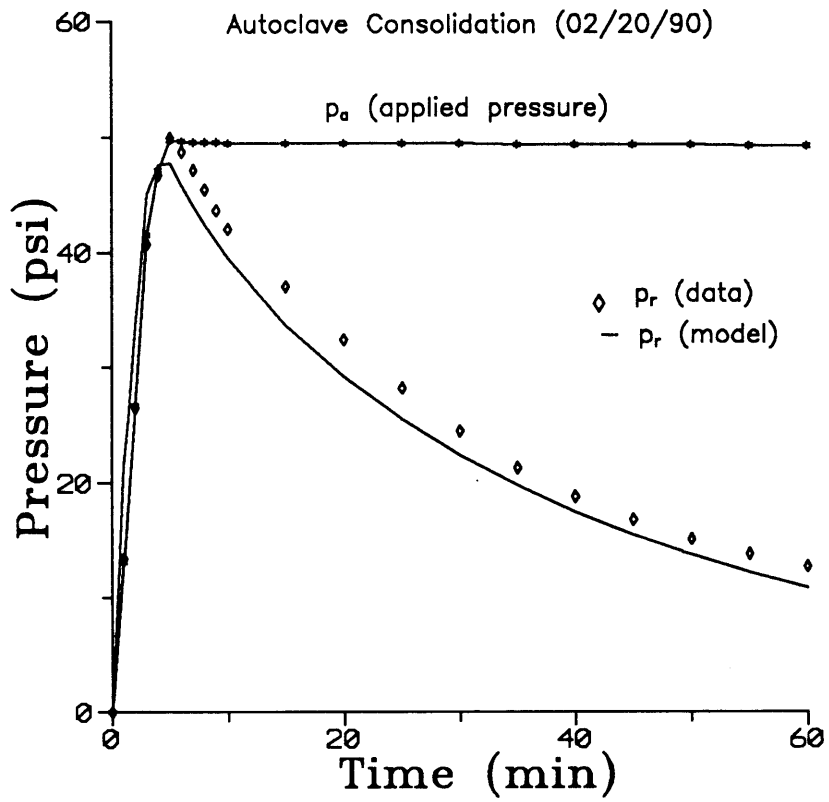This set of test data and computer simulation is plotted in Fig. I-5.

Fig. I-5: Experimental data with computer simulation results of
consolidation of cylindrical parts (autoclave set up)

REFERENCES

1. Springer, G.S., "Resin Flow During the Cure of Fiber Reinforced Composites," *Journal of Composite Materials*, Vol. 16, September 1982, pp. 400-410.

2. Lee, W.I., Loos, A.C., and Springer, G.S., "Heat of Reaction, Degree of Cure, and Viscosity of Hercules 3501-6 Resin," *Journal of Composite Materials*, Vol. 16, November 1982, pp. 510-520.

3. Loos, A.C., and Springer, G.S., "Curing of Epoxy Matrix Composites," *Journal of Composite Materials*, Vol. 17, March 1983, pp. 135-169.

4. Loos, A.C., and Springer, G.S., "Calculation of Cure Process Variables During Cure of Graphite-Epoxy Composites," in <u>Composite Materials, Quality Assurance and Processing</u>, C.E. Browning, Ed., ASTM STP 797, 1983, pp. 110-118.

5. Loos A.C., and Freeman, W.T., Jr., "Resin Flow During Autoclave Cure of Graphite-Epoxy Composites," in <u>High Modulus Fiber Composites in Ground Transportation and High Volume Applications</u>, ASTM STP 873, D.W. Wilson, Ed., 1985, pp. 119-130.

6. Springer, G.S., "Modeling the Cure Process of Composites," *SAMPE Journal*, September/October 1986, pp. 22-27.

7. Tang, J. M., Lee, W.I., and Springer, G.S., "Effects of Cure Pressure on Resin Flow, Voids, and Mechanical Properties," *Journal of Composite Materials*, Vol. 21, May 1987, pp. 421-440.

8. Krolewski, S.M., and Gutowski, T.G., "Effect of the Automation of Advanced Composite Fabrication Processes on Part Cost," *SAMPE Journal*, Vol. 23, No. 3, 1987, pp. 21-26.

9. Munro, M., "Review of Manufacturing of Fiber Composite Components by Filament Winding," *Polymer Composite*, Vol. 9, No. 5, October 1988, pp. 352-358.

10. Wilson, B.A., "Filament Winding - Past, Present, and Future," *34th International SAMPE Symposium*, May 8-11, 1989, pp. 2429-2439.

11. Liu, C.Y., and Chamis, C.C., "Residual Stresses in Filament-Wound Laminates and Optimum Programmed Winding Tension," *Proceedings*, Society of the Plastics Industry, 20th Annual Meeting, 1965, Section 5-D, pp. 1-10.

12. Fourney, W.L., "Residual Strain in Filament-Wound Rings," *Journal of Composite Materials*, Vol. 2, July 1968, pp. 408-411.

13. Dewey, B.R., and Knight, C.E., "Residual Strain Distribution in Layered Rings," *Journal of Composite Materials*, Vol. 3, July 1969, pp. 583-585.

14. Tarnopol'skii, Y.M., and Portnov, G.G., "Variation of Prestress in Filament-Wound Glass-Reinforced Plastics," *Mekhanika Polimerov*, Vol. 2, No. 2, 1966, pp. 278-284.

15. Beil, A.I., Portnov, G.G., Sanina, I.V., and Yakushin, V.A., "Elimination of the Initial Thermal Stresses in Wound Articles Made from Composites by Varying the Winding Angle over the Thickness," *Mechanics of Composite Materials*, Vol. 16, No. 6, November-December 1980, pp. 715-720.

16. Grabovskii, A.P., "Residual Stresses in a Reel of Magnetic Tape," *Soviet Applied Mechanics*, Vol. 20, No. 1, July 1984, pp. 95-100.

17. Altmann, H.C., "Formulas for Computing the Stresses in Center-Wound Rolls," *TAPPI*, Vol. 51, No. 4, April 1968, pp. 176-179.

18. Willett, M.S., and Poesch, W.L., "Determining the Stress Distributions in Wound Reels of Magnetic Tape Using a Nonlinear Finite-Difference Approach," *Journal of Applied Mechanics*, Vol. 55, June 1988, pp. 365-371.

19. Lin, J.Y., and Westmann, R.A., "Viscoelastic Winding Mechanics," *Journal of Applied Mechanics*, Vol. 56, December 1989, pp. 821-827.

20. Reuter, R.C. Jr., "Prediction and Control of Macroscopic Fabrication Stresses in Hoop Wound, Fiberglass Rings," Analysis of the Test Methods for High Modulus Fibers and Composites, ASTM STP 521, American Society for Testing and Materials, 1973, pp. 264-276.

21. Spencer, B.E., "Prediction of Manufacturing Stresses in Thickwalled Orthotropic Cylinders," *Proceedings of 31st International SAMPE Symposium*, April, 1986, pp. 867-879.

22. Spencer, B.E., "Prediction of Manufacturing Stresses in Thick-walled Orthotropic Cylinders," Ph.D. Thesis, *The University of Nebraska-Lincoln*, 1988.

23. Spencer, B.E., "Modeling the Filament Winding Process," *Proceedings of 34th International SAMPE Symposium*, Reno, Nevada, May, 1989, pp. 1556-1570.

24. Calius, E.P., and Springer, G.S., "Modeling the Filament Winding Process," *Proceedings of Fifth International Conference on Composite Materials (ICCM-V)*, August, 1985, pp. 1071-1087.

25. Calius, E.P., and Springer, G.S., "Selecting the Process Variables for Filament Winding," 31st International SAMPE Symposium, April 7-10, 1986, pp. 891-899.

26. Calius, E.P., Springer, G.S., Wilson, B.A., and Hansen, R.S., "Validation of the Filament Winding Process Model," 32nd International SAMPE Symposium, April 6-9, 1987, pp. 670-676.

27. Calius, E.P., and Springer, G.S., "Filament Winding Process Simulation," in The Manufacturing Science of Composites, *Proceedings of Manufacturing International'88*, Vol. 4, edited by T. Gutowski, April, 1988, pp. 49-55.

28. Calius, E.P., Kidron, M., Lee, S.Y., and Springer, G.S., "Manufacturing Stresses and Strains in Filament Wound Cylinders," *SAMPE Journal*, May/June 1988, pp. 7-9.

29. Calius, E.P., "Filament Winding of Composite Cylinders," Ph.D. Thesis, *Stanford University*, 1989.

30. Lee, S.Y., "Filament Winding Process Model," Ph.D. Thesis, *Stanford University*, 1989.

31. Tarnopol'skii, Y.M., and Beil, A.I., "Problems of the Mechanics of Composite Winding," Chapter II in <u>Handbook of Composites</u>, Vol. 4 — *Fabrication of Composites*, edited by A. Kelly and S.T. Mileiko, Elsevier Science Publishers B.V., 1983, pp. 45-108.

32. Tarnopol'skii, Y.M., Portnov, G.G., and Beil, A.I., "Technological Problems in Composite Winding Mechanics," in <u>Mechanics of Composites</u>, edited by I.F. Obraztsov and V.V. Vasil'ev, translated from the Russian by V.I. Ilyushchenko, MIR Publishers, Moscow, 1982, pp. 186-222.

33. Gutowski, T.G., "A Resin Flow/Fiber Deformation Model for Composites," *SAMPE Quarterly*, Vol.16, No.4, July 1985, pp. 58-64.

34. Gutowski, T.G., Morigaki, T., and Cai, Z. "The Consolidation of Laminate Composites," *Journal of Composite Materials*, Vol.21, February 1987, pp. 172-188.

35. Gutowski, T.G., Cai, Z., Bauer, S., Boucher, D., Kingery, J., and Wineman, S., "Consolidation Experiments for Laminate Composites," *Journal of Composite Materials*, Vol.21, July 1987, pp. 650-669.

36. Scheidegger, A.E., <u>The Physics of Flow through Porous Media</u>, U. Toronto Press, 3rd ed. 1974, pp. 73-83.

37. Terzaghi, K., and Peck, R.B., <u>Soil Mechanics in Engineering Practice</u>, John Wiley & Sons, 1967, pp. 58-59.

38. Cai, Z., and Gutowski, T.G., "The General Deformation Behavior of a Lubricated Fiber Bundle," *Proceedings of 34th International SAMPE Symposium*, Reno, Nevada, May 1989, pp. 341-349.

39. Saada, A.S., <u>Elasticity Theory and Applications</u>, Pegamon, 1974, pp. 325.

40. Bhi, S.T., Hansen, R.S., Wilson, B,A., Calius, E.P., and Springer, G.S., "Degree of Cure and Viscosity of Hercules HBRF-55 Resin," 32nd International SAMPE Symposium, April 6-9, 1987, pp. 1114-1118.

41. Maximovich, M.G., and Galeos, R.M., "Rheological Characterization of Advanced Composite Prepreg Materials," 28th National SAMPE Symposium, April 12-14, 1983, pp. 568-580.

42. Tsai, S.W., and Hahn, H.T., _Introduction to Composite Materials_, Technomic, 1980, pp. 396.

43. Bird, R.B., Stewart, W.E., and Lightfoot, E.N., _Transport Phenomena_, John Wiley & Sons, 1960, pp. 310-323.

44. Cravalho, E.G., and Smith, J.L. Jr., _Engineering Thermodynamics_, Pitman, 1981, pp. 350-358.

45. Tsai, S.W., and Hahn, H.T., _Introduction to Composite Materials_, Technomic, 1980, pp. 342.

46. Longcope, D.B., Forrestal, M.J., and Warren, W.E., "Thermal Stresses in a Transversely Isotropic, Hollow, Circular Cylinder," _AIAA Journal_, Vol. 7, No. 11, November 1969, pp. 2174-2176.

47. Misra, J.C., and Achari, R.M., "On Axisymmetric Thermal Stresses in an Anisotropic Hollow Cylinder," _Journal of Thermal Stresses_, Vol. 3, 1980, pp. 509-520.

48. Chen P.Y.P., "Axisymmetric Thermal Stresses in an Anisotropic Finite Hollow Cylinder," _Journal of Thermal Stresses_, Vol. 6, 1983, pp. 197-205.

49. Hyer, M.W., and Cooper, D.E., "Stresses and Deformations in Composite Tubes due to a Circumferential Temperature Gradient," _Journal of Applied Mechanics_, Vol. 53, December 1986, pp. 757-764.

50. Gutowski, T.G., Kingery, J., and Boucher, D., "Experiments in Composites Consolidation: Fiber Deformation," _Proceedings of the Society of Plastics Engineers 44th Annual Technical Conference_, Boston, May 1986, pp. 1316-1320.

51. Curiskis, J.I., and Carnaby, G.A., "Continuum Mechanics of the Fiber Bundle," _Textile Research Journal_, Vol. 55, June 1985, pp. 334-344.

52. van Wyk, C.M., "Note on the Compressibility of Wool," _Journal of Textile Institute_, Vol. 37, 1946, T285-T292.

53. Treloar, L.R.G., "The Stress-Strain Properties of Multiply Cords, Part I: Theory," _Journal of Textile Institute_, Vol. 56, 1956, T477-T488.

54. Hearle, J.W.S., "Theory of the Extension of Continuous Filament Yarns," Ch. 4 in _Structural Mechanics of Fibers Yarns, and Fabrics_, Vol. 1, J.W.S.Hearle, P.Grosberg, and S.Backer, Eds., Wiley-Interscience, 1969, pp. 175-212.

55. Thwaites, J.J., "A Continuum Model for Yarn Mechanics," in _Mechanics of Flexible Fiber Assemblies_, J.W.S.Hearle, J.J.Thwaites, and J.Amirbayat, Eds., Sijthoff and Noordhoff, Alphen aan den Rijn, The Netherlands, 1980, pp. 87-97.

56. Adams, D.F., and Odom E.M., "Testing of Single Fiber Bundles of Carbon/Carbon Composite Materials," _Composites_, Vol.18, No.5, November 1987, pp. 381-385.

57. Soll, W.E., "Behavior of Advanced Thermoplastic Composites in Forming", S.M. Thesis, Dept of M.E., MIT, June 1987.

58. Soll, W.E., and Gutowski, T.G., "Forming Thermoplastic Composite Part", *SAMPE Journal*, May/June 1988, pp. 15-19.

59. Cogswell, F.N., and Groves, D.J., "The Melt Rheology of Continuous Fiber Reinforced Structural Composite Materials," *Proceedings of 10th International Congress of Rheology*, Sydney, Australia, August 1988.

60. Gutowski, T.G. et al., "The Mechanics of Composites Deformation During Manufacturing Processes," *Proceedings of the American Society for Composites*, First Technical Conference, Dayton, Ohio, Oct. 1986, pp. 154-163.

61. Bird, R.B., Amstrong, R.C., and Hassager, O., <u>Dynamics of Polymeric Liquids</u>, Vol. 1, John Wiley & Sons, 1977, pp. 141-148.

62. Middleman, S., <u>Fundamentals of Polymer Processing</u>, McGraw-Hill, 1977, pp. 28-31.

63. Tadmor, Z., and Gogos, C.G., <u>Principles of Polymer Processing</u>, John Wiley & Sons, 1979, pp. 109-117.

64. Cai, Z., "Molding Behavior of Composites," S.M. Thesis, Dept. of M.E., MIT, June 1986.

65. Tsai, S.W., and Hahn, H.T., <u>Introduction to Composite Materials</u>, Technomic, 1980. pp. 388-394.

66. Timoshenko, S.P., and Gere, J.M., <u>Mechanics of Materials</u>, Brooks-Cole, 1972, pp. 354-368.

67. Kingery, J., "Composite Process Modeling: Consolidation of Aligned Fiber Assemblies," S.M. Thesis, Dept. of M.E., MIT, June 1985.

68. Larsen, R.J., and Marx, M.L., <u>An Introduction to Mathematical Statistics and its Applications</u>, Prentice-Hall, 1986, pp. 133-143.

69. Strang, G., <u>Introduction to Applied Mathematics</u>, Wellesley-Cambridge Press, 1986, pp. 373-374.

70. Dahlquist, G., and Bjorck, A., <u>Numerical Methods</u>, Prentice-Hall, 1974, pp. 165-174.

71. Ingersoll, L.R., <u>Heat Conduction: with Engineering, Geological and Other Applications</u>, University of Wisconsin Press, Madison, 1954, pp. 15.

72. Hou, T.H., "A Resin Flow Model for Composite Prepreg Laminate Process," *Proceedings of the Society of Plastics Engineers 44th Annual Technical Conference*, May 1986, Boston, pp. 1300-1305.

73. Dave, R., Kardos, J.L., and Dudukovic, M.P., "A Model for Resin Flow During Composite Processing Part 2: Numerical Analysis for Unidirectional Graphite/Epoxy Laminates," *Polymer Composites*, Vol. 8, No. 2, April 1987, pp. 123-132.

74. Kim, T.W., Yoon, K.J., Jun, E.J., and Lee, W.I., "Compaction Behavior of Composite Laminates During Cure," *SAMPE Journal*, Vol. 24, No.5, Sep/Oct 1988, pp. 33-36.

75. Carlsson, L.A., and Pipes, R.B., Experimental Characterization of Advanced Composite Materials, Prentice-Hall, 1987, pp. 43-52.